ETH Zurich | PhD Dissertation No. 28875

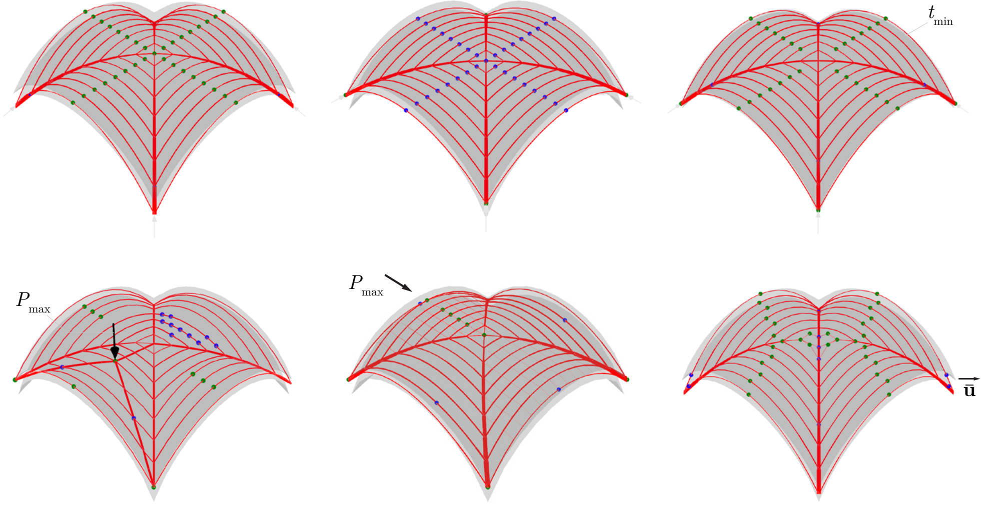

Thrust Network Optimisation for the Assessment of Vaulted Masonry Structures

Ricardo Maia Avelino

Diss. ETH No. 28875

Thrust Network Optimisation for the Assessment of Vaulted Masonry Structures

A thesis submitted to attain the degree of

Doctor of Sciences of ETH Zurich
(Dr. sc. ETH Zurich)

presented by

Ricardo Maia Avelino

Ingénieur diplômé, École Nationale des Ponts et Chaussées, 2018

born on 19.04.1994
citizen of Brazil

Accepted on the recommendation of

Prof. Dr. Philippe Block
Prof. Dr. John Ochsendorf
Dr. Tom Van Mele
Dr. Andrew Liew

2023

To Crizoldo

Acknowledgements

I am grateful for the brilliant and kind people that encouraged me throughout my education and were endless sources of inspiration and motivation.

I especially thank my supervisor, Prof. Dr. Philippe Block, for sharing his knowledge and vision and giving me the freedom to explore my research interests. I also thank my co-supervisor, Dr. Tom Van Mele, for all the computational support and nerdy chats, and Prof. Dr. John Ochsendorf and Dr. Andrew Liew, for joining my doctoral committee and contributing highly to the final version of this dissertation.

My time in Zurich and the friendships I made at the BRG and ETH shaped who I am today. Sharing this journey with you has been a great honour. I especially thank Dr. Juney Lee, Dr. Robin Oval, Dr. Mariana Popescu, and Dr. Antonino Iannuzzo for always believing in me and being a model of inspiration, and Dr. Alessandro Dell'Endice, Lotte Scheder-Bieschin, Mark Tam, Gene Kao, Francesco Ranaudo, Lukas Gebhard, and Julia Boshart, for sharing the struggles, failures, and successes of the PhD life.

I thank my family for teaching me the importance of education, especially my mom, Antonia, who sacrificed so much so my brother and I could keep studying, my aunt, Cleide, and uncle, Bruno, who took care of me in São Paulo, and my father, Crizoldo, who taught me the value of blazing my own trail and whom I miss so much every single day.

Finally, one person in specific has followed all the ups and downs of this journey, giving up so much for me to complete it. I thank my wife, Mariana, for her tireless support, love, and for not letting me forget why I started it. On to the next adventure!

Thank you all for pushing me to keep learning.

Abstract

Masonry structures are ubiquitous in our society, serving as housing for millions worldwide and forming a large part of the world's built heritage. Their assessment and preservation are essential to achieving a more sustainable and resilient built environment.

This dissertation presents a novel computational approach to assess unreinforced vaulted masonry structures. A novel limit-analysis-based framework is developed to search for admissible equilibrium states. The equilibrium solutions considered are represented by compressive thrust networks within the structure's geometry, representing their compressive flow of forces. A modular multi-objective constrained nonlinear optimisation problem is formulated and solved using interior point and sequential least-square quadratic programming techniques to search for admissible networks.

Different objective functions are implemented in the optimisation framework, including the minimum and maximum horizontal thrust states, the maximum Geometric Safety Factor (GSF), maximum vertical and horizontal load multipliers, and the complementary energy minimisation for prescribed foundation displacements. The problem's constraints are formulated to translate the limit analysis admissibility criteria to thrust networks. Gradient vectors and Jacobian matrices are described analytically and computed modularly based on the objective, variables, and constraints selected.

The present formulation requires minimal input, encouraging its future application as a practical numerical tool to assess existing masonry structures. Only the structural envelope, typically obtained through surveys, and the topology and planar geometry of the thrust network are needed for the analysis. The networks' topology is explored, quantifying different patterns. Pattern modification strategies are developed for problems involving different objectives. A new algorithm is described to identify the degrees of freedom in the networks necessary to analyse general topologies. A convex load-path optimisation is formulated and used as starting point for the nonlinear problems.

The framework developed provides a single approach which contributes to three critical open questions in the field:

1. Computing the level of stability of vaulted masonry structures by introducing the stability domain, enabling to compute global safety factors and evaluating the structural robustness.
2. Estimating a lower bound of horizontal and vertical collapse loads by directly maximising a scalar load multiplier, contributing to protecting structures against extreme external actions and evaluating newly imposed loads.
3. Understanding the effects of foundation settlements on crack patterns by investigating minimum energy solutions arising after differential displacements, which can inform the identification and evolution of pathologies in masonry structures.

Throughout the dissertation, several examples are presented to demonstrate the possibilities of the framework. Finally, the implementation is offered as an open-source Python package, enabling future collaboration and further development.

Keywords: masonry structures, limit analysis, thrust network analysis, structural assessment, optimisation, vaults, safety factor, stability, collapse loads, settlements.

Résumé

Les structures en maçonnerie sont omniprésentes dans notre société, servant de logement à des millions de personnes dans le monde et constituant une grande partie du patrimoine bâti mondial. L'évaluation structurale et la préservation des structures maçonnées sont essentielles pour achever un environnement bâti plus durable et résilient.

Cette thèse présente une nouvelle approche informatique pour évaluer les structures de maçonnerie voûtées non renforcées. Cette approche est basée sur l'analyse limite des structures qui permet la recherche des états d'équilibre admissibles. Les états d'équilibre admissibles considérés sont représentés par des réseaux de poussée compressifs contenus dans la géométrie de la structure. Ces réseaux de force modélisent un flux de force de compression dans la structure. Un problème d'optimisation multi-objectif contrainte modulaire est formulé et résolu à l'aide de techniques de programmation non linéaire dont la méthode de point intérieur et la programmation séquentielle des moindres carrés.

Différentes fonctions objectives sont implémentées dans le cadre de l'optimisation : les états de poussée horizontale minimal et maximal, le facteur de sécurité géométrique maximal, les multiplicateurs de charge verticale et horizontale limite et la minimisation de l'énergie complémentaire suite à des tassements. Les contraintes du problème sont formulées pour exprimer les critères d'admissibilité de l'analyse limite aux réseaux de poussée. Les vecteurs de gradient et les matrices jacobiennes sont décrits analytiquement et calculés de manière modulaire en fonction de l'objectif, des variables et des contraintes sélectionnés.

La formulation développée nécessite un apport des données minimal, encourageant son application future en tant qu'outil numérique pratique pour évaluer les structures de maçonnerie. Seules l'enveloppe structurelle, générale-ment obtenue par des sondages, ainsi que la topologie et la géométrie plane du réseau de force sont nécessaires à l'analyse. La topologie des réseaux est explorée, et stratégies pour adapter les réseaux selon différents objectifs sont présentés. Un nouvel algorithme est décrit pour identifier les degrés de liberté dans les réseaux nécessaires à l'analyse des topologies générales. Une optimisation convexe du chemin de charge optimal en compression est formulée et utilisée comme point de départ pour les problèmes non linéaires.

Le cadre développé fournit une approche unique qui peut être utilisée pour étudier trois questions critiques pour l'analyse des structures maçonnées :

1. Le calcul du niveau de stabilité des structures voûtées en maçonnerie en introduisant le domaine de stabilité, permettant de calculer les facteurs de sécurité globaux et d'évaluer la robustesse de la structure.
2. L'estimation d'une limite inférieure des charges d'effondrement horizontales et verticales en maximisant un multiplicateur de charge scalaire, en contribuant à protéger les structures contre les actions externes extrêmes et en évaluant les charges nouvellement imposées.
3. Les effets des tassements sur les fissures couramment observés en étudiant les réseaux de minimum énergie soumis à des de déplacements différentiels, qui peuvent éclairer l'identification et l'évolution de pathologies dans les structures.

Tout au long de la thèse, plusieurs exemples sont présentés pour démontrer les possibilités du framework. Enfin, l'implémentation est proposée sous la forme d'un package Python open source, permettant une collaboration future et un développement ultérieur.

Mots-clefs: structures en maçonnerie, analyse limite, thrust network analysis, évaluation structurelle, optimisation, voûtes, facteurs de sécurité, stabilité structurelle, charges limites, tassements.

Contents

Notation

Symbol	Shape	Description
Γ	-	form diagram
Γ^*	-	force diagram
Γ_d	-	form diagram centroidal dual
G	-	thrust network
Λ	-	masonry envelope
$\Lambda^\mathrm{LB}, \Lambda^\mathrm{UB}, \Lambda^\mathrm{m}$	-	intrados, extrados and middle surfaces
$\tilde{\Lambda}^\mathrm{LB}, \tilde{\Lambda}^\mathrm{UB}, \tilde{\Lambda}^\mathrm{m}$	-	intrados, extrados and middle heightfield
Λ_min	-	masonry minimal envelope
x_i, y_i, z_i	-	coordinates of vertex i
$z_i^\mathrm{LB}, z_i^\mathrm{UB}$	-	intrados and extrados elev. at vertex i
z_i^m	-	middle surface elev. at vertex i
n	-	number of network vertices
m	-	number of network edges
$n_\mathrm{i}, n_\mathrm{b}$	-	number of free and support vertices
n_F	-	number of faces
q_i	-	force density of edge i
l_i	-	cartesian length of edge i
f_i	-	axial force of edge i
k	-	number of independent edges
$\mathbf{x}$, $\mathbf{y}$, $\mathbf{z}$	$[n \times 1]$	vertex coordinates
$\mathbf{x}_\mathrm{i}$, $\mathbf{y}_\mathrm{i}$, $\mathbf{z}_\mathrm{i}$	$[n \times 1]$	free vertex coordinates
$\mathbf{x}_\mathrm{b}$, $\mathbf{y}_\mathrm{b}$, $\mathbf{z}_\mathrm{b}$	$[n_\mathrm{i} \times 1]$	support vertex coordinates
$\mathbf{p}_\mathrm{x}$, $\mathbf{p}_\mathrm{y}$, $\mathbf{p}_\mathrm{z}$	$[n \times 1]$	lumped vertex loads
$\mathbf{p}_\mathrm{z}^\mathrm{ext}$	$[n \times 1]$	external vertical loads

$\mathbf{p}_{\mathrm{h}}^{\mathrm{ext}}$	$[2n \times 1]$	external horizontal loads
$\mathbf{q}$	$[m \times 1]$	force density vector
$\mathbf{q}_{\mathrm{id}}$	$[k \times 1]$	independent force density vector
$\mathbf{C}$	$[m \times n]$	connectivity matrix
$\mathbf{C}_{\mathrm{i}}$	$[m \times n_{\mathrm{i}}]$	connectivity matrix for internal nodes
$\mathbf{C}_{\mathrm{b}}$	$[m \times n_{\mathrm{b}}]$	connectivity matrix for support nodes
$\mathbf{E}$	$[2n_{\mathrm{i}} \times m]$	horizontal equilibrium matrix
$\mathbf{E}_{\mathrm{d}}$	$[2n_{\mathrm{i}} \times m-k]$	dependent hor. equilibrium matrix
$\mathbf{E}_{\mathrm{id}}$	$[2n_{\mathrm{i}} \times k]$	independent hor. equilibrium matrix
$\mathbf{B}$	$[m \times k]$	independent edges transformation matrix
$\mathbf{R}_{\mathrm{x}}$, $\mathbf{R}_{\mathrm{y}}$, $\mathbf{R}_{\mathrm{z}}$	$[n_{\mathrm{b}} \times 1]$	reaction forces at supports
$\mathbf{R}_{i}$	$[3 \times 1]$	reaction forces for support i
$\mathbf{I}_{\mathrm{n}}$	$[n \times n]$	identity matrix of size n
$\mathbf{X}_{\mathrm{proj}}$	$[n \times 3]$	projected coordinates onto middle surface
$\mathbf{V}_0, \mathbf{V}_1$	$[g \times n]$	mapping matrices for tributary weight
$\mathbf{V}_2$	$[g \times n_{\mathrm{F}}]$	mapping matrix for face centroids
$\mathbf{V}_{\mathrm{c}}$	$[n_{\mathrm{F}} \times n]$	matrix to compute mesh face centroids
$\mathbf{a}$	$[g \times 1]$	elementary triangles area
g	-	number of elementary triangles
ρ	-	masonry specific weight
$\mathbf{t}$	$[n \times 1]$	variable local structural thickness
t	-	constant structural thickness
t_0	-	thickness at start of optimisation
t_{min}	-	minimum structural thickness
d	-	orthogonal offset distance
δ_{p}	-	vertical offset distance
$\hat{\mathbf{n}}_{\mathrm{i}}^{\mathrm{UB}}, \hat{\mathbf{n}}_{\mathrm{i}}^{\mathrm{LB}}, \hat{\mathbf{n}}_{\mathrm{i}}^{\mathrm{m}}$	$[3 \times 1]$	normal unit vectors
$\bar{z}_i^{\mathrm{LB}}, \bar{z}_i^{\mathrm{UB}}, \bar{z}_i^{\mathrm{m}}$	-	starting elevations for offset
$b_{\mathrm{x},i}, b_{\mathrm{y},i}$	-	bounds for reaction vector at support i
$F_{\mathrm{x},i}, F_{\mathrm{y},i}$	-	bounding reaction function for support i
$\mathbf{F}_{\mathrm{x}}, \mathbf{F}_{\mathrm{y}}$	$[n_{\mathrm{b}} \times 1]$	vector of bounding reaction functions
$q_{\mathrm{max}}, q_{\mathrm{min}}$	-	bounds on force densities
z_{min}	-	minimum elevation (if no intrados)
$n_{\mathrm{con}}, n_{\mathrm{eq}}, n_{\mathrm{var}}$	-	n. of constraints, equalities and variables
λ_{v}	-	vertical load multiplier
λ_{h}	-	horizontal load multiplier

$\phi, \phi^{\mathrm{ext}}$	-	internal and external load-path
P_{max}	-	maximum applied load
W	-	structure's total self-weight
T	-	horizontal thrust
V	-	vertical support reaction
$W_{\mathrm{c}}, \tilde{W}_{\mathrm{c}}$	-	cont. and discrete complementary energy
$\bar{\mathbf{u}}$	$[n_{\mathrm{b}} \times 3]$	prescribed foundation displacement
ϵ	-	overall stiffness parameter
E	-	Young modulus
A_{s}	-	cross-section bar area
f_{obj}	-	objective function
f_{min}	-	minimise thrust function
f_{max}	-	maximise thrust function
f_{t}	-	minimise thickness function
f_{v}	-	maximise vertical load mult. function
f_{h}	-	maximise horizontal load mult. function
f_{c}	-	minimise complementary energy function
$\mathbf{X}_{\mathrm{c}}$	$[3 \times 1]$	center of diagram or masonry shape
$s_{\mathrm{m}}, s_{\mathrm{LB}}, s_{\mathrm{UB}}$	-	middle, intra- and extrados functions
$R, R_{\mathrm{c}}, R_{\mathrm{o}}$	-	radius, central and oculus radius
$n_{\mathrm{M}}, n_{\mathrm{P}}$	-	number of meridians and parallels
$n_{\mathrm{s}}, n_{\mathrm{x}}, n_{\mathrm{y}}$	-	discretisation parameters
q_{bound}	-	force density value on boundary edges
q_{inner}	-	force density value on inner edges
β	-	dome and vault springing angle
l_0	-	vault base length
s	-	vault span
α	-	support rotation
$l_{\mathrm{x}}, l_{\mathrm{y}}$	-	planar dimensions
h	-	structure's height
a_i'	-	axis of symmetry i
Δ	-	sliding diagram magnitude
λ	-	inclination mixed diagram parameter

Part I

Introduction

Chapter 1

Background

This chapter introduces the present dissertation. First, a brief introduction to masonry structures is given, followed by the main motivation and challenges in analysing masonry buildings. Next, the thesis statement is presented, and the structure of the dissertation is listed.

1.1 Introduction

The assessment of unreinforced masonry structures (URM) is relevant to society since a large part of the world's built heritage was constructed with this technique, and millions of people live in masonry buildings worldwide. Masonry construction techniques are among the most ancient adopted by humankind. They have evolved with our society from simple and heavy arches to complex and efficient building structures still standing after centuries (Huerta, 2020), such as the examples depicted in Figure 1.1. Preserving this cultural heritage and ensuring the safety of masonry buildings are tasks of first concern to the engineering community.

Masonry structures are composed of discrete, individual elements carefully placed to shape the structure. Often, the simplicity of its forming elements – blocks – contrasts with the complexity of its final geometry. At the level of the joints, either a thin layer of mortar or dry joints is used, and the structures stand primarily by virtue of their geometry rather than material strength (Huerta, 2001). Masonry buildings are well suited to construction even in a low technological context and can be erected using simple or natural materials, such as stones and fired clay bricks (Ramage et al., 2010).

(a) (b)

Figure 1.1: Examples of masonry vaults: (a) King's College Chapel in Cambridge, UK, and (b) Sainte Chapelle in Paris, France. (Photos: Author)

However, despite the historical importance of masonry structures, fewer specific analysis tools have been developed to assess masonry structures compared with modern engineering materials, such as reinforced concrete and steel (Tralli et al., 2014). Modelling the structural response of masonry constructions is challenging, especially in vaulted systems, given their complex geometry, anisotropic material behaviour, and the difficulty in acquiring precise mechanical data from the existing buildings and their surroundings (Angelillo et al., 2014).

This dissertation focuses on developing a novel limit-analysis-based approach to assess vaulted masonry structures adapted to the commonly available data from surveys and designed to output relevant information about their level of stability, safety factors, and closeness to the collapse.

The primary motivation for this research is summarised in the following section, and the main challenges for modelling masonry structures are subsequently listed.

1.2 Motivation

This chapter lists the primary motivation for this dissertation.

1.2.1 Lack of practical masonry analysis tools

Assessing masonry structures demands specific analysis tools and methods. Recently, the scientific community has developed a series of modelling strategies to predict and assess the mechanical behaviour of masonry structures (D'Altri et al., 2019). However, most of these methods rely on the material properties of masonry, which are highly anisotropic and hard to determine (Page, 1981). As pointed out in D'Altri et al. (2022); Cattari et al. (2021), assuming conventional mechanical properties provided in national code provisions without proper calibration techniques can lead to inaccurate results. Furthermore, as discussed in Gilbert et al. (2022), detailed modelling strategies broadly adopted in academia are often impractical since cumbersome complex models must be constructed against typical project constraints on time and budget. Consequently, difficulties in modelling masonry mechanical systems increase the risk of proceeding with wrong interventions when assessing masonry structures, with consequences on their structural behaviour post-intervention (Angelillo, 2019).

1.2.2 Lack of knowledge on masonry mechanics

Moved by the population growth and the expansion of the urban centres, new construction methods have been developed, such as reinforced concrete and steel structures. Elastic structural analysis is the predominant tool to analyse these structures, especially with the introduction of Finite Element Analysis (Hughes, 2012). As a reflex, the education of architects and civil engineers shifted towards providing economical design and construction solutions for these new materials. Consequently, masonry mechanics, assessment, and rehabilitation disciplines declined and need to be reintroduced, especially in the context of cultural building heritage (ICOMOS, 1993).

1.2.3 Increasing need for repurposing of infrastructure

Given the climate emergency, the Architectural Engineering and Construction (AEC) industry emissions are being revisited, showing that the industry is responsible for up to 40% of the global resource consumption (OECD, 2019). In this context, the rehabilitation and maintenance of existing infrastructure and housing, partly constructed with masonry techniques, becomes pressing. Rehabilitation projects require the consideration of new loading cases, interaction with new adjacent elements, and adapting existing structures to modern building codes. These analyses should result in estimates of the structural safety levels, collapse loads, and residual capacity considering existing crack patterns and deformations, pointing to the need (or not) for strengthening interventions (e.g., De Lorenzis, 2008). These tasks require appropriate analysis tools and methods to accurately model the mechanics of masonry structures and enable repurposing and maintenance.

1.2.4 Opportunity to design with low-carbon materials

Recent research has demonstrated how adopting masonry-inspired solutions can be an alternative to reduce embodied emissions of building elements, with applications to floor systems (Liew et al., 2017; Hawkins et al., 2019; Oval et al., 2023; Ranaudo et al., 2021; De Wolf et al., 2017; Ramage et al., 2022), as illustrated in Figure 1.2.

Figure 1.2: Examples of funicular floor systems: (a) discrete 3D-printed ribbed concrete floor (Rippmann et al., 2018), (b) thin shell concrete shell floor (Hawkins et al., 2019), (c) discrete thin shell floor (Oval et al., 2023), (d) unreinforced funicular floor at HiLo, Dubendorf (Ranaudo et al., 2021).

Nevertheless, the mismatch in the knowledge, acceptance, and analysis tools available to masonry hinders innovations in masonry-inspired funicular structural design that could have a highly scalable effect on the construction industry (Block et al., 2020).

1.3 Challenges

This section lists the main challenges related to the mechanical behaviour of masonry structures and highlights the difficulties in acquiring their geometrical and mechanical data.

1.3.1 Mechanical behaviour

The mechanics of masonry structures are challenging because of the following specific aspects:

- Masonry structures are heterogeneous, formed by the arrangement of blocks.
- The material presents an anisotropic strength behaviour, with high compressive capacity and low (usually negligible) tensile strength.
- Under the action of even small foundation settlements, cracks might form, creating hinges affecting the structures' stiffness and load-carrying capacity.
- The structure can accommodate large deformations through the development of hinges until it finds a new equilibrium position.
- Masonry structures are highly indeterminate, so finding the exact internal stress state is effectively impossible.

This particular mechanical behaviour precludes the use of general analysis tools without properly considering either material properties or specific modelling the internal joints (Roca et al., 2010). Therefore, given the particular mechanical behaviour of masonry, the application of plastic, instead of elastic, modelling strategies surge as an alternative (Heyman, 1966). Moreover, as argued in Como (2015), the collapse in masonry structures can occur even if the material does not reach its maximum strength. Consequently, the collapse in masonry structures relates to a lack of stability instead of material strength, encouraging the use of equilibrium-based methods to assess their stability (Ochsendorf, 2002; Huerta, 2001).

1.3.2 Data acquisition

Besides the mechanical particularities inherent to masonry modelling, acquiring mechanic and geometric data through surveying is challenging. The main reasons for being so are listed:

- Accurately determining the mechanical properties of masonry structures is complex. Even invasive tests result only in local information that does not necessarily extend throughout the building as these might have been built over long periods and with different materials (Roca et al., 2013). Similarly, the stiffness of the foundations is hard to estimate.

- Masonry structures are usually old and might have undergone a series of interventions. Information about the construction, loading history, and the evolution of deflections and deformations can hardly be retrieved (Wilding et al., 2017).

- Even when detailed surveying is conducted, obtaining the blocks' dimensions and arrangement is nearly impossible, especially since multilayers of masonry are often used, e.g., three-leaf walls. The survey is also susceptible to blind spots and limited access to portions of the structure.

- Transferring the acquired geometry to structural models is challenging and, in many cases, overly simplified to two-dimensional sections (Castellazzi et al., 2015).

The uncertainty in determining the mechanical parameters is a crucial challenge to building accurate models for masonry systems (Angelillo et al., 2018). The difficulties in determining these mechanical parameters favour the adoption of geometry-based methods for the analysis, i.e., methods that do not rely on material properties or foundation stiffness.

There are also critical limits to the geometry detail that can be acquired from existing structures. After geometric surveys, e.g., laser scans or photogrammetry, the output derived corresponds to point clouds of the visible structural geometry. This information enables, at most, the construction of surfaces of intrados and extrados and the main dimensions of load-bearing elements and lateral systems. Consequently, obtaining the actual stereotomy of the building is often irrealistic. Recent approaches assume either a certain level of imperfection (Dell'Endice et al., 2021) or work with representative surfaces of the building (Block and Lachauer, 2014).

1.4 Thesis statement

As shown in Huerta (2001), equilibrium methods provide an inexpensive and straightforward way to analyse the stability in masonry structures supported by the limit analysis theory (Heyman, 1966). The extension of this approach to three-dimensional structures resulted in the development of Thrust Network Analysis (Block, 2009), or TNA, enabling the exploration of three-dimensional equilibrium.

The applications of TNA to the context of assessment present a series of advantages. For example, it allows for direct control over the possible internal force equilibria of the structure, is well-aligned with the assessment needs and the typical geometrical and material data available, can be directly applied to three-dimensional problems, and can be developed and distributed under an open-source license and a collaborative environment.

Therefore, this dissertation builds on the latest developments of TNA to provide a complete framework for masonry assessment. It couples TNA with robust optimisation methods to explore the domain of admissible states in the structure. The framework will then be used to estimate safety levels and collapse loads accurately and model the effect of settlements.

Besides contributing to the intellectual development of lower-bound limit analysis methods, the results of this thesis are implemented in open-source numerical applications that can serve as a practical analysis tool and allow for future collaborative research.

1.5 Thesis structure

This dissertation is divided into four parts and ten chapters. A summary of each part and chapter is presented here.

PART I: Introduction

Part I presents the introduction for the work, including background, literature review, and defining the scope of the work.

Chapter 1: Background

This chapter presents the background and motivation for this dissertation. It highlights the relevance of masonry structures to society and the lack of tools and methods to perform their structural assessment.

Chapter 2: Literature Review

This chapter presents the literature review associated with the structural analysis of historic masonry constructions. A brief overview of historical analysis tools is presented, followed by a list of modern tools currently applied to masonry structures. The chapter focuses on the applications of limit analysis to masonry structures, highlighting its advantages and listing the hypothesis necessary for its application. An overview of equilibrium methods for masonry is presented, listing significant gaps that limit the adoption of such techniques in current engineering practice.

Chapter 3: Scope of the Work

Given the significant gaps that hinder the adoption of equilibrium and limit analysis techniques for masonry structures, this chapter defines the scope of the present dissertation and highlights the research questions that will be addressed.

PART II: Methodology and Implementation

Part II presents the methodology and implementation developed to model and assess masonry structures.

Chapter 4: Equilibrium Force Network

In this chapter, the main elements of Thrust Network Analysis (TNA) are defined, and a numerical description of the equilibrium in force networks is given in terms of force densities. The particular case of networks with fixed horizontal projection is discussed, requiring determining the degrees of freedom. A novel algorithm to automatically find these degrees of freedom is presented. It is used to illustrate the potential to describe the infinite space of equilibrium force networks with fixed horizontal projection.

Chapter 5: Constrained Equilibrium

This chapter describes the search for admissible stress states as a constrained nonlinear optimisation problem (NLP). The constraints from limit analysis are introduced and translated into the context of TNA. Different objective functions relevant to masonry structures are presented, and a numerical description to compute these objectives is derived in terms of the equilibrium variables. The sensitivities and Jacobian matrix for the problem are also derived for a proper description of the NLP. Furthermore, a convex starting point for the NLP is presented.

Chapter 6: Implementation

This chapter presents the implementation of a numerical package to perform the constrained nonlinear optimisation problem mathematically defined in the previous chapter. The features and capabilities of this package are listed, including the strategy adopted to solve the nonlinearly constrained problems.

PART III: Results

Part III lists the main results of this work with three practical applications of the framework developed, computing the level of stability in masonry structures, collapse loads, and studying the effect of foundation displacements.

Chapter 7: Stability of masonry structures

This chapter shows the application of the framework developed to compute the stability of vaulted masonry structures. It proposes a methodology for computing the Geometric Safety Factor (GSF) and computing its stability domain. These metrics enable quantifying stability on vaulted structures. This chapter also discussed the effects of analysing the problem with different form diagrams and how to evaluate these diagrams based on the metrics introduced.

Chapter 8: Collapse loads on vaulted masonry structures

This chapter shows the application of the framework developed to estimate collapse loads in vaulted masonry structures. This well-known problem is relevant for structures undergoing repurposing and for the static simulation of earthquakes. For this problem, the modification of the form diagram is necessary, and practical strategies to adapt the diagram to the applied load are presented. Examples include domes and vaults undergoing non-symmetric loading cases and horizontal actions.

Chapter 9: Understanding the effects of foundation settlements

This chapter shows the application of the framework developed to compute internal stress states compatible with prescribed foundation displacements. Support displacements are common in masonry structures and can lead these structures to collapse. These displacements influence the structure's mechanical behaviour, resulting in frequently observed cracks or fractures. The crack pattern arising at the onset of these displacements is suggested by computing the compatible stress states with given foundation displacements.

PART IV: Conclusions

Part IV closes this dissertation by summarising the main findings and presenting an outlook for future work.

Chapter 10: Conclusions

This chapter summarises the findings of the present dissertation and lists the main contributions of this dissertation. The limitations and opportunities arising from the framework developed are also presented.

Chapter 2

Literature Review

This chapter presents the literature review for the present dissertation. First, the evolution of historical approaches to analysing masonry structures and concepts of graphic statics are presented. Limit analysis is introduced, and modern numerical tools developed according to its principles are listed. Novel lower-bound equilibrium approaches are discussed, which are the theoretical base of this work. Finally, a discussion of current methods available in engineering offices is presented. This section lays the foundation for this dissertation's research objectives.

2.1 Historical approaches

This section discusses the historical evolution of methods to analyse masonry structures introducing graphic statics and thrust line analysis and highlighting the rise and decline of these methods.

2.1.1 Scientific understanding of internal forces

According to Huerta (2006), the construction of masonry structures dates back to at least 2000 BC in Mesopotamia. The first discovered arches would span only around 2 m. With the advances in masonry construction techniques, these spans rose significantly, reaching, e.g., 43 m as in the Roman Pantheon. It is agreed that the development of masonry systems throughout history has been heavily based on experiments and proportion rules transmitted among masons, as in the rules noted in Derand (1643) to estimate the required buttress width for vaulted structures.

The initial scientific understanding of the internal forces in masonry structures appears in Hooke (1676). Hooke writes that: *"As hangs the flexible line, so, but inverted stands the rigid arch"*. Hence, the natural shape obtained from the gravity of a flexible line with distributed weight will, when inverted, represent the ideal shape to equilibrate these weights against gravity in compression. This flexible line is known today as the catenary or funicular. Figure 2.1a shows Hooke's flexible and rigid lines.

Hooke's work has influenced the work of engineers in the following centuries. Poleni (1748) applied the catenary concept to the dome of St. Peter's Basilica in Rome. As reported in Mainstone (1999); Block, DeJong and Ochsendorf (2006), Poleni's analysis divided the dome into lunettes subdivided into 32 portions. Weights proportional to the dome were attached to a rope which took the shape of a modified catenary. Poleni shows that, since the inverted catenary is within the dome's section, a compressive, internal force path is possible in the structure (Figure 2.1b). Therefore, its overall geometry is stable and safe.

a) b)

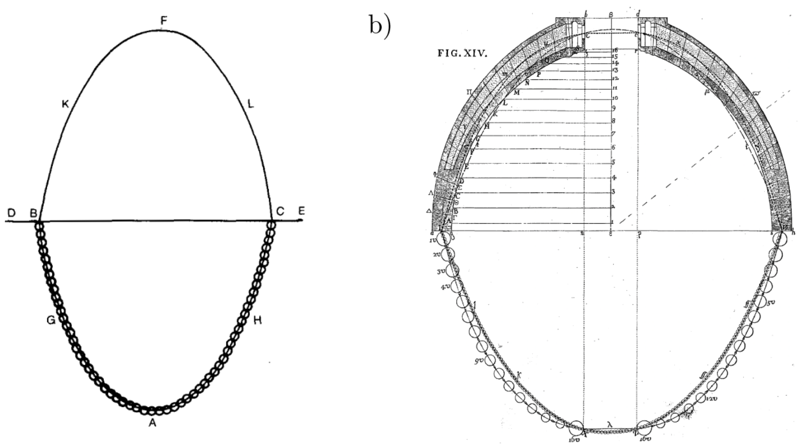

Figure 2.1: (a) Hooke's inverted catenary, and (b) application of this concept to the dome in St. Peter's Basilica in Rome. Image after Poleni (1748).

Hooke's ideas propelled the search for internal forces in arched structures, which advanced the development of graphic statics, as shown in the next section.

2.1.2 Graphic statics

The graphical representation of the equilibrium of forces has its origins in Stevin (1586). In Varignon's *Nouvelle Mechanique ou Statique* (Varignon, 1725), the application of graphical principles to systems of ropes and weights is demonstrated, as depicted in Figure 2.2.

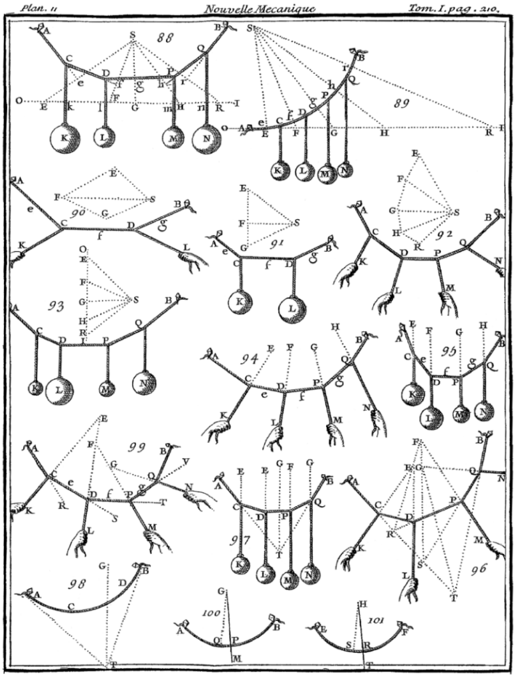

Figure 2.2: Reciprocal figures by Varignon (1725) presenting the equilibrium of flexible hope structures in tension.

Varignon's drawing n.92 is represented in Figure 2.3 to formalise concepts of graphic statics used in this dissertation. The rope system is represented by a primal or form diagram (Γ) in which every edge represents a rope segment, composing the structure (Figure 2.3a). The structure has ten nodes numbered from 1 to 10. Spaces are defined among the edges in the structure noted from A to F. The equilibrium of Γ is then verified by the reciprocal or force diagram Γ^*. These two diagrams have the same number of edges, and each edge e_{ij} in Γ has a corresponding edge e^*_{ij} in Γ^*. Similarly, each node in the primal maps to a face in the dual and vice-versa. The primal and reciprocal diagrams respect the following rules, which will verify the equilibrium in the structure:

- All corresponding edges in the form e_{ij} and force e^*_{ij} diagrams are parallel ($e_{ij} \parallel e^*_{ij}$).
- The length of an edge l^*_{ij} in the force diagram is proportional to the axial force f_{ij}, carried by its corresponding edge in the form diagram.
- Each node i in the form diagram is represented by a closed polygon P^*_i in the force diagram, which will represent its nodal equilibrium

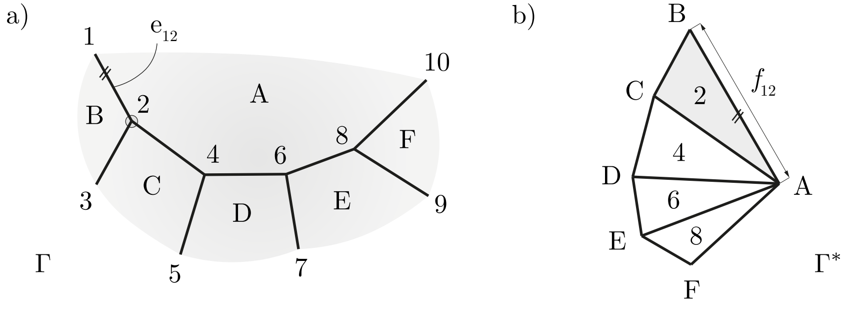

Figure 2.3: (a) Form diagram (Γ) representing Varignon's drawing n.92 (Varignon, 1725), marking the nodes 1 to 10 and spaces A to F. (b) Force diagram (Γ^*) presenting the equilibrium of the structure. The force magnitude at each edge of Γ maps the length of corresponding edges in Γ^*.

In the reciprocal diagrams from Figure 2.3, the force f_{12} in edge e_{12} is equal to the length $\overline{AB}$ of the edge e^*_{AB} in the reciprocal diagram (Γ^*). The pair of reciprocal edges are indeed parallel, as noted. Vertex 2 in Γ is also marked, and its equilibrium is verified by the close polygon 2, highlighted in Γ^*.

These reciprocal rules were formally introduced in Maxwell (1864) and consolidated as a structural analysis theory after Culmann (1866). The development of graphic statics techniques revolutionised the analysis of masonry arches and even the design of novel structures, as in an overview in Lee (2018). When applied to masonry, graphic statics enables searching for the internal states by employing reciprocal diagrams without constructing physical models. Thrust line analysis appeared in this context, as discussed in the following section.

2.1.3 Thrust lines and the slicing technique

A thrust line corresponds to a discrete compressive equilibrium solution representing the internal stress states in masonry structures. It can be applied in combination with graphic statics, as depicted in Figure 2.4. A thrust line (G) is shown within the geometry of an arch (Λ). The thrust line is discretised based on the arch's voussoirs. Each vertical load applied to a vertex i of the thrust line corresponds to the weight (w_i) of the corresponding voussoir. The force diagram comprises the multiple local equilibria in the nodes of the thrust line's vertices. The reaction force (R) is decomposed into its components, horizontal (T) and vertical thrust (V), whose magnitude is obtained by measuring the reciprocal elements in Γ^*.

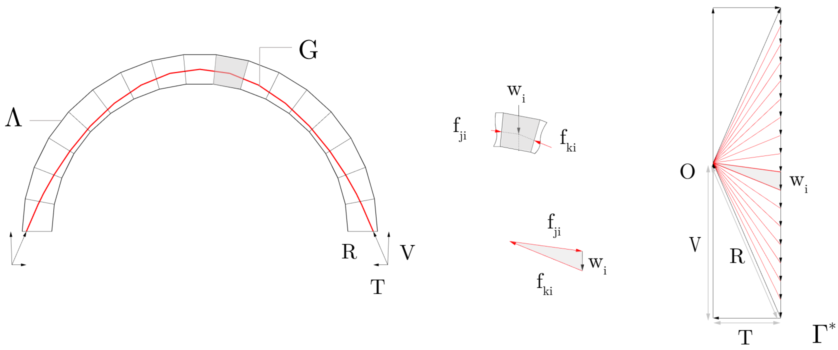

Figure 2.4: Trust line (G) within the semi-circular arch (Λ) highlighting the (equilibrium of) block i. The global equilibrium is described by the force diagram (Γ^*).

This approach finds different equilibrium states in masonry arched structures, supported by the reciprocal relations from graphic statics. A series of analyses were conducted throughout the 19th century applying this concept to arches and bridges (Moseley, 1843; Snell, 1846; Jenkin, 1876). Advances in the technique allowed it to be extended to some three-dimensional symmetric problems, such as domes (Eddy, 1877; Dunn, 1904). These advances resulted in the *slicing technique*, which has been applied since Ungewitter (1890), as depicted in Figure 2.5.

With the slicing technique, each slice of the vault is analysed separately as an arch and verified with thrust lines. In Figure 2.5, the thrusts converge to the diagonals, where they are (graphically) summed up and converge to the

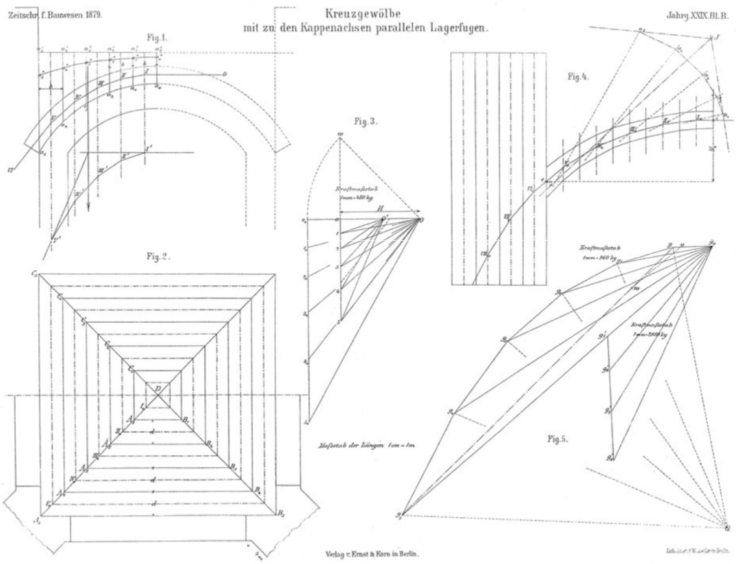

Figure 2.5: Slicing technique applied to a square cross vault from Ungewitter (1890).

corner supports. This technique introduced, for the first time, a procedural approach to dealing with general geometries. Any vaulted structure can be sliced into equivalent arches and analysed. However, the constructions become cumbersome when the geometry becomes complex or even non-symmetrical. For this reason, the method in practice is limited to groin and symmetric vaults, as argued in Block (2009), and it requires high graphical expertise to properly adjust the thrust magnitude in the segments such that all thrust lines are within the vault's geometry.

2.1.4 The decline of graphical methods

The application of thrust lines and graphic statics, in general, declined toward the beginning of the 20th century, influenced by the development of elastic analysis. Elastic analysis computes stresses and deflections in structural systems by assuming a constitutive relationship to the material. The theory applies well to bilateral, homogeneous systems but is limited to describing the mechanics of discrete, unilateral models like masonry (Como, 2015).

Indeed, finding a reliable constitutive law for a heterogenous system of blocks is challenging (Boothby, 2001). Moreover, large stress concentrations are obtained after (even small) support displacements in elastic analyses. However, due to its unilateral behaviour, masonry structures accommodate large foundation settlements by developing hinges or cracks instead of stress concentrations. In Danyzy (1732), the collapse of a series of masonry systems is documented, highlighting that the instability is caused by hinges and displacements instead of stress concentration (Figure 2.6).

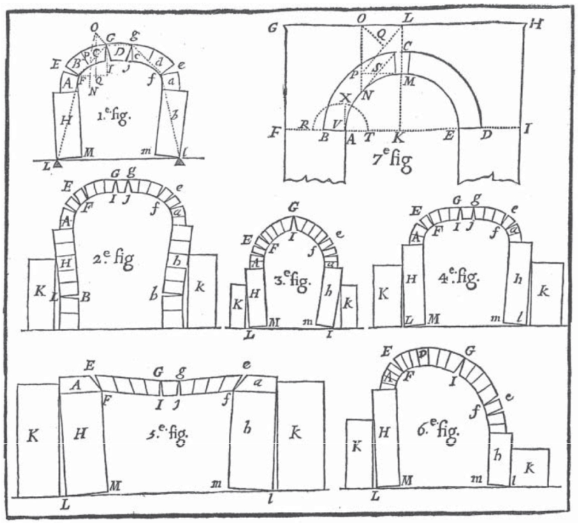

Figure 2.6: Collapse in arches highlighting the creation of structural hinges (Danyzy, 1732).

As argued by Huerta (2020), a series of tests conducted in Engesser (1880); Pippard et al. (1936) pointed to a mismatch in the collapse states obtained in masonry arches with elastic analysis. The work of Pippard et al. (1936) indeed led to the development of plastic and limit analysis as a better-suited foundation for the analysis of masonry structures.

2.2 Limit analysis

Limit analysis is defined in this section. The origins of the method are presented in Section 2.2.1. The assumptions required to apply limit analysis to masonry structures are summarised in Section 2.2.2, and the limit analysis theorems are listed in Section 2.2.3.

2.2.1 Plastic analysis

Plastic analysis developed following the mismatch between collapse loads in structural systems and the results from elastic analysis as noted in Section 2.1.4.

The method was developed initially for steel frames (Symonds and Neal, 1951; Baker et al., 1956; Neal, 1958; Prager, 1959). Under the application of an increasing external load on a steel frame, the collapse does not occur until sufficient hinges are developed in the structure. Hinges develop when the material achieves the yielding criteria, and the stresses are locally redistributed. If the external load exceeds the elastic limit, the plastic region propagates through the structure until the collapse. Therefore, unlike elastic, plastic analysis focuses on the states of the collapse of the structure rather than computing its current stress state.

The search for the collapse states or collapse loads form the so-called limit analysis branch of plastic analysis. The development of plastic analysis allowed for the design of economical steel frames, as the plastic collapse loads are higher than the ones computed with elastic analysis. The extension of plastic analysis to masonry structures is credited to Heyman (1966), after Kooharian (1952), as presented in the next section.

2.2.2 Heymanian model

The application of limit analysis to masonry structures under the Heymanian model (Heyman, 1966) requires verifying three main assumptions on the material as listed below:

(i) masonry's compressive strength is infinite,

(ii) masonry's tensile strength is considered null, and

(iii) no sliding occurs between the elements of the structure.

These assumptions, even if crude, accurately model masonry structures because (i) the levels of stress encountered are usually low, far from the stone's compressive strength; (ii) the structure might be constructed using dry joints, or, even if mortar is applied, the quality of mortar connecting the blocks is usually weak or has decayed, being orders of magnitude inferior to its compressive strength; and, (iii) existing historic URM structures, in general, were built carefully with an appropriate stereotomy or construction detailing to avoid sliding.

Figure 2.7 illustrates a joint's yield interface and equivalent internal stress state. In Figure 2.7a, the resultant (N) is applied within the joint with eccentricity $e < h$. In Figure 2.7b, the resultant is at the edge of the interface, generating an effective moment $M = hN$, creating a hinge. The simplified yield surface is shown in Figure 2.7c as the open triangle AOB. With the resultant at any point internal to this triangle, a hinge will not form, and at lines AO and OB, the hinge appears.

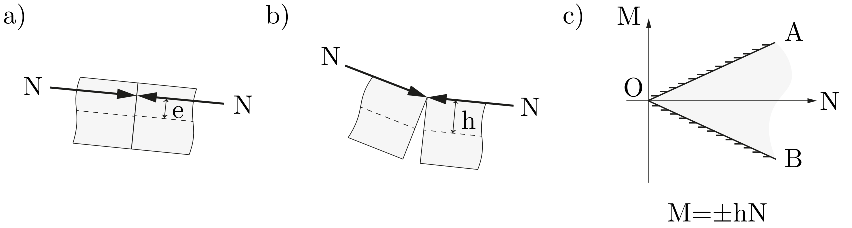

Figure 2.7: Admissible domain for two blocks after Heyman (1966). (a) Internal forces within the joint, at eccentricity $e < h$, (b) criteria for hinge formation ($e = \pm h$), and (c) yield surface for the interface.

2.2.3 Limit analysis theorems

Limit analysis solutions can be found with the applications of the lower-bound, or *safe theorem* and upper-bound, or *unsafe theorem*.

According to the *safe theorem*, a structure is safe if an admissible stress state can be found. Assuming the Heymanian model, admissible stress states are compressive force paths within the structure's geometry. In two dimensions, this set of compressive, internal forces can be represented with a *thrust line* (e.g., Figure 2.4), which corresponds to the line connecting the resultants of the internal forces of the structure. For three dimensions, the internal stress fields extend to a compressive network or a compressive membrane.

On the other hand, the *unsafe theorem* searches for kinematic mechanisms for which the structure would no longer be safe or stable. For example, when studying the problem of a collapse load, each mechanism associates with a given (unsafe) load magnitude. An upper bound of the load magnitude can be computed by proposing different mechanisms or hinge positions in the present case.

For perfect plastic materials, the safe and unsafe theorem should converge to the same collapse state (Prager, 1959).

Section 2.3 gives an overview of lower-bound equilibrium methods, which correspond to the core methods used for this dissertation. An overview of upper-bound limit analysis methods is given in Boothby (2001); Como (2013); D'Altri et al. (2019) with modern applications to three-dimensional geometries in Chiozzi et al. (2017); Scacco et al. (2020). The application of general analysis methods to masonry structure is presented in Section 2.4.

2.3 Lower-bound equilibrium methods

With no claim of completeness, this section lists the recent advances in numerical methods that search for admissible stress states in masonry structures that have influenced the present dissertation. Modern thrust line approaches are listed in Section 2.3.1, and two strategies for finding admissible states in 3D structures are presented: membrane-based approaches (2.3.2) and thrust network approaches (2.3.3). Block-based approaches are presented in Section 2.3.4.

2.3.1 Modern thrust line approaches

As shown in Section 2.1.3, the search for admissible states in two-dimensional arches can be performed by finding thrust lines within the structure. While the graphical construction of these thrust lines is tedious and requires experience, a series of numerical tools have been developed to ease this process.

An algebraic formulation is proposed in Van Mele and Block (2014) to find form and force diagrams without the need to draw them procedurally. This framework is revisited in Alic and Åkesson (2017); Maia Avelino, Lee, Van Mele and Block (2021), and interactive modifications to these diagrams are introduced. Thrust line approaches have been the core of 2D masonry analysis tools such as LimitState Ltd (2020); Obvis (2016).

Thrust line models have been combined with optimisation algorithms to search for specific solutions, such as minimum and maximum thrusts in Marmo (2021) and to compute safety factors in Galassi and Tempesta (2019). A real-time interactive thrust line method is also proposed in Block, Ciblac and Ochsendorf (2006), enabling drawing thrust lines and observing hinge openings for foundation displacements in the arch.

Recent studies have extended thrust line principles to 3D or pseudo-3D structures such as the dome under symmetric loading cases (Aita et al., 2019; Zessin et al., 2010; Paris et al., 2021) and spiral staircases (Angelillo et al., 2021).

These developments increase the options available for analysing arches and axisymmetric structures. However, extending lower-bound methods to 3D is necessary to analyse vaulted systems. Two main strategies have been developed to cope with this problem, revisited in the following sections.

2.3.2 Membrane-based approaches

Membrane-based approaches search for admissible states in spatial masonry as compressive membranes within the structural geometry.

In this method, the equilibrium equations are solved by assuming a Pucher formulation and considering the potential stress (or Airy) functions to describe the internal distribution of the stresses (Fraternali et al., 2002). A second-order differential equation describes the vertical equilibrium with this approach. Different approaches have been developed to solve this differential equation. In Fraternali (2010); Angelillo et al. (2013); Olivieri et al. (2021), an approximation of the relevant functions is made in polyhedral domains, in Fraddosio et al. (2020), a polygonal approximation is used in an equally spaced point grid, in Miki et al. (2015), NURBS surfaces are used, and analytical solutions are obtained for simple geometries in Baratta and Corbi (2010).

The stresses in the membrane are related to the curvature of the Airy stress function. The compression-only requirement is ensured by verifying that the potential function is concave. The membrane's geometry can be updated by modifying the stress function's shape. An interactive approach is proposed in Fraternali (2010) to update the membrane and the potential stress geometry until the membrane is within the structural geometry, i.e., intrados and extrados and the stress function is concave. This iterative procedure applied to a cross vault is depicted in Figure 2.8.

However, the broad application of this method is currently limited due to the difficulties in solving these differential equations. For example, not continuously supported structures are hard to analyse, concentrated loads

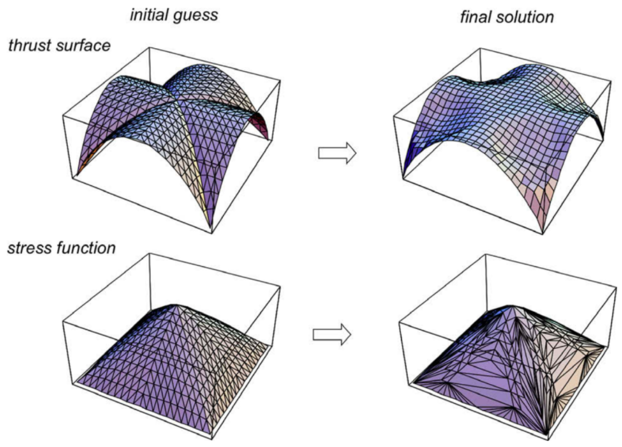

Figure 2.8: Obtaining a compressive thrust membrane iterating on the geometry and the Airy stress function. From Fraternali (2010).

can not be easily applied to the problem, and the method is limited to vertically applied loads.

Alternatively, thrust network approaches analyse this problem in a discretised manner. They are presented in the following section.

2.3.3 Thrust network approaches

As a direct extension of the discrete thrust lines for three dimensions, thrust network approaches search admissible states using compressive force networks.

Even though the equilibrium of force networks had been investigated since Schek (1974); Williams (1990), the first formal application of force networks to the equilibrium problem of masonry vaults is presented in O'Dwyer (1999). In this work, general networks are considered, and optimisation techniques are applied to find compressive equilibrium solutions within the bounds of the masonry. This method, however, does not deal with different horizontal force distributions in a given network and does not allow exploring different degrees of freedom.

Following this work and supported by graphic statics principles, Block and Ochsendorf (2007) proposed Thrust Network Analysis (TNA) as an extension of thrust line analysis for masonry vaulted structures. By constraining the externally applied forces to be vertical, the same reciprocal rules of graphic statics (see Section 2.1.2) can be extended to deal with the horizontal equilibrium in the networks. With TNA, the equilibrium of the spatial thrust networks (G) is controlled by reciprocal form (Γ) and force (Γ*) diagrams. The form diagram is defined as the horizontal projection of the thrust network, where the vertical forces vanish. The force diagram visualises the horizontal equilibrium of the forces. A TNA equilibrium solution is presented in Figure 2.9.

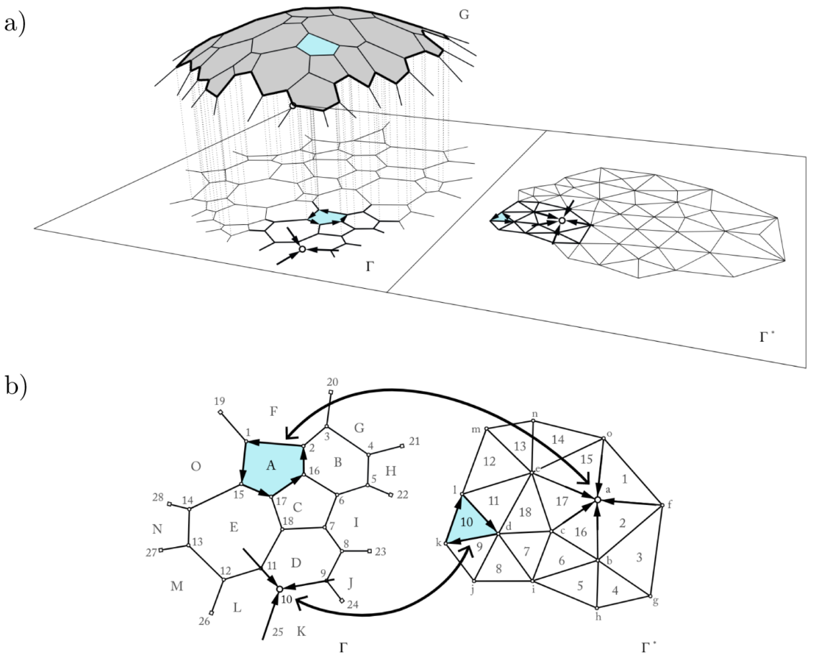

Figure 2.9: (a) Thrust Network (G) and corresponding form (Γ) and force (Γ*) diagrams. (b) Planar form and force with reciprocal relations. From Block et al. (2014).

In Block (2009), the equilibrium is decoupled and solved through sequential linear optimisations. In Rippmann et al. (2012), the horizontal equilibrium is solved graphically by parallelising form and force diagrams, and the vertical equilibrium computes the overall proportional height of the networks.

In Marmo and Rosati (2017), the TNA formulation is revisited, dispensing the use of the dual grid, which also enables the application of horizontal forces to the model.

The decoupled formulation is updated in Block and Lachauer (2014), where a coupled nonlinear optimisation problem is proposed by considering the form diagram fixed and introducing the independent edges. The resulting network is then searched through a best-fit optimisation algorithm (Van Mele et al., 2014), which minimises the vertical least-squares distance between the network and a prescribed target geometry representing the structure. The investigation of different independent edges selection is discussed in Liew et al. (2019).

The coupled approach has been revisited in Fantin and Ciblac (2016) considering disconnected networks and in Bruggi (2020) computing minimum and maximum thrust states using constrained optimisation. Recently, the disconnected problem has been reformulated in Nodargi and Bisegna (2022) as a linear optimisation problem relating the elevation of the disconnected thrust segments to moments acting in the edges of a network projected onto the masonry's middle surface.

The advantages of analysing vaulted masonry structures with TNA include the simple and intuitive control over the force magnitudes and the direct extension of well-known and accepted analysis methods. In addition, its discrete formulation allows TNA to include unsupported boundaries, openings, and external point loads. Recent advances in the method have shown that its combination with optimisation approaches to find specific stress states is also promising.

Nevertheless, there are still barriers that limit the use of TNA in practical assessment scenarios, as the analysis output can not give an idea of the structure's stability level, i.e., only one solution is found. Furthermore, analysing different form diagrams and their effects on the solution is still unexplored. Moved by these limitations, TNA will be the starting point of the development of this dissertation as listed in Chapter 3.

2.3.4 Block-based approaches

While the analysis with membrane-based and thrust network methods considers the masonry as a continuous arcuated system, applying block-based lower-bound approaches enables engineers to consider the stereotomy, friction, and possible benefic effects of interlocking among the voussoirs, as in an overview in Angelillo (2014).

For discrete assemblies, Heyman's assumptions translate into rigid-block models. Livesley (1978, 1992) developed Rigid Block Equilibrium (RBE) as a lower-bound limit analysis method that searches for equilibrium states with rigid blocks. RBE was revisited in Whiting et al. (2009, 2012) adding a quadratic penalty term which enables measuring the structural instability in a given assembly and suggests modifications in the blocks to improve the stability of the assembly. In Figure 2.10a, a coarse model of a church is analysed with RBE, where possible failures are detected. In Kao et al. (2022), this approach is extended to non-convex interfaces, and a nonlinear formulation allows catching detachment and sliding forces.

a) b)

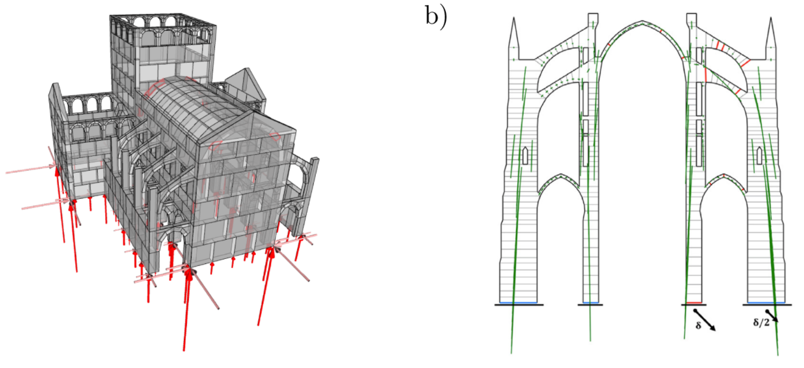

Figure 2.10: (a) Modelling of a church with RBE considering large blocks (Whiting et al., 2009). (b) Internal forces in a Gothic cross-section subjected to settlements with PRD (Iannuzzo et al., 2020).

Rigid-block models can also be employed combined with energy-based dual formulations as proposed in the Piecewise Rigid Displacement (PRD) method (Iannuzzo et al., 2020), developed after Angelillo et al. (2018); Angelillo (2014). With PRD, statics and kinematics are connected in a linear programming dual approach. This enables searching for admissible stress states in the primal problem and obtaining the dual mechanism associated with the solution. In Figure 2.10b, a Gothic cross section is evaluated with PRD subjected to foundation settlements, showing the internal resultants (in green) and the failure sections (in red).

Models with non-associative frictional joints have been analysed in Gilbert et al. (2006) for planar limit analysis problems and in Portioli et al. (2014)

for 3D geometries, solving sequential second-order cone programming problems (SOCP). Further applications of rigid blocks have been studied in Casapulla et al. (2019); Mousavian et al. (2022), analysing further beneficial effects of interlocking among blocks in an assembly and in Chen and Bagi (2020) considering crosswise tensile resistance of masonry patterns due to contact friction.

Limit analysis block-based methods are compelling for studying masonry problems, enabling efficient computation for several problems. These problems include stability analysis assuming a specific block stereotomy, effect of interlocking, studies on friction effects, computation of collapse loads and investigation of collapse mechanisms. However, for this approach, the effect of the stereotomy and parameters such as the friction coefficient highly affect the final solution (Makris and Alexakis, 2013; Wang et al., 2019). In practical assessment applications obtaining information about the precise stereotomy of the structure is usually impractical or impossible, which hinders the application of these methods by practitioners.

2.4 General analysis tools

This section highlights the application of general analysis methods to masonry structures with a focus on the Discrete Element Method (DEM) in Section 2.4.1 and Finite Element Analysis (FEA) in Section 2.4.2.

2.4.1 Discrete Element Method

Discrete Element Methods were initially developed by Cundall (1971) to model the interaction among particles with applications to soil mechanics resulting in the development of the numerical engineering software 3DEC (Itasca, 2020). Lemos (1998) applied DEM to masonry structures by modelling the blocks as rigid and assuming a Mohr-Coulomb criterion in the block interface, which matches Heyman's assumptions from Section 2.2.2. Subsequent works have applied DEM to masonry models under seismic loads (Lemos, 2019), foundation large displacements (McInerney and DeJong, 2015), crack modelling (Iannuzzo, Dell'Endice, Van Mele and Block, 2021; Sarhosis et al., 2019) and imperfections (Dell'Endice et al., 2021; Dell'Endice, 2022).

Recently, DEM has been used as the "ground truth" for analysing rigid block assembly (Kao et al., 2022; Mousavian et al., 2022). Compared with limit analysis block-based methods, DEM also enables the assumption of elastic or plastic material law. Moreover, DEM methods enable considering seismic loads, applying large support displacements, and studying complex collapse mechanisms, supported by the method's efficient interface detection. Nevertheless, besides relying on the need to define a precise geometry for the blocks in the structure, DEM models are still cumbersome, which reflects on them being mainly applied in academic settings and seldomly applied in engineering practice (Roca et al., 2010).

2.4.2 Finite Element Analysis

Finite Element Analysis (FEA) is the most used structural analysis approach to analyse reinforced concrete and steel structures (Hughes, 2012). Linear and nonlinear FEA approaches can be applied to masonry structures, as discussed in the overview of different modelling strategies by D'Altri et al. (2019).

Linear FEA models enable fast computation with solid elements, being used to indicate the overall path of the loads to foundation supports and zones in which tensile stresses might appear (Roca et al., 2013). These models, however, can not incorporate masonry's unilateral material behaviour, heterogeneous nature, and the formation and development of hinges (Shin et al., 2016; Block, 2009).

Nonlinear FEA models can account for nonlinear material behaviour and crack propagation (Lourenço et al., 2022). While highly detailed, these models are computationally cumbersome (Roca et al., 2005; Milani and Tralli, 2012; Zampieri et al., 2017). When applying nonlinear FEA, difficulties remain in determining a suitable elastoplastic law for the material or properly modelling interfaces. Recent research has focused on determining realistic modelling assumptions to apply nonlinear FEA models to masonry structures (D'Altri et al., 2022) and in proposing two-stepped procedures to circumvent the high computational cost (Lourenço et al., 2022).

Among these studies, homogenisation methods have been applied in Zucchini and Lourenço (2009); Reccia et al. (2014), where continuous strain fields are correlated with cracks, and, in Lotfi and Shing (1991), smeared crack models have been developed. Alternatively, nonlinear FEA models can also be used to build discrete models, at the expense of a previous detection on the contact interface (Funari et al., 2022), or modelling the structure with representative blocks and imposing a plasticity criterion for the opening on the hinges (Reccia et al., 2014).

In a recent report about the use of nonlinear FEA analysis on masonry bridges, Gilbert et al. (2022) point to multiple issues that should be considered, such as the differences in stiffness of various parts of the structures (also discussed in Roca et al. (2013)) and convergence problems. Furthermore, proper modelling of three-dimensional vaults is even more challenging with this method as solid elements must be considered, which brings questions about the discretisation employed.

The following section weighs the methods discussed in this Chapter and highlights common tools used in practice for masonry assessment projects.

2.5 Common tools used in practice

The structural analysis of existing masonry structures is challenging given the highly complex architectural configurations, different masonry types, and the anisotropic material behaviour (Huerta, 2008; Roca et al., 2010). Current standard analysis methods, such as Finite Element Analysis (FEA), have been developed to model different structural systems and materials such as steel, concrete, and timber (Iannuzzo, Dell'Endice, Maia Avelino, Kao, Van Mele and Block, 2021). Consequently, fewer numerical analysis software specific to masonry structures are available (Tralli et al., 2014).

As discussed in Gilbert et al. (2022); Roca et al. (2013), Linear FEA models can not account for the anisotropic and plastic behaviour of masonry structures. Nonlinear approaches are better suited but require the definition of multiple parameters regarding the stiffness and strength, which are hard to determine (D'Altri et al., 2022). Moreover, modellers must be aware of the sensitivity in modifying these parameters to the global model behaviour (Cattari et al., 2022). The typical budget and time available in most assessment projects and the difficulties in establishing analysis parameters hinders the application of advanced nonlinear analysis techniques for most problems (D'Altri et al., 2019). Consequently, these sophisticated analyses remain primarily used in academic settings (Tralli et al., 2014).

Similarly, Discrete Element Models enable various analyses considering the structure's unilateral response, but constructing these models is cumbersome (Funari, Mehrotra and Lourenço, 2021). Moreover, the modelling of each voussoir in the structure is also not aligned with the typical data from geometric surveys and can hardly be obtained.

The lack of specialised tools for masonry structures and the limitation in applying conventional ones, e.g., linear FEA, increases the risk of proceeding with wrong or unnecessary interventions in masonry structures. In Figure 2.11, heavy reinforcement is added to the extrados of a historic building. This addition will permanently affect how the structure behaves and add stiffness to the vault, which will be unable to crack to adapt to movements.

Figure 2.11: Heavy reinforcement applied at San Basilio Monastery, L'Aquila, Italy. (Photo: Alessandro Dell'Endice)

Interventions like the ones in Figure 2.11 must be the last resort, only considered after a throughout analysis of the structure for which further adapted analysis tools must still be developed. From the guidelines of cultural monuments from the International Council on Monuments and Sites (ICOMOS), when it comes to the structural preservation of cultural heritage, "no actions should be undertaken without demonstrating that they are indispensable" (ICOMOS, 2003, item 3.4).

In this context, limit analysis methods surge as an inexpensive and accurate way to analyse masonry structures (Ochsendorf, 2002; Angelillo et al., 2018). The application of lower-bound limit analysis can result in a safe, quickly verifiable model well-aligned with the typical data obtained from geometric surveys in masonry buildings (Huerta, 2001).

A few professional lower-bound limit analysis tools have recently been developed to solve this problem for two-dimensional structures and bridges

(LimitState Ltd, 2020; Obvis, 2016). However, there is still a lack of methods to deal with general three-dimensional geometries and able to output relevant information for practical assessments.

In this context, the initial developments of thrust network approaches, listed in Section 2.3.3, are promising, as they enable the analysis of multiple geometries, support conditions, and loads to be considered.

2.6 Summary

This chapter provides an overview of numerical methods used to assess masonry structures. An overview of the development of historical methods to find equilibrium in masonry structures is presented, which resulted in the development of limit analysis to masonry structures.

Significant lower-bound limit analysis approaches are presented as they enable inexpensive and safe computation of admissible stress states in vaulted masonry structures.

General analysis tools are also listed, highlighting the difficulties in applying these to masonry assessment problems.

Among the lower-bound limit analysis methods, recent advances in thurst network approaches show potential to be developed further to assess masonry structures.

Chapter 3

Scope of the Work

Based on the literature review presented in the previous chapter and the background on analysis methods for masonry structures, the scope of this dissertation is described in this chapter. The problems tackled are highlighted, and the research objectives are summarised. This chapter closes the introductory part of this research before proceeding with its methodology and implementation.

3.1 Problem statements

This section presents the problem statements that motivate this dissertation. The assessment workflow with discrete, lower-bound equilibrium methods is revisited in Section 3.1.1, and the specific problems tackled are highlighted in Section 3.1.2.

3.1.1 Assessment workflow

The typical workflow for assessing masonry structures with discrete lower-bound equilibrium methods is illustrated in Figure 3.1. This workflow is listed and defined below.

1. Data acquisition: It includes the geometric survey, executed usually with photogrammetry or laser scanning techniques. Visible crack patterns are annotated to the model as they provide insight into the structure's current state. The geometry needs to be properly transferred to the analysis model, which should, in return, be adapted to work with this data.

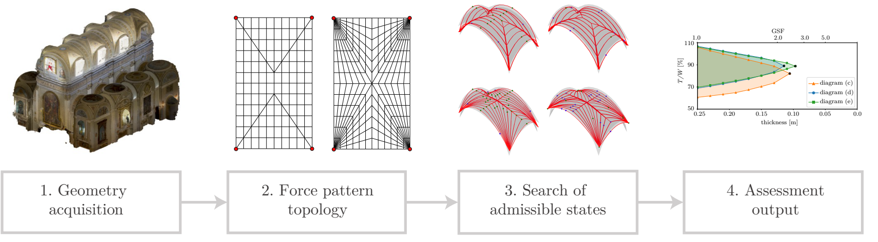

Figure 3.1: Workflow for assessing masonry vaulted structures with discrete equilibrium methods.

2. Force pattern topology: The force pattern representing the layout of the forces within the structure should be selected at the start. It should reflect the structure's main geometric features and support positions and be compatible with observed cracks. It should also connect with externally applied loads or observed settlements that might have provoked variations in the structure's force flow.

3. Search of admissible states: As highlighted in Chapter 2, lower-bound methods verify that the structure is safe by finding (at least one) admissible stress state. This work represents these states by compressive thrust networks within the masonry structural geometry. A robust and targeted search method must be implemented to find these admissible states.

4. Assessment output: Beyond just finding one admissible internal state, to conclude the assessment workflow, a practical assessment output must be provided. It should indicate how far the structure is from its limit state and provide safety factors related to its stability and capacity to sustain additional external loads and foundation settlements.

3.1.2 Problems tackled

This research aims to contribute to the assessment workflow in Figure 3.1 by developing novel methods to search efficiently for admissible stress states, enabling pattern exploration and providing relevant practical outputs to masonry assessment.

The problems tackled in this dissertation are highlighted here:

- Improve the search of admissible equilibrium states:

A robust and efficient numerical procedure is needed to explore the infinite space of admissible equilibrium states that might form in masonry structures. All possible force distributions resulting in admissible thrust networks should be investigated, which is still not available for general vaulted structures.

- Methods to investigate multiple topologies:

  The topology of the force pattern influences the result of the assessment process with TNA. Therefore, investigating different force patterns and adequately defining their degrees of freedom is needed to enable variations in the topology and geometry of these patterns.

- Improve assessment output metrics:

  Currently, computing the level of stability of three-dimensional masonry is challenging. Even if concepts such as the Geometric Safety Factor (GSF) are well-known for arches, their extension for complex three-dimensional structures is not trivial. Therefore, new metrics should be investigated to equip lower-bound methods for assessment scenarios and enable working with general 3D geometries.

- Estimating collapse loads on vaulted structures:

  Similarly, computing vertical and horizontal collapse loads in vaulted structures is challenging. These are sought in masonry structures undergoing rehabilitation or to perform (simplified) analysis against the action of earthquakes.

- Investigate the effect of settlements:

  Masonry structures often present pathologies, such as crack patterns, deformations, or distortions caused by foundation settlements. Understanding the effects of these settlements is still an open question, and including the effects of settlements in masonry models is a complex task. Therefore, better strategies to deal with these observed crack patterns are needed.

- Lack of practical open-source masonry assessment tools:

  As highlighted in Chapter 2, few specific analysis tools are available to analyse masonry structures. Moreover, there is a lack of open-source tools that can be freely shared and collaboratively developed. These would be especially useful for masonry assessment as budget and time are limited and novel methods developed in academia often remain on research papers that can not be easily implemented.

The research objectives to respond to these problems are presented in the next section.

3.2 Research objectives

This dissertation will equip TNA with an optimisation framework to assess masonry structures in multiple practical scenarios. This objective is broken into smaller objectives accomplished through this research.

- Robust search of admissible thrust networks on vaulted structures:

  The main objective of this work is to develop a robust numerical strategy to find admissible thrust networks in vaulted masonry structures. A convenient mathematical description of the networks will be sought to enable encoding this search in a constrained optimisation problem. State of the art solving strategies will be implemented to find specific equilibrium states, and suitable starting points for the optimisation will be discussed. Different objective functions will be implemented to model relevant equilibrium states in masonry structures, respecting the constraints from limit analysis.

- Enabling the analysis with different diagrams:

  The robust search of admissible thrust networks will be equipped with a novel methodology to find the degrees of freedom in a given pattern or form diagram. To enable a variety of typical masonry typologies to be analysed, parametric form diagrams will be implemented and used in different analyses. More importantly, this work will seek to quantify the effectiveness of these different patterns so they can be compared. Practical instructions guiding engineers to choose, test and modify force patterns according to the analysis will be presented.

- Metrics to determine the stability of vaulted structures:

  This work will seek to extend well-known metrics for the level of stability, such as the GSF, to vaulted structures. Additionally, novel metrics will be introduced by computing the structure's stability domain with its extremes of maximum and minimum horizontal thrusts. Beyond computing these metrics to analytical geometries, they will also be extended to scanned geometries obtained through surveys.

- Framework to compute collapse loads:

  Supported by the robust search of admissible states, this work will adapt the optimisation formulation to compute maximum vertical and horizontal load multipliers. This will enable computing a lower bound of the collapse loads in vaulted masonry structures. Strategies to adapt the force pattern to such loads will also be investigated and documented to serve as a guide to use in practical assessment scenarios.

- Connecting foundation settlements and crack pattern:

  This work will investigate the connection between foundation settlements and the appearance of crack patterns in vaulted masonry structures. This connection will be established by introducing an energy criterion in the network and adapting the optimisation framework to minimise the structure's complementary energy. Searching for equilibrium states compatible with foundation displacements can reveal the expected crack pattern at the onset of the motion.

- Collaborative open-source package to perform assessment:

  By combining structural analysis and software development, this dissertation will implement its findings into an open-source Python-based package. This package is used to compute all analyses in this dissertation. It will be shared with the engineering and research community, enabling future collaboration and the continuous development and improvement of the procedures described in this thesis by other researchers. Therefore, beyond developing the mathematical framework to compute the analysis, sharing the tools used can increase the impact of the present work.

By completing these research objectives, this dissertation contributes to the state of the art in applying discrete lower-bound limit analysis methods to better understand, model, and preserve vaulted masonry structures.

Part II

Methodology and Implementation

Chapter 4

Equilibrium Force Network

This chapter lays the foundation of the methodology developed in this dissertation by introducing the numerical formulation for computing the equilibrium in force networks. The chapter revisits the main elements of Thrust Network Analysis (TNA) and the equilibrium equations in terms of force densities from the literature. The particular case of networks with fixed horizontal projection is presented, enabling parametrising the equilibrium in terms of fewer variables or degrees of freedom (DOF). A novel algorithm is presented to find these degrees of freedom in general diagram topologies. This parametrisation will be used to search equilibrium states in this dissertation.

4.1 Definition

In the following sections, the main elements of Thrust Network Analysis (TNA) are presented after Block (2009), and their use in this work is defined.

4.1.1 Thrust network

Thrust networks (G) correspond to a *directed* and *connected* spatial graph. They represent the spatial compressive resultants (or thrusts) within the structure. Each node of the network is in equilibrium with the applied forces via axial force on the edges converging to that node. One example of a thrust network continuously supported is depicted in Figure 4.1.

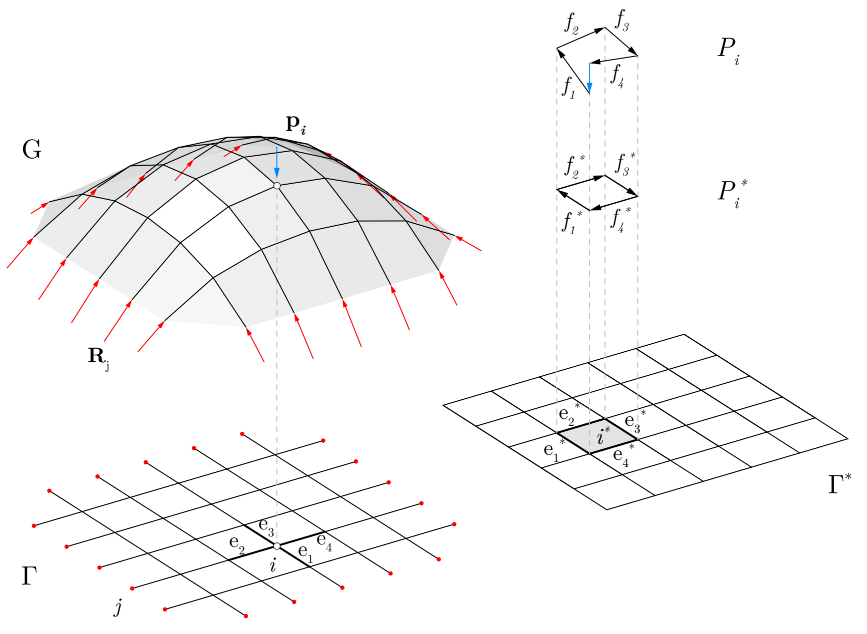

Figure 4.1: Thrust Network (G) with its horizontal projection, the form diagram (Γ). Equilibrium P_i of node i subjected to the vertical applied load $\mathbf{p}_i$ is highlighted. The horizontal projection of P_i is the closed polygon P_i^*. Summing the polygons, the network's force diagram (Γ^*) is obtained.

4.1.2 Form diagram

The form diagram (Γ) is a planar graph constructed from the projection of G (see Figure 4.1). The form diagram stores the network's topology, connectivity, and planar coordinates. Each vertex i in the form diagram with coordinates (x_i, y_i) maps to a vertex in the thrust network with elevation z_i. Similarly, each edge e_i in the form diagram maps to an edge in the thrust network carrying axial force f_i.

4.1.3 Support conditions

Boundary conditions are applied to specific network vertices, usually on the diagram's boundary. Figure 4.1 highlights the support points in the form diagram with a red dot. Reaction forces $\mathbf{R}_j$ arise at supports j such that the structure is in equilibrium.

4.1.4 Loads

Loads, such as the self-weight and externally applied live loads, are applied to the system in the network vertices. Figure 4.1 highlights in blue the application of a vertical load $\mathbf{p}_i$ to node i. The equilibrium of the node can be verified through the construction of closed polygons of force vectors P_i indicated in Figure 4.1. P_i shows a closed cycle containing the scaled vector of the applied load ($\mathbf{p}_i$) and the thrusts f_1, f_2, f_3, and f_4.

4.1.5 Force diagram

As presented in Section 2.3.3, the force diagram (Γ^*) is a graphical representation of the horizontal equilibrium of G. When all loads are parallel, the spatial equilibrium of a node i can be projected onto a plane perpendicular to the loads resulting in a two-dimensional graphic statics problem (see Figure 2.4). In Figure 4.1, the projected equilibrium of node i is the closed polygon P_i^* in which the vertical applied load $\mathbf{p}_i$ vanishes. The horizontal equilibrium is then resolved with the horizontal components of the thrusts $(f_1^*, f_2^*, f_3^*, f_4^*)$. The form ($\Gamma$) and force ($\Gamma^*$) diagrams are reciprocal, such that their corresponding edges e_i, e_i^* are parallel.

Two conventions to display and interact with force diagrams exist, the Cremona convention ($\Gamma^*_{//}$), with parallel reciprocal edges, or the Maxwell convention ($\Gamma^*_{\perp}$), with orthogonal reciprocal edges. Figure 4.2 depicts these conventions, and the Maxwell convention is adopted herein.

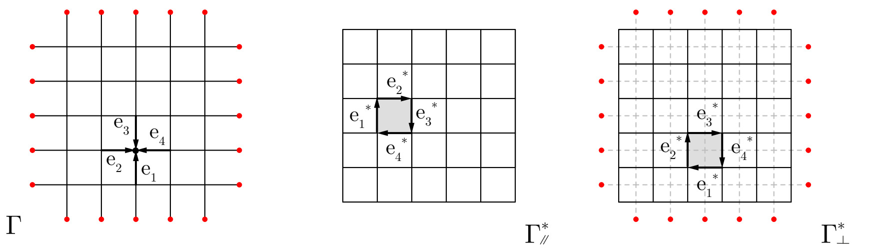

Figure 4.2: Form diagram (Γ) next to force diagram following parallel, or Cremona ($\Gamma^*_{//}$) and orthogonal, or Maxwell convention ($\Gamma^*_{\perp}$).

In this work, the force diagram visualises the force distribution in the networks. The numerical description employed to compute the equilibrium is based on force densities, as presented in the next section.

4.2 Equilibrium equations

This section presents the equilibrium computation for a general force network in which the position of the internal vertices and the axial forces are unknown. The formulation requires the introduction of the *force densities* from the Force Density Method (FDM), as in Schek (1974).

We assume a network composed of m edges and n vertices. We consider n_b supported vertices and n_i free vertices, such that $n = n_\mathrm{i} + n_\mathrm{b}$. Let $\mathbb{E}_i$ represents the group of neighbouring vertices to vertex i, such that edge e_{ij} exists, with axial force f_{ij} and length l_{ij}. The equilibrium of vertex i is computed as

$$\sum_{j \in \mathbb{E}_i} \frac{f_{ij}}{l_{ij}} (x_j - x_i) = p_{\mathrm{x},i}, \tag{4.1a}$$

$$\sum_{j \in \mathbb{E}_i} \frac{f_{ij}}{l_{ij}} (y_j - y_i) = p_{\mathrm{y},i}, \tag{4.1b}$$

$$\sum_{j \in \mathbb{E}_i} \frac{f_{ij}}{l_{ij}} (z_j - z_i) = p_{\mathrm{z},i}, \tag{4.1c}$$

in which the length of an edge l_{ij} is unknown and a function of the spatial geometry of the structure, i.e., a function of x_i, y_i, z_i and x_j, y_j, z_j. Consequently, Eqs. 4.1 are nonlinear.

To linearise these equations, Schek (1974) introduces the edge force density q_i, which is defined as the ratio among the edge's axial force f_i and its length l_i,

$$q_i = \frac{f_i}{l_i}. \tag{4.2}$$

To write Eqs. 4.1 in a matrix form, the connectivity matrix $\mathbf{C}$ $[m \times n]$ is introduced defined as

$$\mathbf{C}_{i,j} = \begin{cases} +1 & \text{if vertex } i \text{ is the head of edge } j, \\ -1 & \text{if vertex } i \text{ is the tail of edge } j, \\ 0 & \text{otherwise.} \end{cases} \tag{4.3}$$

The nodal positions of the network are cast in the vectors $\mathbf{x}, \mathbf{y}, \mathbf{z}$ $[n \times 1]$, and the applied nodes in each direction are collected in $\mathbf{p}_{\mathrm{x}}, \mathbf{p}_{\mathrm{y}}, \mathbf{p}_{\mathrm{z}}$ $[n \times 1]$.

With this description, the nodal equilibrium of the network can be written by introducing the coordinate difference matrices $(\mathbf{U}, \mathbf{V}, \mathbf{W})$ that store on their diagonals the differences $x_j - x_i$, $y_j - y_i$ and $z_j - z_i$ for an edge $\mathbf{e}_{ij}$ and are computed as

$$\mathbf{U} = \mathrm{diag}(\mathbf{C}\mathbf{x}), \tag{4.4a}$$
$$\mathbf{V} = \mathrm{diag}(\mathbf{C}\mathbf{y}), \tag{4.4b}$$
$$\mathbf{W} = \mathrm{diag}(\mathbf{C}\mathbf{y}). \tag{4.4c}$$

By partitioning the connectivity matrix in $\mathbf{C}_{\mathrm{i}}$ $[m \times n_{\mathrm{i}}]$, $\mathbf{C}_{\mathrm{b}}$ $[m \times n_{\mathrm{b}}]$ representing the free and support nodes respectively, and by partitioning the load vectors in $\mathbf{p}_{\mathrm{x,i}}$ $[n_{\mathrm{i}} \times 1]$ and $\mathbf{p}_{\mathrm{x,b}}$ $[n_{\mathrm{b}} \times 1]$ (analogously for y, z directions), the $3n_{\mathrm{i}}$ internal nodal equilibrium equations become

$$\mathbf{C}_{\mathrm{i}}^{\mathrm{T}}\mathbf{U}\mathbf{q} = \mathbf{p}_{\mathrm{x,i}}, \tag{4.5a}$$
$$\mathbf{C}_{\mathrm{i}}^{\mathrm{T}}\mathbf{V}\mathbf{q} = \mathbf{p}_{\mathrm{y,i}}, \tag{4.5b}$$
$$\mathbf{C}_{\mathrm{i}}^{\mathrm{T}}\mathbf{W}\mathbf{q} = \mathbf{p}_{\mathrm{z,i}}, \tag{4.5c}$$

in which the equilibrium variables are the force densities $\mathbf{q}$ $[m \times 1]$. These equations are often rewritten in terms of the unknown free coordinates of the network, which are now a variable of the force densities and the position of the supports $(\mathbf{x}_{\mathrm{b}}, \mathbf{y}_{\mathrm{b}}, \mathbf{z}_{\mathrm{b}})$ $[n_{\mathrm{b}} \times 1]$ as

$$\mathbf{x}_{\mathrm{i}} = \mathbf{D}_{\mathrm{i}}^{-1}\left(\mathbf{p}_{\mathrm{x,i}} - \mathbf{D}_{\mathrm{b}}\mathbf{x}_{\mathrm{b}}\right), \tag{4.6a}$$
$$\mathbf{y}_{\mathrm{i}} = \mathbf{D}_{\mathrm{i}}^{-1}\left(\mathbf{p}_{\mathrm{y,i}} - \mathbf{D}_{\mathrm{b}}\mathbf{y}_{\mathrm{b}}\right), \tag{4.6b}$$
$$\mathbf{z}_{\mathrm{i}} = \mathbf{D}_{\mathrm{i}}^{-1}\left(\mathbf{p}_{\mathrm{z,i}} - \mathbf{D}_{\mathrm{b}}\mathbf{z}_{\mathrm{b}}\right), \tag{4.6c}$$

where $\mathbf{D}_\mathrm{i} = \mathbf{C}_\mathrm{i}^\mathrm{T}\mathbf{Q}\mathbf{C}_\mathrm{i}$ $[n_\mathrm{i} \times n_\mathrm{i}]$, $\mathbf{D}_\mathrm{b} = \mathbf{C}_\mathrm{i}^\mathrm{T}\mathbf{Q}\mathbf{C}_\mathrm{b}$ $[n_\mathrm{i} \times n_\mathrm{b}]$ and $\mathbf{Q} = \mathrm{diag}(\mathbf{q})$ $[m \times m]$.

To conclude, the emerging reaction forces in the support i, $\mathbf{R}_i = [R_{\mathrm{x},i}; R_{\mathrm{y},i}; R_{\mathrm{z},i}]$ can be retrieved from the reaction components $\mathbf{R}_\mathrm{x}$, $\mathbf{R}_\mathrm{y}$, $\mathbf{R}_\mathrm{z}$ $[n_\mathrm{b} \times 1]$ calculated as

$$\mathbf{R}_\mathrm{x} = \mathbf{C}_\mathrm{b}^\mathrm{T}\mathbf{U}\mathbf{q} - \mathbf{p}_{\mathrm{x,b}}, \tag{4.7a}$$

$$\mathbf{R}_\mathrm{y} = \mathbf{C}_\mathrm{b}^\mathrm{T}\mathbf{V}\mathbf{q} - \mathbf{p}_{\mathrm{y,b}}, \tag{4.7b}$$

$$\mathbf{R}_\mathrm{z} = \mathbf{C}_\mathrm{b}^\mathrm{T}\mathbf{W}\mathbf{q} - \mathbf{p}_{\mathrm{z,b}}. \tag{4.7c}$$

With this formulation, the infinite space of equilibrium networks for a given topology (or connectivity) can be explored in terms of the position of the supports $(\mathbf{x}_\mathrm{b}, \mathbf{y}_\mathrm{b}, \mathbf{z}_\mathrm{b})$ and values of the force densities in the edges of the network $(\mathbf{q})$.

In the next section, the particular case in which the networks have their horizontal projection fixed is studied.

4.3 Fixed network projection

As in Block and Lachauer (2014), this work focuses on networks with fixed horizontal projection, i.e., fixed form diagram (Γ). With this assumption, the planar coordinates of the network $(\mathbf{x}, \mathbf{y})$ are defined. As a consequence, the horizontal equilibrium equations (4.5a and 4.5b) can be rearranged, introducing the horizontal equilibrium matrix $\mathbf{E}$ $[2n_\mathrm{i} \times m]$ and the vector of applied horizontal forces nodes in the internal nodes $\mathbf{p}_{\mathrm{h,i}}$ $[2n_\mathrm{i} \times 1]$,

$$\mathbf{E}\mathbf{q} = \mathbf{p}_{\mathrm{h,i}}, \text{ with: } \mathbf{E} = \begin{bmatrix} \mathbf{C}_\mathrm{i}^\mathrm{T}\mathbf{U} \\ \mathbf{C}_\mathrm{i}^\mathrm{T}\mathbf{V} \end{bmatrix}, \mathbf{p}_{\mathrm{h,i}} = \begin{bmatrix} \mathbf{p}_{\mathrm{x,i}} \\ \mathbf{p}_{\mathrm{y,i}} \end{bmatrix}. \tag{4.8}$$

Assuming that the form diagram is fixed means additional constraints to the vector of force densities, such that its components can not be chosen freely. Indeed, the number of force densities that can be chosen freely in Eq. 4.8 corresponds to the number k of degrees of freedom (DOF) of the planar form diagram. In other words, this corresponds to the degree of statical indeterminacy of the network (Pellegrino and Calladine, 1986).

As shown in Van Mele and Block (2014), the number of DOF is equal to the rank deficiency of the matrix $\mathbf{E}$. The free parameters are denoted *independent force densities*, and they relate to specific *independent edges* in the network. The independent force densities $\mathbf{q}_{\mathrm{id}}$ can then be used to compute the dependent ones $\mathbf{q}_{\mathrm{d}}$, with

$$\mathbf{q}_{\mathrm{d}} = -\mathbf{E}_{\mathrm{d}}^{\dagger}\left(\mathbf{E}_{\mathrm{id}}\mathbf{q}_{\mathrm{id}} - \mathbf{p}_{\mathrm{h,i}}\right), \tag{4.9}$$

where $\mathbf{E}_{\mathrm{d}}$ and $\mathbf{E}_{\mathrm{id}}$ are slices of $\mathbf{E}$ related to the dependent and independent edges, respectively, and $\mathbf{E}_{\mathrm{d}}^{\dagger}$ the generalised inverse or Moore-Penrose pseudo-inverse of $\mathbf{E}_{\mathrm{d}}$.

A discussion about finding and interpreting the DOF, i.e., the independent edges, in a form diagram is presented in Section 4.4. Once $\mathbf{q}_{\mathrm{d}}$ is computed from $\mathbf{q}_{\mathrm{id}}$, the vector of force densities $\mathbf{q}$ in the system is retrieved through the linear transformation

$$\mathbf{q} = \mathbf{B}\mathbf{q}_{\mathrm{id}} + \mathbf{d},\ \text{with: } \mathbf{B} = \begin{bmatrix} -\mathbf{E}_{\mathrm{d}}^{\dagger}\mathbf{E}_{\mathrm{id}} \\ \mathbf{I}_{\mathrm{k}} \end{bmatrix},\ \mathbf{d} = \begin{bmatrix} \mathbf{E}_{\mathrm{d}}^{\dagger}\mathbf{p}_{\mathrm{h,i}} \\ \mathbf{0} \end{bmatrix}, \tag{4.10}$$

where $\mathbf{I}_{\mathrm{k}}$ is the identity matrix of size k.

After such variable reduction, the vertical coordinates of the free nodes in the network $\mathbf{z}_{\mathrm{i}}$, described in Eq. 4.11 are a function of $\mathbf{q}_{\mathrm{id}}$ and $\mathbf{z}_{\mathrm{b}}$ as in

$$\mathbf{z}_{\mathrm{i}}\left(\mathbf{q}_{\mathrm{id}}, \mathbf{z}_{\mathrm{b}}\right) = \left(\mathbf{C}_{\mathrm{i}}^{\mathrm{T}}\mathbf{Q}\mathbf{C}_{\mathrm{i}}\right)^{-1}\left(\mathbf{p}_{\mathrm{z,i}} - \left(\mathbf{C}_{\mathrm{i}}^{\mathrm{T}}\mathbf{Q}\mathbf{C}_{\mathrm{b}}\right)\mathbf{z}_{\mathrm{b}}\right). \tag{4.11}$$

Eq. 4.11 will be used to compute the free nodal elevations enabling the constraint optimisation framework described in Chapter 5.

4.4 Degrees of freedom in a projected network

This section discusses the strategies developed to deal with the indeterminacy of the network. An algorithm to find the independent edges is presented in Section 4.4.1. A connection with inextensible mechanisms is shown in Section 4.4.2, and the isolated effect of the independent edges is illustrated in Section 4.4.3.

4.4.1 An algorithm to find independent edges

This section describes the procedure to determine a projected network's degrees of freedom (DOF). This procedure is also described in Maia Avelino, Iannuzzo, Van Mele and Block (2021*a*). As discussed in Section 4.3, the number of independent force density parameters k that can be chosen freely in Eq. 4.8 correspond to the rank deficiency of the matrix $\mathbf{E}$ or to the dimension of the nullspace of the matrix $\mathbf{E}$ computed for the networks as

$$k = m - \mathrm{rank}(\mathbf{E}). \tag{4.12}$$

Given the matrix construction adopted in this work, each column of $\mathbf{E}$ relates to one specific edge in the form diagram according to the numbering assumed when the topology was generated (see the construction of $\mathbf{C}$ in Eq. 4.3).

Therefore, one base of the nullspace of $\mathbf{E}$ corresponds to the largest k such that a combination of k columns arranged in matrix $\mathbf{E}_{\mathrm{id}}$ put next to the remaining $(m-k)$ columns in $\mathbf{E}_{\mathrm{d}}$ will result in

$$\mathrm{rank}(\mathbf{E}_{\mathrm{d}}|\mathbf{E}_{\mathrm{id}}) = \mathrm{rank}(\mathbf{E}_{\mathrm{d}}), \tag{4.13}$$

which means that $\mathbf{E}_{\mathrm{d}}$ is non-singular and can be inverted.

When Eq. 4.13 is verified, the edges corresponding to the k columns from the nullspace are the independent edges of the form diagram. These edges can be found through a sequential Singular Value Decomposition (SVD) approach. In this sequential method, the matrix $\mathbf{E}$ is reconstructed column-by-column. Each time a column is added, the matrix rank is checked through SVD. After such addition, if the matrix's rank is not increased, the column belongs to the nullspace of $\mathbf{E}$, and the corresponding edge can be taken as an independent. The pseudocode for this procedure is presented in Algorithm 1.

Algorithm 1 results in a base of the nullspace of the equilibrium matrix. This approach enables controlling the precision for discarding small singular values. It avoids the accumulation of errors in the row-column operations that arise in Gauss-Jordan Elimination (GSE) (see also Section 6.6.4).

The algorithm is applied to the networks in Figure 4.3. For each case, Table 4.1 lists the number of edges m, internal nodes n_{i}, the shape and rank of $\mathbf{E}$, the number of independent edges k, and inextensible mechanisms c.

Algorithm 1 Finding independent edges in a network

```
i ← 0
inds ← [ ]                          ▷ Empty list to store the independent columns
E_d = E[:, i]                       ▷ Initiate E_d with first column
i = i + 1
while i < m do
    E_temp = [E_d|E[:, i]]
    if rank(E_temp) < ncol(E_temp) then
        inds ← [i]                  ▷ column i belongs to nullspace
    else
        E_d = E_temp
    end if
    i = i + 1
end while
```

Table 4.1: Key parameters used to find a set of independent edges for the topologies depicted in Figure 4.3.

Topology	m	n_{i}	shape($\mathbf{E}$)	rank($\mathbf{E}$)	k	c
(a)	60	25	(50×60)	50	10	0
(b)	84	37	(74×84)	71	13	3
(c)	96	45	(90×96)	88	8	2
(d)	42	22	(44×42)	38	4	6

Figure 4.3 shows one of the multiple possible groups of independent edges for each topology. As discussed in Liew et al. (2019), these groups are not unique and can not be selected randomly for most topologies, such that their choice has a structural meaning, as shown for each topology below.

In the continuously supported orthogonal grid (Figure 4.3a), one independent per group of continuous edges is found. This result derives from the fact that the force density in each group of continuous edges is independent of the others. Consequently, only one static parameter is required at each group (Liew et al., 2019). The effect of a force increase in each independent edge is discussed in Section 4.4.3.

The circular topology (Figure 4.3b) is composed of three circular closed hoops and 12 meridional segments converging to the centre. One independent per hoop is observed, and one independent for all but two meridians converging to the centre, i.e., ten independents for 12 meridians. One inde-

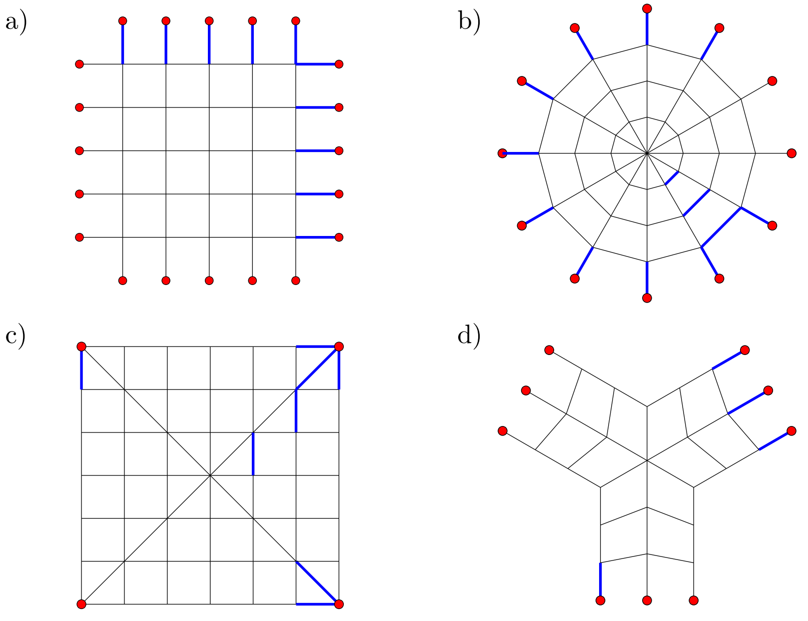

Figure 4.3: Independent edges highlighted in blue for different topologies: (a) an orthogonal grid, (b) a circular arrangement, (c) a cross diagram, and (d) a three-sided diagram.

pendent per hoop is necessary to control the axial force in the hoop, while one independent per meridian is necessary to distribute the loads to the supports. However, not all meridian forces can be freely chosen as they converge to a single point where equilibrium must be ensured. In fact, at the centre, $n = 12$ segments converge to the singular point, and $(n - 2)$ DOF are observed.

For the corner-supported cross diagram of Figure 4.3c, one independent is found at each of the four boundaries, behaving independently of the rest of the structure as they connect directly to two support points. Two independents are found among the four diagonal segments connecting the supports to the singular point at the centre of the pattern, verifying the $(n - 2)$ rule stated above. One independent edge is found per continuous closed strip, as these are analogous to the closed hoops in Figure 4.3b. The effect of a force increase at each edge is discussed in Section 4.4.3.

Finally, for the three-sided diagram in Figure 4.3d, one independent edge is found at each boundary of the pattern, where continuous polylines connect two supports. One independent is also found for the three continuous segments converging to the centre pattern singularity, following the $(n-2)$ rule.

4.4.2 Connection with inextensible mechanisms

This section discussed the connection between the degrees of freedom and inextensible mechanisms in the network by verifying the *extended Maxwell's rule* (Calladine, 1983) to the stability of frames, which is written as

$$k - c = b - 2n + r. \tag{4.14}$$

In which k is the number of independent states of self-stress, c the number of inextensible mechanisms, b the number of bars, n the number of nodes, and r the number of kinematic restraints at the supports (see also Van Mele and Block, 2014). In the present formulation, every support point restraint the nodes in two directions so that the equation can be rewritten, and the number of independent edges (or independent states of self-stress) put in evidence as

$$k = (m - 2n_{\mathrm{i}}) + c. \tag{4.15}$$

Eq. 4.15 allows determining the number of inextensible mechanisms c in the networks. More importantly, it distinguishes the DOF into two types:

(i) $m - 2n_{\mathrm{i}}$ DOF computed from the connectivity or edge counting, and

(ii) c DOF linked to the inextensible mechanisms.

Examples of inextensible mechanisms leading to the second DOF type are highlighted in Figure 4.4. In Block (2009), the DOF are also differentiated in (i) and (ii), but only closed cycles are considered for DOF of type (ii), e.g., Figures 4.4a–b. The SVD analysis enables analysing cases such as patterns with unsupported boundary edges, for which $m - 2n_{\mathrm{i}} < 0$ might arise, as in Figure 4.4c.

Given the unsupported straight boundary of the pattern in Figure 4.4c, the edges corresponding to the mechanisms highlighted in Figure 4.4 are

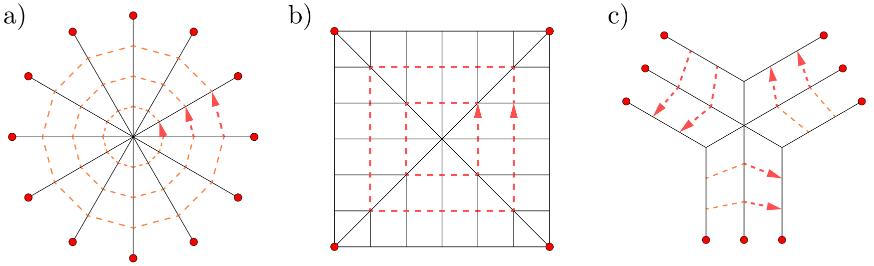

Figure 4.4: Inextensible mechanisms obtained from the extended *Maxwell rule* for patterns, with (a) $c = 3$, (b) $c = 2$, and (c) $c = 6$.

required to be zero. Contrastingly, when the circular mechanisms are observed, one independent per hoop is assigned, and the force does not vanish as discussed in Section 4.4.3.

To obtain these inextensible mechanisms, the nullspace of the row-space of $\mathbf{E}$ can be explored. Combining Eqs. 4.12 and 4.15, the rank deficiency c of the row-space of $\mathbf{E}$ is defined, which is analogous to the statical and kinematical DOF studied for frames in Pellegrino and Calladine (1986)

$$c = 2n_{\mathrm{i}} - \mathrm{rank}(\mathbf{E}). \tag{4.16}$$

In Figure 4.5, the effect of curving the unsupported boundaries is studied for two patterns resulting in a reduction of inextensible mechanisms and, hence, fewer independent edges.

In Figure 4.5a, the boundary of the three-sided diagram is curved. The DOF reduces from $k = 4$ to $k = 2$ since the inextensible mechanisms reduce from $c = 6$ to $c = 4$. Indeed, the curved boundary “locks” some of the inextensible mechanisms from the original pattern. As a result, the boundary forces can not be chosen freely anymore, and there are additional linear relations among the forces at their edges. To this problem, thanks to symmetry, these relations are easy to read and impose that the forces in the three curved unsupported boundaries must be equal. Hence, only the independent in one of them can be selected.

In Figure 4.5b, an orthogonal diagram with two supported and two unsupported boundaries is studied. The diagram has $k = 5$ independent edges

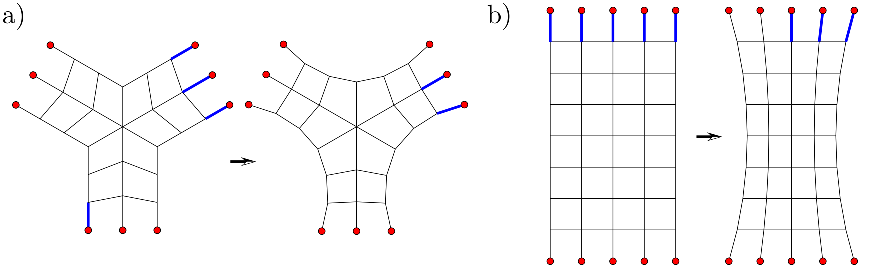

Figure 4.5: Effect of curving unsupported edges in the indeterminacy of the network: (a) reduction on the DOF (independent edges) from $k = 4$ to $k = 2$, and (b) reduction from $k = 5$ to $k = 3$.

at each path between supports and $c = 7$ inextensible mechanisms corresponding to each transverse line. However, when the open edge is curved, the five DOF can not be changed independently anymore. As a result, the DOF decreases to $k = 3$ and the mechanisms to $c = 5$. Indeed, after the symmetry is applied, the transversal edges will get activated and transmit forces among the unsupported curved boundaries.

To conclude, this section has described how independent edges relate to the networks' topology by interpreting their location in selected diagrams (Figure 4.3). It has also shown how these DOF will change by modifying the geometry and locking inextensible mechanisms (Figure 4.5). A global topology-only formula to find DOF in non-triangulated networks is unachievable, as geometry also plays a role. Nevertheless, these DOF can be selected for orthogonal networks based on understanding the support's force flow. Alternatively, Algorithm 1 can be employed. However, errors can occur related to the threshold to disregard zero singular values with the SVD, which will be discussed in Section 6.6.4.

In the next section, each independent edge's effect is demonstrated graphically.

4.4.3 The isolated effect of the independent edges

This section shows the independent force densities' effect on the thrust geometry and the internal force distribution, i.e., its effect on the force diagram.

As argued in Section 4.1.5, a force diagram can be retrieved when no horizontal loads are applied. Van Mele et al. (2012) present an algebraic method to find reciprocal force diagrams from the in-equilibrium force densities in these cases.

The independent edges in the form diagram have corresponding dual independent edges in the force diagram. Modifying the force magnitude in the independent edges allows for searching the infinite equilibria states possible that keep the form diagram fixed. Similarly, by modifying the lengths of the corresponding independent edges in the force diagram, the full range of possible modifications in the force diagram that preserves the orientation of all its edges is explored.

This correspondence is illustrated for the orthogonal (Figure 4.3a) and cross (Figure 4.3c) diagrams. The results are depicted in Figures 4.6 and 4.7, the Maxwell convention is adopted (see Section 4.1.5) for which reciprocal edges are perpendicular.

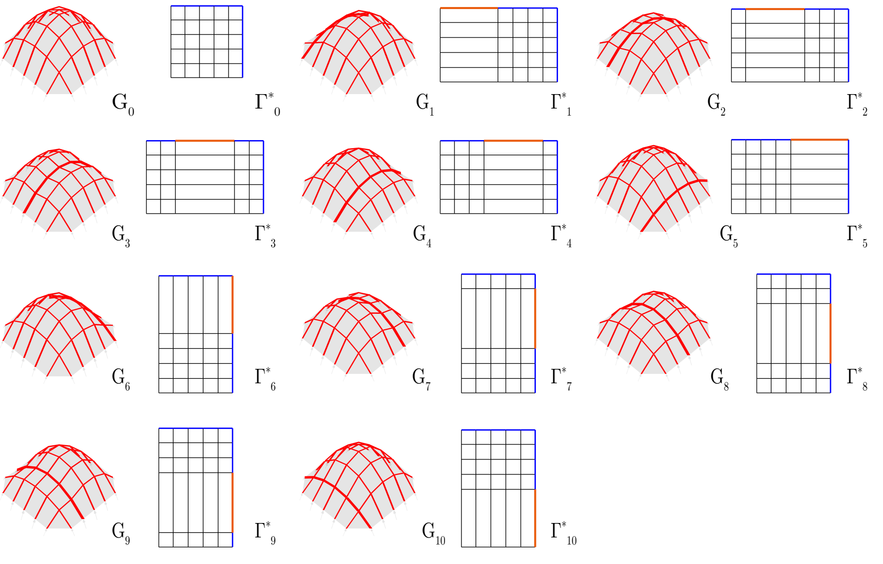

Figure 4.6: Modified force diagram (Γ_i^*) for an increase in the force magnitude in the i-th independent edge, showing the result in the thrust networks (G_i) for an orthogonal continuously supported grid.

For the orthogonal grid, Figure 4.6 shows an equally distributed force diagram Γ_0^* and the resulting thrust network G_0. Next to it, ten different thrust network geometries ($G_1 - G_{10}$) are obtained by increasing the force magnitude in each of the independent edges by a factor of 4.0. The resulting force diagrams ($\Gamma_1^* - \Gamma_{10}^*$) are depicted next to each thrust network. The thickness of the thrust segments is scaled proportionally to the horizontal force magnitude that they carry. For this topology, increasing the force magnitude in each independent increases the force magnitude for the continuous polylines following the independent edge. This increase results in a force attraction at these polylines resulting in shallow arches or creases in the thrust networks (G).

Figure 4.7 shows the effect of the independent edge in the corner supported cross topology, Departing from a symmetric force arrangement (G_0, Γ_0^*), a force increase is applied individually to each independent edge. Its effects on the network geometry can be isolated. Increasing the force on the independent edges laying in the boundary modifies the geometry locally, making the boundary arch shallower ($\Gamma_1^* - \Gamma_4^*$). The independent edges laying on the internal, closed strips ($\Gamma_5^* - \Gamma_6^*$) affect the elevation of the internal nodes, and the independents in the diagonals ($\Gamma_7^* - \Gamma_8^*$) make the diagonals shallow and attract uneven forces to the diagonal supports.

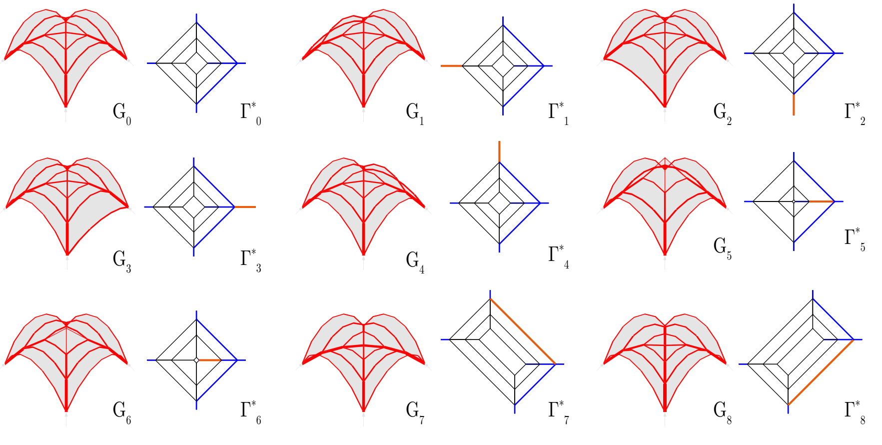

Figure 4.7: Modified force diagram (Γ_i^*) for an increase in the force magnitude in the i-th independent edge, showing the result in the thrust networks (G_i) for a corner supported cross diagram.

Figures 4.6 and 4.7 show the effect of increasing each independent force density in the networks is shown. By combining the effects of all these independent edges, infinite thrust networks with the same horizontal projection can be explored. The linear combination of the forces in the independents will allow for efficiently exploring this infinite space. Moreover, visual feedback on the internal force distribution is obtained by keeping the connection with the force diagrams (Γ^*), which helps interpret the force flow within the network. Throughout this dissertation, when relevant, the force diagram will be shown for specific results to illustrate the internal force distribution.

4.5 Summary

This section provided the numerical formulation and (re)introduced definitions from the literature that will be used throughout the dissertation.

Relevant elements of TNA are presented, and the case for the fixed form diagram is discussed. With a fixed form diagram, the statical parameter describing the elevations of the network simplifies to (i) the force densities in the independent edges and (ii) the elevation of the support points.

An original contribution is made in this chapter by introducing the algorithm to find independent edges and showing its connection with the inextensible mechanisms. The individual effect of increasing the forces in the independent edges is depicted, showing its effect on the elevations of the network and on the geometry of the force diagram.

The results presented offer a robust and general numerical description of the network's geometries. This numerical description will be explored in Chapter 5 on formulating constrained optimisation problems in thrust networks.

Chapter 5

Constrained Equilibrium

This chapter describes the search for admissible equilibrium states as a constrained optimisation problem. The constraints from limit analysis are introduced and translated into the context of TNA. Different objective functions relevant to masonry structures are presented, and a numerical description to compute these objectives in terms of the equilibrium variables is derived. The sensitivities for these objective functions are also presented, and starting points for the optimisation are discussed.

5.1 Problem formulation

In this dissertation, the search for admissible stress solutions will be encoded in a nonlinear optimisation problem, which can be written as

$$
\begin{aligned}
\underset{x \in X}{\text{minimise}} \quad & f_{\text{obj}}(x) && && \text{(5.1a)} \\
\text{subject to} \quad & g_i(x) \geq \mathbf{0}, && \text{for} \quad i = [1, \dots n_{\text{con}}], && \text{(5.1b)} \\
& h_j(x) = \mathbf{0}, && \text{for} \quad j = [1, \dots n_{\text{eq}}]. && \text{(5.1c)}
\end{aligned}
$$

The optimisation variables $x \in X$ will be described in Section 5.2, following the numerical formulation of the previous chapter.

The problem will accept a wide range of objective functions 5.1a that allow for selecting specific admissible stress states for the analysis and will be discussed in Section 5.4.

The problem inequality constraints 5.1b will translate the assumptions on admissible stress states from limit analysis and will be listed in Section 5.3.

Equality constraints 5.1c will be avoided, and the horizontal equilibrium will be verified through the independent edges (parameter reduction) as presented in Section 4.3.

5.2 Problem variables

The problem variables are the equilibrium variables defined in Chapter 4 necessary to describe the elevation of the internal vertices $\mathbf{z}_\mathrm{i}$. They are:

- the independent force densities $\mathbf{q}_\mathrm{id}$ $[k \times 1]$, modelling the internal forces in the network;
- the support's heights $\mathbf{z}_\mathrm{b}$ $[n_\mathrm{b} \times 1]$, modelling the support heights, i.e., boundary conditions, of the networks.

Therefore, the problems studied in this dissertation will have $n_\mathrm{var} \geq k + n_\mathrm{b}$ variables. Further optimisation variables can be included depending on the objective function or additional constraints imposed. One example is the inclusion of the scalar variable t representing the structure's thickness (see 5.4.2).

The following sections list the constraints and objective functions implemented. Their equations are derived in terms of the problem variables described here.

5.3 Constraints from limit analysis

This section shows the implications of the limit analysis assumptions to the equilibrium search executed with TNA.

Heyman (1966) shows that limit analysis can be applied to masonry structures assuming that the masonry has (i) infinite compressive strength, (ii) null tensile strength, and (iii) that no sliding failure occurs (see also Section 2.2.2). The two initial hypotheses reflect in the force and geometry constraints listed in Sections 5.3.1 and 5.3.2 and remarks on the no sliding assumption are listed in Section 5.3.3. Section 5.3.4 presents the algorithm to lump gravity loads based on the structural geometry.

5.3.1 Force constraints

No-tensile force constraints are imposed on the force densities of the edges in the network to comply with the null tensile strength from the Heymanian model. In this work, compressive forces are negative. Therefore, the force densities q_i are constrained to be non-positive as

$$q_i \leq 0, \qquad \text{for} \qquad i = [1, ..., m]. \tag{5.2}$$

Constraint 5.2 adds m linear constraints to the problem. The force density vector $\mathbf{q}$ is obtained linearly from the independent edges with Eq. 4.10.

The consequences of this force constraint can also be seen in the force diagram (Γ^*). As shown in Block (2009), a compression-only state in the network will reflect a force diagram having convex cells (or faces). In contrast, if mixed tension-compression forces arise, the edges of the force diagram intersect, and the polygons are no longer convex (Whiteley et al., 2013; Rippmann, 2016).

Following the assumption of infinite compressive strength, no upper bound on the axial force must be imposed. However, a maximum force density parameter $q_{\max}$ can be added to indirectly model the actual maximum compressive strength of the material. To determine this value, the topology of the network and masonry thickness should be considered. Indeed, the thrusts represent singular stresses acting as resultants in specific masonry cross-sections. Therefore, they can be linked back to stresses by retrieving the sectional dimensions and assuming a stress profile distribution.

The following section highlights the geometry constraints imposed on the networks.

5.3.2 Geometry constraints

The networks are constrained to remain within the masonry's structural geometry Λ, more specifically between the extrados, or upper bound surface Λ^{UB} and the intrados, or lower bound surface Λ^{LB}. As mentioned in Section 5.3.1, the thrusts represent the resultants acting in the cross-sections on a given point of application. As such, if the point of application exits the section, a bending moment would appear, generating tensile stresses.

Following the methodology with a fixed planar projection (Γ), this criterion is verified in the nodal elevations z_i of the network. These elevations are constrained to lay between the elevations of intrados z_i^{LB} and extrados z_i^{UB}

$$z_i^{\mathrm{LB}} \leq z_i \leq z_i^{\mathrm{UB}}, \qquad \text{for} \qquad i = [1, \ldots, n]. \tag{5.3}$$

The constraint in Eq. 5.3 adds $2n$ inequalities to the problem. This constraint is nonlinear since the heights of the free nodes computed through Eq. 4.11 are nonlinear with the force densities.

Figure 5.1 depicts the geometry constraints applied to a thrust network (G) obtained from a radial form diagram (Γ) and contained between intrados (Λ^{LB}) and extrados (Λ^{UB}) of a hemispheric dome shape. In this figure, the support points are marked in red, and their heights ($\mathbf{z}_{\mathrm{b}}$) and emerging reactions $\mathbf{R}$ are highlighted. Two portions of the dome are highlighted to show the implications of the constraints.

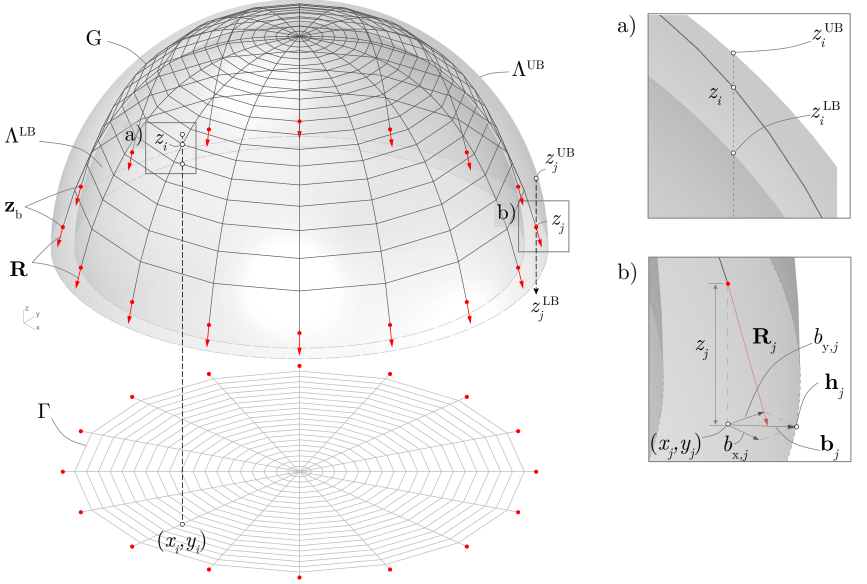

Figure 5.1: Thrust Network (G) obtained from a radial form diagram (Γ) constrained between intrados (Λ^{LB}) and extrados (Λ^{UB}) of a hemispheric dome. Detail on an (a) internal and (b) support node.

In Figure 5.1a, a typical internal node i is shown in a front view. The nodal elevation z_i is within the structural section of the masonry. The limits of this section are defined by the projection of node i, with planar coordinates (x_i, y_i), at the intrados Λ^{LB} and extrados Λ^{UB} surfaces resulting in elevations z_i^{LB} and z_i^{UB}, respectively. From Figure 5.1a, it is clear that Eq. 5.3 is respected for node i.

The constraints applied to a support j are also highlighted in 5.1b. The support point is constrained by the extrados z_j^{UB}, which is obtained from a vertical projection of (x_j, y_j) in Λ^{UB}. However, for the case of a hemispheric dome, the vertical projection in Λ^{LB} is empty, and the constraint for this node is set to a high negative value below the datum, i.e., $z_j^{\mathrm{LB}} = -\infty$.

Furthermore, in the present formulation, the support point defines the point for which the emerging reaction $\mathbf{R}_j$ arises. For some geometries, such as the hemispheric dome, additional constraints are added to the direction and magnitude of $\mathbf{R}_j$. These constraints impose that the extension of $\mathbf{R}_j$ does not surpass the extrados of the structure. In Figure 5.1b, the limit point for the reaction force $\mathbf{h}_j$ is defined as well as the vector $\mathbf{b}_j = [b_{\mathrm{x},j}, b_{\mathrm{y},j}]$, which connects the support projection (x_j, y_j) to $\mathbf{h}_j$. The constraint on the reaction writes

$$F_{\mathrm{x},j} = |b_{\mathrm{x},j}| - \left|\frac{R_{\mathrm{x},j}}{R_{\mathrm{z},j}}\right| z_{\mathrm{b},j} \geq 0, \qquad \text{for} \qquad j = [1, \dots, n_{\mathrm{b}}], \tag{5.4a}$$

$$F_{\mathrm{y},j} = |b_{\mathrm{y},j}| - \left|\frac{R_{\mathrm{y},j}}{R_{\mathrm{z},j}}\right| z_{\mathrm{b},j} \geq 0, \qquad \text{for} \qquad j = [1, \dots, n_{\mathrm{b}}]. \tag{5.4b}$$

More specifically, constraints 5.4 impose that the support rise $(z_{\mathrm{b},j})$ times the reactions slopes $(|R_{\mathrm{x},j}/R_{\mathrm{z},j}|$, or $|R_{\mathrm{y},j}/R_{\mathrm{z},j}|)$ must be bounded by $|b_{\mathrm{x},j}|$, or $|b_{\mathrm{y},j}|$. The absolute values are considered since $R_{\mathrm{x},j}$ and $R_{\mathrm{y},j}$, or $b_{\mathrm{x},j}$ and $b_{\mathrm{y},j}$ may assume positive or negative values according to the position (x_j, y_j) of the support in the plane. The reaction magnitudes $\mathbf{R}_{\mathrm{x}}, \mathbf{R}_{\mathrm{y}}, \mathbf{R}_{\mathrm{z}}$ are written with the problem variables in Eqs. 4.7.

These $2n_{\mathrm{b}}$ constraints are nonlinear. They apply to model systems assuming that no buttressing system is available, such as self-standing domes and arches. Indeed, the analysis can disregard these constraints in cases such as shallow vaults or domes. In these cases, the stability of the buttressing element can be checked a posteriori for the emerging reaction obtained in the analysis.

5.3.3 Remarks about no-sliding assumption

This work analyses the masonry structures through a continuous representative envelope. As such, the results obtained are not attached to any specific stereotomy or arrangement of blocks. Indeed, to verify the no-sliding assumption from Heyman (1966), a stereotomy and friction coefficient must be assumed for the masonry.

As shown in Fantin and Ciblac (2016); Nodargi and Bisegna (2021*b*), a stereotomy can be associated with TNA, having each node in the network representing a voussoir in the structure. These results show that the TNA approach adopted in this dissertation is equivalent to assuming vertical stereotomy to the structure. This assumption corresponds to the least conservative assumption and is far from the well-constructed historical masonry vaults, as claimed in Heyman (1995).

5.3.4 Loads from the masonry geometry

Taking advantage of the fixed form diagram Γ and the definition of the masonry envelope Λ, the loads can be computed from the masonry geometry through a projection of Γ onto the structure's middle surface Λ^{m}. Following the projection on Λ^{m}, the loads are assigned by considering a nodal tributary area A_i times the local thickness t_i of the structure measured orthogonally to Λ^{m}. This process is illustrated in Figure 5.2 for a radial form diagram Γ and a masonry cap geometry Λ with a constant thickness t. The tributary area calculation takes advantage of the definition of a centroidal dual Γ_{d} (Block et al., 2014) connecting the centroids of neighbouring faces of the projected form diagram (Γ_{proj}). An efficient numerical formulation to lump the tributary weights is presented here.

The lumped weights $\mathbf{p}_{\mathrm{z}}$ $[n \times 1]$ are computed from the projected nodal coordinates $\mathbf{X}_{\mathrm{proj}}$ $[n \times 3]$ based on the nodal tributary areas. Each tributary area A_i is divided into g elementary triangles. These triangles have a central node i; one side connecting node i to the midpoint of the edge to a neighbour j, denoted $\mathbf{v}_{\mathrm{e},ij}$; and another side connecting node i to the centroid o of a neighbouring face containing node j, denoted $\mathbf{v}_{\mathrm{c},io}$. In the detail of Figure 5.2, a node i is highlighted surrounded by four neighbouring vertices and four neighbouring faces such as its tributary area A_i is the sum of the eight elementary triangles a_{ijk} highlighted.

To compute the area of these g triangles, a linear transformation is introduced to compute the coordinates of the n_{F} face centroids, where n_{F} is the

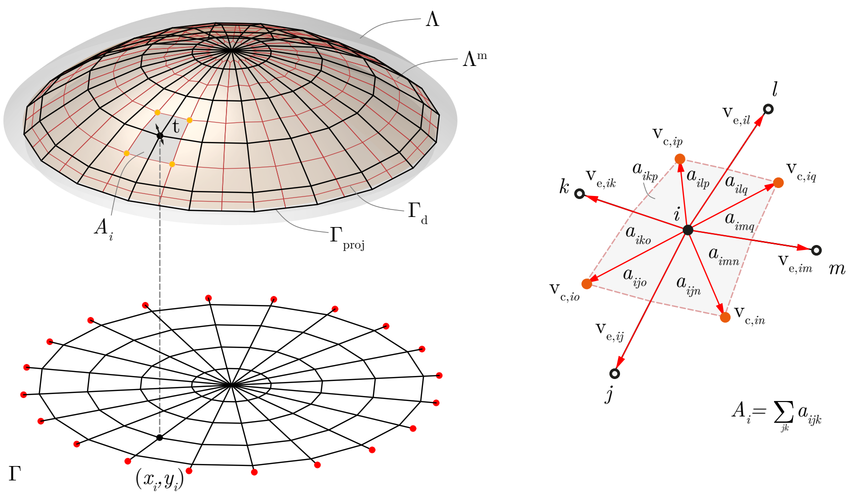

Figure 5.2: Form Diagram Γ and its projection Γ_{proj} at Λ^{m} which is the middle surface of the masonry Λ with orthogonal thickness t. The tributary area A_i of node i comes from the dual projected diagram Γ_{d} and its composing elements $(a_{ijn}, \dots)$ highlighted on the right.

number of faces in the form diagram. We assume that each face i has $n_{\mathrm{v},i}$ corner vertices and introduce the matrix $\mathbf{V}_{\mathrm{c}}$ $[n_{\mathrm{F}} \times n]$ defined as

$$\mathbf{V}_{\mathrm{c}\,i,j} = \begin{cases} 1/n_{\mathrm{v},i} & \text{if vertex } j \text{ is a corner of face } i, \\ 0 & \text{otherwise.} \end{cases} \tag{5.5}$$

Following, the mapping matrices $\mathbf{V}_0$ and $\mathbf{V}_1$ $[g \times n]$ are introduced, mapping the central and the neighbouring vertices. Similarly, $\mathbf{V}_2$ $[g \times n_{\mathrm{F}}]$ mapping the centroids is defined:

$$\mathbf{V}_{0\,i,j} = \begin{cases} 1 & \text{if node } j \text{ is the centre node for triangle } i, \\ 0 & \text{otherwise.} \end{cases} \tag{5.6a}$$

$$\mathbf{V}_{1i,j} = \begin{cases} 1 & \text{if node } j \text{ is a neighbour node for triangle } i, \\ 0 & \text{otherwise.} \end{cases} \tag{5.6b}$$

$$\mathbf{V}_{2i,j} = \begin{cases} 1 & \text{if node } j \text{ is a centroid node for triangle } i, \\ 0 & \text{otherwise.} \end{cases} \tag{5.6c}$$

With these matrices, $\mathbf{v}_\mathrm{e}$ $[g \times 3]$ is computed, storing the vectors pointing to the neighbours, and $\mathbf{v}_\mathrm{c}$ $[g \times 3]$ with the vectors pointing to the centroids,

$$\mathbf{v}_\mathrm{e} = (\mathbf{V}_1 - \mathbf{V}_0)\mathbf{X}_\mathrm{proj}, \tag{5.7a}$$
$$\mathbf{v}_\mathrm{c} = (\mathbf{V}_2\mathbf{V}_\mathrm{c} - \mathbf{V}_0)\mathbf{X}_\mathrm{proj}. \tag{5.7b}$$

The area of the g triangles is computed with the cross product among the pair of vectors stored in $\mathbf{v}_\mathrm{e}$ and $\mathbf{v}_\mathrm{c}$ as

$$\mathbf{a} = \frac{1}{4}|\mathbf{v}_\mathrm{e} \times \mathbf{v}_\mathrm{c}|. \tag{5.8}$$

From these elementary areas $\mathbf{a}$ $[g \times 1]$, the vector of tributary weights $\mathbf{p}_\mathrm{z}$ $[n \times 1]$ can be computed by assuming a density ρ and a thickness vector $\mathbf{t}$ with the local, orthogonal thickness t_i for each node i to the masonry

$$\mathbf{p}_\mathrm{z} = -\rho \ \mathrm{diag}(\mathbf{t}) \ \mathbf{V}_0^\mathrm{T}\mathbf{a}. \tag{5.9}$$

It is worth pointing out that the lumped weights must only be computed at the beginning of the optimisation process since only the vertical coordinates of the nodes in the thrust network will change. This algebraic calculation allows storing the mapping matrices at the beginning of the process and computing derivatives, if necessary. If a constant thickness t is applied, instead of a variable thickness, Eq. 5.9 can be further simplified considering only the scalar t instead of $\mathrm{diag}(\mathbf{t})$.

5.4 Objective functions

This section presents the different objective functions (f_{obj}) that are coupled to the optimisation problem 5.1. Figure 5.3 shows the objective functions implemented to a semi-circular arch. The objective functions implemented and illustrated in Figure 5.3 are:

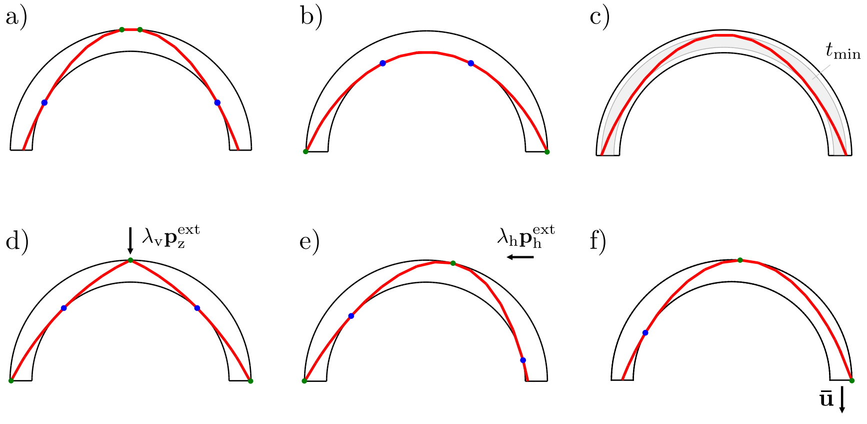

Figure 5.3: Examples of different objective functions on a semicircular arch: (a) minimum horizontal thrust, (b) maximum horizontal thrust, (c) minimum thickness t_{min}, (d) maximum vertical load multiplier λ_{v} associated to an external vertical load $\mathbf{p}_{\mathrm{z}}^{\mathrm{ext}}$, (e) maximum horizontal load multiplier λ_{h} associated to a external horizontal load $\mathbf{p}_{\mathrm{h}}^{\mathrm{ext}}$ and (f) complementary energy for boundary displacement $\bar{\mathbf{u}}$.

(a) minimise the horizontal thrust,

(b) maximise the horizontal thrust,

(c) minimise the structural thickness t_{min},

(d) maximise the vertical load multiplier λ_{v},

(e) maximise the horizontal multiplier λ_{h}, and

(f) minimise the complementary energy for boundary displacement $\bar{\mathbf{u}}$.

In Figure 5.3, the points in which the thrust line touches the extrados (resp. intrados) are marked in green (resp. blue). This convention will be adopted throughout this dissertation. They indicate the location where cracks are expected in the solution. When the thrust touches the intrados (resp. extrados), a crack will form in the extrados (resp. intrados).

The analytical expression of these objectives is presented in Sections 5.4.1–5.4.5. For each objective function, the solution in a shallow cross vault geometry is depicted. The parametric generation of this geometry will be discussed in Section 6.3.1.2. The geometry depicted throughout Sections 5.4.1–5.4.5 is defined with $\beta = 30°$ and $t/s = 0.05$. The form diagram used is a cross topology, as in Figure 4.3c having $n_\mathrm{s} = 16$ divisions along the diagonals. More on the shape definition and form diagram will be presented in Chapter 6.

Following the definition of each objective function, the gradients with regard to the problem variables are presented in Section 5.6.

5.4.1 Minimum and maximum horizontal thrusts

The first pair of objective functions presented minimises or maximises the horizontal thrust in the vaulted structures. The horizontal thrust is computed using the expression of the reaction forces $\mathbf{R}_\mathrm{x}$, $\mathbf{R}_\mathrm{y}$ defined in Eqs. 4.7a–4.7b. The objective function f_min will minimise the sum of the norm of the horizontal reactions $R_{\mathrm{x},i}$, and $R_{\mathrm{y},i}$ at each support i, as

$$f_\mathrm{min} = \sum_{i=1}^{n_\mathrm{b}} \sqrt{R_{\mathrm{x},i}^2 + R_{\mathrm{y},i}^2}. \tag{5.10}$$

As shown in Eqs. 4.7a–4.7b, the horizontal components of the emerging reactions can be computed linearly from the independent force densities $\mathbf{q}_\mathrm{id}$ and do not depend on the height of the supports $\mathbf{z}_\mathrm{b}$.

When minimising the horizontal thrust of a vaulted structure, the deepest thrust network contained within the geometry is obtained, as depicted in Figure 5.4. In the solution, the network touches the extrados in the midspan to maximise its depth and reduce its horizontal reaction component.

To maximise the horizontal reaction component in the vault, it suffices to minimise the opposite of f_min, as presented in the expression of f_max,

$$f_\mathrm{max} = -\sum_{i=1}^{n_\mathrm{b}} \sqrt{R_{\mathrm{x},i}^2 + R_{\mathrm{y},i}^2}. \tag{5.11}$$

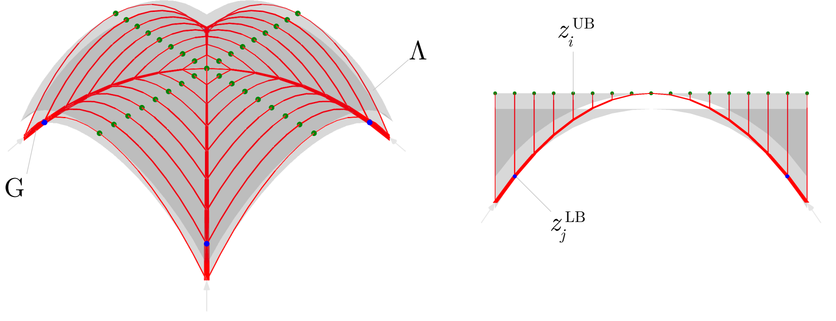

Figure 5.4: Optimisation minimising the horizontal thrust on a shallow cross vault. Left: perspective with a highlight at thrust network (G) and masonry geometry (Λ). Right: side view highlighting the points in which the network touches the extrados z_i^{UB} (green) and intrados z_j^{LB} (blue).

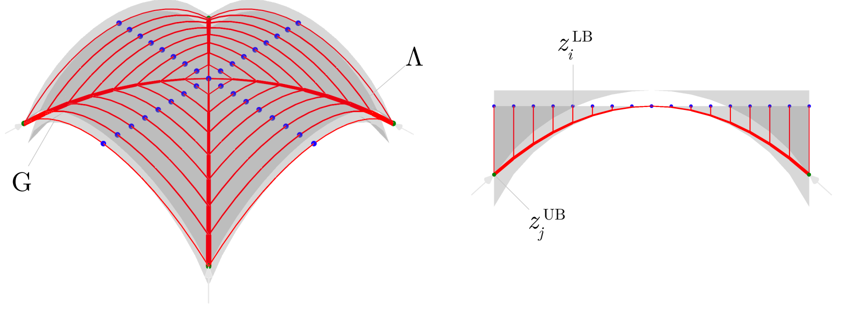

Figure 5.5: Optimisation maximising the horizontal thrust on a shallow cross vault. Left: perspective with a highlight at thrust network (G) and masonry geometry (Λ). Right: side view highlighting the points in which the network touches the intrados z_i^{LB} (blue) and extrados z_j^{UB} (green).

Conversely, when maximising the horizontal thrust of a vaulted structure, the shallowest thrust network contained within the geometry is obtained, as depicted in Figure 5.5. In the solution, the network touches the intrados in the midspan to minimise its depth and increase its horizontal reaction component.

By studying the extremes of thrusts, a better understanding of the size of the space of the domain of admissible stress states is provided. Further discussion and application to various geometries will be presented in Chapter 7.

5.4.2 Minimise the structural thickness

Minimising the structural thickness in masonry structures is relevant to calculating the Geometric Safety Factor (GSF), as shown in Heyman (1969).

In the present formulation, the minimum thickness problem is modelled by introducing an auxiliary scalar variable $t \geq 0$ representing the thickness of the structure, such that the objective function becomes

$$f_{\mathrm{t}} = t. \tag{5.12}$$

The variable thickness t entails an update in the constraints applied to the network (Section 5.3). As the thickness t decreases, the upper and lower bounds for the nodal elevations (z_i^{LB} and z_i^{UB}) need to be adjusted. The problem becomes minimising the thickness such that there is still a compressive thrust network within the updated bounds.

Three different strategies are developed to update the bounds in this work, accounting for cases in which (a) the geometry of intrados and extrados is known analytically, (b) the geometry of intrados and extrados is input as an approximated polygonal mesh, and (c) only the approximated geometry of a single surface is provided, e.g., the middle surface of the vault. These strategies are illustrated in Figure 5.6 and are explained in the following subsections.

5.4.2.1 Based on analytical description

For problems in which the geometry of intrados and extrados can be described analytically as a function of a thickness parameter t, the elevations of the intrados and extrados are updated with

$$z_i^{\mathrm{LB}}(t) = s_{\mathrm{LB}}(x_i, y_i, t), \tag{5.13a}$$
$$z_i^{\mathrm{UB}}(t) = s_{\mathrm{UB}}(x_i, y_i, t), \tag{5.13b}$$

in which s_{LB} and s_{UB} are scalar multi-variable functions that depend on the shape modelled, e.g., dome, cross vault (see Section 6.3). They represent

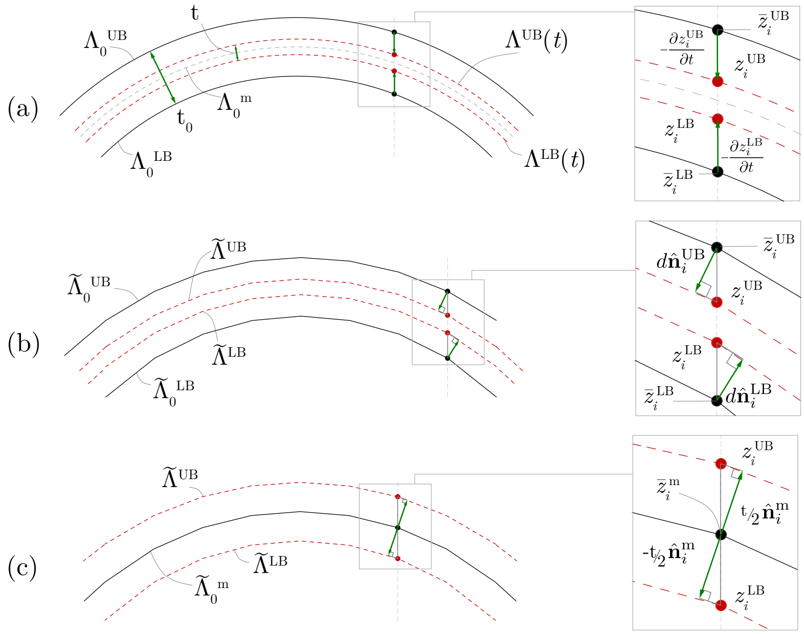

Figure 5.6: Different strategies to minimise the structural thickness based on: (a) the analytical description of the intrados $\Lambda^{\mathrm{LB}}(t)$ and extrados $\Lambda^{\mathrm{UB}}(t)$ as a function of t, (b) an approximated description of intrados $\tilde{\Lambda}^{\mathrm{LB}}$ and extrados $\tilde{\Lambda}^{\mathrm{UB}}$ with normal unit vectors $\hat{\mathbf{n}}_i^{\mathrm{LB}}$ and $\hat{\mathbf{n}}_i^{\mathrm{UB}}$, and (c) an approximated description of the middle surface $\tilde{\Lambda}^{\mathrm{m}}$ with unit normals $\hat{\mathbf{n}}_i^{\mathrm{m}}$.

the elevation of intrados and extrados for a given nodal position in the form diagram (x_i, y_i) and thickness t. As such, the new intrados and extrados, $\Lambda^{\mathrm{LB}}(t)$ and $\Lambda^{\mathrm{UB}}(t)$, are computed analytically as illustrated in Figure 5.6a. For a dome, e.g., the functions s_{LB} and s_{UB} described in Eqs. 6.1. The analytical minimisation of the structural thickness t_{min} for the same shallow cross vault from Section 5.4.1 is presented in Figure 5.7.

5.4.2.2 Based on intrados and extrados heightfields

An offset strategy has been developed for the cases in which only an approximate heightfield of intrados ($\tilde{\Lambda}^{\mathrm{LB}}$) and extrados ($\tilde{\Lambda}^{\mathrm{UB}}$) is available. This offset is computed based on the normal unit vector $\hat{\mathbf{n}}_i$ computed for the

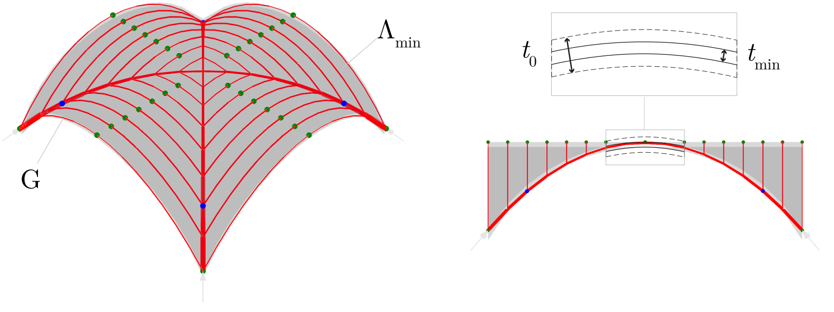

Figure 5.7: Optimisation minimising the thickness on a shallow cross vault. Left: a perspective of the solution with thrust network (G) and minimum masonry geometry ($\Lambda_{\min}$). Right: Elevation showing the initial t_0 and minimum thickness $t_{\min}$.

projection of the form diagram's node i onto the heightfield.

We assume that $\tilde{\Lambda}^{\mathrm{LB}}$ and $\tilde{\Lambda}^{\mathrm{UB}}$ are known for the projection of the points of the form diagram. As such, the initial elevations $\bar{z}_i^{\mathrm{LB}}$ and $\bar{z}_i^{\mathrm{UB}}$, and the normal unit vectors $\hat{\mathbf{n}}_i^{\mathrm{LB}}$ and $\hat{\mathbf{n}}_i^{\mathrm{UB}}$ pointing to the interior of the structural domain can be computed, as shown in Figure 5.6b.

The new bounds are computed by introducing the scalar $d \geq 0$ representing the offset distance from the initial intrados and extrados. The offset is then computed linearly by projecting the normal vectors $\hat{\mathbf{n}}_i$ perpendicularly onto the vertical direction. The magnitude of the vertical offset distance δ_{p} is computed by Eq. 5.14 for a normal vector $\hat{\mathbf{n}}_i = [\hat{n}_{\mathrm{x},i}, \hat{n}_{\mathrm{y},i}, \hat{n}_{\mathrm{z},i}]$ as

$$\delta_{\mathrm{p}}(\hat{\mathbf{n}}_i) = \sqrt{1 + \frac{\hat{n}_{\mathrm{x},i}^2 + \hat{n}_{\mathrm{y},i}^2}{\hat{n}_{\mathrm{z},i}^2}}. \tag{5.14}$$

By considering the vertical projections in the offsets, the new bounds corresponding to each vertex (x_i, y_i) in the form diagram can be linearly calculated to enter the constraints in Eq. 5.3 as

$$z_i^{\mathrm{LB}}(d) = \bar{z}_i^{\mathrm{LB}} + d\,\delta_{\mathrm{p}}(\hat{\mathbf{n}}_i^{\mathrm{LB}}), \tag{5.15a}$$
$$z_i^{\mathrm{UB}}(d) = \bar{z}_i^{\mathrm{UB}} - d\,\delta_{\mathrm{p}}(\hat{\mathbf{n}}_i^{\mathrm{UB}}). \tag{5.15b}$$

The objective function to minimise the structural thickness becomes then the maximisation of d or the minimisation of $-d$

$$f_{\mathrm{t}} = -d. \tag{5.12}$$

5.4.2.3 Based on a single surface heightfield

A similar approach applies if only a single surface is available. This surface can be considered as the ideal vault's middle surface ($\tilde{\Lambda}^{\mathrm{m}}$) or the geometry of its intrados ($\tilde{\Lambda}^{\mathrm{LB}}$).

The case in which the middle surface heightfield ($\tilde{\Lambda}^{\mathrm{m}}$) is available is described in Figure 5.6c. The process is based on the middle surface heights $\bar{z}_i^{\mathrm{m}}$ and the normal vectors $\hat{\mathbf{n}}_i^{\mathrm{m}}$. The new bounds are computed by considering a $t/2$ offset of the middle surface in both directions such that the new constraining elevations are computed as

$$z_i^{\mathrm{LB}}(t) = \bar{z}_i^{\mathrm{m}} - \frac{t}{2}\,\delta_{\mathrm{p}}(\hat{\mathbf{n}}_i^{\mathrm{m}}), \tag{5.16a}$$

$$z_i^{\mathrm{UB}}(t) = \bar{z}_i^{\mathrm{m}} + \frac{t}{2}\,\delta_{\mathrm{p}}(\hat{\mathbf{n}}_i^{\mathrm{m}}). \tag{5.16b}$$

When only the intrados surface ($\tilde{\Lambda}^{\mathrm{LB}}$) is available, the update occurs at the extrados elevations considering the offset from $\bar{z}_i^{\mathrm{LB}}$ by the magnitude of the thickness parameter t as in

$$z_i^{\mathrm{UB}}(t) = \bar{z}_i^{\mathrm{LB}} + t\,\delta_{\mathrm{p}}(\hat{\mathbf{n}}_i^{\mathrm{LB}}). \tag{5.17a}$$

For the cases in which only a single surface is available, the objective remains the same as in Eq. 5.12, minimising the scalar t.

The main advantage of the strategies presented in Sections 5.4.2.2–5.4.2.3 is that by considering the vertical projections in the offsets, the new bounds corresponding to each vertex (x_i, y_i) in the form diagram can be linearly calculated. With these strategies, the structural thickness can be minimised even for practical cases where the vaults' geometry is not provided analytically. Indeed, after the data acquisition, only a point cloud heightfield is obtained when assessing existing masonry structures.

5.4.3 Maximise the vertical load multiplier

Masonry structures might collapse due to additional vertically applied load. In this section, the maximisation of a general vertical load is taken as the objective function of the optimisation problem 5.1. The auxiliary variable $\lambda_{\mathrm{v}} \geq 0$ is introduced, representing the vertical load multiplier associated with an external vertical load $\mathbf{p}_{\mathrm{z}}^{\mathrm{ext}}$ $[n \times 1]$, defining the distribution of the applied external load to the nodes of the structure. The computation of the heights of the network is executed with the following equation:

$$\mathbf{z}_{\mathrm{i}}\left(\mathbf{q}_{\mathrm{id}}, \mathbf{z}_{\mathrm{b}}, \lambda_{\mathrm{v}}\right) = \mathbf{D}_{\mathrm{i}}^{-1}\left(\left(\mathbf{p}_{\mathrm{z,i}} + \lambda_{\mathrm{v}} \mathbf{p}_{\mathrm{z,i}}^{\mathrm{ext}}\right) - \left(\mathbf{C}_{\mathrm{i}}^{\mathrm{T}} \mathbf{Q} \mathbf{C}_{\mathrm{b}}\right) \mathbf{z}_{\mathrm{b}}\right). \tag{5.18}$$

In Eq. 5.18, the additional external load applied to the system is added to the tributary self-weights $\mathbf{p}_{\mathrm{z}}$ computed following Section 5.3.4. The height of the internal vertices in the network is then linear with respect to λ_{v}. Eq. 5.18 should be considered in the constraints on the elevations of the network, i.e., Eqs. 5.3.

Furthermore, the external load will influence the emerging vertical reaction forces of the system, such that Eq. 4.7c is rewritten as

$$\mathbf{R}_{\mathrm{z}} = \mathbf{C}_{\mathrm{b}}^{\mathrm{T}} \mathbf{W} \mathbf{q} - \mathbf{p}_{\mathrm{z,b}} - \lambda_{\mathrm{v}} \mathbf{p}_{\mathrm{z,b}}^{\mathrm{ext}}. \tag{5.19}$$

Such that the effect of Eq. 5.19 needs to be taken into account in case the constraints in the reaction forces (5.4) are activated.

In Figure 5.8, the vector defining the loading case $\mathbf{p}_{\mathrm{z}}^{\mathrm{ext}}$ has null entries for all vertices except for the vertex highlighted in the middle of the vault's web, which has entry -1.0 representing an additional load pointing downwards. To maximise the effect of this load, the scalar parameter λ_{v} is maximised such that the objective then becomes

$$f_{\mathrm{v}} = -\lambda_{\mathrm{v}}. \tag{5.20}$$

The solution in Figure 5.8 shows the thrust network obtained for the maximum applied vertical load. The network topology was modified to allow for direct paths to the supports. These direct paths get activated in the optimal solution. Results obtained with collapse loads are presented in Chapter 8.

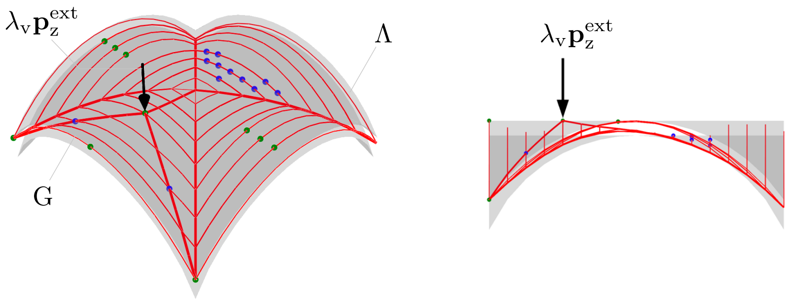

Figure 5.8: Optimisation maximising the vertical load multiplier λ_v associated with an external vertical load applied $\mathbf{p}_z^{ext}$ to the middle of the web in a shallow vault. Left: a perspective of the thrust network (G), masonry geometry (Λ), and applied load. Right: side view showing the force transferred to the supports.

Eq. 5.20 is linear and can be coupled to the developed framework, given that the effects of the added external load are taken into account in the constraints.

5.4.4 Maximise the horizontal load multiplier

A procedure to maximise the effect of a horizontal load case is presented in this section. Similarly to the process presented in Section 5.4.3, an auxiliary variable $\lambda_h \geq 0$ representing the horizontal load multiplier is introduced. This load multiplier is associated with a vector defining the distribution and direction of the applied horizontal load $\mathbf{p}_h^{ext}$ $[2n \times 1]$. The load vector is composed of a stack of the components applied to the x and y directions, respectively $\mathbf{p}_x^{ext}, \mathbf{p}_y^{ext}$ $[n \times 1]$.

The horizontal applied load needs to be feasible, i.e., there should be a compressive pattern to transfer it to the supports. Mathematically, as shown in Bruggi (2020), this can be verified by checking that the vector of horizontally applied loads in the free vertices $\mathbf{p}_{h,i}^{ext}$ does not add a dimension to the rank of the equilibrium matrix, i.e.,

$$\mathrm{rank}(\mathbf{E}) = \mathrm{rank}(\mathbf{E}|\mathbf{p}_{h,i}^{ext}). \tag{5.21}$$

Given that Eq. 5.21 is verified, the loading case can be applied to the form diagram. It influences the horizontal equilibrium, which is solved with the independent edges as described in Eq. 4.10, such that the new expression for the edge force densities accounting for the additional external horizontal load is

$$\mathbf{q}(\mathbf{q}_{\mathrm{id}}, \lambda_h) = \mathbf{B}\mathbf{q}_{\mathrm{id}} + \lambda_{\mathrm{h}} \mathbf{E}_{\mathrm{d}}^{\dagger} \begin{bmatrix} \mathbf{p}_{\mathrm{h,i}}^{\mathrm{ext}} \\ \mathbf{0} \end{bmatrix}. \tag{5.22}$$

From Eq. 5.22, the effect of λ_{h} is accounted for in the edge force densities, which will also influence the heights $\mathbf{z}$ in the structure. Furthermore, the horizontal reactions $\mathbf{R}_{\mathrm{x}}, \mathbf{R}_{\mathrm{y}}$ must also be reformulated to account for λ_{h} and computed as follows

$$\mathbf{R}_{\mathrm{x}} = \mathbf{C}_{\mathrm{b}}^{\mathrm{T}} \mathbf{U}\mathbf{q} - \mathbf{p}_{\mathrm{x,b}} - \lambda_{\mathrm{h}} \mathbf{p}_{\mathrm{x,b}}^{\mathrm{ext}}, \tag{5.23a}$$

$$\mathbf{R}_{\mathrm{y}} = \mathbf{C}_{\mathrm{b}}^{\mathrm{T}} \mathbf{V}\mathbf{q} - \mathbf{p}_{\mathrm{y,b}} - \lambda_{\mathrm{h}} \mathbf{p}_{\mathrm{y,b}}^{\mathrm{ext}}. \tag{5.23b}$$

The objective function becomes then the maximisation of λ_{h}, so the objective function becomes

$$f_{\mathrm{h}} = -\lambda_{\mathrm{h}}. \tag{5.24}$$

This objective function is relevant to modelling, e.g., the static equivalent of seismic forces in masonry vaults (DeJong, 2009). It also corresponds to tilting the vault by a giving rotation angle such that a fraction of the weight is applied horizontally (Zessin, 2012).

In Figure 5.9, the maximum horizontal load is evaluated for the shallow cross vault. The vector defining the loading case $\mathbf{p}_{\mathrm{h}}^{\mathrm{ext}}$ points in the x direction and applies to each node a fraction λ_{h} of its tributary weight. Hence, the optimal $\lambda_{\mathrm{h}}^{\mathrm{opt}}$ represents the maximum horizontal load multiplier (see also Chapter 8). To respect Eq. 5.21, the diagram used for the analysis is modified, enabling the transfer of the horizontal loads to the supports. A diagram sliding is applied with a parabolic profile and maximum magnitude equal to $\Delta = 5\%$ of the span (see Section 6.2.3). This sliding transformation can be seen as the equivalent of tilting the planar diagram to respond to the horizontal loads. The solution in Figure 5.9 shows that the network obtained is admissible and enables the transfer of the horizontal loads to the supports.

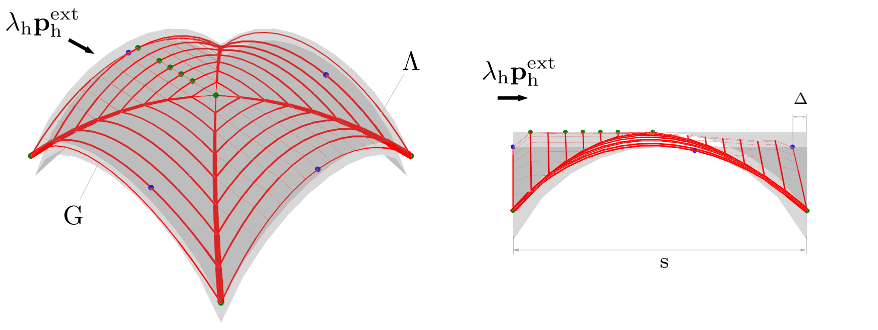

Figure 5.9: Optimisation maximising the horizontal load multiplier λ_h associated with external horizontal load $\mathbf{p}_h^{ext}$ applied to the shallow vault. Left: perspective with a highlight at thrust network (G) and masonry geometry (Λ) and the direction of applied horizontal loads. Right: side view showing the force transferred to the supports.

By coupling Eq. 5.24 to the present framework, the effects of horizontal loads can be studied, given that the effects of λ_h are propagated into the equilibrium equations and constraints, as described in this section.

5.4.5 Minimise the complementary energy

This section describes the last objective function implemented in this dissertation, minimising the complementary energy for a given set of foundation displacements. In continuous mechanics (see Angelillo, 2014), the complementary energy W_c expression for a continuum Ω subjected to boundary displacements $\bar{\mathbf{u}}$ applied to the constrained boundary $\delta\Omega_D$, with internal stress represented by the tensor $\mathbf{T}$ and linear hyperplastic response in compression described by $\mathbf{A}$ as

$$W_c = -\int_{\delta\Omega_b} \mathbf{T} \cdot \bar{\mathbf{u}} \, ds + \frac{1}{2} \int_{\Omega} \mathbf{A}\mathbf{T} : \mathbf{T} \, dV. \tag{5.25}$$

The first term in Eq. 5.25 is linear and accounts for the imposed displacements to the supports $\bar{\mathbf{u}}$. The second quadratic term reflects the internal energy of the structure. For a reticulated system, the internal energy simplifies to its axial component, which for an elastic material is written by introducing the structure's Young modulus E and the cross-sectional areas

$A_{s,i}$. Assuming that the cross-section bar areas are proportional to the axial force that they carry, the expression can be further simplified and written in terms of the force densities q_i as

$$\frac{1}{2}\int_{\Omega} \mathbf{AT} : \mathbf{T}\, dV = \sum_{i}^{m} \frac{f_i^2\, l_i}{2\, E\, A_{s,i}} = \frac{1}{2\epsilon}\sum_{i}^{m} |q_i|\, l_i^2, \tag{5.26}$$

in which the constant ϵ takes into account the stiffness and the axial strength of the bars of the structure. Eq. 5.26 yields in the well-known load-path (Liew et al., 2018, 2019; Baker et al., 2013), which is linear for a system with fixed spatial geometry, but nonlinear in the present case where the nodal elevations vary with the force densities. Section 5.5.1 provides a discussion about the convexity of this term.

With the present formulation, the expression of the complementary energy in a reticular system with stiffness parameter ϵ for a given set of support displacements $\bar{\mathbf{u}}$ $[n \times 3]$ is

$$\tilde{W}_c(\bar{\mathbf{u}}, \epsilon) = -\sum_{i}^{n_b} \mathbf{R}_i \cdot \bar{\mathbf{u}}_i + \frac{1}{2\epsilon}\sum_{i}^{m} |q_i| l_i^2, \tag{5.27}$$

Under the limit analysis assumptions, the internal elastic energy in Eq. 5.27 vanishes for masonry structures. This is equivalent to assuming that the stiffness parameter in the network bars is infinite ($\epsilon \to \infty$), such that the complementary energy expression simplifies to

$$f_c = -\sum_{i}^{n_b} \mathbf{R}_i \cdot \bar{\mathbf{u}}_i. \tag{5.28}$$

Eq. 5.28 will then be used as the objective function for the problem of minimising the complementary energy. f_c is a linear function of the reaction forces. The horizontal components of the reaction forces (Eqs. 4.7a–4.7b) are a linear function of $\mathbf{q}_{id}$, while $\mathbf{R}_z$ is a function of the unknown elevations of the network $\mathbf{z}$ and, therefore, a function of both $\mathbf{q}_{id}$ and $\mathbf{z}_b$.

In Figure 5.10, a shallow cross vault is subjected to a corner foundation displacement $\bar{\mathbf{u}}$ and the optimisation is conducted minimising f_c. The results enable obtaining the thrust network compatible with the prescribed displacement. Chapter 9 discusses how minimising the complementary energy can provide information on possible crack formation in three-dimensional structures at the onset of foundation displacements.

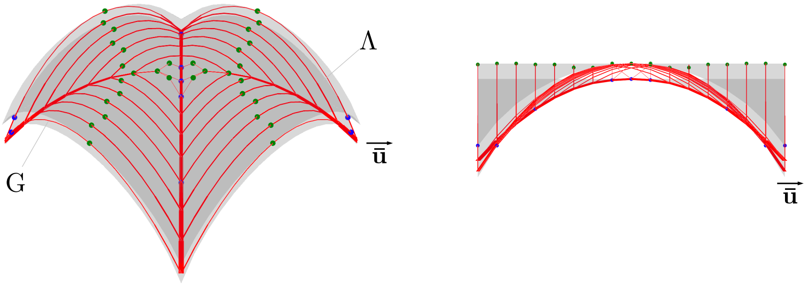

Figure 5.10: Optimisation minimising complementary energy for the corner foundation displacement $\bar{\mathbf{u}}$ on a shallow cross vault. Left: a perspective of the solution with a highlight at thrust network (G) and masonry geometry (Λ). Right: Elevation showing the effect of the applied displacement on the network's pulled diagonal.

5.5 Starting points

This section describes the starting points adopted to solve the optimisation problem in Eqs. 5.1. Since this problem is nonlinear, selecting an appropriate starting point is important to the time consumption and solvability of the nonlinear problem.

Section 5.5.1 presents a convex implementation of the load-path optimisation for a fixed form diagram, which will be the standard starting point strategy in this dissertation. Alternative starting points are discussed in Section 5.5.2.

5.5.1 Load-path optimisation

We recall and rewrite the expression of the load-path (ϕ) in terms of force densities for a reticulated structure previously derived in Section 5.4.5,

$$\phi = \sum_{i}^{m} |q_i| l_i^2. \tag{5.29}$$

The load-path is a scalar representing the volume of a reticulated system, assuming that all bars are equally stressed to their maximum strength in tension σ_t and compression σ_c (Maxwell, 1870). The minimisation the load-path has been introduced in Michell (1904) and applied to multiple research on minimising the material, including applications to trusses (Gilbert and Tyas, 2003; Beghini et al., 2013) and compression-only reticulated shells (Liew et al., 2018, 2019).

The load-path can also be written in terms of the external loads, noted as ϕ^ext, which is equivalent to ϕ, as shown in Maxwell (1870),

$$\phi^\mathrm{ext} = \sum_i^{n_\mathrm{i}} \mathbf{P}_i \cdot \mathbf{r}_i + \sum_i^{n_\mathrm{b}} \mathbf{R}_i \cdot \mathbf{r}_i, \tag{5.30}$$

in which the first term represents the work of the applied loads $\mathbf{P}_i$ in the internal nodes of the network, and the second accounts for the work of the reaction forces $\mathbf{R}_i$. In Eq. 5.30, $\mathbf{r}_i$ represents a vector from the origin to the point i, i.e., (x_i, y_i, z_i).

The expression of ϕ^ext can be rewritten in the following matrix expression as in Liew et al. (2018),

$$\phi^\mathrm{ext} = \mathbf{p}_\mathrm{x,i}^\mathrm{T}\mathbf{x}_\mathrm{i} + \mathbf{p}_\mathrm{y,i}^\mathrm{T}\mathbf{y}_\mathrm{i} + \mathbf{p}_\mathrm{z,i}^\mathrm{T}\mathbf{z}_\mathrm{i} + \mathbf{R}_\mathrm{x}^\mathrm{T}\mathbf{x}_\mathrm{b} + \mathbf{R}_\mathrm{y}^\mathrm{T}\mathbf{y}_\mathrm{b} + \mathbf{R}_\mathrm{z}^\mathrm{T}\mathbf{z}_\mathrm{b}. \tag{5.31}$$

In this work, a convex simplification of Eq. 5.31 is considered, which can be solved efficiently and used as a starting point for the problem in Eq. 5.1. This convex simplification is based on four assumptions:

(i) only vertical loads are applied to the network,

(ii) the network's horizontal projection is fixed,

(iii) the supports are co-planar, and

(iv) only compressive (or tensile) forces are considered.

Eq. 5.31 can, then, be simplified since the assumptions (i–iv) will reflect in:

(i) $\mathbf{p}_\mathrm{x} = \mathbf{p}_\mathrm{y} = \mathbf{0}$;

(ii) $\mathbf{x}_\mathrm{b}, \mathbf{y}_\mathrm{b}$ are known and $\mathbf{R}_\mathrm{x}, \mathbf{R}_\mathrm{y}$ is a linear function of the force densities $\mathbf{q}$ computed per 4.7 as a function of the force densities $\mathbf{q}$;

(iii) $\mathbf{z}_\mathrm{b} = \mathbf{0}$, which also affects the expression of $\mathbf{z}_\mathrm{i}$ per Eq. 4.11; and,

(iv) $\mathbf{D}_\mathrm{i} = \mathbf{C}_\mathrm{i}^\mathrm{T}\mathbf{Q}\mathbf{C}_\mathrm{i} \preccurlyeq \mathbf{0}$, meaning that $\mathbf{D}_\mathrm{i}$ is negative semidefinite.

Eq. 5.31 is then rewritten as

$$\phi^{\mathrm{ext}}(\mathbf{q}) = -\mathbf{p}_\mathrm{z}^\mathrm{T}(\mathbf{C}_\mathrm{i}^\mathrm{T}\mathbf{Q}\mathbf{C}_\mathrm{i})^{-1}\mathbf{p}_\mathrm{z} + (\mathbf{C}_\mathrm{b}^\mathrm{T}\mathbf{Q}\mathbf{C}_\mathrm{b})^\mathrm{T}\mathbf{x}_\mathrm{b} + (\mathbf{C}_\mathrm{b}^\mathrm{T}\mathbf{Q}\mathbf{C}_\mathrm{b})^\mathrm{T}\mathbf{y}_\mathrm{b}, \quad (5.32)$$

in which the first term is the matrix fraction, as defined in Boyd and Vandenberghe (2004), and the following terms are linear with respect to the force densities $\mathbf{q}$.

The convex problem below is solved to find the compression-only thrust network associated with a fixed Γ, having equilibrium matrix $\mathbf{E}$ and subjected to applied vertical loads $\mathbf{p}_\mathrm{z}$

$$\begin{aligned} &\underset{\mathbf{q}}{\text{minimise}} && \phi^{\mathrm{ext}}(\mathbf{q}), && (5.32)\\ &\text{subject to} && \mathbf{q} \leq \mathbf{0}, && (5.33\mathrm{a})\\ & && \mathbf{E}\mathbf{q} = \mathbf{0}, && (5.33\mathrm{b}) \end{aligned}$$

in which, Eq. 5.32 is convex and constraints 5.33a–5.33b are conic and linear such that this problem corresponds to a semidefinite convex optimisation (Boyd and Vandenberghe, 2004).

By performing the optimisation in Eqs. 5.33, a compression-only thrust network is obtained as starting point for the NLP. Furthermore, if no solution is obtained to the problem, a compression-only force distribution in input form diagram Γ might be impossible. In this case, a new topology should be considered. Figure 5.11 shows the results of the load-path optimisation for three structures.

The optimal thrust networks (G) are shown next to the form diagram used in the analysis Γ. In Figure 5.11a, a form diagram inspired by the one used to formfind the Striatus Bridge (Bhooshan et al., 2022) is used. It is composed of 1198 edges and 45 supports. In Figure 5.11b, a continuously supported orthogonal form diagram with 800 edges and 80 supports is considered. In Figure 5.11c, a corner-supported fan diagram with 1600 edges and four supports is used.

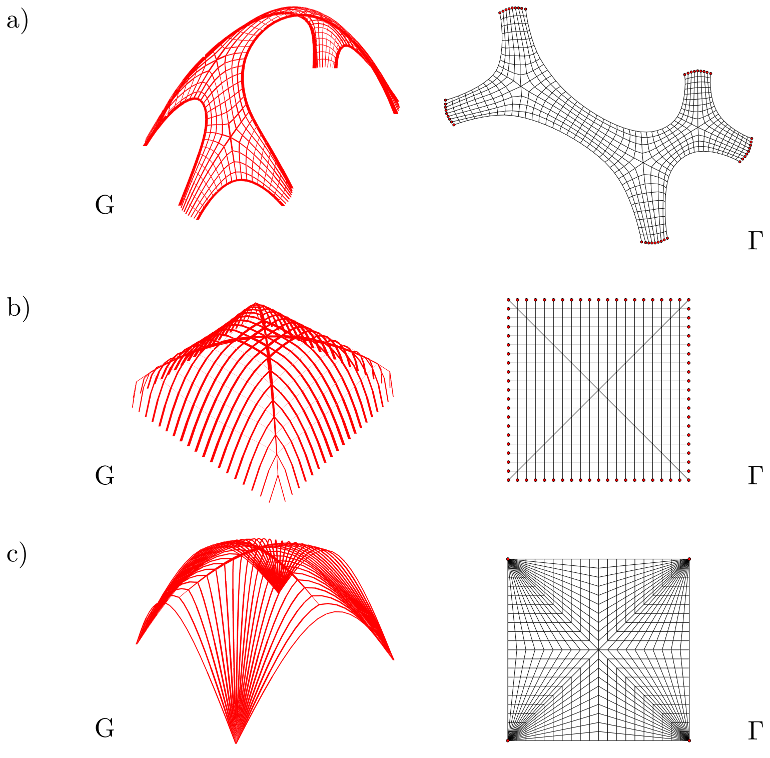

Figure 5.11: Examples of load-path optimised thrust networks (G), presented next to their form diagram (Γ): (a) freeform pattern inspired by the Striatus Bridge (Bhooshan et al., 2022), (b) four-side continuously supported vault, (c) four-corners supported vault.

Based on the solutions from the load-path, the networks can be used as a starting point for the nonlinear optimisation imposing the constraints from Section 5.3.

5.5.2 Alternative starting points

Alternative starting points could also be considered to solve the nonlinear optimisation problem in Eqs. 5.1. Three such alternatives are presented briefly in this section.

One possible strategy is starting from a compression-only thrust network, found through parallelisation. Previous work in TNA (see Section 2.3.3) has developed multiple strategies to explore the compression-only equilibrium using graphic-statics-based approaches. We highlight the example proposed in Rippmann et al. (2012), where the algorithm starts from a form diagram Γ and a dual diagram Γ_{d}, which are not yet reciprocal. The algorithm updates the nodal positions Γ and Γ_{d} until they are parallel (up to a pre-defined tolerance). When the diagrams are parallel, i.e., reciprocal, a set of compressive force densities can be retrieved and used to start the NLP. This strategy applies even to form diagrams which can not yet describe a possible compression-only equilibrium state. The algorithm can be modified by a weighting factor such that the orientation of the edges in Γ is also allowed to change, resulting in a new form diagram to start the NLP.

Alternatively, the starting point could be based solely on applying the Force Density Method (FDM) (Schek, 1974). Indeed, suppose a given distribution of force densities is applied to the edges of the network, e.g., uniform distribution. In that case, an equilibrated geometry is obtained with Eqs. 4.6 and could be used to start the NLP. However, depending on the distribution applied, the network will move in the plan, and the form diagram can become unsuited for the analysis. Nevertheless, this could be combined with optimisation algorithms as in Liew (2020) gaining control over the horizontal nodal movement.

A third strategy listed is a negative (or non-positive) least-squares optimisation, which corresponds to a well-known convex optimisation (Lawson and Hanson, 1995). The problem seeks to find a negative and nonsingular $\mathbf{q} \neq \mathbf{0}$ that respects the horizontal equilibrium Eq. 4.8 and has also been applied in Block (2009).

5.6 Derivatives

This section presents the sensitivities required to solve optimisation 5.1 using gradient-based methods. The fundamental derivatives of the equilibrium equations are presented in Section 5.6.1. The objective functions' gradients are derived in Section 5.6.2, and the Jacobian matrix of the constraints is presented in Section 5.6.3.

5.6.1 Fundamental derivatives

The first fundamental derivatives stores the sensitivity of the vectors of force densities $\mathbf{q}$, computed per Eq. 4.10, with respect to the independent force densities $\mathbf{q}_{\mathrm{id}}$

$$\frac{\partial \mathbf{q}}{\partial \mathbf{q}_{\mathrm{id}}} = \mathbf{B}. \tag{5.34}$$

The sensitivities of the vertical elevations of the thrust network, computed per Eq. 4.11, are described. The elevations are a function of both $\mathbf{q}_{\mathrm{id}}$ and $\mathbf{z}_{\mathrm{b}}$, leading to the sensitivities $\partial \mathbf{z}_{\mathrm{i}}/\partial \mathbf{q}_{\mathrm{id}}$ $[n_{\mathrm{i}} \times k]$ and $\partial \mathbf{z}_{\mathrm{i}}/\partial \mathbf{z}_{\mathrm{b}}$ $[n_{\mathrm{i}} \times n_{\mathrm{b}}]$, which can be computed by applying the chain rule to Eq. 4.11 and the matrix inverse derivative rules in Petersen and Pedersen (2012), resulting in

$$\frac{\partial \mathbf{z}_{\mathrm{i}}}{\partial \mathbf{q}_{\mathrm{id}}} = \frac{\partial \mathbf{z}_{\mathrm{i}}}{\partial \mathbf{q}} \frac{\partial \mathbf{q}}{\partial \mathbf{q}_{\mathrm{id}}} = -\mathbf{D}_{\mathrm{i}}^{-1} \mathbf{C}_{\mathrm{i}}^{\mathrm{T}} \mathbf{W} \mathbf{B}, \tag{5.35}$$

$$\frac{\partial \mathbf{z}_{\mathrm{i}}}{\partial \mathbf{z}_{\mathrm{b}}} = -(\mathbf{C}_{\mathrm{i}}^{\mathrm{T}} \mathbf{Q} \mathbf{C}_{\mathrm{i}})^{-1} \mathbf{C}_{\mathrm{i}}^{\mathrm{T}} \mathbf{Q} \mathbf{C}_{\mathrm{b}}. \tag{5.36}$$

The reaction forces computed per Eq. 4.7 are derived with respect to the independent force densities $\mathbf{q}_{\mathrm{id}}$ resulting in the following derivatives of shape $[n_{\mathrm{b}} \times k]$

$$\frac{\partial \mathbf{R}_{\mathrm{x}}}{\partial \mathbf{q}_{\mathrm{id}}} = \mathbf{C}_{\mathrm{b}}^{\mathrm{T}} \mathbf{U} \mathbf{B}, \tag{5.37a}$$

$$\frac{\partial \mathbf{R}_{\mathrm{y}}}{\partial \mathbf{q}_{\mathrm{id}}} = \mathbf{C}_{\mathrm{b}}^{\mathrm{T}} \mathbf{V} \mathbf{B}, \tag{5.37b}$$

$$\frac{\partial \mathbf{R}_{\mathrm{z}}}{\partial \mathbf{q}_{\mathrm{id}}} = \mathbf{C}_{\mathrm{b}}^{\mathrm{T}} \mathbf{W} \mathbf{B} + \mathbf{C}_{\mathrm{b}}^{\mathrm{T}} \mathbf{Q} \mathbf{C} \begin{bmatrix} -\mathbf{D}_{\mathrm{i}}^{-1} \mathbf{C}_{\mathrm{i}}^{\mathrm{T}} \mathbf{W} \mathbf{B} \\ \mathbf{0} \end{bmatrix}. \tag{5.37c}$$

While $\mathbf{R}_{\mathrm{x}}$ and $\mathbf{R}_{\mathrm{y}}$ are a function of the force densities only, the reactions in the $z-$directions are also function of $\mathbf{z}_{\mathrm{b}}$ with sensitivity $\partial \mathbf{R}_{\mathrm{z}}/\partial \mathbf{z}_{\mathrm{b}}$ $[n_{\mathrm{b}} \times n_{\mathrm{b}}]$ computed as

$$\frac{\partial \mathbf{R}_{\mathrm{z}}}{\partial \mathbf{z}_{\mathrm{b}}} = \mathbf{C}_{\mathrm{b}}^{\mathrm{T}} \mathbf{Q} \mathbf{C} \begin{bmatrix} -\mathbf{D}_{\mathrm{i}}^{-1} \mathbf{D}_{\mathrm{b}} \\ \mathbf{I}_{n_{\mathrm{b}}} \end{bmatrix}. \tag{5.38}$$

The fundamental derivatives presented in this section are used to express the gradients and Jacobians in the following sections.

5.6.2 Gradient functions

The gradient vector for each objective function is presented below. They will be used in the implementation of the optimisation described in Chapter 6.

5.6.2.1 Gradient of minimum and maximum thrusts

The gradient of minimum f_{min} and maximum f_{max} thrusts are presented (see Section 5.4.1). Their expressions are a function of $\mathbf{q}_{\mathrm{id}}$ only, and each of the scalar components j of $\partial f_{\mathrm{min}}/\partial \mathbf{q}_{\mathrm{id}}$ $[k \times 1]$, representing the sensitivity of the objective function to the j-th independent force density, can be obtained applying the chain rule

$$\left(\frac{\partial f_{\mathrm{min}}}{\partial \mathbf{q}_{\mathrm{id}}}\right)_j = \left(\frac{\partial f}{\partial \mathbf{q}}\frac{\partial \mathbf{q}}{\partial \mathbf{q}_{\mathrm{id}}}\right)_j = \pm\sum_i^{n_{\mathrm{b}}} \frac{R_{\mathrm{x},i}\left(\frac{\partial \mathbf{R}_{\mathrm{x}}}{\partial \mathbf{q}_{\mathrm{id}}}\right)_{i,j} + R_{\mathrm{y},i}\left(\frac{\partial \mathbf{R}_{\mathrm{y}}}{\partial \mathbf{q}_{\mathrm{id}}}\right)_{i,j}}{\sqrt{R_{\mathrm{x},i}^2 + R_{\mathrm{y},i}^2}}. \tag{5.39}$$

Where the sign $\pm$ reflects the minimisation or maximisation of the thrust, the notation $()_{i,j}$ represents the (i,j) matrix element, and the terms $\partial \mathbf{R}_{\mathrm{x}}/\partial \mathbf{q}_{\mathrm{id}}$ and $\partial \mathbf{R}_{\mathrm{y}}/\partial \mathbf{q}_{\mathrm{id}}$ are computed using Eqs. 5.37a–5.37b.

5.6.2.2 Gradient of minimum thickness

For the minimum thickness optimisation (see Section 5.4.2), the gradients are obvious since the objective function is simply the auxiliary variable t representing the thickness of the structure. Therefore the gradient with respect to t is

$$\frac{\partial f_{\mathrm{t}}}{\partial t} = 1. \tag{5.40}$$

The auxiliary variable, in this case, will also influence the constraints by updating the structure's new bounds (intrados and extrados). This effect will be discussed in Section 5.6.3.

5.6.2.3 Gradient of maximum load multipliers

The gradients for the maximum vertical (Section 5.4.3) and horizontal (Section 5.4.4) load multipliers are also straightforward with the auxiliary variables introduced, respectively λ_v and λ_h,

$$\frac{\partial f_\mathrm{v}}{\partial \lambda_\mathrm{v}} = \frac{\partial f_\mathrm{h}}{\partial \lambda_\mathrm{h}} = -1. \tag{5.41}$$

However, whenever λ_v, or λ_h are added as variables of the problem, their effect on the elevation of the free nodes, reaction force magnitudes, and equilibrium equation needs to be accounted for. This is discussed in detail in Section 5.6.3.

5.6.2.4 Gradient of complementary energy

The gradient of the complementary energy expression f_c, defined in Eq. 5.28, on the problem variables $\partial f_\mathrm{c}/\partial \mathbf{q}_\mathrm{id}$ $[k \times 1]$ and $\partial f_\mathrm{c}/\partial \mathbf{z}_\mathrm{b}$ $[n_\mathrm{b} \times 1]$ are written in terms of the partial derivatives of the reaction forces, defined in Eqs. 5.37–5.38, as

$$\frac{\partial f_\mathrm{c}}{\partial \mathbf{q}_\mathrm{id}} = -\begin{bmatrix} \dfrac{\partial \mathbf{R}_\mathrm{x}}{\partial \mathbf{q}_\mathrm{id}}^\mathrm{T}, \dfrac{\partial \mathbf{R}_\mathrm{y}}{\partial \mathbf{q}_\mathrm{id}}^\mathrm{T}, \dfrac{\partial \mathbf{R}_\mathrm{z}}{\partial \mathbf{q}_\mathrm{id}}^\mathrm{T} \end{bmatrix} \begin{bmatrix} \bar{\mathbf{u}}_\mathrm{x} \\ \bar{\mathbf{u}}_\mathrm{y} \\ \bar{\mathbf{u}}_\mathrm{z} \end{bmatrix}, \tag{5.42a}$$

$$\frac{\partial f_\mathrm{c}}{\partial \mathbf{z}_\mathrm{b}} = -\frac{\partial \mathbf{R}_\mathrm{z}}{\partial \mathbf{z}_\mathrm{b}}^\mathrm{T} \bar{\mathbf{u}}_\mathrm{z}. \tag{5.42b}$$

5.6.3 Jacobian of the constraints

This section describes the composition of the Jacobian matrix for the NLP described in this Chapter. The Jacobian matrix assumes the shape $[n_\mathrm{con} \times n_\mathrm{var}]$, in which n_con is the number of constraints in the problem and n_var is the number of variables which varies according to the variables used in the problem and constraints activated. Consequently, the Jacobian matrix is modular based on activated variables and constraints. A base case is presented in Section 5.6.3.1 and variations are discussed in Sections 5.6.3.2–5.6.3.4.

5.6.3.1 Base case: minimum thrust optimisation

The minimisation of the horizontal thrust is the base case, which can be described with

- $n_{\text{var}} = k + n_{\text{b}}$ variables, with k the independent edges and n_{b} support elevations.
- $n_{\text{con}} = m + 2n + 2n_{\text{b}}$ constraints, in which m for the compression-only requirement, $2n$ constraining the nodes to remain within the structural thickness and $2n_{\text{b}}$ for constraining the direction and magnitude of the reaction forces.

The arrangement of the Jacobian matrix is shown in the scheme in Figure 5.12.

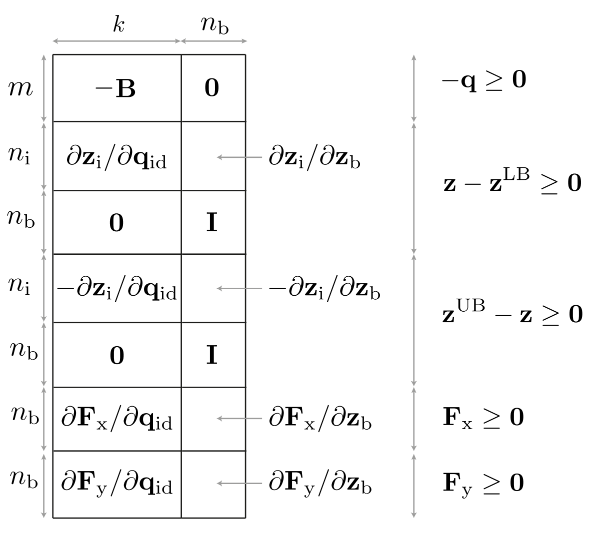

Figure 5.12: Arrangement of the Jacobian matrix for the base case described in this Section.

In which $\partial \mathbf{F}_{\text{x}} / \partial \mathbf{z}_{\text{b}}$ and $\partial \mathbf{F}_{\text{x}} / \partial \mathbf{q}_{\text{id}}$ are defined below and are analogous to the y-direction. By introducing the notation $()_i$ to represent a slice in the i-th line of matrices, the column vector $\partial F_{\text{x},i} / \partial \mathbf{z}_{\text{b}}$ $[n_{\text{b}} \times 1]$ can be expressed as

$$\frac{\partial F_{\mathrm{x},i}}{\partial \mathbf{z}_{\mathrm{b}}} = -\left|\frac{R_{\mathrm{x},i}}{R_{\mathrm{z},i}}\right| (\mathbf{I}_{n_{\mathrm{b}}})_i^{\mathrm{T}} - \frac{z_{\mathrm{b},i}|R_{\mathrm{x},i}|}{R_{\mathrm{z},i}^2} \left(\frac{\partial \mathbf{R}_{\mathrm{z}}}{\partial \mathbf{z}_{\mathrm{b}}}\right)_i^{\mathrm{T}}. \tag{5.43}$$

The term $\partial F_{\mathrm{x},i}/\partial \mathbf{q}_{\mathrm{ind}}$ can be expressed as the column vector $[k \times 1]$ in Eq. (5.44), where the $\pm$ sign reflects the sign of $R_{\mathrm{x},i}$

$$\frac{\partial F_{\mathrm{x},i}}{\partial \mathbf{q}_{\mathrm{ind}}} = -\frac{z_{\mathrm{b},i}}{R_{\mathrm{z},i}^2} \left(|R_{\mathrm{x},i}| \left(\frac{\partial \mathbf{R}_{\mathrm{z}}}{\partial \mathbf{q}_{\mathrm{ind}}}\right)_i \pm |R_{\mathrm{z},i}| \left(\frac{\partial \mathbf{R}_{\mathrm{x}}}{\partial \mathbf{q}_{\mathrm{ind}}}\right)_i\right)^{\mathrm{T}}, \tag{5.44}$$

5.6.3.2 Introduction of thickness parameter

When a thickness parameter t or an equivalent offset magnitude d is introduced (see Section 5.4.2), one new column is added to the Jacobian matrix to account for the new variables. This variable will affect the constraints in the nodal elevations and the reaction vectors.

On the nodal elevations, when the intrados and extrados can be described analytically (Section 5.4.2.1), the derivatives $\partial \mathbf{z}^{\mathrm{UB}}/\partial t$ and $\partial \mathbf{z}^{\mathrm{LB}}/\partial t$ $[n \times 1]$ representing the sensitivities on the upper and lower bounds with regard to a change in the thickness parameter t must be provided (for a hemispheric dome these are provided in Eqs. 6.2).

When analytical descriptions of the bounds are not provided, two strategies were discussed in Sections 5.4.2.2–5.4.2.3. When intrados and extrados are available (Section 5.4.2.2), the derivatives with respect to the offset distance d as

$$\frac{\partial z_i^{\mathrm{LB}}}{\partial d} = \delta_{\mathrm{p}}(\hat{\mathbf{n}}_i^{\mathrm{LB}}), \tag{5.45a}$$

$$\frac{\partial z_i^{\mathrm{UB}}}{\partial d} = -\delta_{\mathrm{p}}(\hat{\mathbf{n}}_i^{\mathrm{UB}}). \tag{5.45b}$$

An analogous procedure applies for the case in which only a single surface is provided (Section 5.4.2.3).

5.6.3.3 Introduction of a vertical load multiplier

The addition of a vertical load multiplier λ_{v} influences the internal elevations of the network $\mathbf{z}_{\mathrm{i}}$ and the reaction vectors in the z-direction $\mathbf{R}_{\mathrm{z}}$ with sensitivities computed as

$$\frac{\partial \mathbf{z}_\mathrm{i}}{\partial \lambda_\mathrm{v}} = \mathbf{D}_\mathrm{i}^{-1}\mathbf{p}_\mathrm{z,i}^\mathrm{ext}, \tag{5.46}$$

$$\frac{\partial \mathbf{R}_\mathrm{z}}{\partial \lambda_\mathrm{v}} = \mathbf{C}_\mathrm{b}^\mathrm{T}\mathbf{QC}\frac{\partial \mathbf{z}_\mathrm{i}}{\partial \lambda_\mathrm{v}} - \mathbf{p}_\mathrm{z,b}^\mathrm{ext}. \tag{5.47}$$

The multiplier does not affect the reactions $\mathbf{R}_\mathrm{x}$ and $\mathbf{R}_\mathrm{y}$ per se and only increases the height near the load point of application. However, given the constrained framework, for still fitting the network within the bounds, higher forces arise at edges linking the applied load to the supports, indirectly increasing the horizontal reactions (see Figure 5.8).

5.6.3.4 Introduction of a horizontal load multiplier

The addition of a horizontal load multiplier λ_h influences the horizontal equilibrium, and therefore the computation of $\mathbf{q}$ per Eq. 4.10, with

$$\frac{\partial \mathbf{q}}{\partial \lambda_\mathrm{h}} = \mathbf{E}_\mathrm{d}^\dagger \begin{bmatrix} \mathbf{p}_\mathrm{h,i}^\mathrm{ext} \\ \mathbf{0} \end{bmatrix}, \tag{5.48}$$

which propagates to the computation of the nodal elevations of the free nodes with the chain rule

$$\frac{\partial \mathbf{z}_\mathrm{i}}{\partial \lambda_\mathrm{h}} = -\mathbf{D}_\mathrm{i}^{-1}\mathbf{C}_\mathrm{i}^\mathrm{T}\mathbf{W}\frac{\partial \mathbf{q}}{\partial \lambda_\mathrm{h}}, \tag{5.49}$$

which also propagates to the reaction forces with sensitivities computed as

$$\frac{\partial \mathbf{R}_\mathrm{x}}{\partial \lambda_\mathrm{h}} = \mathbf{C}_\mathrm{b}^\mathrm{T}\mathbf{UC}\frac{\partial \mathbf{q}}{\partial \lambda_\mathrm{h}} - \mathbf{p}_\mathrm{x,b}^\mathrm{ext}, \tag{5.50a}$$

$$\frac{\partial \mathbf{R}_\mathrm{y}}{\partial \lambda_\mathrm{h}} = \mathbf{C}_\mathrm{b}^\mathrm{T}\mathbf{VC}\frac{\partial \mathbf{q}}{\partial \lambda_\mathrm{h}} - \mathbf{p}_\mathrm{y,b}^\mathrm{ext}, \tag{5.50b}$$

$$\frac{\partial \mathbf{R}_\mathrm{z}}{\partial \lambda_\mathrm{h}} = \mathbf{C}_\mathrm{b}^\mathrm{T}\mathbf{QC}\frac{\partial \mathbf{z}_\mathrm{i}}{\partial \lambda_\mathrm{h}} + \mathbf{C}_\mathrm{b}^\mathrm{T}\mathbf{WC}\frac{\partial \mathbf{q}}{\partial \lambda_\mathrm{h}}. \tag{5.50c}$$

Similarly, the sensitivities of Eqs. 5.50 propagate to constraints involving the planar reaction forces (Eqs. 5.4).

5.7 Summary

This chapter described the mathematical foundation necessary for conceiving a modular multi-objective optimisation framework to search admissible stress states in masonry structures. The optimisation described is nonlinear. A complete description of the variables adopted, constraints imposed, and objective functions implemented has been provided.

The variables adopted come from the mathematical formulation of Chapter 4. The constraints applied are a translation of the limit analysis assumptions to TNA. A series of objective functions relevant to assessing masonry structures have been described. These objective functions are listed in Table 5.1. Cases for which the masonry geometry is described analytically or provided by point clouds can be analysed with the formulation.

This chapter has also presented the gradients of all objective functions and the Jacobian matrix. The Jacobian matrix varies according to each problem's active constraints and variables. The mathematical description provided in this chapter will be implemented in Chapter 6 and will be used to compute the numerical results of this dissertation presented in Chapters 7, 8, and 9.

Table 5.1: Summary of the different objective functions implemented in this work.

objective function	symbol	definition
minimise horizontal thrust	f_{min}	Eq. 5.10
maximise horizontal thrust	f_{max}	Eq. 5.11
minimise thickness	f_{t}	Eq. 5.12
maximise vertical multiplier	f_{v}	Eq. 5.20
maximise horizontal multiplier	f_{h}	Eq. 5.24
minimise complementary energy	f_{c}	Eq. 5.28

Chapter 6

Implementation

This chapter describes the implementation of the search for admissible stress states in masonry structures as a nonlinear optimisation problem. To compute the results presented in this dissertation, the author developed a novel Python-based package named *compas_tno*. The package's workflow, main elements, and protocols are presented. A discussion about solving strategies for constrained nonlinear problems is also included.

6.1 Thrust Network Optimisation

An open-source Python-based package named *compas_tno* (Maia Avelino, 2023), or simply TNO, is introduced in this section. The package has been developed to perform the *Thrust Network Optimisation* introduced in this dissertation. It provides the datastructure necessary to set up and solve the modular multi-objective optimisation framework mathematically defined in Chapter 5 to search for admissible thrust networks in masonry structures.

It fits within the COMPAS (Van Mele, 2017) ecosystem, which provides the basic infrastructure for software development and collaboration within the AEC industry. It links to and inherits from the parent package *compas_tna* (Van Mele et al., 2021), which has been developed to perform the design of compression-only structures with Thrust Network Analysis (TNA) based on graphic form and force diagrams (see also Section 2.3.3).

Owing to its insertion in the Python environment, which has been increasingly used for scientific research, *compas_tno* connects with several open-source optimisations and mathematical packages, such as NumPy, SciPy, and IPOPT (Harris et al., 2020; Virtanen et al., 2020; Wächter and Biegler, 2006). A graphical illustration of the TNO ecosystem is presented in Figure 6.1. Being developed entirely in Python, it does not rely on any specific CAD environment, which brings additional flexibility to professionals working with different CAD software.

The documentation and repository of the project can be accessed at:

- https://blockresearchgroup.github.io/compas_tno/

As a dynamic, growing scientific contribution, *compas_tno* is freely available, and shared with the scientific community to enhance the collaboration of methods. As highlighted in the problem statements of this dissertation, much of the past development of numerical tools for masonry structures has been limited to academic papers, which other researchers can not directly and easily implement. By providing an overview of *compas_tno* in the following sections, the implementation proposed in this dissertation can be used and further developed by others.

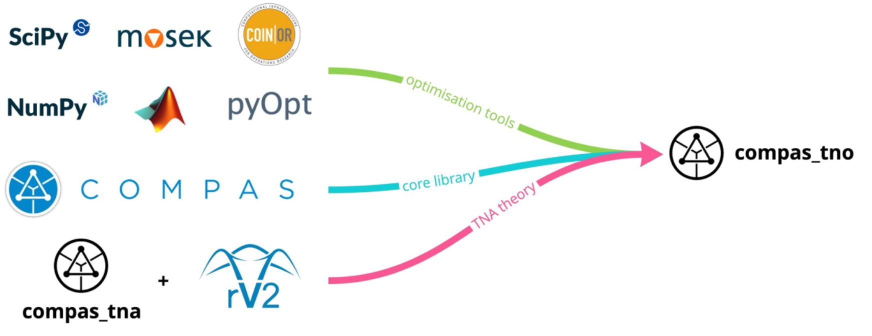

Figure 6.1: Ecosystem in which *compas_tno* is inserted, benefiting from open-source scientific packages available in the Python environment and building upon the COMPAS (Van Mele, 2017) framework and previous related work, such as *compas_tna* (Van Mele et al., 2021).

The workflow for setting up a problem with TNO is depicted in Figure 6.2. The main elements or *classes* are the:

- `FormDiagram`: defining the flow of forces in the structure.
- `Shape`: defining the masonry geometry to be analysed.
- `Optimiser`: storing the information about the optimisation settings.

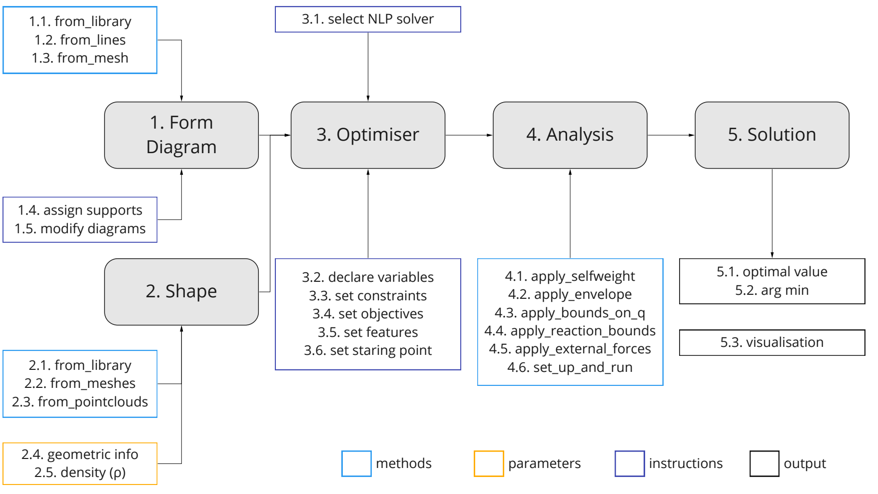

Figure 6.2: General workflow of *compas_tno* which enables setting up and solving constrained optimisation problems with thrust networks.

- `Analysis`: gathering the form diagram, shape, and optimiser objects, performing preconditioning operations, and running the optimisation.
- `Solution`: summarising the output of the optimisation.

In the following sections, these classes are introduced.

6.2 FormDiagram

Constituting the base of the TNA method, the `FormDiagram`, as defined in Section 4.1.2, represents the geometry of the projected thrust network.

The input form diagram comes from different sources accessed through the three main methods highlighted in Figure 6.2 and listed:

1.1. `from_library`: which creates a series of parametric form diagrams that fit common rectangular and circular footprints.

1.2. `from_lines`: create the form diagram from lines provided by the user.

1.3. `from_meshes`: create the form diagram from meshes provided by the user, where the connection with topology generating algorithms, such *compas_singular* (Oval, 2019), is possible.

After creating a `FormDiagram` object, additional functions are available to modify the diagram.

1.4. **assign supports:** based on the information about the structure's boundary conditions, supports on specific vertices of the input form diagram can be selected.

1.5. **modify diagrams:** a few standard modifications are introduced to the diagrams to increase their variations.

The following sections specify how to generate form diagrams and modify their geometry and topology.

6.2.1 Parametric diagrams

A few common topologies have been implemented parametrically in TNO. Four of these parametric implementations are described here and will be used throughout the applications in this dissertation. They are illustrated in Figure 6.3 and described herein:

- **radial diagram:** polar diagram defined by two discretisation parameters being the number of meridians n_{M} and the number of circular parallels, or hoops n_{P}. The location is defined by the central point position $\mathbf{X}_{\mathrm{c}}$ and the size by the radius R. Oculus openings can be considered with the parameter R_{o}. This diagram will be used to analyse problems on hemispheric domes (see Sections 7.2.1). A diagram with $(n_{\mathrm{P}}, n_{\mathrm{M}}) = (12, 16)$, $R = 5.0$ and $R_{\mathrm{o}} = 0.75$ is depicted in Figure 6.3a.

- **orthogonal diagram:** the orthogonal diagram is defined through two discretisation parameters $(n_{\mathrm{x}}, n_{\mathrm{y}})$, and the start and end dimensions of two opposite corners $[[x_0, x_{\mathrm{f}}], [y_0, y_{\mathrm{f}}]]$. This diagram is suitable for performing analysis of continuously supported vaults, such as pavillion vaults. Supports can be assigned to the continuous boundaries of the pattern. A square orthogonal diagram is presented in Figure 6.3b with $(n_{\mathrm{x}}, n_{\mathrm{y}}) = (14, 14)$.

- **cross diagram:** corresponds to the orthogonal diagram added with the main diagonals. The parameters are identical to the ones necessary to construct the orthogonal diagram; however, for this topology, $n_{\mathrm{s}} = n_{\mathrm{x}} = n_{\mathrm{y}}$. Supports can be applied to the corners or the full perimeter. Based on the support assigned, different vaults can be studied. The cross diagram with $n_{\mathrm{s}} = 14$ and corner support is presented in Figure 6.3c.

- **fan diagram:** unlike the orthogonal arrangement, the parallel segments arriving at the diagonals are directed to the corners. The parameters are identical to the ones necessary to construct the cross diagram. Supports can be applied to the corners or the full perimeter. The fan diagram in a square footprint with $n_\mathrm{s} = 14$ is presented in Figure 6.3d.

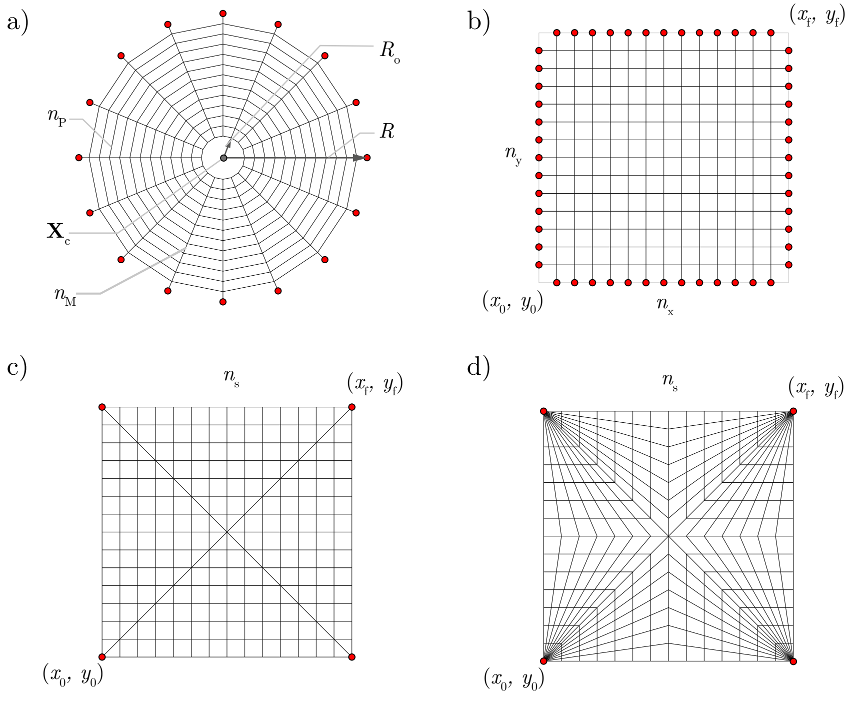

Figure 6.3: Examples of parametric diagrams available in *compas_tno*, namely, (a) radial, (b) orthogonal, (c) cross, and (d) fan diagram.

These diagrams will be used to model examples in this dissertation, which correspond to common masonry typologies, such as groin vaults, cloister vaults, and domes. In *compas_tno*, they are completed by general input mesh options and mesh transformations discussed in the following sections.

6.2.2 General input meshes

Mesh generator input sources can be connected to TNO, such as the topology finding algorithm implemented in *compas_singular* (Oval et al., 2017, 2018) that generate patterns based on singularities, line and point features. Figure 6.4 shows meshes created with *compas_singular*.

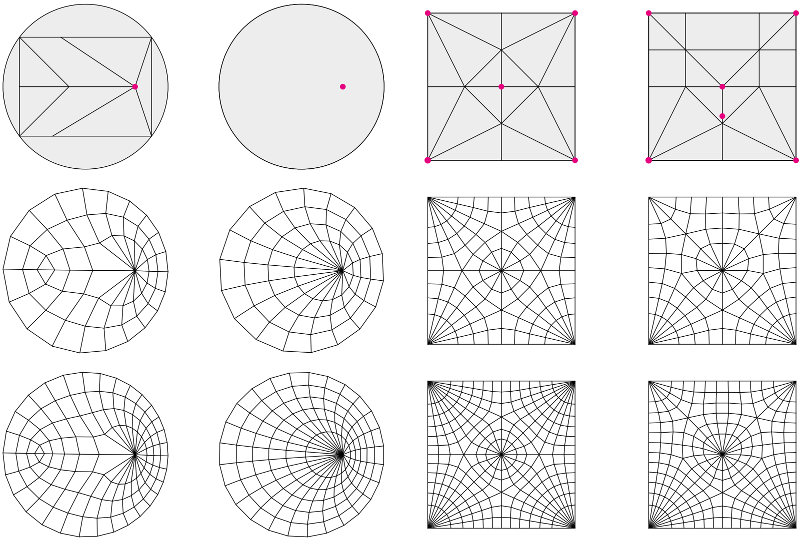

Figure 6.4: Feature-based topology finding performed with *compas_singular* (Oval, 2019). Coarse quad meshes (top row) with singularities (pink) are densified with different discretisation levels and smoothed circular or square footprints.

6.2.3 Mesh transformations

Pragmatic geometric modifications can also be applied to patterns in TNO, increasing the diversity of patterns used to study masonry problems. These transformations are presented in Figure 6.5 and listed below:

- **scale and shear:** simply scaling or shearing the meshes expand the possible shapes generated, e.g., modifying the geometry of the radial diagram with different scale factors leads to an oval footprint (see Figure 6.5a).

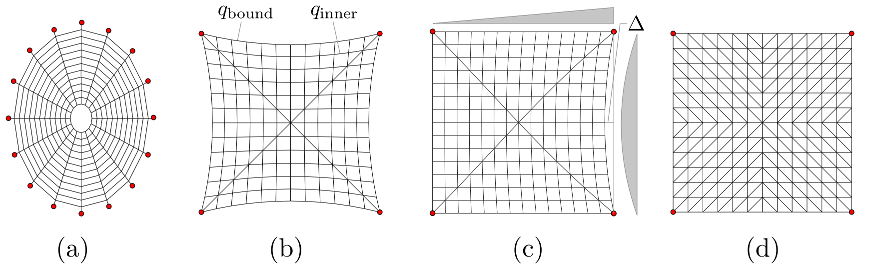

Figure 6.5: Geometric transformations applied to the diagrams: (a) scale and shear, (b) sag defined by force densities in the boundary q_{bound} and inner q_{inner} edges, (c) slide of magnitude Δ, and (d) addition of members, e.g., diagonals.

- **sag:** straight boundaries in non-continuously supported diagrams, as the cross diagram (see Figure 6.3c), induce zero forces on edges arriving at the straight boundary (see also Section 4.4). Curving the unsupported boundaries enables three-dimensional interaction among elements, as the edges pointing to the curved boundary can distribute compressive forces to them. A sag strategy is applied in this work by increasing the force densities in the open boundaries q_{bound} and performing an update in the geometry allowing the nodes to move in the plan. Figure 6.5b shows the cross diagram after setting $q_{\text{bound}} = 10.0$ and $q_{\text{inner}} = 1.0$.

- **slide:** a mathematical profile, e.g., a parabola, can be imposed to slide nodes in the diagram in one direction up to a magnitude Δ (Figure 6.5c). The sliding profile can be combined with a tapered profile in the orthogonal direction to create a planar field for sliding the nodes. The slide transformation has been applied to the diagram analysing the maximum horizontal multiplier in Section 5.4.4. This transformation is equivalent to tilting the planar form diagram to enable a path for the horizontal forces to the supports.

- **adding members:** the addition of new edges, e.g., diagonals to the quad (structured) elements of the mesh, enables additional load paths in the structure (see Figure 6.5d). In Section 8.2.2, these additional paths will increase the maximum value of collapse loads. Not only can diagonals be added, but also additional paths to the supports can be superimposed to the diagram, as in the problem of the shallow cross vault presented, where straight paths were added (see Section 5.4.3).

6.3 Shape

The `Shape` class is responsible for storing the geometry of the masonry structure used to constrain the form diagram. Three input sources are available in TNO:

2.1. `from_library:` a series of parametric shapes is available in TNO, they correspond to the typical masonry typologies. Examples include domes, cross, and pavillion vaults.

2.2. `from_meshes:` create the shape from user-defined meshes of its intrados and extrados.

2.3. `from_pointclouds:` interpolate in the point clouds to find meshes used as intrados and extrados.

Two general parameters act on the definition of the shape:

2.4. **geometric information**: Information such as thickness, central point, radius, discretisation, etc., used to define the geometry.

2.5. **density** (ρ): density assumed to the masonry for lumping the self-weights.

Based on the input source and the parameters defined, the shape object has three main *properties*: `intrados`, `extrados`, and `middle` representing the key surfaces used for the problem formulation. Intrados and extrados meshes are used to constrain the elevations of the nodes in the form diagram, as described in Section 5.3.2. The middle surface is used to compute the total area, and hence volume, and to distribute the self-weights lumped in the nodes of the form diagram, as formalised in Section 5.3.4.

The next section describes parametric shapes, followed by the strategy adopted to deal with data from point clouds.

6.3.1 Parametric shapes

Three parametric shapes defined in TNO are presented in this section, corresponding to hemispheric domes, cross vaults, and pavillion vaults. These geometries will be analysed throughout Chapters 7–9.

6.3.1.1 Hemispheric dome

The geometry of the hemispheric dome is defined in Figure 6.6a. Its geometry is defined parametrically based on the thickness t, the central radius R_c, and the centre point coordinates $\mathbf{X}_c$. We assume that the thickness is applied orthogonally to the middle surface. A dome with thickness-over-radius $t_0/R_c = 0.10$ is depicted in Figure 6.6b.

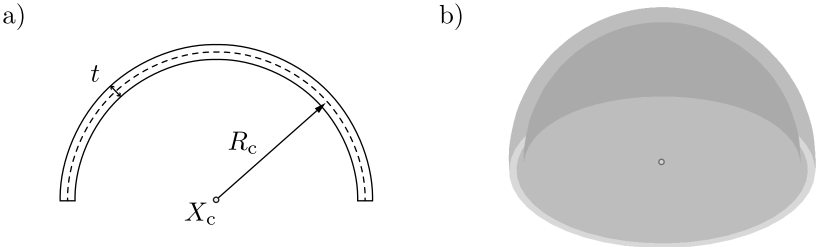

Figure 6.6: Dome geometry: (a) principal cross section and parameters, and (b) intrados and extrados surfaces obtained for $t/R_c = 0.10$.

Based on these parameters, the geometry of the dome can be obtained analytically through the functions s_m, s_{LB} and s_{UB} describing its middle, intrados, and extrados geometry. For a dome centred in the origin $\mathbf{X}_c = [0, 0, 0]$, these equations are:

$$s_m(x_i, y_i) = \sqrt{R_c^2 - x_i^2 - y_i^2}, \tag{6.1a}$$

$$s_{UB}(x_i, y_i, t) = \sqrt{(R_c + \tfrac{t}{2})^2 - x_i^2 - y_i^2}, \tag{6.1b}$$

$$s_{LB}(x_i, y_i, t) = \begin{cases} \sqrt{(R_c - \frac{t}{2})^2 - x_i^2 - y_i^2} & \text{if } x_i^2 - y_i^2 \leq (R_c - \frac{t}{2})^2, \\ -z_{\min} & \text{otherwise.} \end{cases} \tag{6.1c}$$

Eqs. 6.1 describe the geometry of the dome's intrados and extrados in terms of the variable thickness t and, therefore, enable the direct minimum thickness minimisation described in Section 5.4.2. The sensitivities of the intrados and extrados elevations for a point (x_i, y_i) are used for the minimum thickness problem as described in Section 5.6.3.2 and are computed for the dome as:

$$\frac{\partial z_i^{\mathrm{UB}}(t)}{\partial t} = +\frac{1}{2}\frac{R_{\mathrm{c}} + t/2}{z_i^{\mathrm{UB}}(t)}, \tag{6.2a}$$

$$\frac{\partial z_i^{\mathrm{LB}}(t)}{\partial t} = -\frac{1}{2}\frac{R_{\mathrm{c}} - t/2}{z_i^{\mathrm{LB}}(t)}. \tag{6.2b}$$

6.3.1.2 Parametric cross vaults

A parametric scheme is also introduced to model cross vaults. Cross vaults are generated by the intersection of two barrel vaults having the same profile. This profile is defined in Figure 6.7a by four parameters: its base length l_0, the radius R, the springing angle β, and the thickness t. In Figure 6.7b, a cross vault with $t/s = 0.050$, $R/l_0 = 0.71$, and $\beta = 20°$ is depicted.

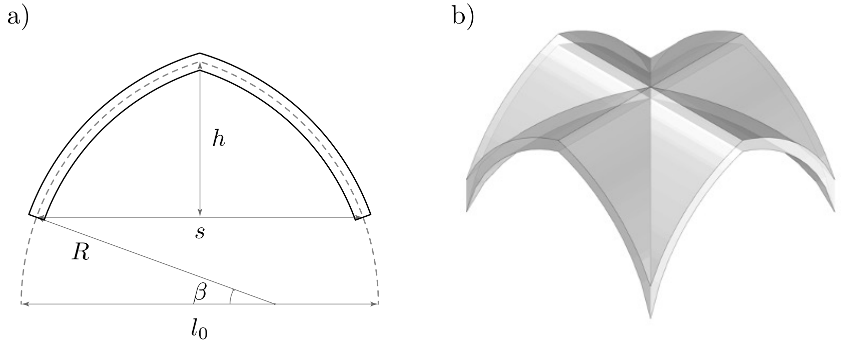

Figure 6.7: Cross vault geometry: (a) principal cross section and parameters and (b) geometry obtained for $t/s = 0.050$, $R/l_0 = 0.71$, and $\beta = 20°$.

These parameters enable effectively modelling different cross vaults by varying their "pointiness" defined by (R/l_0), their springing angle (β), and thickness-over-span (t/s). This parametrisation is adopted in Maia Avelino, Iannuzzo, Van Mele and Block (2021*c*) after Huerta (2004); Romano and Ochsendorf (2010). The parameters adopted in the proposed analysis, particularly referring to the springing angle β, allow detailed modelling of the typical fill near the supports of groin vaults. Analytical sensitivities for minimisation of the thickness are also obtained, as for the dome, since the pointed cross vaults result in circular sections.

6.3.1.3 Parametric pavillion vaults

Pavillion or groin vaults are also among the most common typologies of masonry. A parametric model is implemented to consider pavillion vaults following the same definition as the cross vaults. Geometrically, pavillion vaults are also built from the intersection of two circular profiles. However, instead of presenting open boundary edges, as in the cross vaults, their profile is lowered to create a base. The cross-section and parameters adopted are described in Figure 6.8a. A pavillion vault with $\beta = 30°$, $R/l_0 = 0.50$, and $t/s = 0.050$ is depicted in Figure 6.8b.

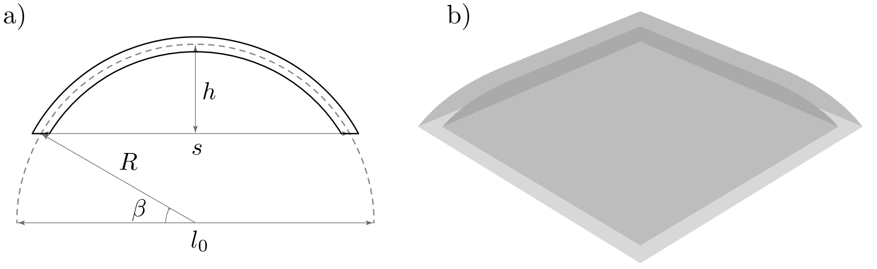

Figure 6.8: Pavillion vault geometry: (a) principal cross section and parameters and (b) geometry obtained for $t/s = 0.050$, $\beta = 30°$, and $R/l_0 = 0.50$.

6.3.2 Shapes from meshes and pointclouds

compas_tno offers the basic infrastructure to deal with polyhedral meshes or point clouds. One example of such geometries will be analysed in Section 7.4. In Figure 6.9a, the intrados mesh obtained after a survey at St. Angelo Church, Italy (see Section 7.4), is depicted. Figure 6.9b shows the intrados (Λ^{LB}), extrados (Λ^{UB}) and middle (Λ^{m}) meshes interpolated from the surveyed data.

To efficiently deal with geometries after scanning, which often have hundreds of thousands of faces (see Figure 6.9a), TNO works with a "low-poly" projection of the form diagram on these surfaces. As such, only the information needed for the analysis, i.e., the intrados and extrados elevations at the form's nodes are stored, reducing geometry's complexity, and used in the algorithms described in Sections 5.4.2.2–5.4.2.3. The middle surface is defined by interpolating the heights of the intrados and extrados meshes, as shown in Figure 6.9b. Indeed, when the intrados, extrados, and mid-

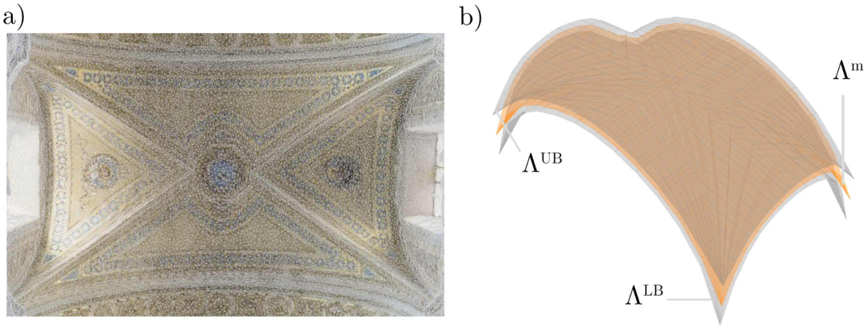

Figure 6.9: (a) Intrados mesh obtained after a survey at St. Angelo Church, Italy, with 2.900.000 faces. (b) Intrados (Λ^{LB}), extrados (Λ^{LB}) and middle (Λ^{m}) meshes used in the analysis.

dle meshes are topological twins of the form diagram, evaluating bounding elevations and tributary areas is straightforward.

6.4 Optimiser

The `Optimiser` object stores instructions to set the optimisation variables, constraints, objectives, features, and starting points. It also stores information on the nonlinear programming solver applied to the problem. The scheme in Figure 6.10 depicts the modular framework developed and lists the main options that can be passed to the `Optimiser`. These options come from the general workflow (Figure 6.2) and are described below.

3.1. Selecting the NLP solver

   The selection among two nonlinear programming solvers (NLS) is passed to the `Optimiser`. Either a Sequential Least Squares Programming (`SLSQP`) or a dual interior point optimisation (`IPOPT`) can be selected. Details about the solver selection and solving strategies are presented in Section 6.6.

3.2. Declare variables

   The variables are set as keywords passed in a *list* to the `Optimiser`. The keywords available are listed in Table 6.1, where the mathematical symbol used in this work is also referenced (see Chapter 5).

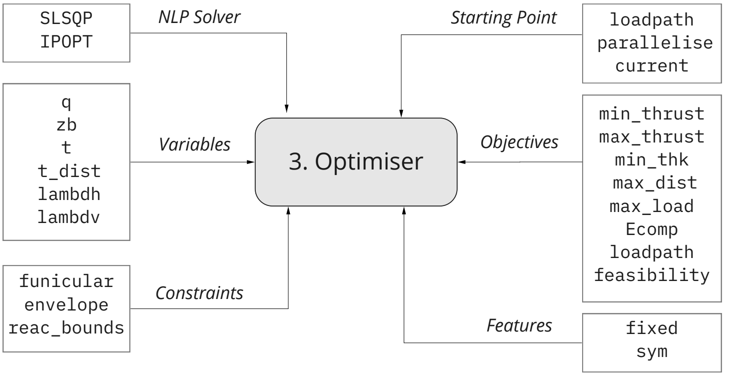

Figure 6.10: `Optimiser` and information to be added to the modular framework. The keywords employed are listed in this section.

Table 6.1: Selection of variables passed as keywords to the optimiser

keyword	variable	symbol
`q`	force densities	$\mathbf{q}$
`zb`	support elevations	$\mathbf{z}_\mathrm{b}$
`t`	thickness	t
`t_dist`	magnitude offset	d
`lambdh`	horizontal load multiplier	λ_h
`lambdv`	vertical load multiplier	λ_v

3.3. Set constraints

The variables are set as keywords passed in a *list* to the `Optimiser`. The keywords available are listed in Table 6.2.

3.4. Set objectives

The objective functions selected are passed to the `Optimiser` as a keyword. The keywords available are listed in Table 6.3, with pointers to the sections where these objectives are defined.

3.5. Set features

Two features are added to the solving pipeline. The first imposes that the form diagram will remain `fixed` in the plan, as described in

Table 6.2: Selection of constraints passed as keywords to the optimiser

name	constraint
`funicular`	subject members to compressive forces
`envelope`	constrain vertex elevations within envelope
`reac_bounds`	bounds the extension of the reaction forces

Table 6.3: Objective functions passed as keywords to the optimiser

name	objective	section
`min_thrust`	min. horizontal thrust	5.4.1
`max_thrust`	max. horizontal thrust	5.4.1
`min_thk`	min. thickness	5.4.2
`max_dist`	max. offset distance	5.4.2
`max_load`	max load multiplier	5.4.3–5.4.4
`Ecomp`	min. complementary energy	5.4.5
`loadpath`	min. load-path	5.5.1
`feasibility`	constant obj. function	–

Section 4.3. It triggers the computation of the independent edge per Algorithm 1. The problem proceeds by taking the independent force densities as only static variables.

The second feature imposes symmetry (`sym`) to the forces in the network's edges based on prescribed axes of symmetry. In Figure 6.11a, one axis of symmetry a'_1 is imposed to the problem, and a pair of symmetric edges e_{sym} is highlighted. In Figure 6.11b, three axis are applied (a'_1, a'_2, a'_3) a group of eight symmetry edges (e_{sym}) is shown. Based on the groups of symmetry obtained, additional linear equalities are imposed on edges' force densities, which reduces the number of variables in the optimisation.

3.6. Set the starting point

The selected starting point is provided to the `Optimiser`, trigerring a pre-conditioning step according to the options discussed in Section 5.5. Among these options, the standard is the `loadpath` optimisation. Alternatively, a form-and-force `parallelise` algorithm can be applied, or the problem can start from the `current` force densities distribution.

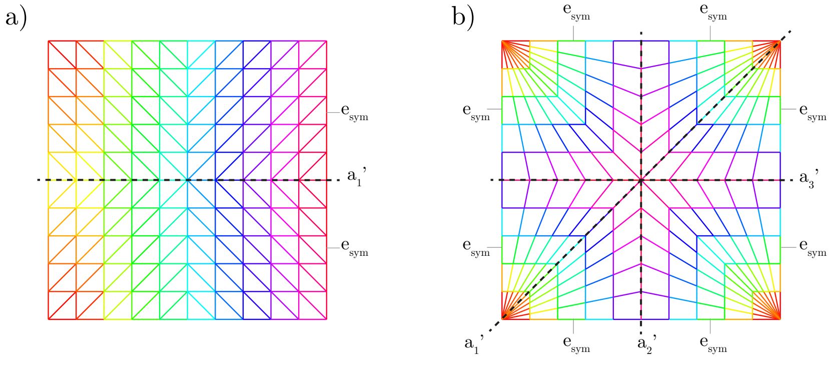

Figure 6.11: Color plot showing the symmetric edges identified based on the selected topology and symmetry axes imposed. (a) cross topology with diagonals and one axis of symmetry (a'_1,) (b) fan diagram with three axes of symmetry (a'_1, a'_2, a'_3). A group of symmetric edges is highlighted by e_{sym}.

6.5 Analysis

The `Analysis` object executes methods to modify the form diagram and run the analysis. The main methods applied are listed below:

- `apply_selfweight`: lump tributary weights in the nodes of the network according to the procedure described in Section 5.3.4.
- `apply_envelope`: stores the intrados and extrados elevation for every vertex based on the `Shape` of the problem, ensuring the application of the geometric constraints described in Section 5.3.2.
- `apply_bounds_on_q`: assign a q_{min} and q_{max} to bound the force densities, representing the force constraints from Section 5.3.1.
- `apply_reaction_bounds`: apply constraints on the emerging reaction forces based on the `Shape` of the problem, also described in Section 5.3.2.
- `apply_external_forces`: apply external vertical or horizontal loads according to the prescribed list of vertices and magnitude for application of such load cases.
- `set_up_and_run`: set up all matrices and vectors and call the optimisation.

The solving strategies adopted to compute the optimisation are presented in the following section.

6.6 Solving strategies

This section provides an overview of the solving strategies in *compas_tno* to find admissible thrust networks. A discussion about the solving strategies for the starting point (load-path) is listed in Section 6.6.1. The nonlinear optimisation solvers (NLS) implemented are presented in Section 6.6.2 followed by a comparison of their performance in Section 6.6.3. A discussion about the precision in determining independent edges is done in Section 6.6.4, and the solving pipeline is summarised in Section 6.6.5.

Whenever solving times are listed in this section, they have been computed in a laptop with a 2.2 GHz Intel Core i7 (I7-8750H) processor and 16 GB of RAM.

6.6.1 Load-path solvers

The load-path problem formulated in Section 5.5.1 is the default starting point for the optimisation process. It corresponds to a semidefinite programming problem (SDP). Two convex solvers have been implemented in *compas_tno* to solve this problem: MOSEK and SDPT3.

6.6.1.1 MOSEK

MOSEK (ApS, 2019) is a library that enables solving large-scale convex optimisation problems. *compas_tno* connects with MOSEK through CVXPY (Diamond and Boyd, 2016; Agrawal et al., 2017), which is a python package for disciplined convex programming. The connection with CVXPY is established within the Python environment. MOSEK is used as the default convex solver in *compas_tno*. MOSEK version 9.3 is used.

The three problems in Figure 5.11 are revisited to show the performance of MOSEK. The complexity of the problems is presented in terms of the number of edges in the diagram (m) and the number of supports (n_{b}). The running time, number of iterations, and optimal load-path value (ϕ_{opt}) are presented in Table 6.4. The running times with MOSEK vary from 4.64 seconds in example 5.11b with 800 edges and 80 supports to 41.7 seconds in example 5.11c on the diagram with 1600 edges and four supports. These

Table 6.4: Comparison of convex solvers MOSEK and SDPT3 for the load-path starting point optimisation executed in the examples from Figure 5.11.

solver	example	m	n_{b}	ϕ_{opt}	n. iter	time [sec]
MOSEK	5.11a	1198	45	254.9	34	12.9
	5.11b	800	80	226.9	33	4.64
	5.11c	1600	4	443.4	34	41.7
SDPT3	5.11a	1198	45	254.9	54	14.7
	5.11b	800	80	226.8	41	5.11
	5.11c	1600	4	443.5	73	22.0

results are listed in Table 6.4 in comparison with the second solver implemented, presented in the next section.

6.6.1.2 SDPT3

SDPT3 (Toh et al., 1999) is a semidefinite programming solver that is implemented in the CVX (Grant and Boyd, 2014, 2008) library for MATLAB. To date, this solver has not yet been written to Python, and the connection to SDPT3 is made through MATLAB. Therefore, the implementation of SDPT3 requires moving data between Python and MATLAB. MATLAB version 2022b and SDPT3 version 4.0 were used in the analysis.

The same examples from Figure 5.11 are analysed with SDPT3. The optimal load-path value (ϕ_{opt}), number of iterations, and running times are listed in Table 6.4. For problems with lower densities, e.g., $m < 1200$, SDPT3 and MOSEK perform similarly, e.g., 14.7 versus 12.9 seconds in problem 5.11a and 5.11 versus 4.64 seconds in problem 5.11b, with slightly faster runs calculated with MOSEK. Nevertheless, for denser meshes, e.g., $m > 1500$, such as example 5.11c, SDPT3 performed better with 22.0 versus 41.7 seconds. Finally, the optimal load-path values obtained in all examples are similar, up to minor numerical errors ($< 0.1\%$).

In *compas_tno*, MOSEK is selected as the standard load-path solver as it simplifies the data handling and installation process, being independent of MATLAB. Nevertheless, given the better performance of SDPT3 on denser meshes, this solver is still available as an option to users.

Regarding the mesh densities analysed, as discussed in Chapters 7–9, most networks used in the analysis will have less than 1000 edges.

6.6.2 Nonlinear solvers

Following the starting point optimisation defined in Section 6.6.1, this work's core nonlinear optimisation problem must be solved. Two solving strategies are implemented and presented here.

They correspond to a simpler (and faster) implementation of the Sequential Least-Squares Problem (SLSQP), followed by a more robust implementation of an interior point algorithm (IPOPT) which is the general solver of the package. As highlighted in Nocedal and Wright (2006*b*), these two competing strategies are the most suitable for handling inequality-constrained nonlinear problems. Both solvers and their performance are presented in the following subsections.

6.6.2.1 Sequential Least-Squares Programming

A version of the Sequential Least-Squares Programming (SLSQP) (Kraft, 1988), available in the open-source Python library Scipy (Virtanen et al., 2020), is implemented. This solver treats the problem as a sequence of constrained least-squares problems. The algorithm optimises successive second-order (quadratic/least-squares) approximations of the objective function with first-order (affine) approximations of the constraints.

Most of the objectives implemented (see Chapter 5) are already second-order or linear and are unaffected by these approximations. Nevertheless, the constraints are always nonlinear. Indeed, these constraints are calculated via Eq. 4.11 from the variables $\mathbf{q}_{\mathrm{ind}}$ and $\mathbf{z}_{\mathrm{b}}$, requiring the inverse of the matrix $\mathbf{D}_{\mathrm{i}}^{-1} = (\mathbf{C}_{\mathrm{i}}^{\mathrm{T}}\mathbf{Q}\mathbf{C}_{\mathrm{i}})^{-1}$. Therefore, the affine approximations of the constraints might be imprecise in some circumstances. The constraints applied in nodal elevations are smooth and usually are handled well by SLSQP. However, the constraints in Eqs. 5.4 are harder to approximate, which makes problems where these constraints are activated, such as the dome, less suitable for solving with SLSQP. Nevertheless, these simplifications benefit the solving time, and problems usually run faster in SLSQP. SLSQP always requires an appropriate, compression-only starting point to solve the NLPs in this dissertation. The load-path optimisation presented in Section 6.6.1 is usually a good starting point. The performance of this solver is also affected by the number of variables, and problems with more than 1000 edges can hardly be solved with SLSQP and finish without attaining convergence.

6.6.2.2 Interior Point Optimisation

The dual interior point optimisation (IPOPT) from Wächter and Biegler (2006) is implemented as the default solver in *compas_tno*. IPOPT represents the preferred strategy to solve large-scale, gradient-based optimisation problems. It implements an interior point line search filter method that finds a local optimum for problems, handling equality and inequality constraints.

Among the advantages of this solver are good precision and robustness in searching for the solution. The solver performs a line search combined with an adaptative barrier strategy that improves the sensitivity (Nocedal et al., 2009; Pirnay et al., 2012). Due to the line search procedure, IPOPT can be slow near the convergence, and it has been observed that it is susceptible to bad-scaled problems. Incidentally, the problems of this dissertation, when evaluated with engineering unities, tend to be bad-scaled, e.g., the minimum thickness problem of the dome (measured in meters) (see Section 7.2.1) in engineering units will lead to a difference in the weight of the dome and the minimum thickness of up to four orders of magnitude. To avoid these effects, the density assumed for the problems is set as default to 1.0, while the usual specific density of masonry is around 20.0 kN/m^3. A comment on bad-scaled problems and local minima is provided in Section 6.6.3.3.

In Section 6.6.3, the optimisation problems performed in Chapter 5 are revisited, comparing the performance of SLSQP and IPOPT.

6.6.3 Solving benchmarks

This section presents a benchmark study conducted on the NLS implemented in *compas_tno*. The performance of the solvers is compared on two different geometries: a cross vault in Section 6.6.3.1 and a dome in ction 6.6.3.2

6.6.3.1 Performance on cross vault problem

This section presents the results obtained for the optimisation in Chapter 5 to benchmark the NLS implemented in *compas_tno*. The optimisations were performed with a square cross vault having $R/l_0 = 0.5$ and $\beta = 30°$ and (initial) thickness $t = 0.50$ m (see Section 6.3.1). The form diagram is the cross diagram (see Section 6.2.1) with a footprint of 10×10 m and level of discretisation $n_\mathrm{s} = 16$. The results for minimum thrust, minimum thickness, and maximum horizontal and vertical load multipliers are listed in Table 6.5. The optimal values are reported in the analysis conducted

Table 6.5: Solver comparison on different nonlinear optimisation problems computed in a rounded cross vault.

solver	problem	opt. val.	n. iter	time [s]	Figure
IPOPT	`min_thk`	0.151	24	1.8	5.7
	`min_thrust`	52.9	24	1.4	5.4
	`max_load` (λ_{h})	0.179	36	1.8	5.9
	`max_load` (λ_{v})	6.09	57	3.0	5.8
SLSQP	`min_thk`	0.151	15	0.8	5.7
	`min_thrust`	52.9	6	0.2	5.4
	`max_load` (λ_{h})	0.179	21	0.4	5.9
	`max_load` (λ_{v})	6.09	26	0.6	5.8

with $\rho = 1.0$. A reference to the Figure containing the solution for each analysis is also referenced in Table 6.5.

Table 6.5 shows that for the cross vault example, SLSQP solves the problems with shorter run times than IPOPT. The optimal value obtained by the solvers is the same. The solving times observed with IPOPT range from 1.4–3.0 versus 0.2–0.8 seconds obtained with SLSQP.

The minimum thickness problem (`min_thk`) is solved with an optimal value of 0.151, corresponding to 1.51% of the vault's span. A complete study of cross vaults will be presented in Section 7.2.2. The minimum thrust problem (`min_thrust`) results in the optimal value of 52.9, representing a thrust-over-weight $T/W = 97\%$. These values will be discussed in Section 7.3.2.

Regarding the maximum load problem (`max_load`), the optimisation is set to maximise the horizontal (λ_{h}) and vertical (λ_{v}) multipliers. For the optimisation of the horizontal load multiplier (λ_{h}), the optimal value obtained is 0.179, i.e., the maximum applied load computed in the problem is 17.9% of the self-weight. For the vertical load multiplier (λ_{v}), the optimal result results in a load multiplier of $\lambda_{\mathrm{v}}^{\max} = 6.09$, which corresponds to a normalised pointed load of $P_{\max}/W = 11.2\%$ applied at the vault's web (see Figure 5.8). Applications of the horizontal and vertical maximum load will be discussed in Chapter 8.

A sensitivity study at the time of the analysis is presented in Table 6.6. It shows the increase in the computational time for an increase on the diagram level of discretisation n_{s} from 10 to 20. The number of edges m and the

Table 6.6: Sensitivity study of the `min_thk` problem of for the cross vault varying the discretisation level (n_s) of the mesh.

n_s	m	n_var	SLSQP time [s]	opt.val.	IPOPT time [s]	opt.val.
10	240	15	0.48	0.140	1.60	0.140
12	336	16	0.69	0.148	2.03	0.148
14	448	17	1.07	0.151	2.67	0.151
16	576	18	1.66	0.150	3.78	0.150
18	720	19	2.14	0.150	4.61	0.150
20	880	20	2.28	0.153	6.13	0.152

number of variables in the optimisation problem n_var are shown for each discretisation level. For the minimum thickness problem, the variables of the problem are $n_\mathrm{var} = k + n_\mathrm{b} + 1$ (see Section 5.4.2). The time consumption for the SLSQP increases from 0.48 to 2.28 seconds, while for IPOPT, it varies from 1.60 to 6.13 seconds. The optimal value encountered using both optimisers is the same up to rounding errors.

As a conclusion for the study on the cross vault problem, SLSQP performs better, as this problem has a small number of variables $n_\mathrm{var} \leq 20$. In the following subsection, the problem of a hemispheric dome is revisited.

6.6.3.2 Performance on dome problem

The problem of a hemispheric dome (see Section 6.3.1) is analysed with the IPOPT and SLSQP solvers in this section. This problem will be revisited in Chapter 7 of this dissertation. The dome's geometry is obtained with $t = 0.5$ m and $R_\mathrm{c} = 5.0$ m. The circular diagram used in the analysis has a level of discretisation set to $(n_\mathrm{P}, n_\mathrm{M}) = (16, 20)$ (see Section 6.2.1). Table 6.7 presents the results, including the number of variables (n_var) in the optimisation problem, the optimal value, the number of iterations, time consumption, and a corresponding Figure displaying the results in subsequent chapters.

For the dome problem, IPOPT successfully solves the optimisation for all objective functions while only the minimum thrust problem (`min_thrust`) converges with SLSQP. This relates to the fact that for the dome problem, the constraints on the reaction forces get activated. Furthermore, this prob-

Table 6.7: Solver comparison on different nonlinear optimisation problems on the hemispheric dome with $t/R_c = 0.10$ and diagram discretisation $(n_P, n_M) = (16, 20)$. (* symmetry applied)

Solver	problem	n_{var}	opt. val.	n. iter	time [s]	Fig.
IPOPT	`min_thk`	54	0.205	34	4.0	7.2
	`min_thrust`	53	15.4	23	2.6	7.12
	`max_load` (λ_v)	54	11.1	35	5.2	8.2
	`max_load` (λ_h)	339	0.144	186	789	8.12
	`max_load`* (λ_h)	196	0.144	103	399	8.12
SLSQP	`min_thk`	54	-	-	-	7.2
	`min_thrust`	53	15.4	9	0.6	7.12
	`max_load` (λ_v)	54	-	-	-	8.2
	`max_load` (λ_h)	339	-	-	-	8.12

lem presents a significantly higher number of variables than the cross vault problem since the boundary is continuously supported.

Regarding the results obtained with IPOPT, the minimum thickness problem (see Section 7.2.1) yields a minimum thickness of 0.205 m, with a running time of 4.0 seconds. The minimum thrust result results in an optimal value of 15.4 and solving time of 2.6 seconds. It corresponds to a thrust-over-weight ($T/W = 19.9\%$) as further discussed in Chapter 7.

For the maximum vertical load, the problem of a concentrated load applied at the apex is presented in Table 6.7. This problem is discussed in Section 8.2.1. The optimal value obtained is 11.1, corresponding to a concentrated load equivalent to $P_{max}/W = 14.4\%$ of the dome's weight. The solving time for this problem is reported as 2.6 seconds.

Finally, for the maximum horizontal load, additional diagonal members are added to the form diagram (see Section 8.3.1). The new members increase the number of independent edges, increasing the number of variables of the optimisation ($n_{var} = 339$). As a consequence, the solving time is longer, 789 seconds. Symmetry features (see Section 6.4) can be applied to this problem, considering one axis of symmetry parallel to the direction of the load applied, reducing the number of variables to $n_{var} = 196$ and the running time to 399 seconds.

In conclusion, while running times are lower with SLSQP, IPOPT can solve more complex problems with more variables and efficiently deal with non-continuously differentiable constraints. For this reason, IPOPT is selected as the standard solver of *compas_tno*.

6.6.3.3 A comment on local minima

The problems computed in *compas_tno* are nonlinear and prone to local minima. Users can carry out a series of practical mitigation strategies to avoid being trapped in local minima, especially for problems for which an analytical solution is not available. Some of these strategies are listed in this section.

- Change the optimisation starting point:

  Different starting points can be used (see Section 5.5), including, e.g., the best fit to the masonry geometry (Van Mele et al., 2014). Similarly, a pre-conditioning optimisation can be computed to obtain a starting point already admissible, e.g., computing a minimum thrust solution before computing a minimum thickness or a maximum load problem.

- Parameter stressing:

  The initial parameters can be stressed after obtaining a particular solution, e.g., the value of minimum thickness t_{min} obtained can be challenged by constraining the problem to a $t' < t_{\text{min}}$ to ensure its non-feasibility. It also applies, e.g., for checking the non-feasibility of an external load $P' > P_{\text{max}}$.

- Problem scaling:

  It is well known that gradient-based nonlinear solving processes are vulnerable to scaling (Nocedal and Wright, 2006*a*). Therefore, changing the dimensions of the problem, e.g., meters instead of millimetres, can alter the stopping criteria of the solving process. No automatic scaling process is performed in the current version of *compas_tno*. However, at the end of the optimisation, the range of the problem variables is presented. Users can then manually adjust load magnitudes or scale the input geometry based on these values.

- Incremental diagram discretisation:

  Starting at a coarse discretisation can avoid stationary points and save time as the results should converge progressively to a lower-bound solution (see, e.g., Table 6.6 or Figure 7.1).

- Varying the solver and stochastic optimisation:

  Minimum values can be confronted using different solvers. Besides SLSQP and IPOPT, the entire library of solvers available in SciPy (Virtanen et al., 2020) can be accessed through *compas_tno*, including stochastic solvers, e.g., genetic algorithm and differential evolution. These could be used to stress a particular solution searching for potential better objective functions in the vicinity of the optimal point.

The listed strategies can mitigate the effect of local minima in the results obtained with *compas_tno*.

6.6.4 Independent edges precision

The independent edges concept presented in Section 4.4 is essential to the numerical formulation of the present dissertation. They enable proper control over the DOF in the networks. Nevertheless, as the definition of the independent edges relies on SVD, the threshold to determine zero singular values influences the selection of independent edges when the patterns are not triangulated. Indeed, for non-triangulated structures, some of these DOF relate to inextensible mechanisms (see Figure 4.4), which will be identified based on the null singular values from the sequential SVD process. When the DOFs are not correctly defined, the optimisation fails regardless of the solver selected.

Therefore, before initiating the optimisation, a check is performed on the independent edges by checking the minimum singular value of $\mathbf{E}_{\mathrm{d}}$ prior to computing its Moore–Penrose pseudoinverse (see Eqs. 4.10). Moreover, a tolerance parameter can be selected beforehand to define the SVD precision in the rank calculation. This tolerance enters in the rank computation of Algorithm 1 to find the independent edges. If the set of independents does not pass the test above, the tolerance can be reduced, or the heuristics discussed in Section 4.4 can lead to a new set of independents.

6.6.5 Solving workflow

To conclude, the solving pipeline to find admissible thrust networks with *compas_tno* is illustrated in Figure 6.12, including possible pitfalls and a protocol to recompute the optimisation problem. A description of the workflow is listed here:

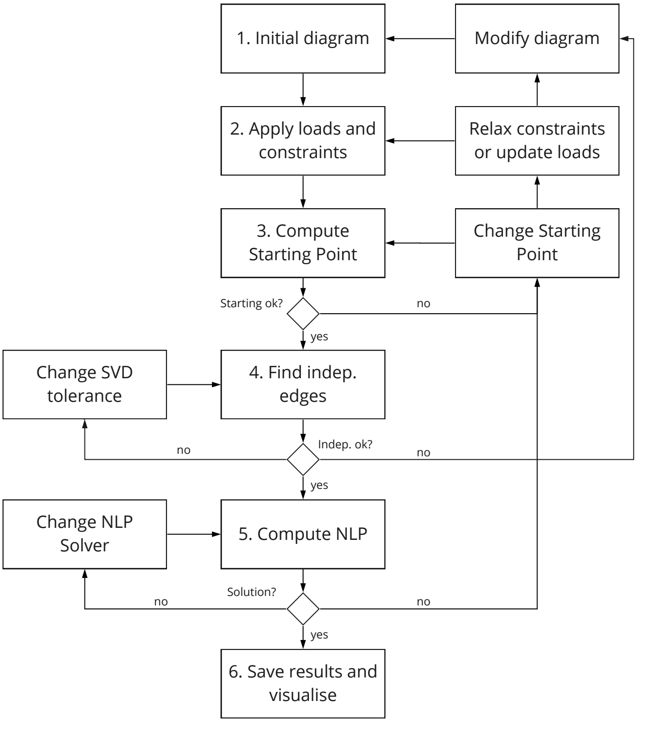

Figure 6.12: Solving pipeline adopted at *compas_ tno*.

1. The workflow starts with the form diagram selected for the analysis.
2. Loads and constraints are applied to the diagram based on the `Shape` adopted to the problem and following the options passed to the `Optimiser`.
3. The starting point is computed following the solving strategy adopted in Secion 6.6.1. If the starting point, i.e., a compressive network, can not be found, the loads should be checked, or the diagram should be modified.
4. After the starting point is computed, the independent edges are found and checked as described in Section 6.6.4. In case the independents are not suitable for the analysis, the tolerance of the SVD process can be modified, or the diagram can be updated.

5. The nonlinear optimisation can then be computed following the solver selection discussed in Section 6.6.2. The problem is prone to not finding a solution. If no solution is found, the starting point can be modified, loads and constraints can be checked or relaxed, or the diagram can be modified.

6. Finally, when a solution is found, results can be saved and visualised.

The problem might be infeasible if no solution is found even after the modifications suggested in the workflow. This might represent, e.g., that the thickness of the structure is insufficient, the applied loads are too high, or the diagram is not a suitable force flow for the problem.

From a lower-bound perspective, when an admissible stress state can not be found, it still does not mean the structure is unsafe, only that the approach applied can not determine that it is safe. The framework developed in this thesis aims to minimise the cases in which the latter happens. Through the implementation of different solvers and the definition of checking protocols, this implementation is designed to be the core of a reliable lower-bound TNA-based analysis tool.

6.7 Summary

This chapter described the implementation developed to set up and solve the modular multi-objective constrained optimisation problem described in the previous chapter. A Python-based software package named *compas_tno* has been developed for this purpose. The datastructure of the package is presented alongside some of its core functionalities. Among these functionalities, the definition of parametric form diagrams and parametric masonry geometries have been presented, enabling its application to relevant case studies in masonry structures. Two different nonlinear optimisation solvers were implemented in the package. These solvers were presented in this chapter, along with a performance test. The full pipeline for the solving process has also been presented, listing possible pitfalls and limitations of the methodology. The framework developed is available open-source, enabling further collaboration and continuous development. In the following chapters, the tool is applied to relevant case studies.

Part III

Results

Chapter 7

Stability of masonry structures

This chapter introduces a methodology to compute the level of stability in vaulted masonry structures. First, a methodology to compute their Geometric Safety Factor (GSF) is presented and applied to domes and parametric cross vaults. The GSF is obtained through the computation of the minimum thickness problem. Beyond computing the GSF, the stability domain of the structures is also obtained. This domain is obtained for analytical geometries and those obtained from point clouds. Through the combined study of the GSF and the stability domain, this chapter offers a novel and robust methodology to measure the stability of vaulted structures.

7.1 The problem

7.1.1 Overview

Finding one admissible stress state informs whether the structure in its configuration is safe, but it does not provide information about the level of stability. For practical assessment scenarios, determining the latter is needed. It implies answering how far the structure is from the collapse state and how stable it is in its current configuration. This work answers the first question by evaluating the Geometric Safety Factor (GSF), while the second by computing the structure's stability domain.

The GSF is defined as the ratio between the current structural thickness and the minimum thickness of the tightened cross-section, which still contains an admissible stress state (Heyman, 1966). While the GSF is an accepted measure of stability, applying it to three-dimensional structures is challenging. It requires a proper way to quantify the vault's thickness, especially when applied to non-analytical geometries, i.e., structures obtained from point clouds.

A minimal thickness structure is said to be at its limit state, as only one admissible stress state is possible. For a structure that is not in the limit state, i.e., not in the imminence of collapse, its level of stability corresponds to the size of its domain of admissible stress states. A reasonable measure of this domain is represented by the ratio among its extreme (maximum and minimum) thrusts. The maximum and minimum thrusts usually correspond to different stress states and have distinct horizontal thrust values. However, at the limit state, minimum and maximum thrust coincide.

By exploring these two concepts, the level of stability in masonry structures can be adequately evaluated. However, there is currently no straightforward way to compute these measures for general masonry structures. The developed methodology will address this research gap in this chapter.

7.1.2 Opportunities

This work searches for lower-bound admissible networks through a constrained optimisation procedure. While previous work has focused on finding only one admissible solution (e.g., Block and Lachauer, 2014; Fraternali, 2010; Bruggi, 2020), the constrained framework presented in this dissertation enables exploring the entire space of admissible stress states and, therefore, effectively computing stability measures.

Understanding how the stability domain changes as a function of the thickness give a direct measure of the robustness of the structure from its initial state until the collapse state. This robustness can be associated with the structure's capacity to carry additional imposed loads or undergo external settlements.

Furthermore, the domain of admissible states can be enlarged by evaluating different form diagrams. Having developed a general numerical procedure that enables multiple topologies to be analysed, this chapter will discuss and quantify how changing the force flow increases the GSF value and the size of admissible stress states.

7.1.3 Implementation

This chapter will compute the GSF of masonry structures by minimising the structural thickness. The minimum thickness is obtained by solving the problem described in Section 5.4.2. The problem will be applied to a hemispherical dome and vaults. For both cases, the geometric constraints on the nodal elevations apply following Section 5.3.2. For the dome analysis, the additional constraints from Eqs. 5.4 apply to bound the reaction forces at the base. The starting point for each optimisation is the minimum load-path solution (Section 5.5). After finding the minimum thickness of the problem, the GSF can simply be computed by the ratio between the real and the minimum thickness.

To compute the stability domain, successive minimum and maximum thrust optimisations are performed for reduced thickness values until the structure reaches its limit state. The mathematical problems (min/max) to be solved are presented in Section 5.4.1.

The results summarised in this chapter have been the subject of the following publications by the author: Maia Avelino, Iannuzzo, Van Mele and Block (2021*a*,*b*,*c*).

7.2 Minimum thickness problem

This section presents the study of the minimum thickness problem with Trust Network Optimisation. Applications include a hemispheric dome in Section 7.2.1 and parametric cross vaults in Section 7.2.2.

7.2.1 Minimum thickness in the masonry dome

The geometry of the hemispheric dome is defined by the parameters presented in Section 6.3.1.1. The dome is described by its thickness-over ratio t/R_{c}, with thickness computed orthogonally to the dome's middle surface and considering the central radius R_{c}.

The form diagram is selected following the well-known dome's meridian and hoop stresses. The diagram is defined by the tuple $(n_{\mathrm{P}}, n_{\mathrm{M}})$ representing the number of parallels n_{P} and number of meridians n_{M}, as described in Section 6.2.1.

A sensitivity study varying the parameters $(n_{\mathrm{P}}, n_{\mathrm{M}})$ is carried out for $n_{\mathrm{P}} = [4, 8, \ldots, 24]$ and $n_{\mathrm{M}} = [12, 16, \ldots, 24]$, and the dome's minimum thickness is computed for the 24 diagram combinations. The results are summarised in the graph of Figure 7.1. As a benchmark, the results are compared with the minimum thickness of a masonry hemispherical dome obtained in Heyman (1967), $(t_{\min}/R_{\mathrm{c}})_{\mathrm{ref}} = 0.042$.

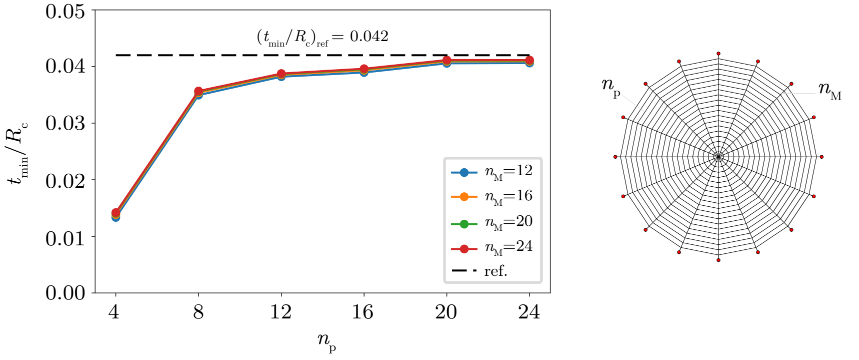

Figure 7.1: Sensitivity analysis of minimum thickness $(t_{\min}/R_{\mathrm{c}})$ obtained for the dome problem computed varying the number of meridians n_{M} and parallels n_{P}. Values are compared to the benchmark $(t_{\min}/R_{\mathrm{c}})_{\mathrm{ref}} = 0.042$ (Heyman, 1967).

The results of the sensitivity study show that the minimum thickness value varies only with the number of parallels n_{P} since the solutions corresponding to different n_{M} values collapse to the same curve (Figure 7.1). The deviation against the minimum reference thickness decreases significantly with the increase in the density of parallels. For $n_{\mathrm{P}} \geq 20$, the difference of the minimum thickness results decreases to less than 2%. These results validate the methodology against the analytical study, showing that good approximations are achieved for a fine diagram discretisation.

The solution obtained for $(n_{\mathrm{P}}, n_{\mathrm{M}}) = (20, 16)$ is analysed in detail assuming a dome with initial thickness-over-radius $t_0/R_{\mathrm{c}} = 0.10$ and $R_{\mathrm{c}} = 5$ m.

The solution of the minimum thickness problem for $(n_{\mathrm{P}}, n_{\mathrm{M}}) = (20, 16)$ is depicted in Figure 7.2. In these plots, the thickness of the edges is proportional to the force carried. Consequently, edges carrying zero force vanish. Following the convention from Chapter 5, the vertices touching the intrados (resp. extrados) are denoted with blue (resp. green) dots. The minimum thickness-over-span obtained for this problem is $t_{\min}/R_{\mathrm{c}} = 0.041$. The Geometric Safety Factor (GSF) of the structure based on the initial thickness

t_0 can then be computed as GSF $= t_0/t_{\min} = 2.44$.

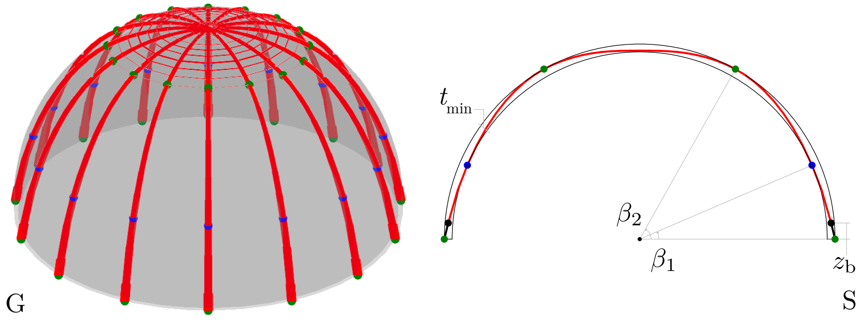

Figure 7.2: Minimum thickness obtained ($t_{\min}/R_c = 0.041$) for the hemispheric dome with $(n_P, n_M) = (20, 16)$. Perspective on the left and main cross-section (S) on the right highlighting the angles β_1, β_2 where the cracks are observed and the elevation of the support nodes z_b.

Regarding the internal distribution of the forces in the minimum thickness solution, a bi-axial compressive cap is observed in the upper portion of the dome, and a uniaxial stress state forms towards the supports, where the hoop forces vanish (Figure 7.2). The normalised horizontal thrust at the base is $T_{\text{limit}}/W = 24.3\%$. This value matches the minimum thrust obtained at the limit thickness computed in Nodargi and Bisegna (2021*b*).

A six-hinges symmetric crack pattern appears in the dome's main cross-section. In the perimeter of the top compressive cap, the thrust network touches the extrados of the structure at angle $\beta_2 = 60.6°$ from the springings corresponding to a cylindrical crack visible from the intrados of the dome. Near the base, the thrust network touches the intrados of the dome at angle $\beta_1 = 23.3°$, indicating a cylindrical crack in the dome visible from the extrados. The supports height is $z_b = +0.421$ m, as highlighted in Figure 7.2, in a position such that the vector of the reaction forces extends to the outer perimeter of the dome, resulting in the final structural hinges observed in the cross-section.

The internal state obtained follows the one described in Heyman (1967). In the limit state, the expected collapse mechanism will occur following a detachment of the dome's meridional segments with the crown descending vertically. Theoretically, a hemispheric dome constructed with such dimensions would be on the verge of collapse, and any additional load or foundation displacement affecting the structure would cause its failure. In practice, however, constructed hemispheric domes have significantly larger (or tapered) thickness-over-radius values making them safe. Nevertheless, this theoretical result is relevant to compute the GSF of stable domes as executed in this section.

In Section 7.3.1, the dome problem is revisited by constructing its stability domain considering sufficient and realistic thicknesses.

7.2.2 Minimum thickness of parametric cross vaults

This section studies the problem of the minimum thickness in square cross vaults as published by the author in Maia Avelino, Iannuzzo, Van Mele and Block (2021*c*).

The geometry of the vaults is parametrised following the definition in Section 6.3.1.2. The parameters adopted correspond to the radius-over-length R/l_0, which defines the "pointiness" of the vaults and the springing angle β. The geometries generated by varying these parameters in the ranges $R/l_0 = [0.5 - 1.0]$ and $\beta = [0° - 40°]$ are depicted in Figure 7.3.

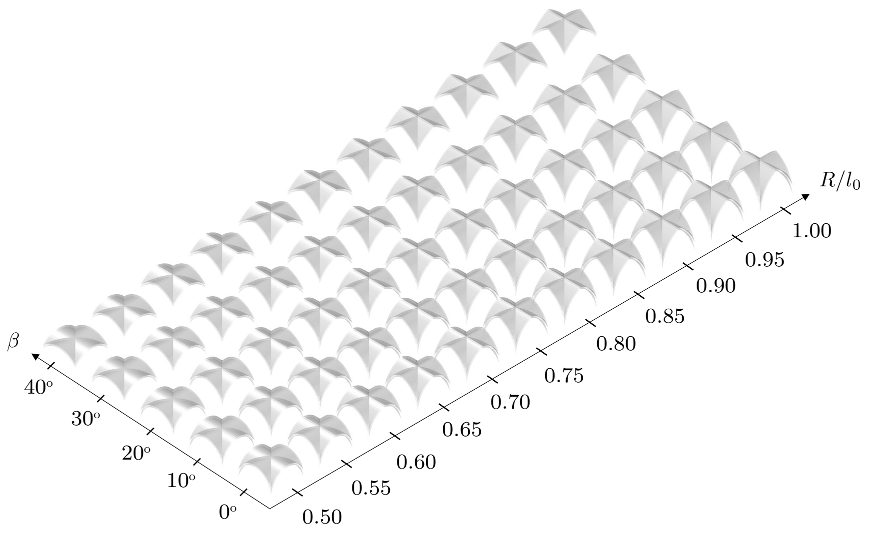

Figure 7.3: Cross vault geometries obtained varying $R/l_0 = [0.5 - 1.0]$ and $\beta = [0° - 40°]$. All vaults are plotted with thickness-over-span $t/s = 0.05$.

The minimum thickness is reported as the thickness-over-span t/s, where the effective span s, i.e., the distance among the springs, is considered.

Unlike the dome case, the form diagram representing the flow of forces for a cross vault is not trivial and has been debated historically, as in the overview in Huerta (2009); Gaetani et al. (2016). This study will demonstrate the difference in analysing the minimum thickness problem with different diagrams. Initially, the two diagrams depicted in Figure 7.4 are employed. The first diagram corresponds to the fan diagram, while the second corresponds to the cross diagram (see also Section 6.2.1).

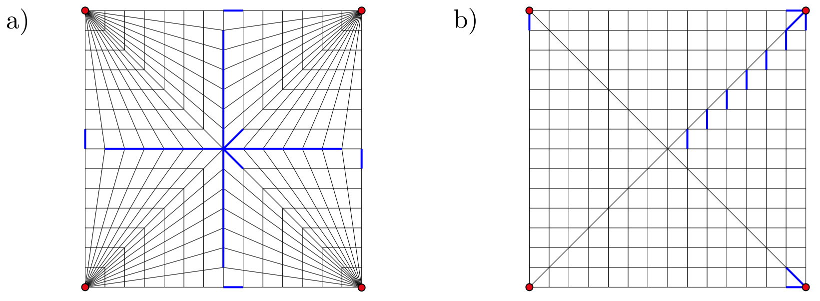

Figure 7.4: Diagrams used in this analysis with a highlight on the independent edges (blue) and support positions (red) for the (a) fan diagram and (b) cross diagram.

The fan diagram links the ridges of the structure directly to the supports. In 3D, this topology represents a series of inclined arches spanning from two of the corner supports. The pattern is composed of 784 edges and 30 independent edges shown in Figure 7.4a.

The cross diagram comprises parallel arches that carry the loads to the diagonals that are then directed to the supports. The diagram has 448 edges and 12 independents (Figure 7.4b). Both diagrams are generated with the same level of discretisation $n_\mathrm{s} = 14$, meaning that the unsupported boundary edges are divided into 14 segments.

The minimum thickness problem is solved for the parametric cross vaults, and the results are depicted in Figures 7.5a and 7.5b, for the fan and cross diagrams, respectively. The minimum thicknesses are presented in functions of R/l_0 and are grouped in five curves corresponding to different springing angles $\beta = [0°, 10°, 20°, 30°, 40°]$.

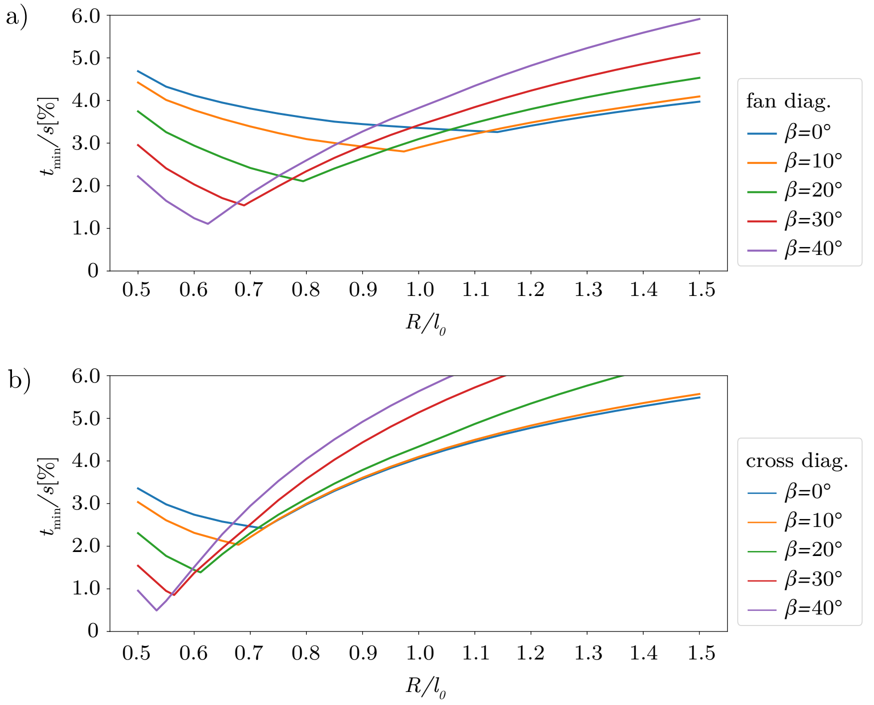

Figure 7.5: Normalised Minimum thickness ($t_{\min}/s$) for (a) fan and (b) cross diagrams. Curves are grouped considering different springing angles $\beta = [0°, 10°, 20°, 30°, 40°]$.

Figure 7.5 shows that the curves observed in the analysis of both diagrams present a distinct non-continuous minimum (cusp). This minimum represents the optimal R/l_0 value for each springing angle, i.e., the best achievable geometry once β has been defined. Overall, increasing β results in lower global values of minimum thickness. However, after a certain R/l_0 is reached, this beneficial trend is no longer observed, and lowering the springing angle reduces the minimum thickness values. It is also noticeable that the optimum R/l_0 decreases with increasing β, meaning that for higher springing angles, the optimal R/l_0 is less "pointy". The optimal values of R/l_0, i.e., the singular points in the graph, and the corresponding minimum thicknesses are listed in Table 7.1.

For the fan diagram (Figure 7.5a), the thrust networks obtained at the op-

Table 7.1: Values of minimum thickness $t_{\min}/s$ and optimal R/l_0 reported for the minimum value for each springing angle β.

diagram	fan diagram		cross diagram	
β	R/l_0	$t_{\min}/s$	R/l_0	$t_{\min}/s$
0°	1.14	3.3%	0.72	2.4%
10°	0.97	2.8%	0.68	2.0%
20°	0.79	2.1%	0.61	1.4%
30°	0.69	1.5%	0.56	0.9%
40°	0.62	1.1%	0.53	0.5%

timum R/l_0 for $\beta = [0°, 20°, 40°]$ are depicted in Figure 7.6. The results enable visualising the geometric trade-off between the springing angle and the pointiness (R/l_0). When $\beta = 0°$, the minimum thickness is 3.3% of the effective span, and the corresponding vault is defined by $R/l_0 = 1.14$ (Figure 7.6a/Table 7.1), which corresponds to a highly pointed vault. Conversely, for $\beta = 40°$, the minimum thickness corresponds to only 1.1% of the effective span and results in a less pointed vault with $R/l_0 = 0.62$ (Figure 7.6c/Table 7.1).

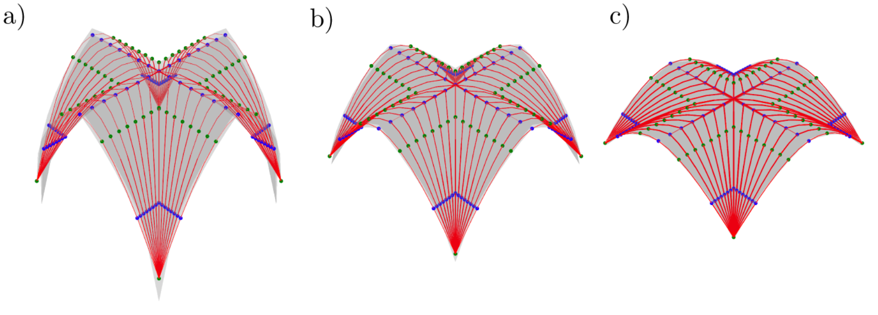

Figure 7.6: Minimum thickness solution obtained with the fan diagram for (a) $\beta = 0°$ with $t_{\min}/s = 3.3\%$, (b) $\beta = 20°$ with $t_{\min}/s = 2.1\%$, and (c) $\beta = 40°$ with $t_{\min}/s = 1.1\%$.

Qualitatively, the networks obtained with the fan diagram present the same 7-hinges mechanism. The edges connecting the fan segments have zero force and therefore vanish in Figure 7.6. It indicates that all the fan lines can be considered as separate arches, spanning from the supports across the vault's ridge. The only non-negligible connection among these arches can be found along the midspan of the vault, transferring the thrust along the inclined arches. Consequently, each inclined arched can be analysed as a separate mechanical system; i.e., the equilibrium can be described as a pseudo-3D solution, as is common when using the slicing technique (Huerta, 2001; Block, Ciblac and Ochsendorf, 2006).

The solutions obtained with the fan diagram are equivalent to the pointed arch problem described in Lengyel (2018) for which the exact 7-hinges mechanism is described for the optimal pointiness of the arch.

The same trend in the values of R/l_0 is observed for the cross diagram (Figure 7.5b). However, the optimal R/l_0 for this diagram is found earlier than for the fan diagram, i.e., for lower values of R/l_0. The minimum thickness solution for the optimal R/l_0 for $\beta = [0°, 20°, 40°]$ is shown in Figure 7.7. For $\beta = 0°$, the minimum thickness is smaller in comparison with the fan diagram, equals 2.4% of the span (instead of 3.3%), and is achieved earlier for $R/l_0 = 0.72$ (instead of 1.14). The same trend is observed for larger β.

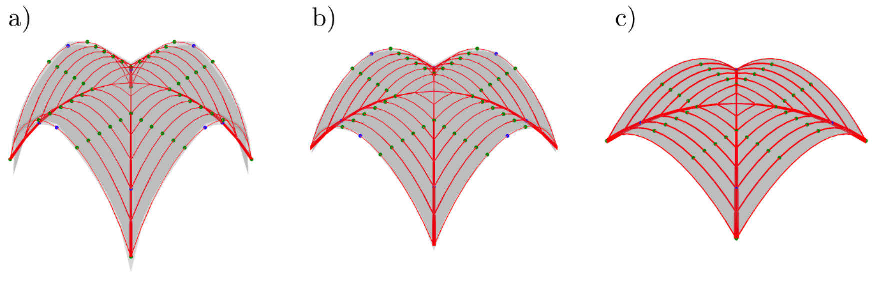

Figure 7.7: Minimum thickness solution obtained with the cross diagram for (a) $\beta = 0°$ with $t_{\min}/s = 2.4\%$, (b) $\beta = 20°$ with $t_{\min}/s = 1.4\%$, and (c) $\beta = 40°$ with $t_{\min}/s = 0.5\%$.

Regarding the hinge configuration (Figure 7.7), this flow of forces behaves as a series of arches that thrust to the main diagonals and then towards the supports. Consequently, these arches have different spans and do not present the same individual hinge behaviour as in the fan diagram. Instead, a global 7-hinge mechanism appears in the vault (Figure 7.7a) with two hinges forming at the supports, two hinges points in the diagonals, two hinge lines extending through the diagonals, and a hinge point in the apex of the arch in the boundary.

Regarding the behaviour of both diagrams, the cross outperforms the fan diagram for lower R/l_0. This indicates that the vault tends to behave as individual arches for higher values of R/l_0, while it preferably bears on the diagonals for values before that.

Nevertheless, the discontinuous minimum observed for these diagrams suggests that there must be a family of diagrams outperforming cross and fan diagrams for intermediate values of R/l_0, as noted in Maia Avelino, Iannuzzo, Van Mele and Block (2021*b*).

Two parametric strategies are proposed to enlarge the space of form diagrams analysed. The first strategy adds diagonals to the cross diagram. Due to the straight unsupported boundaries, the diagonals can not activate unless a curvature is applied. This is done by imposing a parabolic sliding (see Section 6.2.3) with magnitude Δ, as shown in Figure 7.8a. The parameter Δ/s is varied from $[0-7.14\%]$. The addition of diagonals is disregarded to compute the tributary areas. Hence, for $\Delta = 0$, the diagram obtained is equivalent to the cross diagram. The diagram obtained for $\Delta/s = 7.14\%$ is depicted in Figure 7.8a.

a)

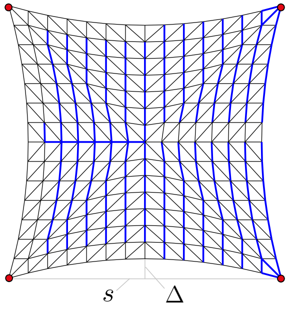

b)

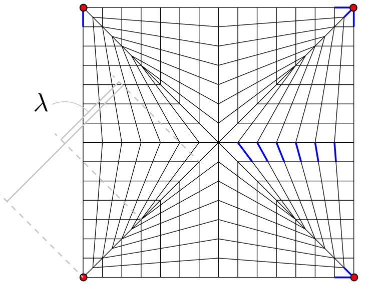

Figure 7.8: Modified diagrams considered in the analysis: (a) curved diagram with $\Delta/s = 7.14\%$, and (b) parametric diagram obtained for $\lambda = 0.5$.

The second transformation starts from the cross diagram and inclines the parallel arches according to an inclination parameter $0 \leq \lambda \leq 1$. For $\lambda = 0$, the cross diagram itself is obtained. For $\lambda = 1$, the fan diagram is retrieved. Figure 7.8b depicts the parametric diagram obtained for $\lambda = 0.5$. This diagram was proposed in Nodargi and Bisegna (2022).

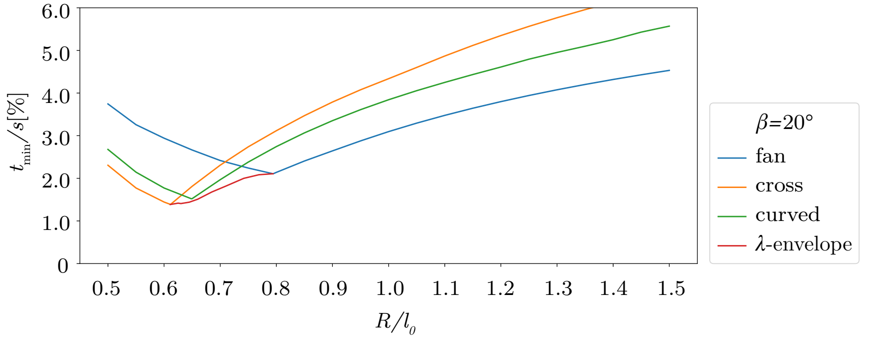

Figure 7.9: Values of minimum thickness obtained for $\beta = 20°$ for all diagrams in this study: fan, cross, curved ($\Delta/s = 7.14\%$), and λ-envelope minima for $\lambda \in [0 - 1]$.

These diagrams are used to investigate the minimum thickness problem for $\beta = 20°$, and the results are plotted in Figure 7.9.

The result for the minimum thickness problem using the curved diagram with $\Delta/s = 7.14\%$ is depicted in Figure 7.9 plotted in green. The curve obtained follows the same trend as before, having a singular minimum point. This diagram shows the minimum at $R/l_0 = 0.65$ with $t_{\text{min}}/s = 1.5\%$. It outperforms the original fan and cross diagrams from $R/l_0 = [0.63 - 0.74]$. Adding the diagonals enables new force paths to form to the support and creates a combined behaviour between the fan and cross diagrams.

The results for the λ-parametrisation are also shown. The diagram is analysed for nine intermediate values of $\lambda = [0.1, 0.2, \ldots, 0.9]$. In Figure 7.9, the minima for these curves are plotted. This diagram links the low points obtained with the fan and cross diagram and outperforms them for the range $R/l_0 = [0.61 - 0.79]$. This transition diagram results in solutions where the inclined arches do not converge directly at the supports but rather are directed to the main diagonals.

The results of this section are combined to create the contour plot in Figure 7.10. In this diagram, the minimum thickness can be quickly checked for various cross vaults based on their pointiness R/l_0 and springing angle β. The safest zone, i.e., the zone with minimal thicknesses, is obtained for $\beta = [30° - 40°]$ and $R/l_0 = [0.5 - 0.6]$ resulting in shallow and rounded vaults.

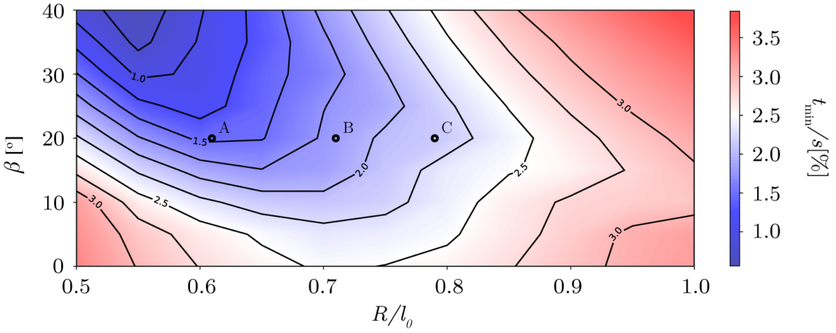

Figure 7.10: Contour plot for the minimum thicknesses computed by the present study considering all diagrams. Highlight points A, B, and C will be analysed further in the following sections.

Practitioners could employ this chart to quickly benchmark the minimal thickness of cross vaults during field expeditions. In addition, future research might improve and extend these results by testing other form diagrams. In Section 7.3.2, selected vaults A, B, and C, highlighted in Figure 7.10 will be revisited, and their stability domain is computed considering the parametric diagrams introduced in this section.

7.3 Stability domain

In this section, the stability domain of vaulted structures is investigated. The problem is applied to a dome in Section 7.3.1 and selected cross vaults in Section 7.3.2.

7.3.1 Stabiliy domain on the masonry dome

This section constructs the stability domain of the hemispheric dome analysed in Section 7.2.1 with $t_0/R_c = 0.10$, $R_c = 5$ m and diagram discretisation $(n_P, n_M) = (20, 16)$. The sequential optimisation starts at the minimum thickness obtained and computes the minimum and maximum thrust states for increasing thickness values. The computed minimum $T_{\min}/W$ and maximum $T_{\max}/W$ normalised thrusts are computed and plotted in the graph of Figure 7.11. This graph represents the stability domain of this structure, limited by the lines of maximum (red) and minimum (blue) thrust that meet the limit state (black). A secondary horizontal axis is placed at the top of the graph and enables obtaining the GSF for the limit state, which is 2.44 for this problem. The stability domain shrinks parabolically towards the limit state, which gives an idea of the stability drop for reduced thickness values.

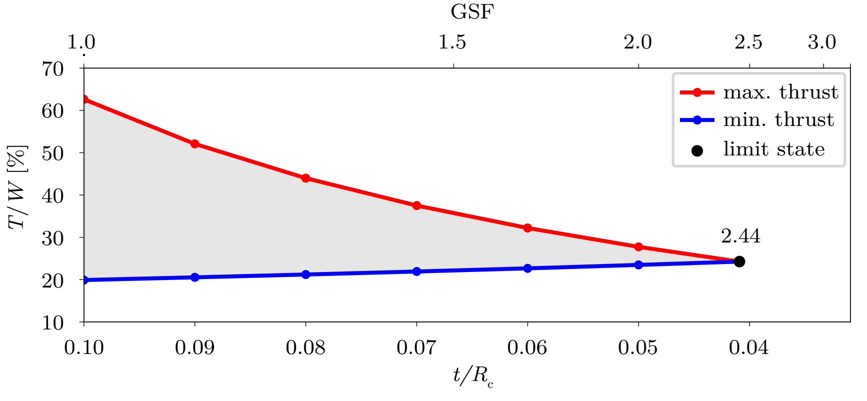

Figure 7.11: Stability domain for the dome with $t/R_\mathrm{c} = 0.10$ and diagram $(n_\mathrm{P}, n_\mathrm{M}) = (20, 16)$. At the limit state, the GSF is highlighted as 2.44.

From the stability domain of Figure 7.11, the minimum and maximum thrust for the dome is $T_\mathrm{min}/W = 19.9\%$, and $T_\mathrm{max}/W = 62.6\%$. The minimum thrust value matches values from the literature, as in Nodargi and Bisegna (2021*b*). As observed in Section 7.2.1, in the limit state, the normalised thrust is $T_\mathrm{limit}/W = 24.3\%$.

The minimum and maximum thrust states are depicted in Figures 7.12 and 7.13, respectively.

The minimum thrust state (Figure 7.12) returns a solution which is similar to the one from the minimum thickness problem (Figure 7.2). A top biaxial cap forms at the dome's crown, and a uniaxial state appears toward the support. The cross-section depicts the formation of four symmetric hinges. A pair of hinges formed by the thrust touching the extrados (green) is obtained at the perimeter of the biaxial cap, at $\beta_2 = 67.6°$. A second pair touches the intrados near the supports at $\beta_1 = 18.6°$. Numerically, this state can form since the height of the supports is encountered below the reference datum $z_\mathrm{b} = -0.322$ m. In Figure 7.12, the support point is not shown as it is below the datum. This convention will be consistently used during this work.

Regarding crack pattern, this solution matches and confirms Heyman's "orange-slice" mechanism for the supports' outward (passive) radial displacement. In this mechanism, cracks form along the meridians where the hoop forces are null, and a top cap is preserved uncracked. This crack pattern has been documented for historical domes, as in Poleni (1748).

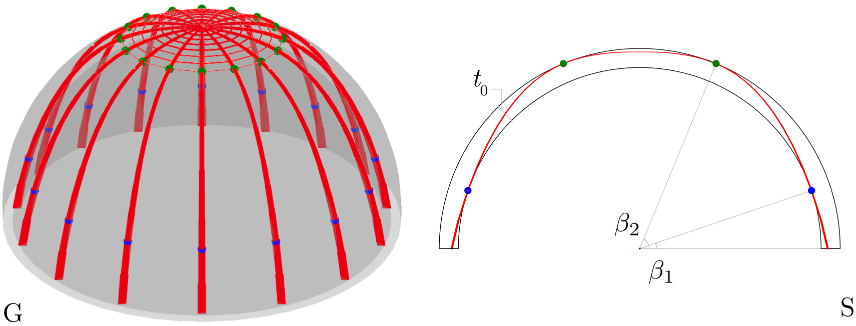

Figure 7.12: Minimum thrust solution for a hemispheric dome with $t_0/R_c = 0.10$ with diagram discretisation $(n_P, n_M) = (20, 16)$. Perspective (left) and main cross-section (right) with angles β_1, β_2 indicating hinge locations (S).

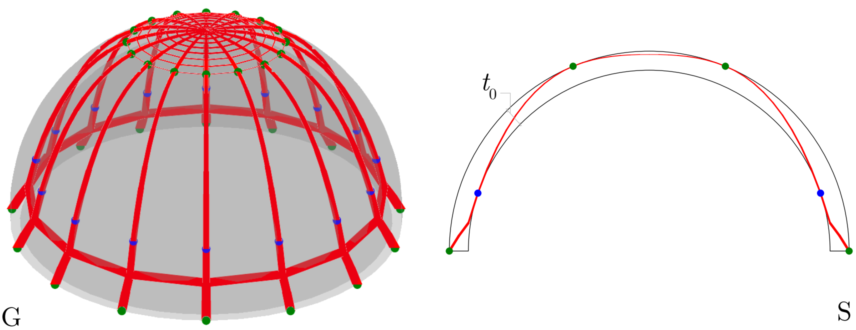

Figure 7.13: Maximum thrust solution for a hemispheric dome with $t_0/R_c = 0.10$ with diagram discretisation $(n_P, n_M) = (20, 16)$. Perspective (left) and main cross-section (S) (right).

For the maximum thrust solution (Figure 7.13), a compressive ring is activated in the dome's base, and the extreme points touching intrados and extrados remain at the same location as in the previous solution. Under inward (active) displacement of the supports, a global mechanism for the dome is not activated, and the compressive ring in the base ensures stability. It is also noted that this ring creates a discontinuity on the thrust, as depicted in the section (Figure 7.13).

This theoretical solution would represent an active, radial movement in the base of the dome, which is unlike as high forces would be required to provoke such a state. Depending on the discretisation near the base, the force in the ring could attain infinity, which would increase the stability domain of Figure 7.11. From the safe theorem, the stability domain computed is a lower bound of the actual size of the domain of admissible stress states. Strategies to increase this domain will be discussed in the following section.

7.3.2 Stabiliy domain on selected cross vaults

In this section, three cross vaults (A, B, C) from the parametric study conducted in Section 7.2.2 are revisited, and their stability domain is computed. The cross vaults selected have $\beta = 20°$ and pointiness $(R/l_0)_\mathrm{A} = 0.61$, $(R/l_0)_\mathrm{B} = 0.71$ and $(R/l_0)_\mathrm{C} = 0.79$. They are highlighted in the contour plot in Figure 7.10. The thickness adopted in this analysis is $t/s = 0.05$ for all the vaults.

Figure 7.14 shows the stability domain of the structures. The vault's minimum and maximum thrusts, GSF, and the diagrams for which these states appear can be directly retrieved from this graph. The individual domains for cross ($\lambda = \Delta = 0$), fan ($\lambda = 1.0$) and curved ($\Delta/s = 7.14\%$) diagrams are depicted together with the $\Delta/s \in [0-7.14\%]$ and the $\lambda \in [0-1]$ parametric envelopes (see Section 7.2.2).

The stability domain of structure A (Figure 7.14a) shows that the maximum and minimum thrusts are obtained with the curved and cross diagrams, respectively. The fan diagram's results are a subspace of the orthogonal diagram. This is evident when the λ-envelope is shown. For this structure, the λ-envelope does not increase the stability space obtained with the cross ($\lambda = 0.0$) diagram. The Δ-envelope, however, increases the stability domain on the maximum thrust side, as curved bounds enable larger thrusts to appear. Finally, the cross arrangement achieves an overall minimum thickness value, resulting in a GSF of 3.6.

Looking at structure B (Figure 7.14b), both the cross and fan diagrams present similar minimum thickness values. The λ-parametrisation extends the stability domain beyond the cross and fan space for this problem. The

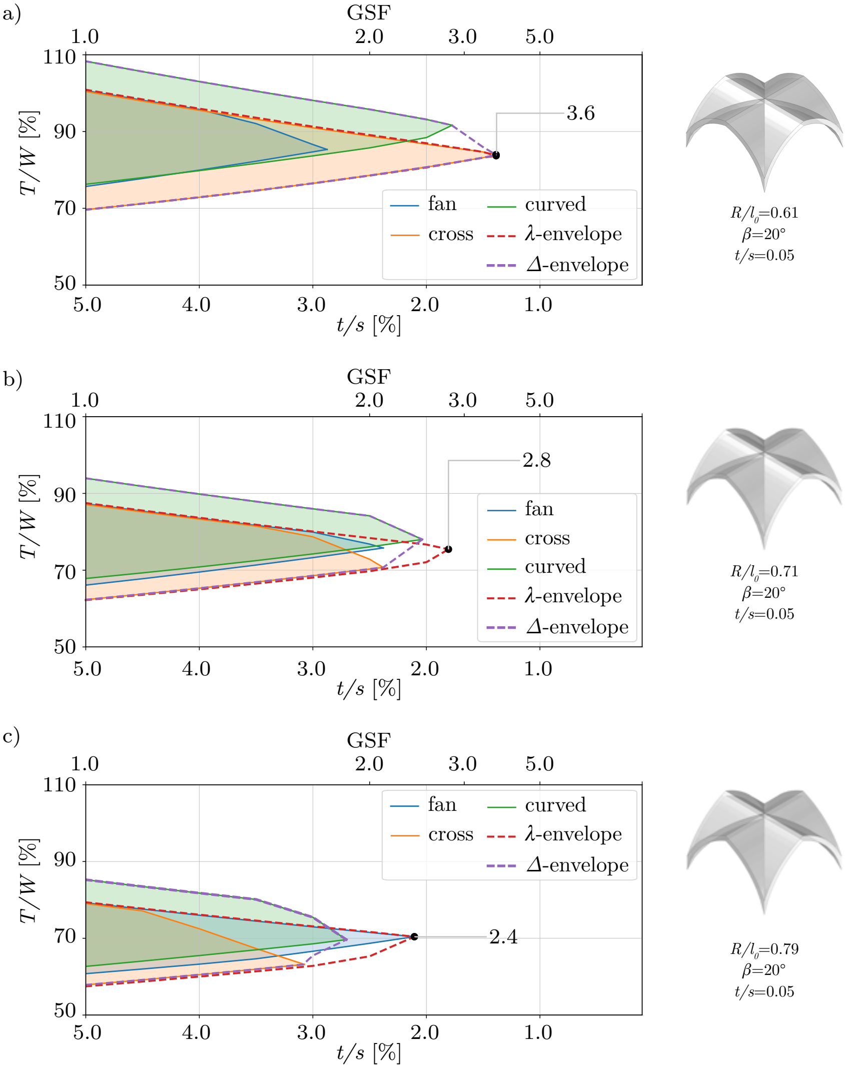

Figure 7.14: Stability domain for selected cross vaults A, B, and C, using the different diagram assumptions presented in this chapter.

minimum thickness and largest GSF are found for this diagram family, more specifically, when $\lambda = 0.7$ resulting in the GSF of 2.8. The maximum thrust behaviour for this example is again obtained with the curved diagram and the Δ-envelope.

For structure C (Figure 7.14c), the fan diagram provides the global minimum thickness, resulting in a GSF of 2.4. However, this diagram is not responsible for the observed minimum and maximum overall thrusts achieved for cross and curved diagrams, respectively. The GSF is not improved by looking at the envelope achieved for the λ-parametrisation, as the fan diagram itself results in the optimum GSF. However, the stability domain is enlarged for values of $t/s \in [2\% - 3\%]$.

The study presented in this section provides a complete analysis of the behaviour of cross vaults. It highlights that a combined selection/choice of the form diagrams is crucial to describe their mechanics. As argued in Huerta (2001), cross vaults behave elastically (i.e., a unilateral reversible mechanical system) and can adapt to different support displacements, which induce minimum and maximum thrust states.

This conclusion offers a new perspective on the classical debate about the force flow in Gothic vaults, as in the overview in Huerta (2009), after Abraham (1934). The loads in the Gothic cross vaults do not follow a fixed arrangement, and neither can be precisely identified. Instead, they are in constant change following, e.g., foundation settlements induced by the surrounding elements, additional imposed loads, active or passive states in the building etc.

The tools offered by this work offer a novel way to perform such analyses, enabling meaningful conclusions about the vault's structural behaviour. Even more intricate admissible states will be investigated in Chapter 9, in which, beyond the minimum and maximum states, their response to nonsymmetrical foundation displacement can be studied.

Based on these conclusions, the following section shows how TNA applies to a real case study conducted in an existing vaulted structure, where the pattern must adapt to predetermined structural geometry constraints.

7.4 Applications to an existing vault

In this Section, the concepts developed in this chapter are applied to a case study with geometry obtained from digital surveys. The case study is the St. Angelo Church in Anagni, Italy, depicted in Figure 7.15, showing a southwest (SW) aerial view and the vaults at the main nave. The access to the church and equipment for conducting the survey were provided during the 3rd International Summer School on Historic Masonry Structures in 2021 (HIMASS, 2021). The geometric survey and findings about the history of this monument were summarised in Maia Avelino, Oliveri, Donval, Fugger, Lai, Lasorella, Saretta, Weichbrodt and Sangirardi (2022). The following sections demonstrate how the proposed methodology can be applied to compute the stability levels in the main nave vaults.

Figure 7.15: Left: SW Aerial view of St. Angelo Church, in Anagni, Italy. Right: Photography of the main vaults inside the church.

7.4.1 Geometry acquisition

Terrestrial and aerial close-range photogrammetry were executed by tutors and students of the summer school acknowledged in Maia Avelino, Oliveri, Donval, Fugger, Lai, Lasorella, Saretta, Weichbrodt and Sangirardi (2022). Approximately 300 images were captured from the interior, and 110 other aerial images were obtained with a drone. Eight ground control points (GCPs) were defined to scale the model and connect interior and exterior imaging data. The images obtained were treated with Metashape (AgiSoft, 2021), resulting in a dense point cloud. This point cloud was then used to compute textured meshes with approximately 450.000 faces for the exterior mesh and 2.600.000 for the interior mesh. These meshes are presented in Figure 7.16.

Access to the extrados of the vaults was possible where the thickness $t = 0.25$ m was measured at an opening in the vault's keystone. Measures were taken to estimate the geometry of the fill present in the extrados. Based

Figure 7.16: Digital model obtained after the survey. Perspectives of the (a) interior and (b) exterior surveyed meshes.

on the analysis of the material of the church and surrounding buildings, the specific weight of the vaults has assumed for the vault $\rho_{\text{vault}} = 20$ kN/m^3 and fill $\rho_{\text{fill}} = 14.0$ kN/m^3. In the following sections, the focus is given to the geometry and structural analysis of the vaults of the main nave.

7.4.2 Structural analysis

Based on the survey, the geometry of the vault and the fill were obtained as depicted in Figure 7.17. The structural section of the vault and the fill are highlighted in Figure 7.17a. The fill is considered only as loads, and the networks are constrained to remain within the structural volume. This is a conservative assumption, especially given that the fill is heavy and well-packed. Also, it is assumed that the thrust is transferred to the lateral system of the vault only at the corners, i.e., the vault is unsupported along the boundaries.

Main dimensions are reported as $l_x = 5.74$ m, $l_y = 3.34$ m and $h = 2.33$ m. The typology of the vault corresponds to a mix between a rectangular cross vault and a barrel vault with lunettes. Figure 7.17b depicts the vaults' main features, highlighting the creases and level curves. The creases do not meet at the keystone but leave a clear space where simple curvature is observed. Along the lunettes, double curvature is observed.

Based on the features described and highlighted in Figure 7.17b, the form

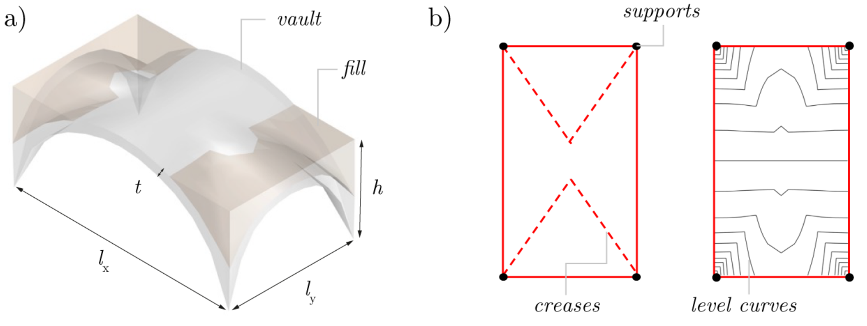

Figure 7.17: Geometry considered for the structural analysis with highlights in the structural section, main dimensions, and the fill. Supports, creases, and level curves in the vaults are highlighted.

diagrams depicted in Figure 7.18 are employed in the analysis. As discussed in Section 7.3.2, considering different form diagrams is required to define the structural behaviour. For real applications, constraints on geometric features, supports, and curvature must be considered in the search for the force flows. The rationale behind each pattern is listed for (a)-(e):

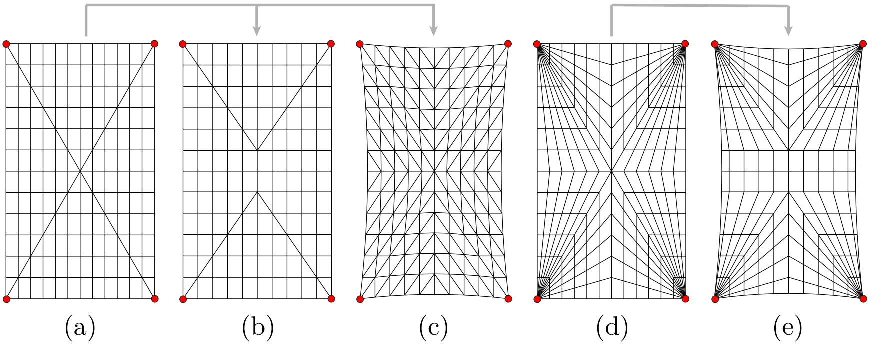

Figure 7.18: Form diagrams adopted to assess the cross vault in this section.

(a) it corresponds to the orthogonal diagram from Section 7.2.2 adjusted to the rectangular footprint of the vault,

(b) adapted cross diagram matching the diagonal to the creases in the geometry,

(c) obtained by modifying diagram (a) through the Δ-parametrisation described in Section 7.3.2, this diagram adds diagonal members and curves the four unsupported boundaries,

(d) it corresponds to the fan diagram from Section 7.2.2 adjusted to the vault's footprint,

(e) modification of diagram (d) to match the creases in the vault and curvature applied to the unsupported boundaries as in diagram (c).

The minimum thickness problem adopting the strategy described in Section 5.4.2.2 is performed by decreasing the structural section based on the offset of intrados and extrados meshes. The values of minimum thickness obtained for the five patterns and their minimum and maximum thrust in the original geometry ($t = 0.25$ m) are depicted in Table 7.2.

Table 7.2: Minimum thickness and normalised extremes of horizontal thrust for form diagrams (a)-(e).

diagram	$t_{\min}$ [m]	GSF	$T_{\max}/W$	$T_{\min}/W$
(a)	-	-	-	-
(b)	0.249	1.0	74%	64%
(c)	0.106	2.4	106%	61%
(d)	0.115	2.2	107%	69%
(e)	0.097	2.6	106%	70%

From the results in Table 7.2, diagram (a) does not allow finding an admissible stress state for this problem and, therefore, no values of $t_{\min}$ and GSF are reported.

Patterns (b)-(e) resulted in admissible solutions for the geometry and loads of the problem. The highest GSF is obtained for diagram (e), where the minimum thickness is $t_{\min} = 0.097$m. The minimum and maximum overall thrusts are obtained for diagrams (c) and (d). Diagram (b) allows finding one admissible stress state, but it results in a low GSF equal to 1.0 after rounding. Consequently, diagrams (c), (d), and (e) are more appropriate to the problem studied. The stability domain for this vault, assuming diagrams (c), (d), and (e), is depicted in Figure 7.19.

From the stability domain, besides identifying the minimum and maximum states for the original vault, also depicted in Table 7.2, minimum and maximum thrusts are also shown until the collapse state. Figure 7.19 shows that

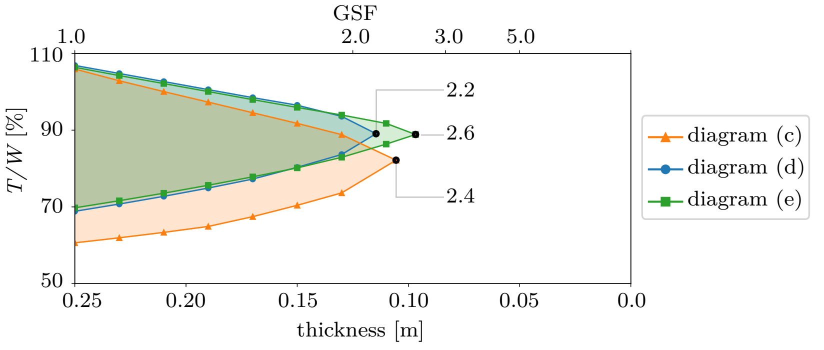

Figure 7.19: Stability domain for the vault studied with diagrams (c), (d), and (e).

the minimum thickness is always obtained with diagram (c) and that diagram's (d) stability domain is a subspace of the one obtained with diagram (e). The thrust networks obtained for the key points in this diagram are depicted in Figure 7.20.

Figure 7.20a depicts the overall minimum thrust obtained with diagram (c). This solution corresponds to the deepest network within the vault. Two orthogonal continuous cracks are suggested by the model running in the two ridges of the vault. Figure 7.20b depicts the maximum thrust obtained for this problem, achieved using diagram (d), corresponding to the shallowest solution encountered. The supports move up and touch the extrados of the vault, and the network touches the intrados at several points. Even if these networks are admissible for the local vaults, the obtained reactions should be transmitted to the nave's cross-section and transferred to the supports to ensure overall structural safety (see Ochsendorf, 2002; Huerta, 2004). However, in this work, such global stability analysis is not performed.

Figure 7.20c depicts the minimum thickness solution in the already updated, tightened envelope with $t_{\min} = 0.097$ m, showing that a thin solution of $t_{\min}/l_{\mathrm{x}} = 1.7\%$ of the main span is needed to find at least one admissible thrust network. This solution is obtained with diagram (e), which is the diagram better matching the level curves for this vault. Diagram (e) follows the creases in the structure and models the force flow near the lunettes as a series of inclined arches (fan arrangement). Near the keystone, this pattern presents a parallel arrangement, which enables a uniaxial state matching

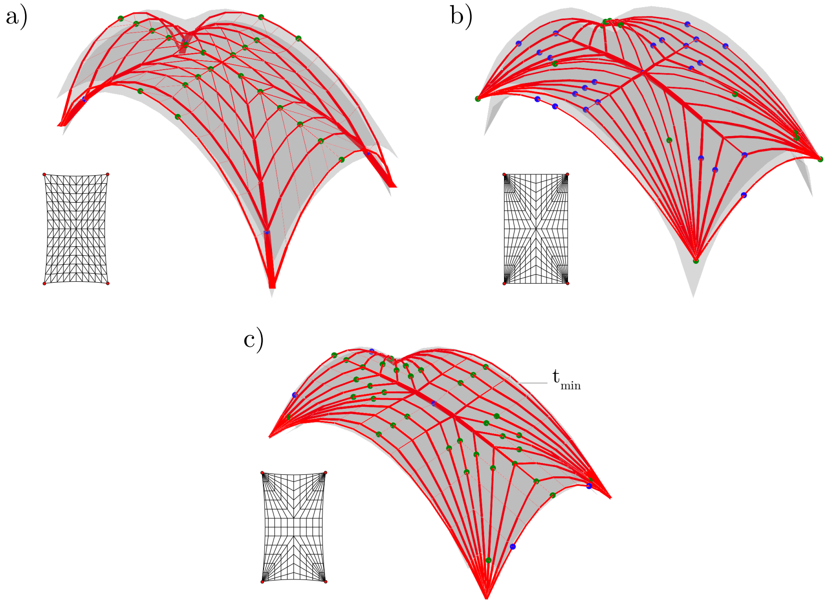

Figure 7.20: Best solution obtained for (a) minimum thrust, (b) maximum thrust, and (c) minimum thickness $t_{\min}$ for the St. Angelo vault. Diagrams adopted are shown next to each analysis.

the location where the geometry is similar to a barrel vault.

This study shows how the proposed approach can be applied to a practical assessment scenario. Indeed, the stability domain approach is useful for studying different diagrams and understanding the mechanical behaviour in the vaults. Nevertheless, it also shows the difficulties of constructing form diagrams suitable to highly constrained structural envelopes. Moreover, the vault's extrados is also hard to obtain. In the present case, thanks to the high level of fill, the thickness of the vaults near the springs could not be measured and were safely considered equal to the keystone, which is probably over-conservative. Moreover, difficulties arise in picking up the self-weight, especially when fill is added to the vault.

Therefore, even if the method enables a variety of new analyses in existing masonry vaults, more advances are necessary to transfer the geometries to the analysis and model the interaction between the vault and fill.

7.5 Summary

This chapter shows how the methodology developed can be used to investigate the structural stability of vaulted masonry structures. It offers an integrated methodology for computing the Geometric Safety Factor (GSF) and obtaining the structure's stability domain discrete lower-bound equilibrium methods.

The GSF is obtained by minimising the structural thickness of the structure. The minimum thickness problem was calculated for a hemispheric dome, validating results from the literature. An extensive parametric campaign has been performed to investigate the stability of square cross vaults. The results enable a lower-bound estimate of the minimum thickness necessary for these structures. Finally, a minimum thickness map in groin vaults has been presented that engineers can use in practice to quickly assess existing structures.

The stability domain is drawn for domes and vaults. It represents a novel way to visualise and quantify the level of stability in general structures. It enables a comparison of different form diagrams or families of form diagrams that surge after proper parametrisations. More importantly, by plotting the domain of specific diagrams, this work reflects on the admissible equilibrium space that the analysis can not yet capture and can guide strategies to update the diagram and enlarge these domains.

Finally, this chapter also applied its findings to structure with geometry obtained through a digital survey. For this application, a safe estimation of the GSF has been presented. The stability domains can also be obtained based on different form diagrams. It has been encountered that the diagram better matching the structure's curvature achieved the highest GSF. However, a series of difficulties and limitations are revealed when applying the methodology to a real case study. They require pragmatic modelling assumptions to estimate thicknesses and fill loads exemplified in the analyses.

Finally, the presented results enable a robust search over the admissible solutions space in masonry vaulted structures, as was not possible before. The following chapters will elaborate on the metrics and procedures presented in this chapter to study further limit states.

Chapter 8

Collapse loads on vaulted masonry structures

This chapter investigates collapse loads on vaulted masonry structures. Using the modular multiobjective optimisation framework described in this dissertation, vertical and horizontal load multipliers are maximised in a direct optimisation. The applications enable obtaining a lower-bound estimate of the maximum load applied to three-dimensional systems. The solution obtained also identifies where cracks would form before the structure collapses. Examples presented include domes and cross vaults subjected to vertical and horizontal loads.

8.1 The problem

8.1.1 Overview

Masonry structures might fail due to the action of extreme vertical or horizontal loads. Failing over the action of vertical loads is rare, given the usually elevated self-weight of masonry structures. Nevertheless, incidents like the fire in the Notre Dame Cathedral in Paris might result in exceptional loads applied to the vaults, resulting in the loss of significant cultural monuments and entailing complex repairs (Praticò et al., 2020; Manuello Bertetto et al., 2021). Furthermore, the current necessity to rehabilitate and reuse existing buildings might demand the application of additional large loads to masonry systems. Therefore, understanding the mechanical behaviour of vaults under externally applied loads is a pressing issue.

Understanding the failure of masonry structures under horizontal load is critical, especially in seismic zones. Recent seismic events have demonstrated that reevaluating masonry structures to horizontal loads is necessary (Indirli et al., 2013; Morandi et al., 2022). The failure by horizontal or vertical load action relates to support displacements, as argued in Ochsendorf (2002). As the load increases, the supports give in, forming a mechanism. For cathedrals and vaulting systems, these supports are usually buttresses, which might rotate, spreading the supports of the vaults that then collapse.

A series of difficulties arise in modelling the collapse loads in masonry structures. Determining the position and opening of the hinges in three-dimensional systems is especially challenging (Milani and Tralli, 2012). Furthermore, there are no specific analysis tools to deal with this problem systematically.

8.1.2 Opportunities

Applying lower-bound equilibrium methods brings opportunities to study this problem by obtaining safe estimates of the maximum load in three-dimensional structures. Using the modular multiobjective optimisation framework described in this dissertation, vertical and horizontal load multipliers are maximised until the structures hit their limit, i.e., until an admissible solution is no longer found. An estimated location for the formation of cracks is obtained without predefining possible fracture planes. The method is applied to general three-dimensional structures under nonproportional loading cases.

8.1.3 Implementation

The maximum vertical applied load is obtained by directly maximising the scalar λ_{v} representing the load multiplier associated with a given external loading case. This optimisation is described in Section 5.4.3.

The maximum horizontal applied load is computed by directly maximising the horizontal load multiplier λ_{h}, following the description in Section 5.4.4. For the analysis with the horizontal loads, a check must be performed previously, as mentioned in Section 5.4.4, ensuring that there are compressive paths to transfer these loads to the supports or adapting the pattern to enable this force transfer if necessary.

8.2 Maximum vertical load multiplier

Four applications of the maximisation of vertical loads are presented in this Section. Sections 8.2.1 and 8.2.2 investigate a hemispheric dome with an applied pointed load at its crown and off-centred. Section 8.2.3 presents a cross vault subjected to a travelling pointed load, and Section 8.2.4 revisits the example of St. Angelo church and computes a collapse line load.

8.2.1 Dome loaded in the crown

The problem of a pointed load applied in the hemispheric dome's crown is studied in this section. The dome's geometry is defined by the thickness over radius $t/R_c = 0.10$. The sensitivity study executed in Section 7.2.1 will be repeated, varying the number of meridians n_M and the number of parallels, or hoops n_P. The normalised maximum load obtained in the dome's crown is presented in the graph of Figure 8.1, where the curves are combined for each n_M.

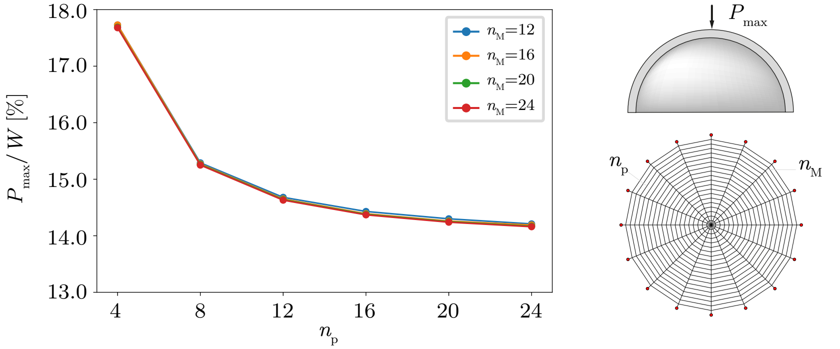

Figure 8.1: Sensitivity study for the normalised maximum load P_{max}/W applied in the dome's apex. Results are grouped by the number of meridians n_M.

The maximum load obtained varies according to the number of parallels n_P only, as the results for different n_M collapse to the same curve. This behaviour is similar to the one obtained for the minimum thickness problem (see Section 7.2.1). Given the symmetry of this problem, it can also be tackled by slicing the dome in lunettes and analysing thrust lines separately. As the discretisation increases, the maximum load decreases until a convergence point. Denser diagrams enable more constraints to be applied to the nodes, resulting in a lower estimate of the maximum load. From the present analysis, for diagrams with $n_{\mathrm{P}} = 24$, the maximum normalised load applied at the crown corresponds to $P_{\max}/W = 14.2\%$.

The solution obtained for a level of discretisation $(n_{\mathrm{P}}, n_{\mathrm{M}}) = (16, 20)$ is depicted in Figure 8.2. The hoop forces vanish for this solution. The resulting thrust lines in the dome's section are pointy at the load's application point. Indeed, whenever the hoops get activated, the thrust network (and consequently their sectional thrust lines) becomes flatter, i.e., less pointy (see Section 7.2.1), which would be inefficient for carrying the pointed load in the crown.

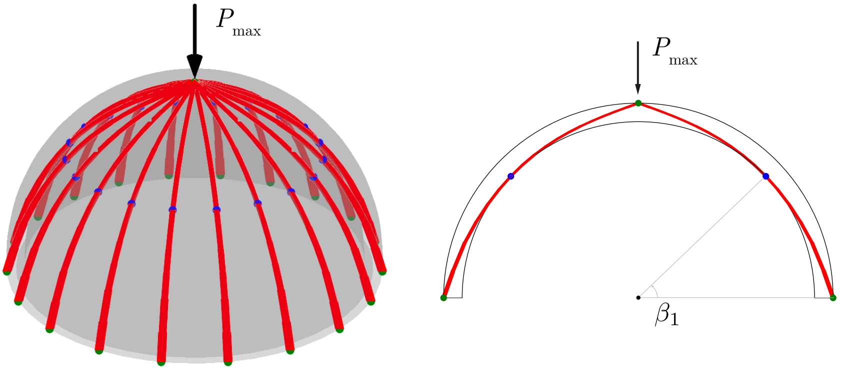

Figure 8.2: Maximum apex load for the dome $P_{\max}/W = 14.4\%$ with $(n_{\mathrm{P}}, n_{\mathrm{M}}) = (16, 20)$. Left: Perspective view, right: the main cross-section with an indication of the extrados hinge angle β_1.

Looking at the cross-section in Figure 8.2, a symmetric 5-hinge mechanism is observed. One hinge is obtained at the point of load application, where the thrust touches the extrados, a pair of hinges touches the intrados at $\beta_1 = 43.6°$, and another pair touches the extreme of the extrados near the supports. The mechanism suggested by this solution presents cracks running up to the dome's crown, a lowering of the dome's apex, and a rotation of the central part of the dome.

The cracking pattern described matches the results observed for the load testing of a masonry cap in Lau (2006), the kinematic mechanism described for masonry domes in Chiozzi et al. (2017), and for the study at the St. Peter's Dome in Funari, Silva, Mousavian and Lourenço (2021).

The maximum load obtained here is a lower bound of the collapse load and has been validated against the collapse load on unreinforced masonry structure in experiments (Fugger et al., 2022). Externally reinforced masonry structures could also be investigated with this approach, considering that the added reinforcement introduces a tensile capacity enabling the thrust network to go outside the structural section, as in Fabbrocino et al. (2015); López López et al. (2022).

Finally, this section provides benchmarks for the maximum load applied to the dome's crown with a simple and verifiable methodology. While the problem of the maximum load at the crown has already been discussed in the literature, applying the load off-centred is a more challenging problem for which an axisymmetric solution is insufficient. This problem is discussed in the following section.

8.2.2 Off-centred load in the dome

The problem of maximising a pointed load applied at 3/4 of the dome's diameter is studied. The problem is initially solved with the same symmetric diagram from Section 8.2, where the parametric analysis for $(n_\mathrm{P}, n_\mathrm{M})$ discretisations is performed and plotted in the graph of Figure 8.3.

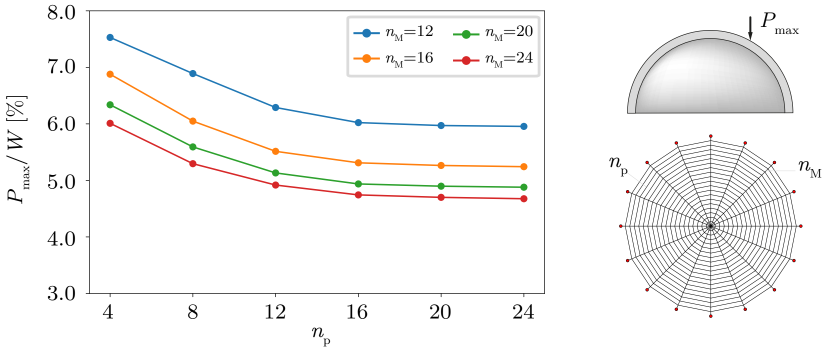

Figure 8.3: Sensitivity study for the normalised maximum load P_max/W applied off-centred to the dome. Results are grouped by the number of meridians n_M.

Unlike the results in Figure 8.1, the curves for a different number of meridians n_M do not converge, showing that a decrease in the maximum applied load is observed for a higher number of parallels. This difference indicates

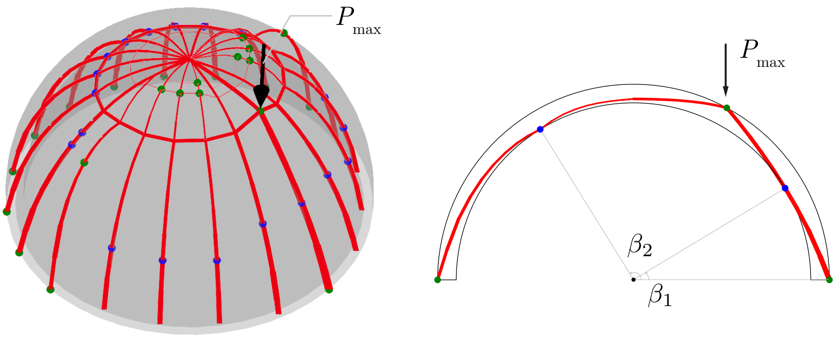

Figure 8.4: Maximum load off-centred for the dome $P_{\text{max}}/W = 4.9\%$ with $(n_{\text{P}}, n_{\text{M}}) = (16, 20)$. Left: Perspective view, right: the main cross-section with angles β_1 and β_2 indicating asymmetric cracks.

that the solution obtained is not symmetric and can not be approximated simply through axisymmetric sections. To depict this effect, the solution obtained for $(n_{\text{P}}, n_{\text{M}}) = (16, 20)$ is presented in Figure 8.4.

As observed in the thrust network from Figure 8.4, only a local mechanism effectively gets activated to transfer the applied load. The external load travel to the support through the meridian where the load is directly applied. Limited force distribution occurs by activating the hoop where the load is applied. The main cross-section is also highlighted. The thrust is tilted and pointed at the point of application to accommodate the load. The two pairs of hinges relocate to maximise the applied load and are now found at $\beta_1 = 31.2°$ and $\beta_2 = 121.8°$. Finally, the maximum load decreases and is equal to $P_{\text{max}}/W = 4.9\%$ for the discretisation assumed.

New diagrams are studied to transfer the applied load effectively and engage a fully three-dimensional behaviour in the dome. The new diagrams and the logic behind their creation are depicted in Figure 8.5.

Four new patterns are proposed. They are created based on the singular elements of the problem, which are highlighted in Figure 8.5. These elements are the geometric singularity at the dome's crown ($\mathbf{x}_{\text{dome}}$), the singular point of application of the load ($\mathbf{x}_{\text{load}}$) and the continuous circular supports available ($\mathbf{x}_{\text{b}}$). Based on these elements, the following strategies lead to new diagrams:

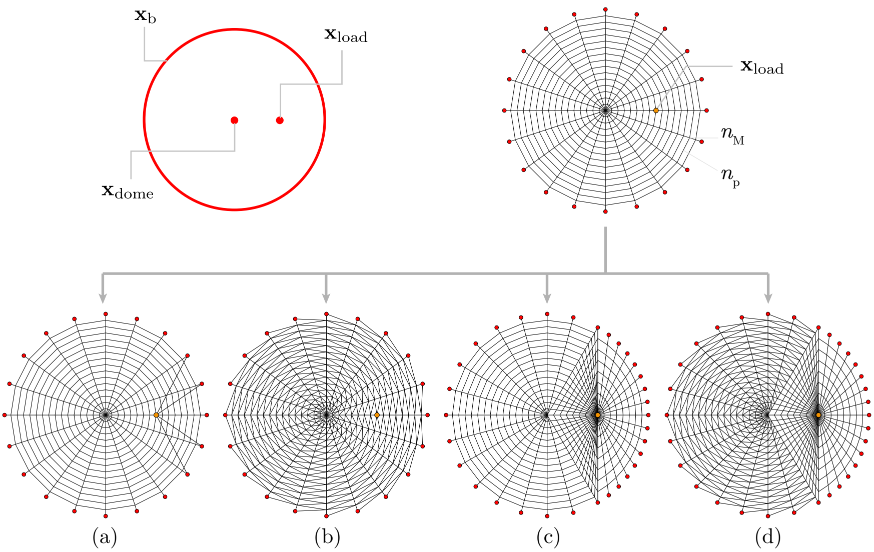

Figure 8.5: Adapting symmetric patterns to account for singularities of the problem, such as the load applied at $\mathbf{x}_{\mathrm{load}}$, geometry pole $\mathbf{x}_{\mathrm{dome}}$ and circular supports $\mathbf{x}_{\mathrm{b}}$. Modifications applied are (a) the addition of direct paths to supports, (b) diagonals, (c) a second pole, and (d) the pole and diagonals.

(a) addition of direct paths from $\mathbf{x}_{\mathrm{load}}$ to the nearest supports,

(b) the addition of diagonals in the quads of the original pattern to engage a three-dimensional response,

(c) the addition of a pole at $\mathbf{x}_{\mathrm{load}}$ with additional paths to the supported boundary, and

(d) the addition of a pole at $\mathbf{x}_{\mathrm{load}}$ and diagonals to the quads of the pattern.

Strategies (a) and (b) enable keeping the same number of discrete supports to the dome, while strategies (c) and (d) increase it. While this is expected to affect the maximum load obtained, as shown in the sensitivity study (Figure 8.3), additional paths to the support reduce the applied load, i.e., are on the conservative side. The analysis of maximum applied loads for the new patterns generated is shown in Figure 8.6. An overview of their number of edges, independents, supports, and the maximum applied loads are summarised in Table 8.1.

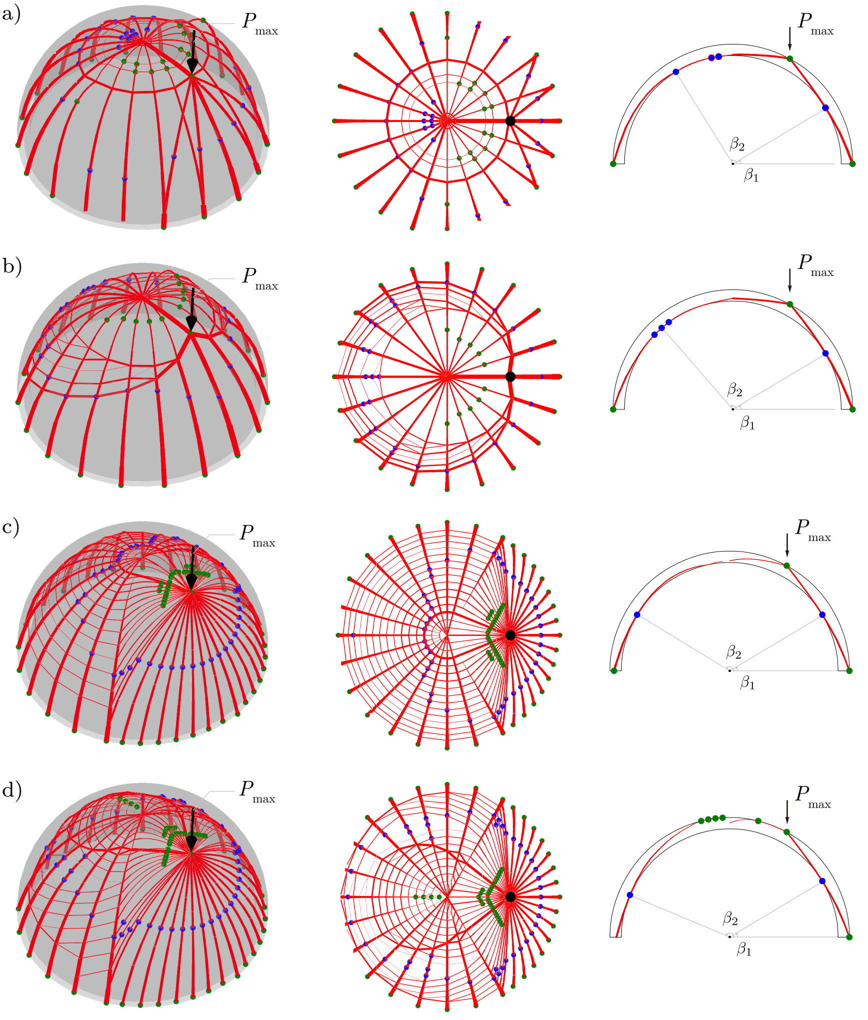

Figure 8.6: Perspective, planar and sectional view for the modified diagrams (a)–(d) subjected to their maximum applied load P_{max}. Location of extrados cracks indicated by angles β_1, β_2.

Table 8.1: Results obtained with the adapted meshes to the off-centred maximum load $P_{\max}$ on the dome.

diagram	$P_{\max}/W$	diff.	m	n_{b}	k	β_1	β_2
ref.	4.9%	-	620	20	33	31.2°	121.8°
(a)	7.3%	+48%	684	20	36	31.2°	121.8°
(b)	9.2%	+86%	920	20	318	31.2°	131.1°
(c)	9.9%	+101%	1232	32	53	31.2°	148.8°
(d)	10.2%	+107%	1472	32	293	31.2°	157.1°

The results increased the maximum load for all strategies (Table 8.1). For diagram (d), the load increases to $P_{\max}/W = 10.2\%$, representing an increase of 107% on the maximum load compared to the results using the symmetric diagram. For the most straightforward strategy, i.e., strategy (a), the increase in the applied load is already 48%, showing how adding new paths to the supports effectively increases the maximum load.

Table 8.1 also shows the number of edges, supports, and independent edges. From Chapter 5, the number of variables of the problem relates to the number of independent edges, which is significantly increased for strategies (c) and (d).

The force flow obtained enables an interpretation of the mechanisms activated for each diagram. For diagram (a), the additional paths to the support are activated, transferring the loads to adjacent supports (Figure 8.6a). On the main cross-section, the extrados cracks are encountered at the same angles (β_1, β_2) as in the symmetric solution. Indeed, due to the discretisations adopted, β_1 is the same for all patterns.

In diagram (b), besides following the shortest paths to the supports, diagonal forces get activated that direct the applied load to supports on the opposite side of the dome, representing a global instead of a local resisting behaviour as in diagram (a), which consequently increases the maximum load to 86% higher than the reference (Table 8.1 / Figure 8.6b). The cracks at the level of the supports extend through the dome's perimeter. In the main section, the crack on the opposite side of the load application is closer to the ground ($\beta_2 = 131.1°$).

The additional pole added in diagram (c) adds new force paths direct to the supports, which get activated (Figure 8.6c). This additional pole also distributes the load to the opposite side of the dome. From this redistribution, the hoop forces along the base get activated. A global mechanism is again seen in this solution. Intrados cracks extend through the dome's perimeter, and the extrados crack at the main section is found at $\beta_2 = 148.8°$.

Diagram (d) improves the solution by adding diagonals to the problem (Figure 8.6d). Consequently, the load applied flows to the closest supports and, through oblique paths, to the supports located on the opposite side of the dome, as in diagram (b). A global mechanism is again evident, with cracks along the dome's perimeter and low extrados crack at the main section ($\beta_2 = 157.1°$). A tilted compressive cap also appears in this solution, helping to resist the pointed load.

This study is the first to maximise the off-centred load in a masonry dome. Such load case is unlike for hemispheric domes since the loads to activate a collapse would be too high due to their high self-weight. Nevertheless, the results validate the strategies adopted to modify the diagrams and confirm that various lower-bound equilibrium solutions can be investigated with the present methodology.

8.2.3 Pointed load travelling a cross vault

In this section, a square cross vault is subjected to a pointed load travelling its ridge considering an adapted form diagram, as in Section 8.2.2.

The cross vault geometry is constructed with the parametrisation described in Section 6.3, for which $t/s = 0.05$, $R/l_0 = 0.50$ and $\beta = 30°$ are taken.

The form diagram analysed corresponds to the cross topology (see Section 6.2) for which the discretisation level assumed is $n_\mathrm{s} = 14$. The pointed vertical load is applied to seven nodes along the vault's ridge, from its centre until its unsupported boundary. Figure 8.7a shows the pattern used in this analysis and the (0–7) positions in which the downward unit load is applied. For each position, the maximum vertical load multiplier is computed.

Two transformations of the cross diagram are considered to investigate the effect of the pointed load travelling the cross vault. These modifications have been introduced in Section 6.2.3 and are used to create the patterns (b)–(d) illustrated in Figures 8.7b–d and described here:

(b) This pattern is created by applying a sag to the diagram using force densities. The force density in the inner edges is set to $q_\mathrm{inner} = 1.0$ in the boundary $q_\mathrm{bound} = 25.0$. This modification moves the boundary

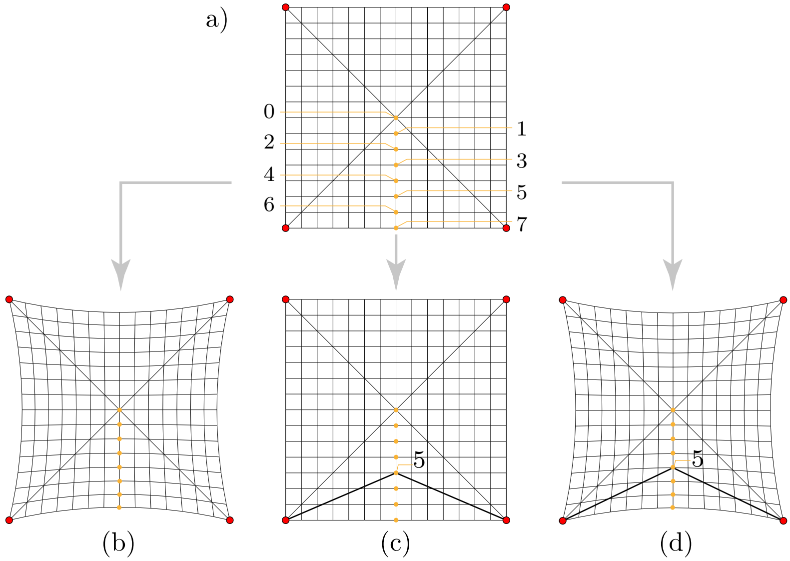

Figure 8.7: Diagrams for the cross vault analysis: (a) original arrangement and 0–7 load positions, (b) diagram transformed with sag, (c) diagram transformed with direct paths to the supports, and (d) combined effects of adding paths to the supports and sag.

edges inward by around $\Delta \sim 5\%$ of the span and enables the loads to travel orthogonally to the unsupported boundaries.

(c) This pattern is created by adding a direct path from the point of application of the load to the adjacent supports.

(d) This diagram combines strategies (b) and (c).

The maximum applied load is presented in Table 8.2 for each position 0–7. The results are reported in terms of normalised maximum load ($P_{\max}/W$). The graph in Figure 8.8 depicts the maximum applied load per load position, grouping the results by the diagram used.

For the load applied in position 0, a normalised maximum load $P_{\max}/W =$ 72.6% is found using the original cross diagram. As the pointed load moves outside the centre, the maximum applied load drops significantly (see Figure 8.8). At position 1, this value decreases to 14.0% and less than 10.0% as the load travels towards the open edge. This result derives from the fact

Table 8.2: Normalised maximum load (P_{max}/W) applied in positions 0-7 for each strategy adopted.

load position	strategy adopted (a)	(b)	(c)	(d)
0	72.6%	72.8%	72.6%	72.6%
1	14.0%	19.9%	39.9%	43.8%
2	6.3%	9.5%	25.3%	27.2%
3	3.7%	6.9%	14.1%	16.8%
4	2.1%	4.5%	9.3%	13.2%
5	1.4%	3.0%	6.2%	9.9%
6	1.1%	2.2%	6.3%	7.2%
7	3.7%	6.1%	3.7%	6.1%

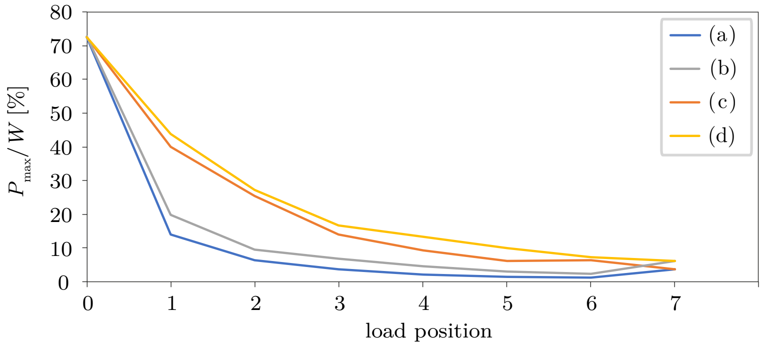

Figure 8.8: Graph with the normalised maximum load (P_{max}/W) applied grouped per diagram strategy adopted. (a) original diagram, (b) sag applied, (c) paths added to the supports, and (d) sag and paths to the supports.

that the force flow is fixed in the original diagram and can not adapt to the new force applied. Figure 8.9 shows the results obtained for the load applied in positions 0, 2, 3, 4, 5, and 7. The force flow obtained is symmetric, and the additional load needs to travel to the main diagonals before going toward the supports.

The following results consider the same problem using the three modified diagrams shown in Figure 8.7b-d. The results are depicted in Figure 8.10

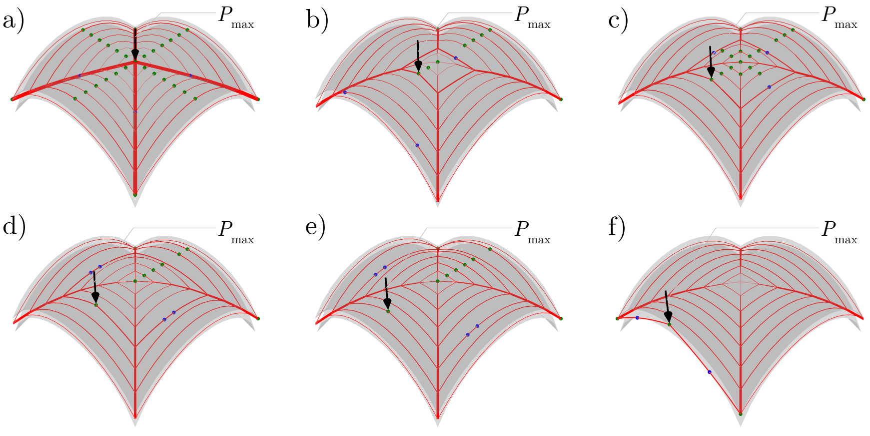

Figure 8.9: Results for the maximum load P_{max} obtained travelling the ridge of the cross vault for the orthogonal diagram. Results for the load applied to the positions (a) 0, (b) 2, (c) 3, (d) 4, (e) 5, and (f) 7.

for the loads in positions 2, 4, and 6. The results are discussed in detail below.

When the sag transformation is applied to the diagram, an average 72% increase in the maximum load is obtained. From the solutions in Figures 8.10b-2,4,6, new force paths can form as the lines curve inwards, and the applied loads are distributed among them. The loads do not need to move to the diagonals exclusively and are shared among the curved lines following alternative paths to the supports.

When direct paths to the supports are added, an average increase of 240% is observed. As shown in Figure 8.10c-2,4,6, when the direct line is added to the pattern, this is the preferred path to the loads, resulting in a significant increase in the limit loads. Consequently, the curve for this diagram in Figure 8.8 is smoother than the curves obtained before, showing that this simple modification in the form diagram result in a better transition for the problem of the load travelling the ridge of the cross vault.

The last result reported in this section combines the sag and the added lines to the supports. Results are depicted in Figure 8.10d-2,4,6. This strategy results in the best values obtained. On average, the maximum loads obtained were increased by 330%. The loads flow directly to the support through the

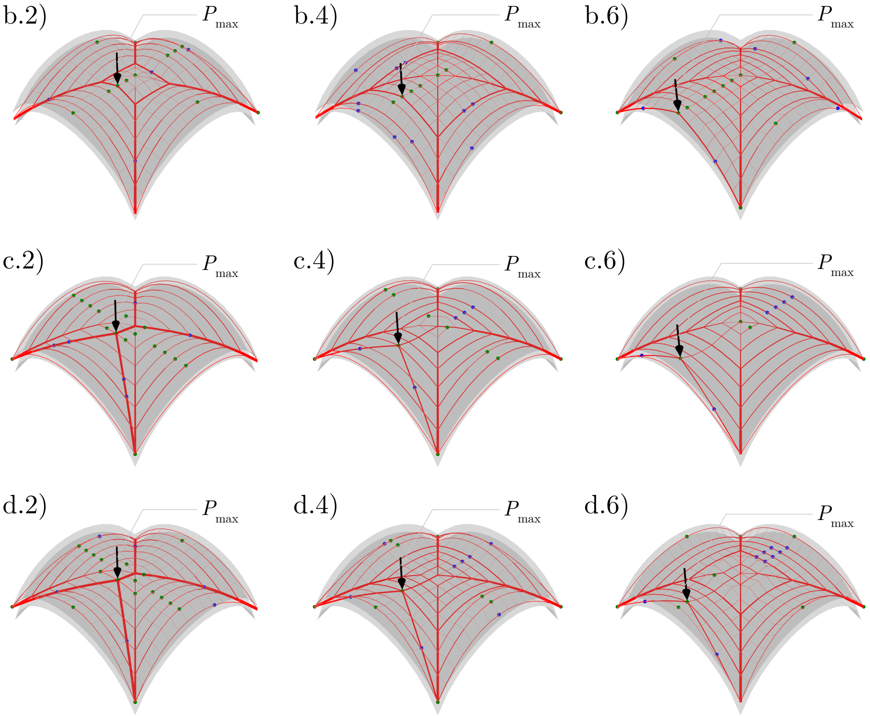

Figure 8.10: Results for the maximum load $P_{\max}$ obtained travelling the ridge of the cross vault following the proposed modifications in the patterns suggested in this section. Results are displayed for the strategies (b), (c), and (d) with the load applied in positions (2), (4), and (6).

added lines and engage the parallel arches. Consequently, additional force paths are available to transfer the pointed load to the supports, increasing the maximum load values.

This section evaluated the problem of a maximum load applied in a cross vault. Pragmatic transformations are applied to the diagrams, and the maximum loads are re-computed. The results show that this problem's maximum load estimation can be increased three-fold, reducing the conservatism of the analysis.

8.2.4 Line load applied to an existing vault

In this section, the scanned geometry from St. Angelo church is revisited and subjected to a line load applied at 1/3 of its main span. The results are depicted in Figure 8.11, and the values of the maximum load line obtained are presented in Table 8.3.

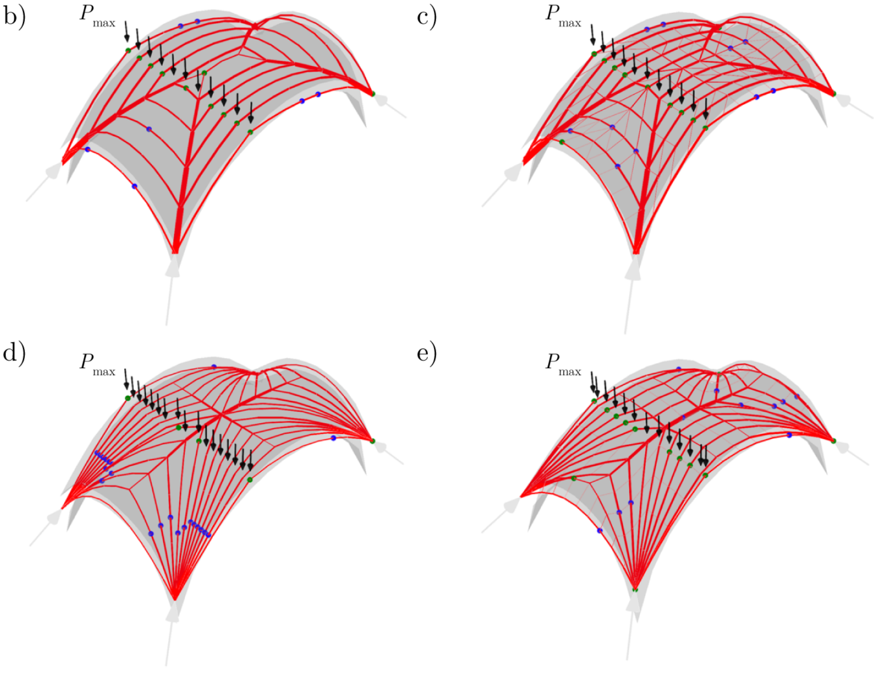

Figure 8.11: Results of maximum line load $P_{\max}$ applied at 1/3 of the span in the vaults of St. Angelo church. Results reported for meshes (b)–(e) from Figure 7.18.

The diagrams used for the GSF analysis in Section 7.4 are repeated in this section. The maximum load obtained with diagrams (b)–(e) is computed and shown next to the GSF previously calculated. From the values in Table 8.3, the maximum load is obtained for diagram (c), resulting in $P_{\max} = 13.5$ kN/m. The solution obtained with this diagram is depicted in Figure 8.11c. In this solution, the diagonals get activated. A line crack (visible from the intrados) and a kink are visible where the load is applied.

Table 8.3: Maximum line load applied at the vault of St. Angelo church

diagram	$P_{\max}$ [kN/m]	GSF (see 7.4)
(b)	9.13	1.0
(c)	13.5	2.4
(d)	6.10	2.2
(e)	5.39	2.6

Interestingly, this solution was not the one for which the maximum GSF was obtained; as for diagram (c), the GSF obtained is 2.4. On the other hand, the diagram with the best GSF (diagram (e)) resulted in the lowest maximum load value $P_{\max} = 5.39$ kN/m, which reinforces the importance of analysing different diagrams and indicates how the flow of forces in masonry structures adapts to the boundary conditions applied.

The values of maximum load should, nevertheless, be analysed in combination with the church's cross-section, considering its interaction with the buttressing systems so the maximum load can be defined appropriately (see Ochsendorf, 2002; Huerta, 2004). This study, however, goes beyond the focus of the present chapter.

This section highlights opportunities to apply the methodology developed in this dissertation to estimate collapse loads in a masonry vault with non-analytical geometry. A conservative result can be quickly obtained and used by engineers to assess safety factors in masonry structures.

In the following section, the problem of horizontal loads is studied.

8.3 Maximum horizontal load multiplier

In this section, the maximum horizontal load problem in three-dimensional structures is investigated and discussed for a dome in Section 8.3.1 and a square cross vault in Section 8.3.2.

8.3.1 Tilting of the dome

This section evaluates the maximum horizontal multiplier of a hemispheric dome. As discussed in Zessin et al. (2010), this problem is the equivalent of tilting the dome of a given angle for which a fraction of the vertical weight is applied as a statical horizontal force.

A difficulty arises when modelling horizontal forces with the fixed diagram assumption. A compressive path must exist to transfer the applied horizontal loads to the supports in compression. This can be done by checking the rank of the equilibrium matrix stacked with the vector of the applied loads as discussed in Section 5.4.4. In most cases, the diagram must be updated to enable a compressive solution. Furthermore, the analysis is more time-consuming than the other analysis presented in this dissertation (see solving benchmarks in Section 6.6.3). The computational time can be reduced by applying symmetry features, as described in Section 6.4. For the present analysis, a horizontal symmetry axis is considered parallel to the load crossing the dome's centre, which reduces the analysis time by 42% (see comparison in Table 6.7).

The strategy adopted to enable the horizontal loads in the dome is the addition of diagonals which is performed here for a radial diagram with $(n_{\mathrm{P}}, n_{\mathrm{m}}) = (16, 20)$ similar to the one used in Section 8.2.1. The diagram with diagonals is the mirrored version of the diagram depicted in Figure 8.5b. The solution obtained with this diagram is depicted in Figure 8.12, and the maximum horizontal multiplier obtained is $\lambda_{\mathrm{h}}^{\max} = 14.4\%$, i.e., the maximum horizontal load applied is $P_{\max}/W = 14.4\%$.

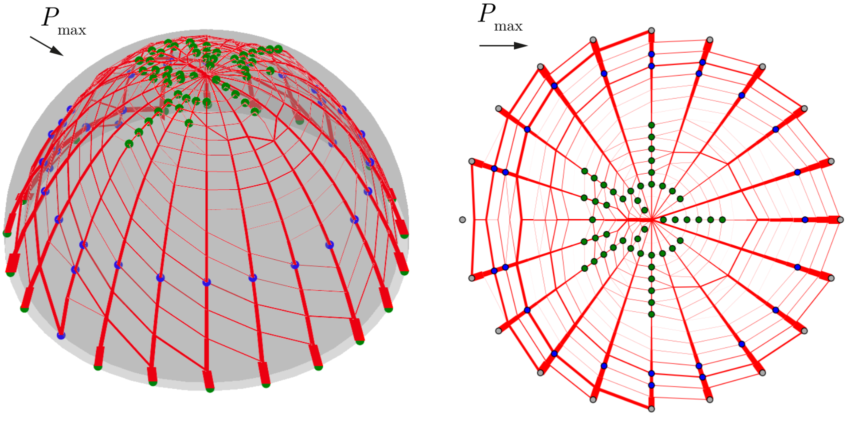

Figure 8.12: Results for maximising the horizontal force applied to a hemispheric dome with $P_{\max}/W = 14.4\%$. Results are shown in perspective and in planar view.

The solution obtained can be compared quantitative and qualitatively to the literature. In Zessin et al. (2010), the tilting test with physical models on a dome with $t/R_{\mathrm{c}} = 0.10$ resulted in $\lambda_{\mathrm{h}} = 18.0\%$. Recently, a multiplier of $\lambda_{\mathrm{h}} = 17.6\%$ has been computed in Nodargi and Bisegna (2021*a*). The value obtained in this dissertation is conservative. However, it presents a difference of 20% to the values obtained in the literature, meaning that further diagram modifications are necessary to achieve a better approximation.

Regarding the crack pattern, a circular crack appears near the dome's base, where the network touches the intrados (blue points). These cracks match the opening in the voussoirs observed in Zessin et al. (2010) and the unilateral cracks claimed in Nodargi and Bisegna (2021*a*). Cracks are also observed near the crown where the network touches the extrados. The references also suggest this as the collapse involves the dome's crown descending and sliding. The hoop forces in the solution vanish, and the diagonal segments activate, bringing the loads down to the supports.

This solution shows how the methodology can be used to investigate admissible stress states considering horizontal load. Unlike the graphical TNA approach from Block (2009), the problem is not limited to gravity loads. Also, even if the horizontal loads applied here are proportional to the self-weight, this fact is not exploited by the analysis, which can compute the problem for general horizontal loads (given that the diagram can transfer the loads in compression to the supports). Nevertheless, horizontal loads add complexity to the model and are especially hard to deal with by keeping the horizontal projection fixed. Future work should also explore additional topologies for the flow of force in this problem, possibly in combination with topology generators such as the ones proposed in Oval et al. (2018).

In the following section, the case of cross vaults is considered, which due to their unsupported edges, require new strategies to update the diagram.

8.3.2 Tilting of cross vaults

The final section of this chapter deals with the horizontal loads in cross vaults. The geometry analysed is identical to the one used in Section 8.2.3, with $t/s = 0.05$, $R/l_0 = 0.50$, and $\beta = 30°$. The base diagram adopted is the cross topology with discretisation level $n_{\mathrm{s}} = 14$ (see Section 6.2).

This problem is challenging due to the unsupported boundaries in the cross vault since horizontal loads can not be applied orthogonally to the edges located in these boundaries. Therefore, the diagram is curved following the Δ-strategy applied in Section 7.2.2 combined with a tapering field in the orthogonal direction (see Section 6.2.3). The base diagram is then modified with $\Delta/s = 5\%$.

Finally, the optimisation for maximising the horizontal multiplier is computed. The maximum value obtained for this problem is $\lambda_{\mathrm{h}}^{\max} = 18.9\%$, meaning that the maximum horizontal load applied to the dome is equal to $P_{\max}/W = 18.9\%$. The solution is depicted in Figure 8.13. In addition, the magnitude of the reaction forces (R_1, R_2) is highlighted in Table 8.4.

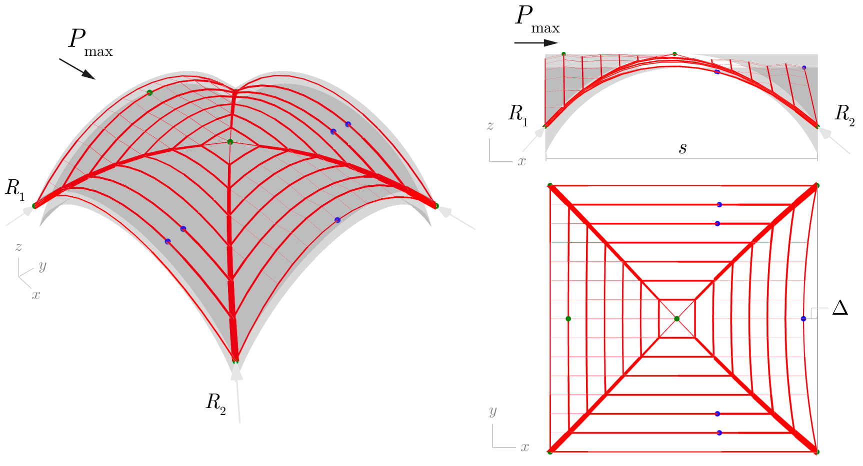

Figure 8.13: Results for the maximum horizontal force $P_{\max}/W = 18.9\%$ applied to the cross vault with a horizontal slide of the nodes of the pattern of $\Delta/s = 5\%$ and a highlight on two reactions R_1 and R_2.

Table 8.4: Reaction forces R_1, R_2 at the highlighted corners of the cross vault subjected to $\lambda_{\mathrm{h}}^{\max} = 18.9\%$.

Reaction	$R_{\mathrm{x},i}/W$	$R_{\mathrm{y},i}/W$	$R_{\mathrm{z},i}/W$
R_1	21.5%	22.0%	24.0%
R_2	-30.9%	26.1%	26.0%

The action of the horizontal forces results in a tilted thrust network, as depicted in Figure 8.13. Consequently, the components of the reaction forces are uneven (Table 8.4). The vertical components of the reaction forces are larger on the side opposite to the applied horizontal load ($R_{\mathrm{z},2}/W = 26\%$)

than on the side facing it ($R_{z,1}/W = 24\%$). The supports on the opposite side take the horizontal forces, with increased $R_{x,2}/W = -30.9\%$. Indeed, the sum of the four reactions in the x-direction results in the reaction to the applied horizontal multiplier $\lambda_h^{max} = 18.9\%$.

Further analysis could be performed to update the topology of this diagram. The only paths currently available to transfer the loads to the supports are the main diagonals, which are now curved thanks to the sliding applied to the nodes. By providing additional paths, this value can be increased.

8.3.3 Stability domain under horizontal loads

The final analysis of this chapter shows how the applications of horizontal loads described here can be combined with the previously studied stability domains (Chapter 7). The geometry and the form diagram from Section 8.3.2 are employed. The vault is now subjected to a horizontal multiplier of $\lambda_h = 10.0\%$, which is inferior to its maximum calculated $\lambda_h^{max} = 18.9\%$, resulting in a Load Safety Factor LSF=1.89. As the vault can withstand $\lambda_h = 10.0\%$, we can draw its stability domain to further analyse its maximum and minimum horizontal thrust states. The stability domain for the cross vault is presented in Figure 8.14, in which states of minimum (T_{min}) and maximum (T_{max}) thrust and minimum thickness (t_{min}) are depicted.

From the analysis in Figure 8.14, we can successfully combine horizontal load and the stability domain. The crack patterns arising even before the horizontal load reaches its maximum are identified by looking at the equilibrium states in the extreme points of the diagram. As discussed in Ochsendorf (2002), the supports are expected to spread out (even if slightly) as the horizontal load increases towards collapse. Therefore, the horizontal load $\lambda_h = 10.0\%$ might induce a state of minimum thrust (T_{min}) owing to the spread of the supports. The crack pattern is highlighted for this case in Figure 8.14, revealing a crack line in the web opposite to the load. Furthermore, the GSF can be computed for this loading case, equal to 1.51. Therefore, the GSF for the horizontal load can be used as an additional metric to the LSF=1.89 computed above.

The results presented in this section show how cross vaults can be analysed against horizontal loads with the present methodology. The results of horizontal loads in general in this chapter are initial and have not been precisely the focus of the work in this dissertation. A more detailed treat-

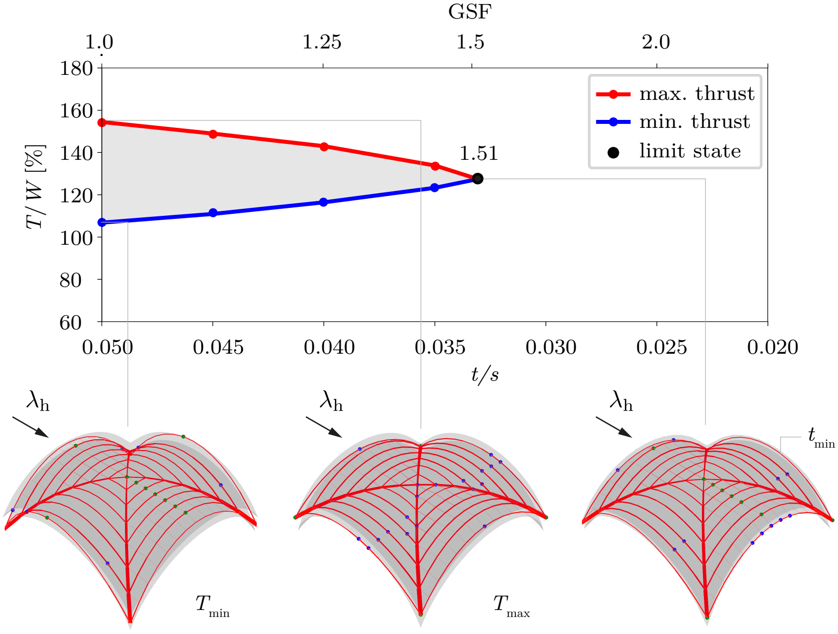

Figure 8.14: Stability domain for the cross vault problem subjected to $\lambda_h =$ 10.0%. Highlight in the thrust network at minimum (T_{min}) and maximum (T_{max}) thrusts and at the limit state, i.e., minimum thickness (t_{min})

ment of the form diagrams should be considered to progress further in this direction. Nevertheless, they are promising since they can be implemented in the same modular framework and applied to general three-dimensional structures.

8.4 Summary

This chapter demonstrates the application of the framework developed to maximise horizontal and vertical applied loads. The results correspond to a lower bound of the collapse loads in masonry structures. Accurately determining these values is critical for masonry assessment to ensure safety over extreme events, such as earthquakes, or to evaluate structures undergoing rehabilitation where new loads might be introduced.

Maximum loads for general three-dimensional geometries are obtained through a direct constrained optimisation in the modular framework developed. Several applications showcase how the method can be applied to typical masonry typologies, such as cross vaults and domes.

The external loads modify the force flow in the structure and require adapting the form diagrams. This chapter has implemented practical strategies to adapt these patterns to the load applied. Compared to the starting diagrams, the adaptation strategies have increased the maximum vertical load estimation by up to 107% in domes and up to 330% in cross vaults.

Applications considering horizontal loads have also been presented. The results obtained for the dome were conservative and were also applied to problems with unsupported boundaries, such as cross vaults.

Besides giving a safe estimate of the collapse loads, the location where fractures are more likely to develop is identified, which could be used to plan maintenance in the structures if needed. The method could be further combined with kinematic tools, performing analysis to compute the development of the suggested collapse mechanisms.

This chapter also showed a combination of the external loads and the stability domains from the previous chapter. This combination enables the study of further admissible states that might arise when the loads are applied so that the supports settle, inducing minimum or maximum thrust states.

The combination of external forces and general support settlements will be further discussed in the following chapter.

Chapter 9

Understanding the effects of foundation settlements

In this chapter, we demonstrate the application of the method developed to the search for admissible internal states arising in masonry structures after the action of prescribed boundary displacements. These foundation displacements represent a significant cause of the collapse of masonry structures. The problem formulation and opportunities for applying TNA are highlighted. A list of relevant applications in two- and three-dimensional structures is presented.

9.1 The problem

9.1.1 Overview

Unlike elastic systems, foundation settlements applied to masonry structures lead to the development of cracks and the creation of rigid macro-blocks (Ochsendorf, 2002). In engineering practice, one of the major challenges when assessing existing structures is how to associate the observed cracks, or pathologies, with foundation settlements (Ochsendorf, 2006; Como, 2013).

This can be done by introducing an energy-based criterion that minimises the structure's complementary energy for a given foundation displacement (Angelillo, 2014). This approach has been applied to a normal, rigid, no-tension (NRNT) material in Angelillo et al. (2018), with applications to 2D structures in Iannuzzo, Dell'Endice, Van Mele and Block (2021); Iannuzzo et al. (2020).

Upper-bound methods have also been employed to study this problem in arches in Zampieri et al. (2018) and semi-circular arches in Coccia et al. (2015). As mentioned in Section 2.2.3, this method assumes the position of the hinges, and a collapse multiplier is computed for that specific hinge consideration. The upper bound of this collapse multiplier can then be estimated by varying the position of the hinges, usually with stochastic methods. However, defining the collapse mechanisms in 3D is a complicated task, as discussed in Scacco et al. (2020).

Therefore, understanding cracks in three-dimensional masonry structures is still an open and challenging question.

9.1.2 Opportunities

A series of opportunities exist to study this problem under the lower-bound, three-dimensional framework developed in this dissertation. The optimisation framework can be coupled with an energy criterion minimising the complementary energy for given foundation settlements.

By searching among infinite admissible stress states, the ones compatible with specific settlements, the locations where cracks are most likely to form following these movements are revealed. The outcome helps to understand the mechanical behaviour of the vaulted masonry structures at the onset of foundation settlements.

Unlike upper-bound procedures as in Scacco et al. (2020), the locations of the hinges do not need to be defined a priori, and the input remains only the structural envelope and the form diagram. Unlike Iannuzzo et al. (2020); Gesualdo et al. (2019), it applies to general three-dimensional geometries. Furthermore, the presented method allows for the computation of the combined effects of external horizontal loads and settlements, which might arise when analysing structures subjected to earthquakes. These would affect the neighbouring supporting structures.

9.1.3 Implementation

The solutions presented in this chapter are computed by minimising the complementary energy introduced in Section 5.4.5. The constraints from limit analysis apply as described in Section 5.3.

The results presented in this chapter have been published in a recent paper by the author in Maia Avelino, Iannuzzo, Van Mele and Block (2022).

9.2 Crack patterns from settlements

This section demonstrates how the proposed approach can be applied to suggest the location in which cracks will form for arches (Section 9.2.1), domes (Sections 9.2.2 and 9.2.3), and vaults (Section 9.2.4).

9.2.1 Analogy on the masonry arch

The first structure to be analysed is a semi-circular arch subjected to a unitary displacement on its right support. It validates the methodology and evidences its intuitive physical result. The geometry of the arch is defined in Figure 9.1.

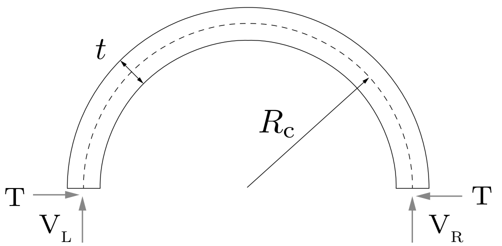

Figure 9.1: Geometry of the arch as a function of the central radius R_c and thickness (t). Reaction forces are decomposed in the horizontal thrust (T) and vertical reactions on the left (V_L) and right support (V_R).

The thickness over (central) radius $t/R_c = 0.20$ is considered for the analysis. The arch is subjected to four sets of settlements $\bar{\mathbf{u}}_i$ applied to the right support: outwards $\bar{\mathbf{u}}_1 = [1, 0]$, inwards $\bar{\mathbf{u}}_2 = [-1, 0]$, downwards $\bar{\mathbf{u}}_3 = [0, -1]$ and upwards $\bar{\mathbf{u}}_4 = [0, 1]$. A linear form diagram with 50 nodes is used in the analysis with supports at both extremities. The self-weight (W) is lumped into the diagram nodes according to its tributary areas after projection in the arch's central geometry (see also Section 5.3.4).

The results are presented in Figure 9.2, highlighting the points in which the thrust line touches intrados and extrados with blue and green dots. When the thrust line touches the intrados (resp. extrados), a crack forms on the extrados (resp. intrados). The obtained value of the objective function, i.e., complementary energy ($\tilde{W}_c$), and the normalised thrust (T) and vertical reaction (V_R) of the right support are presented in Table 9.1.

For the outward and inward displacements (Figures 9.2a–b), the arch as-

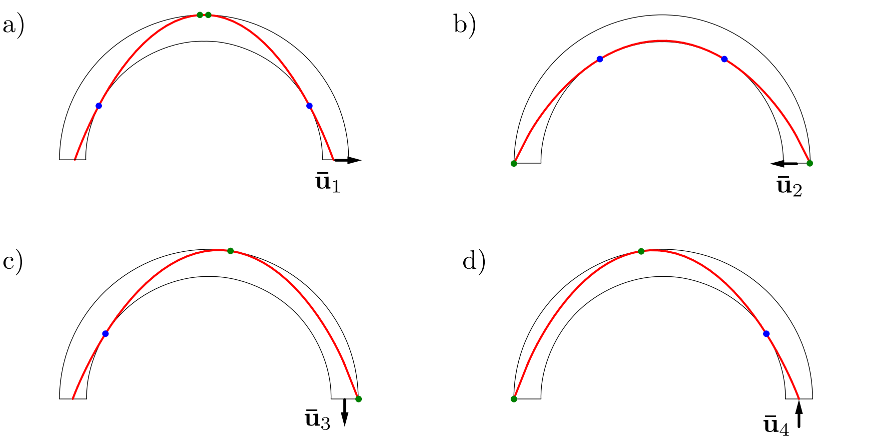

Figure 9.2: Thrust line obtained for the unitary foundation settlement (a) $\bar{\mathbf{u}}_1$, (b) $\bar{\mathbf{u}}_2$, (c) $\bar{\mathbf{u}}_3$, (d) $\bar{\mathbf{u}}_4$ applied to the right support.

Table 9.1: Results of complementary energy $\tilde{W}_c$ and normalised reaction forces for the orthogonal displacements $\bar{\mathbf{u}}_1$– $\bar{\mathbf{u}}_4$.

Displacement	T/W	V_R/W	$\tilde{W}_c/W$
$\bar{\mathbf{u}}_1$	15.8%	50.0%	15.8%
$\bar{\mathbf{u}}_2$	25.5%	50.0%	-25.5%
$\bar{\mathbf{u}}_3$	18.9%	47.7%	47.7%
$\bar{\mathbf{u}}_4$	18.9%	52.3%	-52.3%

sumes the well-known minimum and maximum thrust states (Ochsendorf, 2006; Heyman, 1995; Huerta, 2006). The normalised horizontal reactions are $T_{\min}/W = 15.8\%$ and $T_{\max}/W = 25.5\%$. These solutions correspond to the arch's deepest and shallowest possible thrust lines. For the deepest, an intrados hinge in the apex and two extrados symmetric hinges appear. For the maximum, a pair of hinges appear in the extrados and another in the intrados at the supports.

The downward and upward settlements (Figure 9.2c–d) produce a tilted thrust line with uneven vertical reaction forces. For the downward, passive displacement, the vertical component of the settled support reduces to $V_R/W = 47.8\%$, the horizontal thrust is $T_{\text{down}}/W = 18.9\%$, and the objective function is equal to $\tilde{W}_{\mathrm{c}}/W = 47.7\%$. For the upward settlement, a mirrored thrust line with the same T/W ratio is obtained, and the vertical component of the settled support is increased to $V_{\mathrm{R}}/W = 52.3\%$.

This simple example demonstrates the intuitive results obtained. Only unilateral cracks can form in the arch, i.e., cracks opening at the opposite side to the touch-point. In the following sections, three-dimensional structures are revisited, resulting in more complex crack patterns.

9.2.2 The masonry dome

In this section, a hemispheric dome is analysed. The geometry of the dome considers $t/R_{\mathrm{c}} = 0.10$. A radial diagram comprising $n_{\mathrm{M}} = 20$ meridians and $n_{\mathrm{P}} = 16$ hoops is adopted in the analysis. The diagram is depicted in Figure 9.3a, with a highlight on the independent edges and supports.

The dome is subjected to two sets of unitary foundation displacements. A spreading displacement $\bar{\mathbf{u}}_1$ (Figure 9.3b), and a splitting displacement $\bar{\mathbf{u}}_2$ (Figure 9.3c) dividing the dome into two halves.

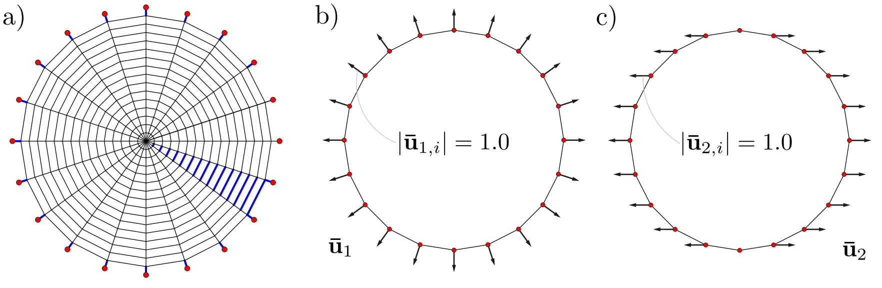

Figure 9.3: (a) Radial form diagram with $n_{\mathrm{M}} = 20$ meridians and $n_{\mathrm{P}} = 16$ hoops showing independent edges (blue) and supports (red). (b) Unitary outward $\bar{\mathbf{u}}_1$ and (b) unitary splitting $\bar{\mathbf{u}}_2$ displacements applied to the $n_{\mathrm{b}} = 20$ supports.

Figure 9.4 shows the minimum of the complementary energy once the spreading displacement $\bar{\mathbf{u}}_1$ has been applied to the radial diagram. The normalised objective function reported is $\tilde{W}_{\mathrm{c}}/W = 19.9\%$. The solution matches the minimum thrust solution obtained in Section 7.3.1. Likewise, the objective function obtained matches the normalised horizontal thrust $T_{\mathrm{min}}/W = 19.9\%$ reported in 7.3.1.

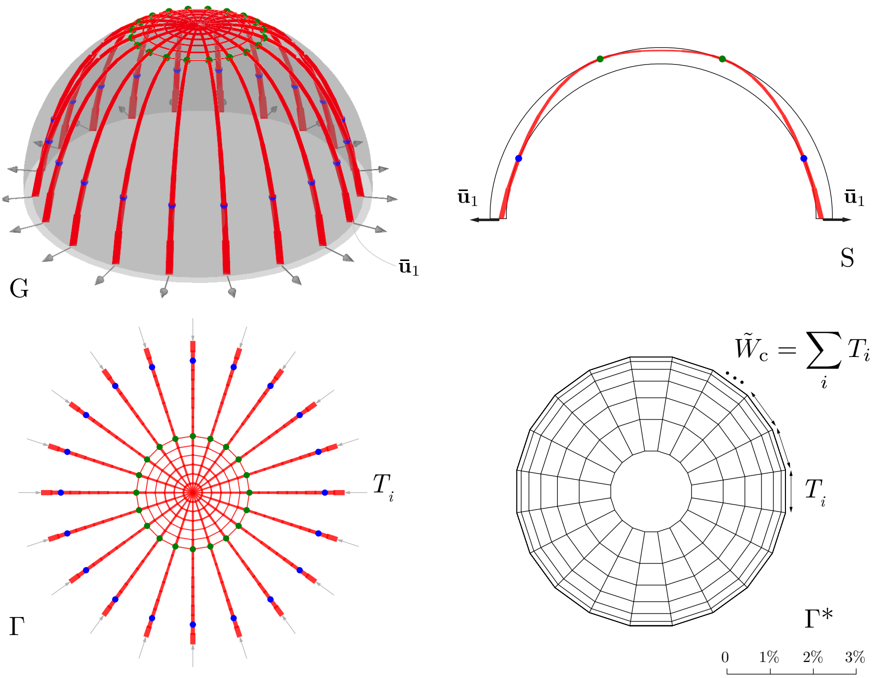

Figure 9.4: Thrust network (G), main cross-section (S), form (Γ) and force (Γ*) diagrams for the minimum complementary energy in the dome assuming the outward displacement $\bar{\mathbf{u}}_1$ and radial diagram.

The internal force distribution presents a bi-axial compression cap in the upper part of the dome and a uniaxial stress field near the supports. Two cylindrical crack lines are identified by neighbouring vertices touching the intrados (blue) and the extrados (green). The internal force distribution for this solution is shown by looking at its reciprocal force diagram (Γ*). In Γ*, the lengths of the perimetral edges measure the magnitude of the radial horizontal thrust emerging (e.g., T_i) and, therefore, the perimeter of Γ* corresponds to $\tilde{W}_c$ for the spreading displacement. For this reason, the solution for the support spreading and minimum thrust match.

The solution in Figure 9.5 shows the thrust network obtained for the radial diagram under splitting displacement $\bar{\mathbf{u}}_2$. The normalised objective function reported is $\tilde{W}_c/W = 11.3\%$. The settlement induces the two halves of the dome to tilt inwards, increasing the pressure onto the central strip of the dome orthogonal to the settlements, which assumes a maximum thrust state. The increased force is evident by the increased length of the corresponding edges in Γ^* (see T_i). For the split displacement $\bar{\mathbf{u}}_2$, $\tilde{W}_\mathrm{c}$ corresponds to the sum of the $x-$components of the reaction forces, which is represented by the height of Γ^*, as noted in Figure 9.5. The new internal force distribution decreases the height of the diagram when compared with Figure 9.4.

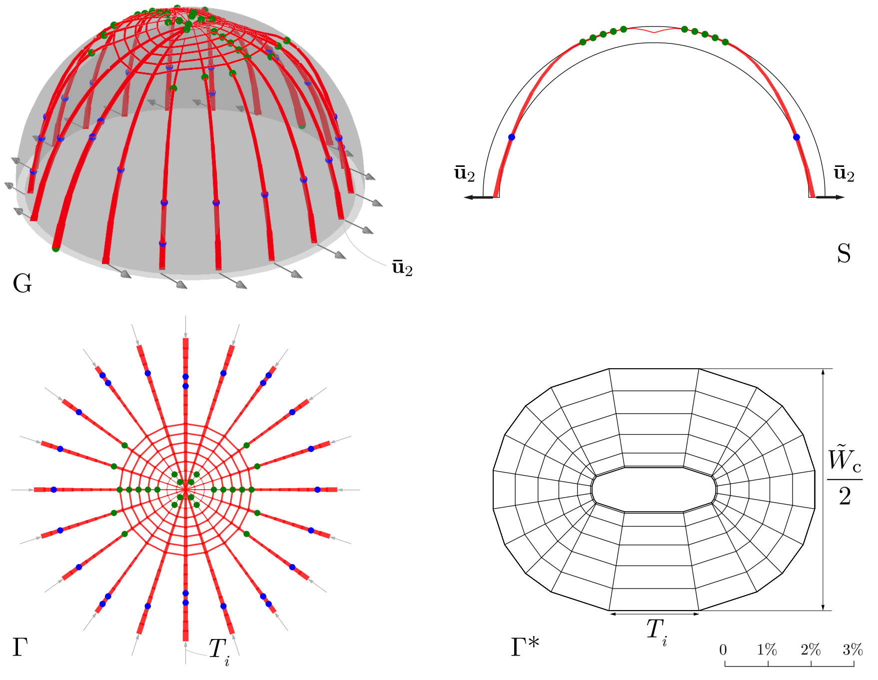

Figure 9.5: Thrust network (G), main cross-section (S), form (Γ) and force (Γ*) diagrams for the minimum complementary energy in the dome assuming the splitting displacement $\bar{\mathbf{u}}_2$ and radial diagram.

Finally, the solutions presented in this section connect the results of minimum thrust and horizontal spreading displacement in the supports and illustrate how a new range of phenomena can be modelled by considering general foundation displacements. The form diagram is modified in the following section to better catch the new behaviour induced by the prescribed displacement.

9.2.3 Form diagram exploration

Different form diagrams are studied for the dome problem subjected to the splitting displacement (Figure 9.3c). A topology change is proposed to modify the direction of the meridional members (Oval et al., 2018). The radial diagram's central pole (P) is removed, and a pair of two-valent singularities (S) is introduced. Consequently, the circular hoops become oval, and the meridians arrive at the support oblique to the prescribed support displacement. This modification is shown schematically in Figure 9.6.

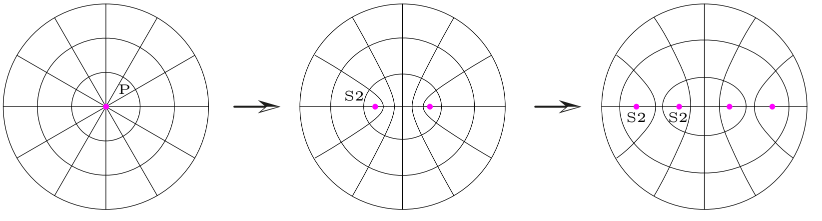

Figure 9.6: Topology modification performed by removing the pole (P) and adding a pair of two-valent (S2) singularities. Other singularities can be added, reducing the number of meridians going to the centre.

The logic described in Figure 9.6 is applied to the diagram in Figure 9.3a. The number of supports ($n_\mathrm{b} = 20$) and the same discretisation level to the central horizontal meridian (16) are kept. The diagrams obtained are presented in Figure 9.7a–d, with highlights on the set of independent edges (blue) and support points (red). An overview of the number of edges m and independent edges k for the patterns are presented in Table 9.2.

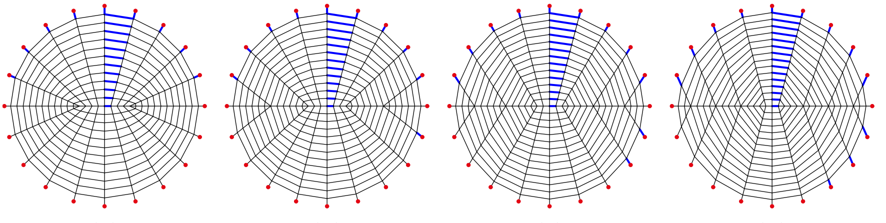

(a) (b) (c) (d)

Figure 9.7: Patterns (a)–(d) resulting after the topology change.

The modified patterns are analysed for the splitting displacement. The results of normalised complementary energy $\tilde{W}_c/W$ and the difference, compared to the results obtained with the radial diagram, are also shown in Table 9.2.

From the values of complementary energy, pattern (d) behaves the best. For this diagram, a reduction of 40% is obtained, with $\tilde{W}_c/W = 6.8\%$. Diagrams (a)–(c) also reduce the objective function by at least 13%.

Table 9.2: Results after a topology variation for the problem of the dome under splitting displacement.

Pattern	m	k	$\tilde{W}_c/W$	diff. (%)
a	468	21	9.9%	-13%
b	458	23	9.6%	-15%
c	424	25	8.5%	-25%
d	430	27	6.8%	-40%

The geometry of the optimal thrust networks for the new patterns is presented in Figure 9.8, with its form (Γ) and force Γ^* diagrams. The inclined meridians get activated in the solutions obtained, enabling an alternative force flow oblique to the applied settlement. This new force flow elongates Γ^* and reduces its height, and hence $\tilde{W}_c$. Indeed, the reduction in the objective function noted in Table 9.2 is verified graphically by the incremental decrease in the height of the force diagrams from (a) to (d). Regarding the internal force distribution, hoop forces also vanish toward the supports, suggesting possible inclined meridian cracks. A curved crack line appears near the base, equivalent to the cylindrical cracks seen for the spreading displacement, but these are no longer symmetrical. A depression in the network is observed in the central (vertical) strip, as this portion of the structure concentrates the loads due to the two halves leaning inwards. In all diagrams, near this central strip, the network touches the extrados suggesting crack lines along this region.

Based on this topology exploration, the solution in Figure 9.8d represents an internal stress state better fitting for the imposed spitting displacement. More importantly, the procedure described here enables the exploration of different possible force flows in connection with a given masonry geometry and settlement. The topology search was non-exhaustive, and further diagrams can still be proposed for this problem, further decreasing the complementary energy value.

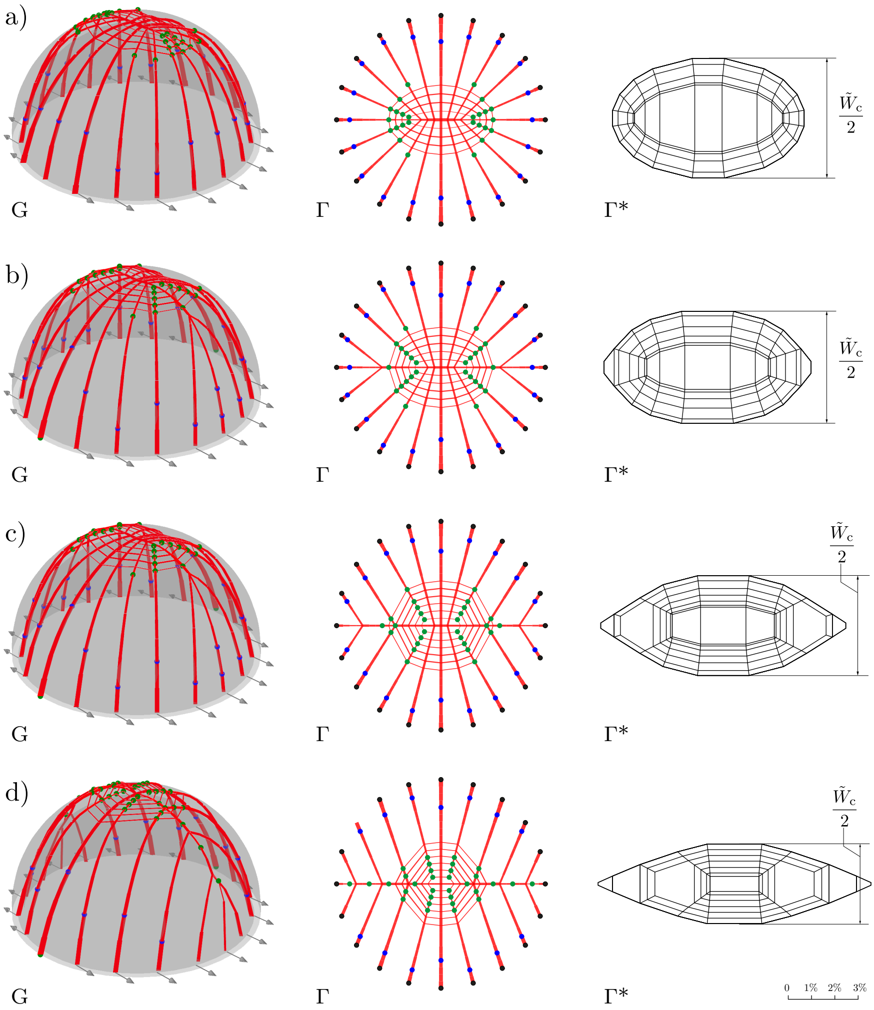

Figure 9.8: Thrust network (G), form (Γ) and force (Γ*) diagrams for the dome subjected to displacement $\bar{\mathbf{u}}_2$ for diagrams (a)–(d).

In the following section, cross and pavilion vaults are also investigated under general foundation displacements, and a discussion on their crack pattern is presented.

9.2.4 Cross and pavillion vaults

In this section, foundation displacements are applied to cross and pavilion vaults. The results show the locations where the crack patterns are more likely to form.

The geometries are obtained following the parametrisation presented in Section 6.3.1. The vaults are generated through the intersection of two barrel vaults with the same semicircular profile ($R/l_0 = 0.5$), with a springing angle $\beta = 30°$ and a thickness over span $t/s = 0.05$.

The orthogonal diagram topology is used to analyse both geometries (see Section 6.2.1), the difference being that for modelling the pavillion vault, the boundary of the pattern is continuously fixed. Consequently, more DOF (and independent edges) exist. This diagram is depicted in Figure 9.9a. For the corner-supported cross diagram, readers are referred to Figure 7.4.

The displacement field applied to the cross vault is depicted in Figure 9.9b and corresponds to a unitary corner horizontal outward displacement $\bar{\mathbf{u}}_1$.

The displacement field applied to the pavillion vault problem is a unitary outward sliding of one of its line-supports $\bar{\mathbf{u}}_2$ and is depicted in Figure 9.9c.

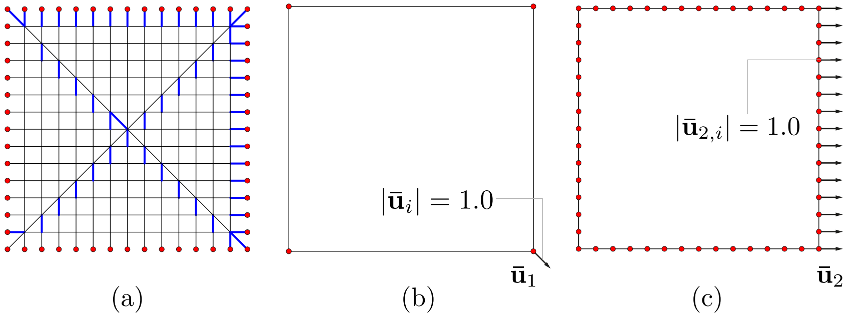

Figure 9.9: (a) Orthogonal pattern used in the pavilion vault analysis with highlights on supports and independent edges. (b) Outward displacement $\bar{\mathbf{u}}_1$ applied to the corner of the cross vault. (c) Line horizontal outward displacement $\bar{\mathbf{u}}_2$ applied to the pavillion vault problem.

The results for these two analyses are depicted in Figures 9.10 and 9.11.

The minimum complementary energy for the cross vault problem is depicted in Figure 9.10. The value of the normalised objective function is

$\tilde{W}_c/W = 20.4\%$. The outward diagonal displacement reflects a spreading of the webs crossing the pulled diagonal. This spreading results in two crack lines crossing that diagonal, obtained by connecting adjacent vertices touching the extrados (green). Uneven horizontal thrusts are observed, decreasing the horizontal thrust in the displaced corner (T_i) and increasing the pressure applied to the opposite diagonal (T_j). This uneven horizontal reaction is reflected in the elongated shape of Γ^*. Graphically, the value of $\tilde{W}_c$ corresponds to the length of T_i in Γ^* as the horizontal component of that reaction is parallel to the foundation displacement.

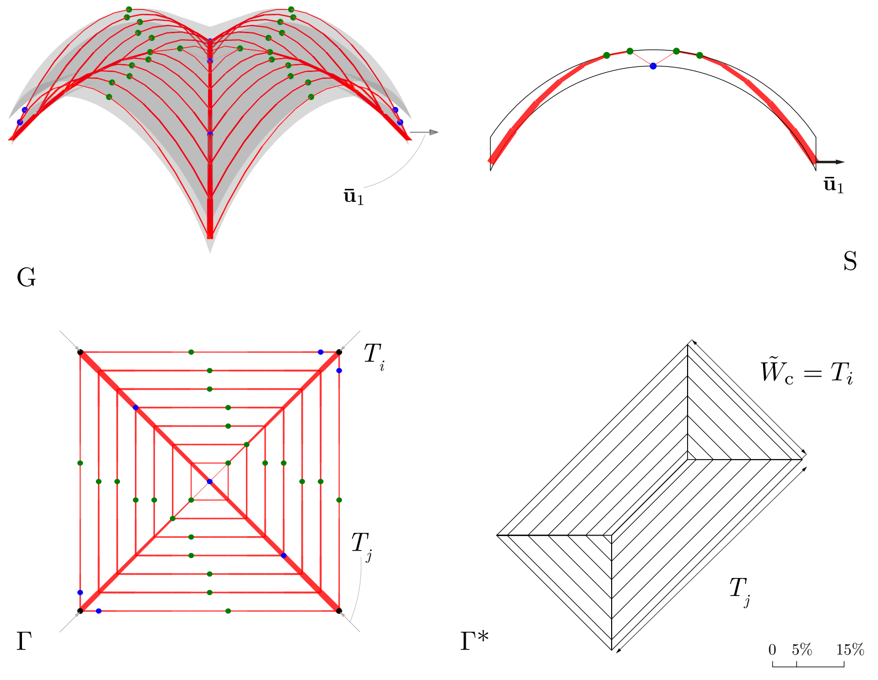

Figure 9.10: Thrust network (G), main cross-section (S), form (Γ) and force (Γ^*) diagrams for the minimum complementary energy in the cross vault for the corner displacement $\bar{\mathbf{u}}_1$ and orthogonal diagram.

Figure 9.11 depicts the minimum complementary energy for the pavillion vault problem. The value of the normalised objective function is $\tilde{W}_c/W = 2.6\%$. The support movement suggests crack lines in the intrados on the web adjacent to the settlement. The force paths parallel to the settlement assume a minimum thrust behaviour (e.g., T_i) or vanish. Consequently, the loads flow in the perpendicular direction in which the force paths assume a maximum thrust configuration (e.g., T_j). This is evident in Γ^*, where the magnitudes of T_i and T_j are highlighted, and the diagram assumes an elongated shape having a low height and hence low $\tilde{W}_c$.

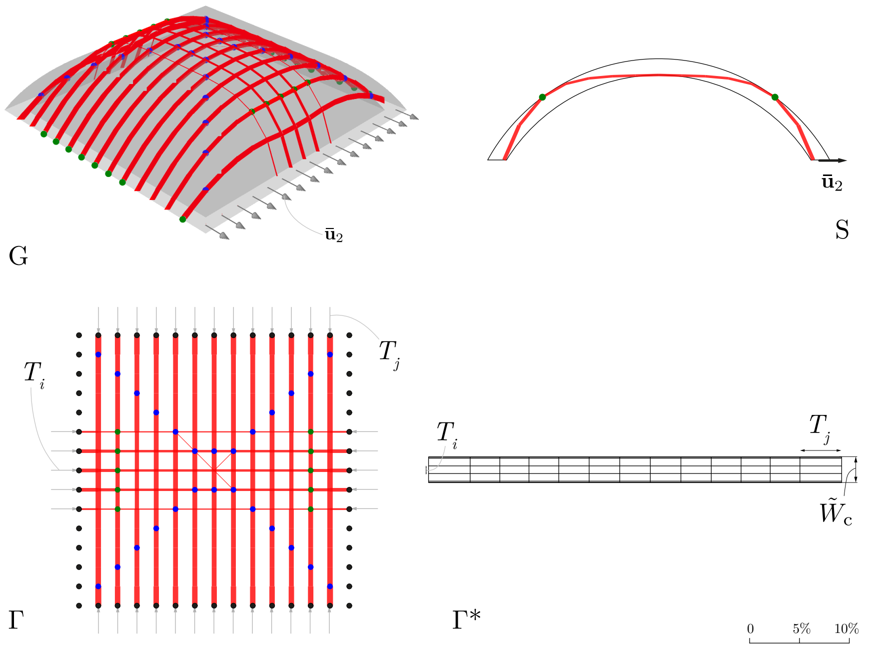

Figure 9.11: Thrust network (G), main cross-section (S), form (Γ) and force (Γ^*) diagrams for the minimum complementary energy in the pavillion vault for the line settlement $\bar{\mathbf{u}}_2$ and considering the orthogonal continuously supported diagram.

A comparison with the results reported in this section can be made with works in the literature using Discrete Element Modelling (DEM). For the cross vault problem, the crack patterns described in the webs in Figure 9.10 match the results obtained in McInerney and DeJong (2015). The problem of the pavillion vault subjected to the leaning of one of its supporting walls has been recently studied in Dell'Endice et al. (2021) in which the cracks suggested in the webs (see Figure 9.11) have also be encountered. Still, for this work, the resultant contact forces in the section parallel to the settlement are depicted and are equivalent to the sectional thrust line shown in Figure 9.11S. In these studies, the structures are displaced until they collapse. Indeed, this is a major difference from the results obtained with TNA. Here, only the crack pattern at the onset of the displacement can be obtained, and the nonlinear effects of displacing the geometry are not considered.

Finally, this section shows how specific compatible admissible solutions can be obtained by coupling TNA and the complementary energy formulation. This can be used to improve the understanding of the crack patterns arising in three-dimensional structures and to search for specific stress states on these structures. In the following section, we will show how the complementary energy can be combined with concepts presented in previous chapters, such as the stability domain.

9.3 Stability domain for general settlements

This section revisits the stability domain concept, taking advantage of the new possibilities presented by imposing general foundation displacements. The stability domain obtained for a rotation in one support of a circular arch is presented in Section 9.3.1, and the domain obtained for a rotation in one support of a cross vault is presented in Section 9.3.2.

9.3.1 Arch under rotational support displacement

The semi-circular arch described in Section 9.2.1 is revisited. The unitary support displacement is parametrised with the rotational angle α. The foundation displacement vector becomes then $\bar{\mathbf{u}}(\alpha) = [\cos\alpha, \sin\alpha]$. The rotation angle is evaluated into 36 positions, having an interval of 10°. The angle α is then computed for the interval $\alpha \in [0°, 10°, \ldots, 350°]$.

The minimum complementary energy is computed for each displacement position. The results are depicted in the graph of Figure 9.12 in which the x-axis shows the normalised horizontal thrust (T/W) and the y-axis shows the normalised vertical reaction in the displaced corner (V_R/W).

In the graph of Figure 9.12, each vertex (a)–(f) corresponds to one thrust line mechanism. From the 36 positions of the vector $\bar{\mathbf{u}}(\alpha)$ computed, six unique corners appear in the diagram, which means that the thrust line assumes the same geometrical configuration and crack position for a range of the angle $[\alpha_{\min}, \alpha_{\max}]$. This range is illustrated graphically next to each vertex in Figure 9.12 and is indicated in Table 9.3.

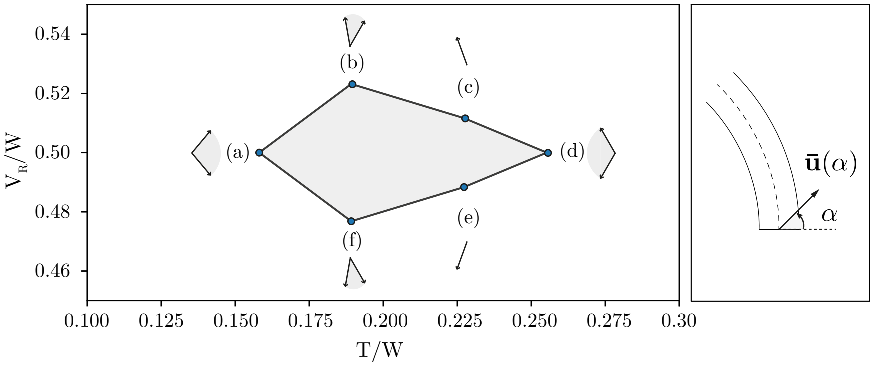

Figure 9.12: Left: Stability domain for the minimum complementary energy obtained rotating the unitary vector $\bar{\mathbf{u}}(\alpha)$. Right: Schematic representation of the unitary vector $\bar{\mathbf{u}}(\alpha)$ and rotation α

Table 9.3: Intervals of mechanism obtained by minimising the complementary energy $\tilde{W}_c$ for the rotating displacement $\bar{\mathbf{u}}(\alpha)$.

Mechanism	$\alpha_{\min}$	$\alpha_{\max}$	T/W	V_R/W	$\tilde{W}c/W$
(a)	$-50°$	$50°$	15.8%	50.0%	15.8%
(b)	$60°$	$100°$	18.9%	52.3%	-52.3%
(c)	$110°$	$110°$	22.7%	51.2%	-55.9%
(d)	$120°$	$240°$	25.5%	50.0%	-25.5%
(e)	$250°$	$250°$	22.7%	48.8%	38.1%
(f)	$260°$	$300°$	18.9%	47.7%	47.7%

The mechanisms in (a) and (d) correspond to the minimum and maximum thrust solution depicted in Figure 9.2a-b. The mechanisms (b) and (f) correspond to the up and down displacement fields depicted in Figure 9.2c-d. The arch's stability to the rotational displacement correlates with the area of the diagram highlighted in grey in Figure 9.12. When the thickness of the arch is reduced, this domain reduces similarly to the domains from Chapter 7. The domain reduces to a point for the limit thickness $t_{\min}$.

The following sections will explore this stability domain for a cross vault.

9.3.2 Cross vault under rotational displacement

In this section, the cross vault from Section 9.2.4 is revisited. The structure is now subjected to a rotational support settlement contained in the plane of the vault's diagonal. The unitary displacement is rotated on that plane with the angle α. The vector is evaluated in 36 positions with $\alpha \in [0°, 10°, \ldots, 350°]$. For each position, the complementary energy problem is computed assuming two form diagrams: the cross and fan corner supported diagrams depicted in Figure 7.4. The result for each support displacement is plotted in the graph in Figure 9.13. This graph reports the normalised vertical (V_i/W) and horizontal (T_i/W) reactions for the rotated support i. The results referring to the cross (resp. fan) diagram are shown in blue (resp. orange). The solution in selected points (a)–(d) is highlighted, and the thrust network solution is presented, showing the obtained crack pattern.

From the results in Figure 9.13, we observe that the domain of stability obtained with the cross diagram for this geometry is larger than the one obtained with the fan diagram. The fan's domain is a subset of the domain obtained with the cross diagram. Hence, the cross force flow will likely form under the support displacements studied. The analysis with the λ-parametrisation (see Section 7.3.2) was also executed for this problem, but the topologies obtained were all subsets from the cross diagram, i.e., within the blue domain.

The domain obtained with the cross diagram has 17 vertices, meaning that the 36 settlements studied resulted in 17 unique networks. Four of them are presented in Figure 9.13 noted as (a)–(d). The angle range for which this displacement occurs is also highlighted.

Point (a) corresponds to the outwards solution from Figure 9.10, this network is the solution for $\alpha \in [-30°, 60°]$.

Point (b) is the minimum overall vertical reaction force and occurs for $\alpha = 270°$. The thrust network obtained is tilted, increasing the vertical reactions in the opposite diagonal, resulting in cracks in the intrados of the diagonal pulled.

Point (c) reports the maximum horizontal thrust and occurs for $\alpha \in [150°, 240°]$. The network obtained corresponds to a mechanism for which the diagonal support is pushed inwards, suggesting cracks on the web's extrados near the displaced support and in the intrados near the keystone.

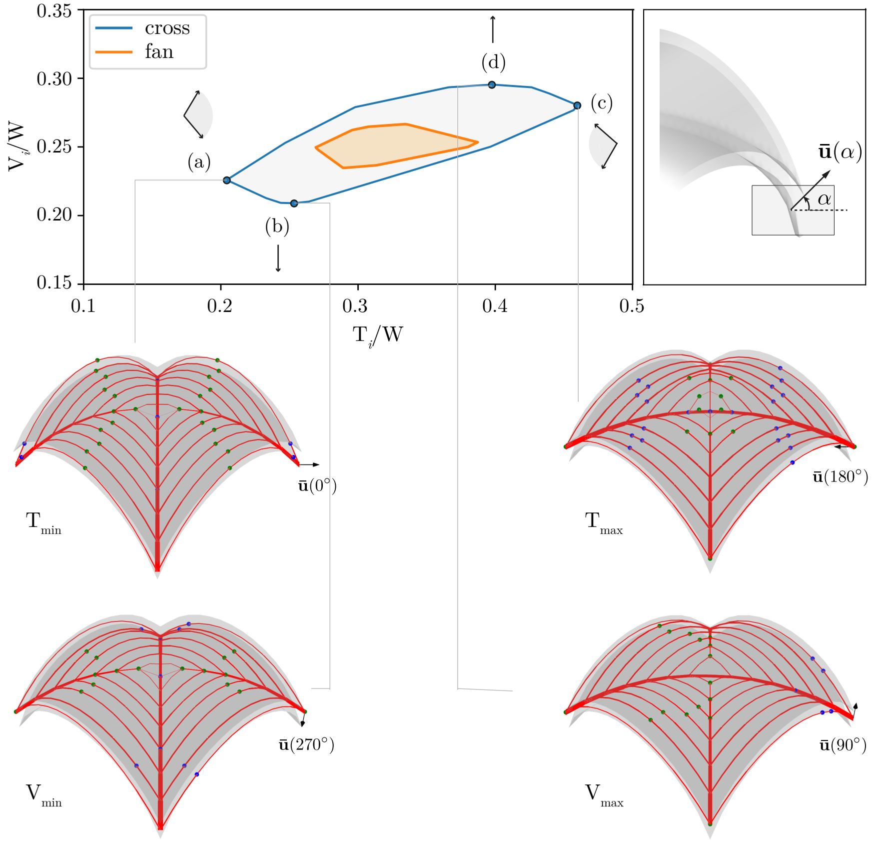

Figure 9.13: Stability domain for the cross vault studied under a rotational support displacement. Highlight on selected solutions from this diagram, corresponding to (a) minimum T_{min} and (c) maximum T_{max} thrusts, and (b) minimum V_{min} and (d) maximum V_{max} vertical reactions. The settlement applied $\bar{\mathbf{u}}(\alpha)$ is reported for each state highlighted.

Point (d) is the maximum overall vertical reaction force and arises for a displacement of the supports upwards $\alpha = 90°$. The resulting network suggests cracks in the extrados near the displaced support and in the intrados of the opposite webs.

For part of this domain, the mechanisms are active, i.e., occurs with the supports pushing the vault, which is rare. To check if the displacement is active or passive, it suffices to look at the objective function's value. When $\tilde{W}_\mathrm{c} > 0$ (resp. $\tilde{W}_\mathrm{c} < 0$), the displacement is passive (resp. active), i.e., displacements (a), (b) (resp. (c), (d)), in Figure 9.13.

Therefore, this section shows that the complementary energy investigation can be combined with the metrics provided by the stability domain from Chapter 7. This combination offers a novel and powerful way to investigate the admissible equilibrium domain for vaulted masonry structures subjected to general foundation displacements.

The following section combines the energy criterion with the application of horizontal loads.

9.4 Combined effect of settlements and horizontal loads

This section revisits the pavillion vault from Section 9.2.4 to show the coupled effects of horizontal loads and foundation settlements.

The pavillion vault is evaluated under the same foundation line displacement $\bar{\mathbf{u}}_2$ applied in Section 9.2.4, but now simultaneously subjected to a horizontal external load $\mathbf{p}_\mathrm{h}^\mathrm{ext}$ $[2n \times 1]$.

The horizontal external load is applied to the network's vertices in the $x-$direction. For each vertex, the load applied to the $x-$direction has the same magnitude as its lumped self-weight. This horizontal external load is multiplied by the horizontal load multiplier $\lambda_\mathrm{h} = 30\%$.

Horizontal load multipliers are often used to approximate the effect of earthquakes in masonry vaults (DeJong, 2009). By combining settlements and horizontal loads, e.g., the leaning of supporting walls during an earthquake can be modelled. One could associate this displacement $\bar{\mathbf{u}}_2$ imposed here, e.g., to the leaning of a not-properly supported wall during an earthquake.

The minimum complementary energy solution for the pavillion vault problem with $\lambda_\mathrm{h} = 0.30$ is depicted in Figure 9.14. The objective function value is $\tilde{W}_\mathrm{c}/W = 28.9\%$. The thrust network obtained is tilted against the horizontal loads, as shown in the main section (Figure 9.14S). Furthermore, the loads flow orthogonally to $\bar{\mathbf{u}}_2$ and to the corners, alleviating the thrust acting on the displaced support.

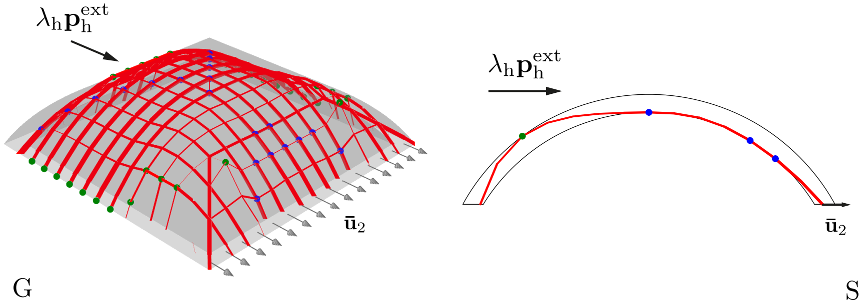

Figure 9.14: Results obtained for the pavillion vault subjected to line support outward displacement $\bar{\mathbf{u}}_2$ and horizontal load with a multiplier $\lambda_h = 30\%$ for an applied horizontal external load $\mathbf{p}_h^{ext}$. Left: Perspective and right: main sectional view.

This solution not only shows that the pavillion vault studied can withstand the horizontal loads applied, but it also enables an exploration of the domain of admissible solutions for particular movements of the supports. This gives a full range of possibilities to engineers facing complex problems in which the foundation might displace under the action of external loads. For this problem, further optimisation and variation of the form diagram topology could be envisaged to model the reduction of the thrust over the settled supports. Another way to exploit the present solution is using the observed crack pattern to inform displacement-based methods that could then predict the mechanism evolution of the structure over a continuous spreading of the supports.

9.5 Summary

This chapter applied the methodology developed in this dissertation to determine the effects of foundation settlements in masonry structures. When the settlements arise, the internal equilibrium state of the solution changes. This change can be modelled by coupling the minimisation of the complementary energy with the constrained optimisation framework from Chapter 5. This combination offers a new range of possibilities for engineers seeking to model settlements in masonry, which are common because of their high self-weight, long-term effects, or applied external loads.

Several problems in common masonry typologies have been analysed. The results suggest the location where cracks might arise. The points where the network touches the intra- or extrados indicate unilateral cracks in the model. These unilateral cracks are seen, e.g., in the arch. Further cracks arise at portions where the network's compressive forces vanish, indicating possible "wrinkle" fractures, or smeared cracks, as in the dome. For 3D problems, an indication of crack lines is provided by connecting neighbouring vertices touching sectional limits.

In this chapter, the minimum complementary energy solutions have been combined with the stability domain concept. Doing so enables a measure of the stability, or fragility, for a given set of foundation displacements, enabling a comparison among different models and force flows.

Finally, this chapter also described the combined effects of applying horizontal loads and subjecting the structure to foundation displacements. It shows the range of applications of the method, able to analyse multiple relevant assessment problems in masonry structures.

This chapter closes the results of this dissertation. A summary of the main contributions to this work is presented on the following pages.

Part IV

Conclusions

Chapter 10

Conclusions

This chapter summarises the contributions of the work, lists its main limitations, and provides an outlook for future research in the field. A final reflection is also provided, highlighting the impact of the present work.

10.1 Contributions

This section lists the main contributions of this work following the research objectives from Chapter 3.

10.1.1 Robust search of admissible stress states

This work developed *Thrust Network Optimisation* (TNO), a modular multi-objective optimisation framework that enables the search of admissible stress states in masonry structures. This framework equips Thrust Network Analysis (TNA) (Block, 2009) with the procedures necessary to find specific equilibrium states relevant to practical assessment scenarios.

This search is encoded in a nonlinear constrained optimisation problem (NLP) described analytically in this dissertation. By extending TNA with a robust optimisation procedure, TNO becomes a novel flexible lower-bound assessment tool. The tool is especially suitable for practical applications due to its independence of mechanical parameters and specific structural stereotomy. The analysis requires only the structural envelope of the masonry and an assumed force pattern as inputs. This input is well adapted to the data available in typical assessment projects, which often come from geometric surveying.

Among the specific equilibrium states that can be obtained with TNO are the determination of the minimum and maximum horizontal thrusts, the maximisation of the structure's Geometric Safety Factor (GSF), the computation of maximum horizontal and vertical collapse loads, and the search for equilibrium states compatible with foundation displacements. The framework developed enables all these analyses with a single approach.

The analyses in TNO are executed considering a fixed horizontal projection of the equilibrium networks, i.e., a fixed form diagram. Fixing the form diagram reduces the indeterminacy of the problem, resulting in an efficient formulation of the NLP. It comes, nevertheless, with the cost that the diagram must be carefully selected.

A new algorithm to automatically identify the diagram's degrees of freedom has been developed for the fixed topology approach. It is based on the computation of sequential Singular Value Decomposition (SVD) of the problem's equilibrium matrix. This procedure is general and enables the analysis with different topologies.

The lack of such a robust, flexible optimisation framework has prevented TNA from being applied in practical masonry assessment scenarios. Building on TNA's simplicity and acceptability as a discrete equilibrium-based lower-bound method, the contributions in this dissertation bring it one step closer to being a relevant assessment tool for engineering practice.

10.1.2 Exploring and quantifying force patterns

Given the discrete equilibrium formulation, the solutions obtained with TNA depend on the form diagram's geometry, topology, and support condition. Finding suitable form diagrams is especially challenging when assessing existing structures. In these cases, the diagram should follow the structure's specific geometric and mechanic features, such as ribs, creases, curvature, openings, boundary conditions, externally applied loads, and settlements.

In this work, analysing different asymmetrical form diagrams is possible, and general masonry geometries can be considered. Regarding the modifications of the form diagram for a given problem, heuristics have been developed to adapt the pattern to the geometric features and loading cases.

More importantly, this work enables the comparison of multiple diagrams for the same problem by introducing quantitative measures, such as maximising their GSF, maximising applied loads, or comparing the size of their stability domains.

The results from this dissertation reinforce that infinite equilibrium states develop in masonry structures depending, e.g., on the loads to which they are subjected or the foundation displacements applied to them. This change in the internal force flow often entails a new internal force distribution requiring an update in the form diagram. While an exploration of the infinite (and discrete) space of topologies is beyond the scope of this thesis, the procedure for evaluating the stability level combined with the pattern exploration is a novel and powerful tool to visualise and compare different patterns.

10.1.3 Computing the level of stability

This work contributes to quantifying the level of stability for vaulted masonry structures. As discussed, finding one admissible stress state informs whether or not the structure is safe, but it does not provide information about its level of stability. For practical assessment scenarios, determining the latter is crucial.

Even if this concept from limit analysis is well-known, its application to general three-dimensional masonry structures has been limited. This work contributes by analysing general vaulted structures by drawing their stability domain and computing their GSF.

Through the analysis using the stability domain, a new perspective is provided on the classical debate about the force flow in Gothic vaults, as in the overview in Huerta (2009), after Abraham (1934). The loads in Gothic cross vaults are in constant change, following, e.g., foundation settlements induced by the surrounding elements or additional imposed loads, and can not be assumed fixed for a given geometry.

The introduction of the stability domain in this thesis represents not only a novel way to visualise and quantify the level of stability but provokes a reflection on the admissible equilibrium space that the lower-bound analysis can not yet capture. Other researchers can further explore the proposed stability domain to demonstrate how novel methods compare with the present work and the literature in general. Incidentally, the stability domains from the analysis at Chapter 7 initially published in Maia Avelino, Iannuzzo, Van Mele and Block (2021*c*) have been revisited and enlarged in Nodargi and Bisegna (2022).

10.1.4 Estimating collapse loads in masonry

This work has also contributed to computing a lower bound of the vertical and horizontal collapse loads in vaulted masonry structures with applications to a hemispheric dome and vaults.

Beyond determining a conservative approximation of the collapse loads, the analysis with TNO detects the locations where cracks are more likely to form in the structure. By revealing the crack locations in the models, these can be compared against observed cracks in the structure occurring after additional externally applied loads are introduced, e.g., after a repurposing or a retrofit of an ancient existing building.

Moreover, this dissertation provides a mathematical formulation to maximise non-proportional horizontal load multipliers. These analyses are especially challenging for the current fixed diagram approach that needs to be updated so the loads can travel to the supports. Nevertheless, in Chapter 8, solutions are achieved by introducing pragmatic modifications to the form diagram, such as adding diagonals and sliding the nodes horizontally. These initial results are promising since horizontal multipliers can model simplified action of earthquakes in masonry structures (DeJong, 2009), which is a topic of utmost importance for heritage conservation in seismic areas (Funari, Mehrotra and Lourenço, 2021).

10.1.5 Investigating foundation settlements

This work has developed a framework to relate general foundation settlements to possible three-dimensional crack pattern locations in the structure. Due to masonry's discrete nature and unilateral behaviour, cracks appear following foundation displacements. Cracks are indicated in the models by the points in which the thrust network touches intrados and extrados (unilateral cracks) and by portions of the structure, where forces vanish, indicating smeared cracks.

This work introduces an energy-based criterion that minimises the complementary energy in thrust networks for a given foundation displacement. By searching among the infinite admissible stress states, the ones compatible with specific settlements, the locations where cracks are most likely to form following these movements are revealed. The outcome helps to understand the mechanical behaviour of the vaulted masonry structures without the need to previously define the possible crack lines as it would be necessary when adopting upper-bound approaches.

10.1.6 Collaborative open-source implementation

Beyond providing the mathematical formulation and algorithmic description of the procedures included in TNO, the methodology of this dissertation has been implemented in an open-source Python package named *compas_tno*.

This package is freely available (Maia Avelino, 2023), enabling future collaboration and the continuous development and improvement of the procedures described in this thesis by other researchers.

Moreover, sharing the implementation enables it to be used by practitioners as a practical analysis tool for masonry structures. The simple and comprehensive TNA approach has the potential to be quickly adopted in practice.

The package has been developed independently of any CAD software such that further developments could create user interfaces for different CAD applications or even distribute the numerical implementation of the package as standalone software.

10.2 Limitations

The main limitations of the present approach are listed in this section.

- Lack of a pattern generation strategy:

  The results of the analysis are dependent on the pattern selected. Therefore, alternative diagrams must be sought if the chosen pattern is not feasible. While heuristic and parametric diagrams have been used, a pattern generation strategy should still be added to the current framework. This generation could be guided by the diagram comparisons and metrics presented in this work.

- Nonlinear formulation:

  The optimisation problem solved in this dissertation is nonlinear. Therefore, its solvability is prone to variations in the starting point, scaling problems, and convergence errors. Moreover, the formulation prevents the problem from scaling up to highly refined meshes, e.g., with more than 2000 edges. Nevertheless, strategies to improve the solvability and avoid pitfalls in the optimisation have been presented.

- Precision on the selection of independent edges:

The independent edges (or DOF) selection on the form diagrams relates to the nullspace of the equilibrium matrices. Therefore, this selection is prone to tolerance errors in identifying the null singular values, which might arise if the matrices are badly conditioned. Further studies on varying this precision threshold are needed to improve and extend the current formulation.

- Disregard of the joints among the blocks:

  The approach adopted does not consider the joints among the blocks, disregarding possibly beneficial effects of friction and interlocking associated with the structural stereotomy. Instead, the masonry is analysed as a continuous envelope, which is a more conservative approach.

- Disregard of tensile effects:

  By adopting Heyman's assumptions, no tensile capacity is considered in masonry. However, in some cases, it might be realistic to assume a small tensile strength of the material, which would require that the network goes outside the bounds of the masonry. Such cases are not studied in this dissertation.

- Limitation to small foundation displacements:

  The analysis with foundation settlements is limited to small (differential) displacements. An update in the geometry would be necessary to account for large displacements, as the structure would settle into new equilibrium positions as the supports move. The present approach can not account for this behaviour.

10.3 Outlook and future investigations

This section outlines possible future investigations arising from the present research. These future investigations are not only linked to the current limitations but also to promising developments in parallel fields where intersections can be beneficial.

10.3.1 A new perspective on optimal form diagrams

This dissertation has shown how TNA's form diagram selection influences the analysis of diverse problems, i.e., minimum and maximum thrusts, minimum thicknesses, and maximum loads. It makes an even stronger statement that there is no "right" pattern for a given geometry, and this pattern changes according to the load scenario, geometric features, boundary conditions, etc. Future research on discrete three-dimensional lower-bound methods should incorporate these findings.

10.3.2 Data-driven methods and pattern generation

Unlike optimising forces within a pattern, exploring its topological space corresponds to a combinatorial problem, which can not be described in continuous variables (Oval, 2019). In this context, data-driven methods are promising alternatives to help explore this combinatorial space and automate the generation of form diagrams. More importantly, they can learn the performance of the generated patterns relying on the metrics developed in this dissertation, i.e., GSF, stability domain, maximum load multipliers, complementary energy value, and searching for more adequate diagrams. Research in this direction has been recently performed for structural design (Saldana Ochoa et al., 2021; Tam et al., 2022).

Furthermore, recent research in auto-differentiation (AD) tools has demonstrated how AD can be a robust and scalable method to compute derivatives (or losses) and is available in open-source libraries (Paszke et al., 2019). Recent research in structural engineering has benefited from such a framework to compute derivatives (Cuvilliers, 2020; Pastrana et al., 2023) sometimes faster than with analytical approaches. Adding AD to the TNO framework could ease including new objectives or constraints, dispensing the need to compute the gradients analytically for each case.

10.3.3 Understanding TNA's conservatism

As stated in the Limitations (10.2), this research limited its scope to connected networks, which do not assume a specific stereotomy to the blocks in the structure and, therefore, can not capture the effects of friction between the blocks or even the beneficial interlocking effects known by masons (Chen and Bagi, 2020). In approaches like Fantin and Ciblac (2016), TNA is revisited considering the block's joints which reflected in a disconnected network (Nodargi and Bisegna, 2022).

Assuming the structure's stereotomy would reduce the TNA's conservatism. For these cases, future research should elaborate on how much more capacity is gained by assuming a giving stereotomy. The metrics developed in this work come in handy for this application.

10.3.4 Framework for inverse analysis

The results obtained in Chapter 9 showed how cracks are induced after support displacements and how they connect to minimal energy modes. Future work can rely on TNO analysis to study the inverse problem of determining the foundation displacements that resulted in the cracked configuration observed. Indeed, such studies are currently limited (Iannuzzo et al., 2018; Ye et al., 2018) and could be investigated for general vaulted masonry structures with TNO.

10.3.5 Emerging scanning technologies

The geometry-based input required for the analysis with TNO opens possibilities for closer integration of structural analysis and surveying (Riveiro et al., 2016). Emerging technologies such as augmented reality (AR) promise seamless interaction between real and virtual environments. New possibilities arise for the automatic segmentation of spaces, which could apply to identifying features and cracks in heritage buildings (El-Hakim et al., 2007) and obtaining faster and more precise three-dimensional models that could integrate with the analysis in TNO.

10.3.6 A new approach to design

TNA has already been applied to the design of compressive shell structures (Rippmann, 2016), including designing through a best-fit approach to a prescribed geometry representing the overall design intent (Van Mele et al., 2014). The constrained approaches from TNO offer an effective control over the structure's envelope instead of only its target geometry. In this design scenario, TNO could be used simultaneously as a design and assessment tool. The designed shell could, e.g., be optimised to enlarge the stability domain subjected to a limited amount of material.

Nevertheless, given the climate emergency, future design has to shift towards sustainable, low-carbon initiatives. In this context, discrete funicular floor applications have emerged for which the mechanical principles of masonry structures apply (Rippmann et al., 2018; Oval et al., 2023). Therefore, the tools developed could also be extended to this context, helping to identify and assess natural crack lines and hinges in the material for plausible foundation displacements or extreme loads.

10.4 Final reflections

Masonry structures have been standing for centuries and testified to the development of our civilisation's construction techniques. Paradoxically, in the 21st century, we lack appropriate analysis tools to ensure their structural safety.

Most of these structures have been conceived with simple equilibrium concepts, from which derive the theory of thrust lines and, more recently, lower-bound limit analysis and thrust network analysis. However, the lack of developments in novel equilibrium methods has limited its use to analysis "by hand" executed for trivial geometries.

The present work has developed *Thrust Network Optimisation* as a constrained optimisation-based framework that contributes to this lack of appropriate tools to model masonry structures. The developments are implemented in a Python-based package named *compas_tno*, which enables continuous development and collaboration.

By equipping equilibrium-based methods with robust optimisation procedures, this dissertation has effectively extended the range of applications of lower-bound limit analysis methods to vaulted masonry structures. It enables automating multiple assessment outputs in a single approach, some of which could not be done before for arbitrary geometries.

This dissertation's findings advocate for exploring the constrained compressive equilibrium space to understand masonry structures. This philosophy extends to general structures and offers a bridge between the fields of assessment and sustainable structural design. Multiple future research directions arise from this work. The framework developed can be used to perform inverse problems in masonry assessment and be integrated with data-driven and modern scanning techniques.

Preserving and rehabilitating existing buildings is more needed than ever. In this context, the contributions of this dissertation can have a real impact by offering reliable, comprehensive, collaborative, and accessible analysis tools to assess their stability.

List of Figures

List of Tables

Bibliography

Abraham, P. (1934), *Viollet-le-Duc et le rationalisme médiéval*, Vincent, Fréal & Cie, Paris. URL: https://www.persee.fr/doc/bulmo_0007-473x_1934_num_93_1_10100

AgiSoft (2021), "AgiSoft ProtoScan Professional - Metashape - Version 1.7". URL: http://www.agisoft.com/

Agrawal, A., Verschueren, R., Diamond, S. and Boyd, S. (2017), "A Rewriting System for Convex Optimization Problems". doi:10.48550/arxiv.1709.04494.

Aita, D., Barsotti, R. and Bennati, S. (2019), A parametric study of masonry domes equilibrium via a revisitation of the Durand-claye method, *in* "Proceedings of the 7th International Conference on Computational Methods in Structural Dynamics and Earthquake Engineering (COMPDYN 2015)", Institute of Structural Analysis and Antiseismic Research School of Civil Engineering National Technical University of Athens (NTUA) Greece, Crete, Greece, pp. 663–672. doi:10.7712/120119.6947.19313.

Alic, V. and Åkesson, D. (2017), "Bi-directional algebraic graphic statics", *Computer-Aided Design* **93**, 26–37. doi:10.1016/j.cad.2017.08.003.

Angelillo, M. (2014), Practical applications of unilateral models to Masonry Equilibrium, *in* F. Pfeiffer, F. G. Rammerstorfer, E. Guazzelli, B. Schrefler, P. Serafini and M. Angelillo, eds, "Mechanics of Masonry Structures", Vol. 551, Springer Vienna, Vienna, pp. 109–210. doi:10.1007/978-3-7091-1774-3_4.

Angelillo, M. (2019), "The model of Heyman and the statical and kinematical problems for masonry structures", *IJMRI* **4**(1/2), 14. doi:10.1504/IJMRI.2019.096820.

Angelillo, M., Babilio, E. and Fortunato, A. (2013), "Singular stress fields for masonry-like vaults", *Continuum Mechanics and Thermodynamics* **25**(2-4), 423–441. doi:10.1007/s00161-012-0270-9.

Angelillo, M., Fortunato, A., Gesualdo, A., Iannuzzo, A. and Zuccaro, G. (2018), "Rigid block models for masonry structures", *IJMRI* **3**(4), 349. doi:10.1504/IJMRI.2018.095701.

Angelillo, M., Lourenço, P. B. and Milani, G. (2014), Masonry behaviour and modelling, *in* M. Angelillo, ed., "Mechanics of Masonry Structures", CISM International Centre for Mechanical Sciences, Springer, Vienna, pp. 1–26. doi:10.1007/978-3-7091-1774-3_1.

Angelillo, M., Olivieri, C. and DeJong, M. J. (2021), "A new equilibrium solution for masonry spiral stairs", *Engineering Structures* **238**(April), 112176. doi:10.1016/j.engstruct.2021.112176.

ApS, M. (2019), The MOSEK optimization toolbox for MATLAB manual. Version 9.3., Technical report. URL: http://docs.mosek.com/9.3/toolbox/index.html

Baker, S. J., Horne, M. R. and Heyman, J. (1956), *The Steel Skeleton: Volume 2, Plastic Behaviour and Design*, Cambridge University Press. URL: https://books.google.ch/books?id=Tg5wSgAACAAJ

Baker, W. F., Beghini, L. L., Mazurek, A., Carrion, J. and Beghini, A. (2013), "Maxwell's reciprocal diagrams and discrete Michell frames", *Struct Multidisc Optim* **48**(2), 267–277. doi:10.1007/s00158-013-0910-0.

Baratta, A. and Corbi, O. (2010), "On the equilibrium and admissibility coupling in NT vaults of general shape", *International Journal of Solids and Structures* **47**(17), 2276–2284. doi:10.1016/j.ijsolstr.2010.04.024.

Beghini, A., Beghini, L. L. and Baker, W. F. (2013), Applications of Structural Optimization in Architectural Design, *in* "Structures Congress 2013", American Society of Civil Engineers, Pittsburgh, Pennsylvania, United States, pp. 2499–2507. doi:10.1061/9780784412848.218.

Bhooshan, S., Bhooshan, V., Dell'Endice, A., Chu, J., Singer, P., Megens, J., Van Mele, T. and Block, P. (2022), "The Striatus bridge: Computational design and robotic fabrication of an unreinforced, 3D-concrete-printed, masonry arch bridge", *Archit. Struct. Constr.* **2**(4), 521–543. doi:10.1007/s44150-022-00051-y.

Block, P. (2009), Thrust Network Analysis: Exploring Three-dimensional Equilibrium, PhD thesis, Massachusetts Institute of Technology, Cambridge. URL: https://dspace.mit.edu/handle/1721.1/49539

Block, P., Ciblac, T. and Ochsendorf, J. (2006), "Real-time limit analysis of vaulted masonry buildings", *Computers & Structures* **84**(29-30), 1841–1852. doi:10.1016/j.compstruc.2006.08.002.

Block, P., DeJong, M. and Ochsendorf, J. (2006), "As Hangs the Flexible Line: Equilibrium of Masonry Arches", *Nexus Netw J* **8**, 13–24. doi:10.1007/s00004-006-0015-9.

Block, P. and Lachauer, L. (2014), "Three-dimensional funicular analysis of masonry vaults", *Mechanics Research Communications* **56**, 53–60. doi:10.1016/j.mechrescom.2013.11.010.

Block, P., Lachauer, L. and Rippmann, M. (2014), Thrust network analysis: Design of a cut–stone masonry vault, *in* S. Adriaenssens, P. Block, D. Veenendaal and C. Williams, eds, "Shell Structures for Architecture: Form Finding and Optimization", Vol. 9781315849, Taylor & Francis - Routledge, London, pp. 71–87.

Block, P., Mele, T. V., Rippmann, M., Ranaudo, F., Barentin, C. C. and Paulson, N. (2020), "Redefining Structural Art : Strategies , necessities and opportunities Redefining Structural Art : Strategies , necessities and opportunities", *The Structural Engineer* **98**(January), 66–72. URL: http://hdl.handle.net/20.500.11850/405942

Block, P. and Ochsendorf, J. (2007), "Thrust network analysis: A new methodology for 3D equillibrium", *Journal of the International Association for Shell and Spatial Structures* **48**(155), 1–7. URL: https://web.mit.edu/masonry/papers/block_ochs_IASS_2007.pdf

Boothby, T. E. (2001), "Analysis of masonry arches and vaults", *Progress in Structural Engineering and Materials* **3**(3), 246–256. doi:10.1002/pse.84.

Boyd, S. and Vandenberghe, L. (2004), *Convex Optimization*, first edn, Cambridge University Press. doi:10.1017/CBO9780511804441.

Bruggi, M. (2020), "A constrained force density method for the funicular analysis and design of arches, domes and vaults", *International Journal of Solids and Structures* **193–194**, 251–269. doi:10.1016/j.ijsolstr.2020.02.030.

Calladine, C. R. (1983), *Theory of Shell Structures*, Cambridge University Press. doi:10.1017/CBO9780511624278.

Casapulla, C., Mousavian, E. and Zarghani, M. (2019), "A digital tool to design structurally feasible semi-circular masonry arches composed of interlocking blocks", *Computers & Structures* **221**, 111–126. doi:10.1016/j.compstruc.2019.05.001.

Castellazzi, G., D'Altri, A. M., Bitelli, G., Selvaggi, I. and Lambertini, A. (2015), "From Laser Scanning to Finite Element Analysis of Complex Buildings by Using a Semi-Automatic Procedure", *Sensors* **15**(8), 18360–18380. doi:10.3390/s150818360.

Cattari, S., Calderoni, B., Caliò, I., Camata, G., de Miranda, S., Magenes, G., Milani, G. and Saetta, A. (2022), "Nonlinear modeling of the seismic response of masonry structures: Critical review and open issues towards engineering practice", *Bull Earthquake Eng* **20**(4), 1939–1997. doi:10.1007/s10518-021-01263-1.

Cattari, S., Camilletti, D., D'Altri, A. M. and Lagomarsino, S. (2021), "On the use of continuum Finite Element and Equivalent Frame models for the seismic assessment of masonry walls", *Journal of Building Engineering* **43**, 102519. doi:10.1016/j.jobe.2021.102519.

Chen, S. and Bagi, K. (2020), "Crosswise tensile resistance of masonry patterns due to contact friction", *Proceedings of the Royal Society A: Mathematical, Physical and Engineering Sciences* **476**(2240), 20200439. doi:10.1098/rspa.2020.0439.

Chiozzi, A., Milani, G. and Tralli, A. (2017), "A Genetic Algorithm NURBS-based new approach for fast kinematic limit analysis of masonry vaults", *Computers & Structures* **182**, 187–204. doi:10.1016/j.compstruc.2016.11.003.

Coccia, S., Di Carlo, F. and Rinaldi, Z. (2015), "Collapse displacements for a mechanism of spreading-induced supports in a masonry arch", *Int J Adv Struct Eng* **7**(3), 307–320. doi:10.1007/s40091-015-0101-x.

Como, M. (2013), *Statics of Historic Masonry Constructions*, Vol. 1 of *Springer Series in Solid and Structural Mechanics*, Springer Berlin Heidelberg, Berlin, Heidelberg. doi:10.1007/978-3-642-30132-2.

Como, M. (2015), Statics of Historic Masonry Constructions: An Essay, *in* D. Aita, O. Pedemonte and K. Williams, eds, "Masonry Structures: Between Mechanics and Architecture", Springer International Publishing, Cham, pp. 49–72. doi:10.1007/978-3-319-13003-3_3.

Culmann, C. (1866), *Die graphische Statik*, Meyer & Zeller. doi:10.3931/E-RARA-20052.

Cundall, P. (1971), "A computer model for simulating progressive, large-scale movements in blocky rock systems", *International Journal of Rock Mechanics, Mining Sciences, and Geomechanics Abstracts* **25**(3), 107–116. URL: https://cir.nii.ac.jp/crid/1574231876066779904

Cuvilliers, P. E. (2020), The Constrained Geometry of Structures : Optimization Methods for Inverse Form-Finding Design, PhD thesis, Massachusetts Institute of Technology, Cambridge. URL: https://dspace.mit.edu/handle/1721.1/127853

D'Altri, A. M., Cannizzaro, F., Petracca, M. and Talledo, D. A. (2022), "Nonlinear modelling of the seismic response of masonry structures: Calibration strategies", *Bull Earthquake Eng* **20**(4), 1999–2043. doi:10.1007/s10518-021-01104-1.

D'Altri, A. M., Sarhosis, V., Milani, G., Rots, J., Cattari, S., Lagomarsino, S., Sacco, E., Tralli, A., Castellazzi, G. and de Miranda, S. (2019), "Modeling Strategies for the Computational Analysis of Unreinforced Masonry Structures: Review and Classification", *Archives of Computational Methods in Engineering* . doi:10.1007/s11831-019-09351-x.

Danyzy, A. (1732), Méthode générale pour déterminer la résistance qu'il faut opposer à la poussée des voûtes, *in* "Histoire de La Société Royale Des Sciences: Établie à Montpellier", (1788, 2: 40-53), Lyon, p. 43.

De Lorenzis, L. (2008), Strengthening of masonry structures with fibre-reinforced polymer (FRP) composites, *in* L. C. Hollaway and J. G. Teng, eds, "Strengthening and Rehabilitation of Civil Infrastructures Using Fibre-Reinforced Polymer (FRP) Composites", Woodhead Publishing Series in Civil and Structural Engineering, Woodhead Publishing, pp. 235–266. doi:10.1533/9781845694890.235.

De Wolf, C., Ramage, M. and Ochsendorf, J. (2017), "Low Carbon Vaulted Masonry Structures", *Journal of the International Association for Shell and Spatial Structures* **57**(4), 275–284. doi:10.20898/j.iass.2016.190.854.

DeJong, M. J. (2009), Seismic Assessment Strategies for Masonry Structures, PhD thesis, Massachusetts Institute of Technology, Cambridge. URL: https://dspace.mit.edu/handle/1721.1/49538

Dell'Endice, A. (2022), Structural Assessment and Design of Unreinforced Masonry Structures Using Discrete Element Modelling, PhD thesis, ETH Zurich. doi:10.3929/ethz-b-000596377.

Dell'Endice, A., Iannuzzo, A., DeJong, M. J., Van Mele, T. and Block, P. (2021), "Modelling imperfections in unreinforced masonry structures: Discrete element simulations and scale model experiments of a pavilion vault", *Engineering Structures* **228**, 111499. doi:10.1016/j.engstruct.2020.111499.

Derand, F. (1643), *L'architecture des voutes, ou L'art des traits et coupe des voutes*, Sebastien Cramoisy, Paris. URL: https://plume.epfl.ch/idurl/1/1464

Diamond, S. and Boyd, S. (2016), "CVXPY: A python-embedded modeling language for convex optimization", *J. Mach. Learn. Res.* **17**(1), 2909–2913. doi:10.48550/arXiv.1603.00943.

Dunn, W. (1904), "Notes on the Stresses in Framed Spires and Domes", *Journal of the Royal Institute of British Architects* **11**, 401–412.

Eddy, H. T. (1877), *New Constructions in Graphical Statics*, D. Van Nostrand, New York. URL: https://books.google.ch/books?id=PG0OAAAAYAAJ

El-Hakim, S., Gonzo, L., Voltolini, F., Girardi, S., Rizzi, A., Remondino, F. and Whiting, E. (2007), "Detailed 3D Modelling of Castles", *International Journal of Architectural Computing* **5**(2), 199–220. doi:10.1260/1478-0771.5.2.200.

Engesser, F. (1880), "über die Lage der Stützlinie in Gewölben", *Deutsche Bauzeitung* **14**, 184–186.

Fabbrocino, F., Farina, I., Berardi, V. P., Ferreira, A. J. M. and Fraternali, F. (2015), "On the thrust surface of unreinforced and FRP-/FRCM-reinforced masonry domes", *Composites Part B: Engineering* **83**, 297–305. doi:10.1016/j.compositesb.2015.08.061.

Fantin, M. and Ciblac, T. (2016), "Extension of thrust network analysis with joints consideration and new equilibrium states", *International Journal of Space Structures* **31**(2-4), 190–202. doi:10.1177/0266351116661814.

Fraddosio, A., Lepore, N. and Piccioni, M. D. (2020), "Thrust Surface Method: An innovative approach for the three-dimensional lower bound Limit Analysis of masonry vaults", *Engineering Structures* **202**(October 2019), 109846. doi:10.1016/j.engstruct.2019.109846.

Fraternali, F. (2010), "A thrust network approach to the equilibrium problem of unreinforced masonry vaults via polyhedral stress functions", *Mechanics Research Communications* **37**(2), 198–204. doi:10.1016/j.mechrescom.2009.12.010.

Fraternali, F., Angelillo, M. and Fortunato, A. (2002), "A lumped stress method for plane elastic problems and the discrete-continuum approximation", *International Journal of Solids and Structures* **39**(25), 6211–6240. doi:10.1016/S0020-7683(02)00472-9.

Fugger, R., Maia Avelino, R., Iannuzzo, A., Block, P. and de Felice, G. (2022), A new numerical limit analysis-based strategy to retrofit masonry curved structures with FRCM systems, *in* "8th European Congress on Computational Methods in Applied Sciences and Engineering", CIMNE, Oslo, Norway. doi:10.23967/eccomas.2022.020.

Funari, M. F., Mehrotra, A. and Lourenço, P. B. (2021), "A Tool for the Rapid Seismic Assessment of Historic Masonry Structures Based on Limit Analysis Optimisation and Rocking Dynamics", *Applied Sciences* **11**(3), 942. doi:10.3390/app11030942.

Funari, M. F., Silva, L. C., Mousavian, E. and Lourenço, P. B. (2021), "Real-time Structural Stability of Domes through Limit Analysis: Application to St. Peter's Dome", *International Journal of Architectural Heritage* **0**(0), 1–23. doi:10.1080/15583058.2021.1992539.

Funari, M. F., Silva, L. C., Savalle, N. and Lourenco, P. B. (2022), "A concurrent micro/macro FE-model optimized with a limit analysis tool for the assessment of dry-joint masonry structures", *International Journal for Multiscale Computational Engineering* **20**. doi:10.1615/IntJMultCompEng.2021040212.

Gaetani, A., Monti, G., Lourenço, P. B. and Marcari, G. (2016), "Design and Analysis of Cross Vaults Along History", *International Journal of Architectural Heritage* **10**(7), 841–856. doi:10.1080/15583058.2015.1132020.

Galassi, S. and Tempesta, G. (2019), "The Matlab code of the method based on the Full Range Factor for assessing the safety of masonry arches", *MethodsX* **6**(May), 1521–1542. doi:10.1016/j.mex.2019.05.033.

Gesualdo, A., Calderoni, B., Iannuzzo, A., Fortunato, A. and Monaco, M. (2019), "Minimum energy strategies for the in-plane behaviour of masonry", *Frattura ed Integrità Strutturale* **14**(51), 376–385. doi:10.3221/IGF-ESIS.51.27.

Gilbert, M., Casapulla, C. and Ahmed, H. M. (2006), "Limit analysis of masonry block structures with non-associative frictional joints using linear programming", *Computers & Structures* **84**(13-14), 873–887. doi:10.1016/j.compstruc.2006.02.005.

Gilbert, M., Cole, G., Smith, C. and Melbourne, C. (2022), Guidance on the assessment of masonry arch bridges, Technical Report C800F, CIRIA. URL: https://www.ciria.org/CIRIA/CIRIA/Item_Detail.aspx?iProductCode=C800F&Category=FREEPUBS

Gilbert, M. and Tyas, A. (2003), "Layout optimization of large-scale pin-jointed frames", *Engineering Computations* **20**(8), 1044–1064. doi:10.1108/02644400310503017.

Grant, M. and Boyd, S. (2008), Graph implementations for nonsmooth convex programs, *in* V. Blondel, S. Boyd and H. Kimura, eds, "Recent Advances in Learning and Control", Lecture Notes in Control and Information Sciences, Springer-Verlag Limited, pp. 95–110. doi:10.1007/978-1-84800-155-8_7.

Grant, M. and Boyd, S. (2014), "CVX: Matlab software for disciplined convex programming, version 2.1". URL: http://cvxr.com/cvx

Harris, C. R., Millman, K. J., van der Walt, S. J., Gommers, R., Virtanen, P., Cournapeau, D., Wieser, E., Taylor, J., Berg, S., Smith, N. J., Kern, R., Picus, M., Hoyer, S., van Kerkwijk, M. H., Brett, M., Haldane, A., del Río, J. F., Wiebe, M., Peterson, P., Gérard-Marchant, P., Sheppard, K., Reddy, T., Weckesser, W., Abbasi, H., Gohlke, C. and Oliphant, T. E. (2020), "Array programming with NumPy", *Nature* **585**(7825), 357–362. doi:10.1038/s41586-020-2649-2.

Hawkins, W., Orr, J., Shepherd, P. and Ibell, T. (2019), "Design, Construction and Testing of a Low Carbon Thin-Shell Concrete Flooring System", *Structures* **18**, 60–71. doi:10.1016/j.istruc.2018.10.006.

Heyman, J. (1966), "The stone skeleton", *International Journal of Solids and Structures* **2**(2), 249–279. doi:10.1016/0020-7683(66)90018-7.

Heyman, J. (1967), "On shell solutions for masonry domes", *International Journal of Solids and Structures* **3**(2), 227–241. doi:10.1016/0020-7683(67)90072-8.

Heyman, J. (1969), "The safety of masonry arches", *International Journal of Mechanical Sciences* **11**(4), 363–385. doi:10.1016/0020-7403(69)90070-8.

Heyman, J. (1995), *The Stone Skeleton*, Cambridge University Press. doi:10.1017/CBO9781107050310.

HIMASS (2021), "Historic Masonry Summer School (Ed. 2021)". URL: https://www.himass.org

Hooke, R. (1676), *A Description of Helioscopes, and Some Other Instruments*, printed by T.R. for John Martyn, London. doi:10.3931/e-rara-2171.

Huerta, S. (2001), Mechanics of masonry vaults: The equilibrium approach, *in* P. Lourenço and P. Roca, eds, "Historical Constructions. Possibilities of Numerical and Experimental Techniques", Universidade do Minho, Guimarães. URL: https://oa.upm.es/569/

Huerta, S. (2004), *Arcos, bóvedas y cúpulas. Geometría y equilibrio en el cálculo tradicional de estructuras de fábrica*, E.T.S. Arquitectura (UPM), Madrid. URL: https://oa.upm.es/1136/

Huerta, S. (2006), "Galileo was wrong: The geometrical design of masonry arches", *Nexus Netw J* **8**(2), 25–52. doi:10.1007/s00004-006-0016-8.

Huerta, S. (2008), "The Analysis of Masonry Architecture: A Historical Approach", *Architectural Science Review* **51**(4), 297–328. doi:10.3763/asre.2008.5136.

Huerta, S. (2009), The Debate about the Structural Behaviour of Gothic Vaults: From Viollet-le-Duc to Heyman, *in* "Proceedings of the Third International Congress on Construction History", Vol. 2, Cottbus, p. 9. URL: https://oa.upm.es/2497/

Huerta, S. (2020), Block models of the masonry arch and vault, *in* B. Addis, ed., "PHYSICAL MODELS: Their Historical and Current Use in Civil and Building Engineering Design", John Wiley & Sons, Ltd, chapter 2, pp. 31–77. doi:10.1002/9783433609613.ch2.

Hughes, T. J. R. (2012), *The Finite Element Method: Linear Static and Dynamic Finite Element Analysis*, Courier Corporation. URL: https://books.google.ch/books?id=E9IoAwAAQBAJ

Iannuzzo, A., Angelillo, M., De Chiara, E., De Guglielmo, F., De Serio, F., Ribera, F. and Gesualdo, A. (2018), "Modelling the cracks produced by settlements in masonry structures", *Meccanica* **53**(7), 1857–1873. doi:10.1007/s11012-017-0721-2.

Iannuzzo, A., Dell'Endice, A., Maia Avelino, R., Kao, G., Van Mele, T. and Block, P. (2021), COMPAS Masonry: A Computational Framework for Practical Assessment of Unreinforced Masonry Structures, *in* "12th International Conference on Structural Analysis of Historical Constructions", CIMNE. doi:10.23967/sahc.2021.054.

Iannuzzo, A., Dell'Endice, A., Van Mele, T. and Block, P. (2021), "Numerical limit analysis-based modelling of masonry structures subjected to large displacements", *Computers & Structures* **242**, 106372. doi:10.1016/j.compstruc.2020.106372.

Iannuzzo, A., Van Mele, T. and Block, P. (2020), "Piecewise rigid displacement (PRD) method: A limit analysis-based approach to detect mechanisms and internal forces through two dual energy criteria", *Mechanics Research Communications* **107**, 103557. doi:10.1016/j.mechrescom.2020.103557.

ICOMOS (1993), Guidelines for Education and training in the conservation of Monuments, Ensembles and Sites, Technical report. URL: https://www.icomos.org/charters/structures_e.pdf

ICOMOS (2003), Principles for the analysis, conservation and structural restoration of architectural heritage, Technical report, ICOMOS. URL: https://www.icomos.org/

Indirli, M., S. Kouris, L. A., Formisano, A., Borg, R. P. and Mazzolani, F. M. (2013), "Seismic Damage Assessment of Unreinforced Masonry Structures After The Abruzzo 2009 Earthquake: The Case Study of the Historical Centers of L'Aquila and Castelvecchio Subequo", *International Journal of Architectural Heritage* **7**(5), 536–578. doi:10.1080/15583058.2011.654050.

Itasca (2020), "Three-Dimensional Distinct Element Code, Ver. 7.0.". URL: https://www.itascacg.com/software/3dec

Jenkin, H. C. F. (1876), "Bridges", *Encyclopedia Britanica* **9th edition**, 284–341. URL: https://digital.nls.uk/193322693

Kao, G. T.-C., Iannuzzo, A., Thomaszewski, B., Coros, S., Van Mele, T. and Block, P. (2022), "Coupled Rigid-Block Analysis: Stability-Aware Design of Complex Discrete-Element Assemblies", *Computer-Aided Design* **146**, 103216. doi:10.1016/j.cad.2022.103216.

Kooharian, A. (1952), "Limit Analysis of Voussoir (Segmental) and Concrete Archs", *JP* **49**(12), 317–328. doi:10.14359/11822.

Kraft, D. (1988), *A Software Package for Sequential Quadratic Programming*, Wiss. Berichtswesen d. DFVLR. URL: https://books.google.ch/books?id=4rKaGwAACAAJ

Lau, W. (2006), Equilibrium Analysis of Masonry Domes, PhD thesis, Massachusetts Institute of Technology, Cambridge. URL: https://dspace.mit.edu/handle/1721.1/34984

Lawson, C. L. and Hanson, R. J. (1995), *Solving Least Squares Problems*, Society for Industrial and Applied Mathematics. doi:10.1137/1.9781611971217.

Lee, J. (2018), Computational Design Framework for 3D Graphic Statics, PhD thesis, ETH Zurich, Zurich. doi:10.3929/ethz-b-000331210.

Lemos, J. V. (1998), "Discrete Element Modelling Of The Seismic Behaviour Of Stone Masonry Arches", *Computer Methods in Structural Masonry* **4**, 220–227.

Lemos, J. V. (2019), "Discrete Element Modeling of the Seismic Behavior of Masonry Construction", *Buildings* **9**(2), 43. doi:10.3390/buildings9020043.

Lengyel, G. (2018), "Minimum thickness of the gothic arch", *Archive of Applied Mechanics* **88**(5), 769–788. doi:10.1007/s00419-018-1341-6.

Liew, A. (2020), "Constrained Force Density Method optimisation for compression-only shell structures", *Structures* **28**(October), 1845–1856. doi:10.1016/j.istruc.2020.09.078.

Liew, A., Avelino, R., Moosavi, V., Van Mele, T. and Block, P. (2019), "Optimising the load path of compression-only thrust networks through independent sets", *Struct Multidisc Optim* **60**(1), 231–244. doi:10.1007/s00158-019-02214-w.

Liew, A., López, D. L., Van Mele, T. and Block, P. (2017), "Design, fabrication and testing of a prototype, thin-vaulted, unreinforced concrete floor", *Engineering Structures* **137**, 323–335. doi:10.1016/j.engstruct.2017.01.075.

Liew, A., Pagonakis, D., Van Mele, T. and Block, P. (2018), "Load-path optimisation of funicular networks", *Meccanica* **53**(1-2), 279–294. doi:10.1007/s11012-017-0714-1.

LimitState Ltd (2020), "Limit State:RING - Industry Leading Masonry Arch Analysis Software | Limit State". URL: https://www.limitstate.com/ring

Livesley, R. K. (1978), "Limit analysis of structures formed from rigid blocks", *International Journal for Numerical Methods in Engineering* **12**(12), 1853–1871. doi:10.1002/nme.1620121207.

Livesley, R. K. (1992), "A computational model for the limit analysis of three-dimensional masonry structures", *Meccanica* **27**(3), 161–172. doi:10.1007/BF00430042.

López López, D., Roca, P., Liew, A., Méndez Echenagucia, T., Van Mele, T. and Block, P. (2022), "A three-dimensional approach to the Extended Limit Analysis of Reinforced Masonry", *Structures* **35**, 1062–1077. doi:10.1016/j.istruc.2021.06.013.

Lotfi, H. R. and Shing, P. B. (1991), "An appraisal of smeared crack models for masonry shear wall analysis", *Computers & Structures* **41**(3), 413–425. doi:10.1016/0045-7949(91)90134-8.

Lourenço, P. B., Funari, M. F. and Silva, L. C. (2022), Building resilience and masonry structures: How can computational modelling help?, *in* "Computational Modelling of Concrete and Concrete Structures", CRC Press. doi:10.1201/9781003316404-4.

Maia Avelino, R. (2023), "Compas TNO: Finding admissible thrust networks in vaulted masonry structures". doi:10.5281/zenodo.7895617.

Maia Avelino, R., Iannuzzo, A., Van Mele, T. and Block, P. (2021*a*), "Assessing the safety of vaulted masonry structures using thrust network analysis", *Computers & Structures* **257**, 106647. doi:10.1016/j.compstruc.2021.106647.

Maia Avelino, R., Iannuzzo, A., Van Mele, T. and Block, P. (2021*b*), New Strategies to Assess the Safety of Unreinforced Masonry Structures Using Thrust Network Analysis, *in* "12th International Conference on Structural Analysis of Historical Constructions", CIMNE, Barcelona, Spain, pp. 2124–2135. doi:10.23967/sahc.2021.162.

Maia Avelino, R., Iannuzzo, A., Van Mele, T. and Block, P. (2021*c*), "Parametric Stability Analysis of Groin Vaults", *Applied Sciences* **11**(8), 3560. doi:10.3390/app11083560.

Maia Avelino, R., Iannuzzo, A., Van Mele, T. and Block, P. (2022), "An energy-based strategy to find admissible thrust networks compatible with foundation settlements in masonry structures", *Mechanics Research Communications* **125**, 103978. doi:10.1016/j.mechrescom.2022.103978.

Maia Avelino, R., Lee, J., Van Mele, T. and Block, P. (2021), An interactive implementation of algebraic graphic statics for geometry-based teaching and design of structures, *in* "International Fib Symposium - Conceptual Design of Structures 2021", Attisholz-Areal, Switzerland, pp. 447–454. doi:10.35789/fib.PROC.0055.2021.CDSymp.P054.

Maia Avelino, R., Oliveri, C., Donval, E., Fugger, R., Lai, M., Lasorella, M., Saretta, Y., Weichbrodt, A. and Sangirardi, M. (2022), "An Integrated Approach To The Structural Assessment Of Historic Buildings: The Case Of St. Angelo Church In Anagni", *Structural* **241**, 1–23. doi:10.12917/STRU241.13.

Mainstone, R. J. (1999), "The Dome of St Peter's: Structural Aspects of its Design and Construction, and Inquiries into its Stability", *AA Files* (39), 21–39. URL: https://www.jstor.org/stable/29544154

Makris, N. and Alexakis, H. (2013), "The effect of stereotomy on the shape of the thrust-line and the minimum thickness of semicircular masonry arches", *Arch Appl Mech* **83**(10), 1511–1533. doi:10.1007/s00419-013-0763-4.

Manuello Bertetto, A., D'Angella, P. and Fronterre', M. (2021), "Residual strength evaluation of Notre Dame surviving masonry after the fire", *Engineering Failure Analysis* **122**, 105183. doi:10.1016/j.engfailanal.2020.105183.

Marmo, F. (2021), "ArchLab: A MATLAB tool for the Thrust Line Analysis of masonry arches", *Curved and Layered Structures* **8**(1), 26–35. doi:10.1515/cls-2021-0003.

Marmo, F. and Rosati, L. (2017), "Reformulation and extension of the thrust network analysis", *Computers & Structures* **182**, 104–118. doi:10.1016/j.compstruc.2016.11.016.

Maxwell, J. C. (1864), "On reciprocal figures and diagrams of forces", *Philosophical Magazine and Journal of Science* **27**(182), 250–261. doi:10.1080/14786446408643663.

Maxwell, J. C. (1870), "On Reciprocal Figures, Frames, and Diagrams of Forces", *Transactions of The Royal Society of Edinburgh* **26**(1), 1–40. doi:10.1017/S0080456800026351.

McInerney, J. and DeJong, M. J. (2015), "Discrete Element Modeling of Groin Vault Displacement Capacity", *International Journal of Architectural Heritage* **9**(8), 1037–1049. doi:10.1080/15583058.2014.923953.

Michell, A. (1904), "LVIII. The limits of economy of material in frame-structures", *The London, Edinburgh, and Dublin Philosophical Magazine and Journal of Science* **8**(47), 589–597. doi:10.1080/14786440409463229.

Miki, M., Igarashi, T. and Block, P. (2015), "Parametric self-supporting surfaces via direct computation of airy stress functions", *ACM Trans. Graph.* **34**(4), 1–12. doi:10.1145/2766888.

Milani, G. and Tralli, A. (2012), "A simple meso-macro model based on SQP for the non-linear analysis of masonry double curvature structures", *International Journal of Solids and Structures* **49**(5), 808–834. doi:10.1016/j.ijsolstr.2011.12.001.

Morandi, P., Butenweg, C., Breis, K., Beyer, K. and Magenes, G. (2022), "Latest findings on the behaviour factor q for the seismic design of URM buildings", *Bull Earthquake Eng* **20**(11), 5797–5848. doi:10.1007/s10518-022-01419-7.

Moseley, H. (1843), On the Theory of the Arch, *in* J. Weale, ed., "Theory, Practice and Architecture of Bridges", Architectural Library, London, pp. 1–72.

Mousavian, E., Bagi, K. and Casapulla, C. (2022), "Interlocking joint shape optimization for structurally informed design of block assemblages", *Journal of Computational Design and Engineering* **9**. doi:10.1093/jcde/qwac054.

Neal, B. G. (1958), "The Plastic Methods of Structural Analysis", *J. R. Aeronaut. Soc.* **62**(569), 390–391. doi:10.1017/S0368393100068905.

Nocedal, J., Wächter, A. and Waltz, R. A. (2009), "Adaptive Barrier Update Strategies for Nonlinear Interior Methods", *SIAM J. Optim.* **19**(4), 1674–1693. doi:10.1137/060649513.

Nocedal, J. and Wright, S. J. (2006*a*), *Numerical Optimization*, Springer Series in Operations Research, 2nd ed edn, Springer, New York.

Nocedal, J. and Wright, S. J. (2006*b*), Sequential Quadratic Programming, *in* "Numerical Optimization", Springer Series in Operations Research and Financial Engineering, Springer, New York, NY, pp. 529–562. doi:10.1007/978-0-387-40065-5_18.

Nodargi, N. A. and Bisegna, P. (2021*a*), "Collapse capacity of masonry domes under horizontal loads: A static limit analysis approach", *International Journal of Mechanical Sciences* **212**, 106827. doi:10.1016/j.ijmecsci.2021.106827.

Nodargi, N. A. and Bisegna, P. (2022), "Generalized thrust network analysis for the safety assessment of vaulted masonry structures", *Engineering Structures* **270**, 114878. doi:10.1016/j.engstruct.2022.114878.

Nodargi, N. and Bisegna, P. (2021*b*), "A new computational framework for the minimum thrust analysis of axisymmetric masonry domes", *Engineering Structures* **234**, 111962. doi:10.1016/j.engstruct.2021.111962.

Obvis (2016), "ArchieM. Version 2.5.1", Obvis Ltd. URL: http://www.obvis.com/archie-m/

Ochsendorf, J. (2002), Collapse of Masonry Structures, PhD thesis, University of Cambridge, Cambridge. URL: https://doi.org/10.17863/CAM.14048

Ochsendorf, J. (2006), "The masonry arch on spreading supports", *The Structural Engineer* (January). URL: https://www.istructe.org/journal/volumes/volume-84-(published-in-2006)/issue-2/the-masonry-arch-on-spreading-supports/

O'Dwyer, D. (1999), "Funicular analysis of masonry vaults", *Computers & Structures* **73**(1-5), 187–197. doi:10.1016/S0045-7949(98)00279-X.

OECD (2019), *Global Material Resources Outlook to 2060: Economic Drivers and Environmental Consequences*, OECD. doi:10.1787/9789264307452-en.

Olivieri, C., Angelillo, M., Gesualdo, A., Iannuzzo, A. and Fortunato, A. (2021), "Parametric design of purely compressed shells", *Mechanics of Materials* **155**(January), 103782. doi:10.1016/j.mechmat.2021.103782.

Oval, R. (2019), Topology Finding of Patterns for Structural Design, PhD thesis, Université Paris-Est. URL: https://www.researchgate.net/publication/340096530

Oval, R., Nuh, M., Costa, E., Madyan, O. A., Orr, J. and Shepherd, P. (2023), "A prototype low-carbon segmented concrete shell building floor system", *Structures* **49**, 124–138. doi:10.1016/j.istruc.2023.01.063.

Oval, R., Rippmann, M., Mele, T. V. A. N., Baverel, O. and Block, P. (2017), Patterns for Masonry Vault Design, *in* "Proceedings of the IASS Annual Symposium 2017 - "Interfaces: Architecture.Engineering.Science"", pp. 1–10. URL: https://hal.science/hal-01883502

Oval, R., Rippmann, M., Mesnil, R., van Mele, T., Baverel, O. and Block, P. (2018), Topology Finding of Structural Patterns, *in* "Advances in Architectural Geometry", Gothenburg, Sweden. URL: https://hal.archives-ouvertes.fr/hal-01883505

Page, A. (1981), "The biaxial compressive strength of brick masonry", *Ice Proceedings* **71**, 893–906. doi:10.1680/iicep.1981.1825.

Paris, V., Ruscica, G. and Mirabella Roberti, G. (2021), "Graphical Modelling of Hoop Force Distribution for Equilibrium Analysis of Masonry Domes", *Nexus Netw J* **23**(4), 855–878. doi:10.1007/s00004-021-00556-x.

Pastrana, R., Ohlbrock, P. O., Oberbichler, T., D'Acunto, P. and Parascho, S. (2023), "Constrained Form-Finding of Tension–Compression Structures using Automatic Differentiation", *Computer-Aided Design* **155**, 103435. doi:10.1016/j.cad.2022.103435.

Paszke, A., Gross, S., Massa, F., Lerer, A., Bradbury, J., Chanan, G., Killeen, T., Lin, Z., Gimelshein, N., Antiga, L., Desmaison, A., Köpf, A., Yang, E., DeVito, Z., Raison, M., Tejani, A., Chilamkurthy, S., Steiner, B., Fang, L., Bai, J. and Chintala, S. (2019), PyTorch: An imperative style, high-performance deep learning library, *in* "Proceedings of the 33rd International Conference on Neural Information Processing Systems", number 721, Curran Associates Inc., Red Hook, NY, USA, pp. 8026–8037. doi:10.5555/3454287.3455008.

Pellegrino, S. and Calladine, C. R. (1986), "Matrix analysis of statically and kinematically indeterminate frameworks", *International Journal of Solids and Structures* **22**(4), 409–428. doi:10.1016/0020-7683(86)90014-4.

Petersen, K. and Pedersen, M. (2012), The Matrix Cookbook, Technical report, Technical University of Denmark. URL: http://www2.compute.dtu.dk/pubdb/pubs/3274-full.html

Pippard, A. J. S., Tranter, E. and Chitty, L. (1936), "The mechanics of the voussoir arch. (includes appendix).", *Journal of the Institution of Civil Engineers* **4**(2), 281–306. doi:10.1680/ijoti.1936.14795.

Pirnay, H., López-Negrete, R. and Biegler, L. T. (2012), "Optimal sensitivity based on IPOPT", *Math. Prog. Comp.* **4**(4), 307–331. doi:10.1007/s12532-012-0043-2.

Poleni, G. (1748), *Memorie istoriche della gran cupola del tempio vaticano, e de'danni di essa, e de'ristoramenti loro, divise in libri cinque ...*, Stamperia del Seminario, Padova. doi:10.3931/e-rara-13403.

Portioli, F., Casapulla, C., Gilbert, M. and Cascini, L. (2014), "Limit analysis of 3D masonry block structures with non-associative frictional joints using cone programming", *Computers & Structures* **143**, 108–121. doi:10.1016/j.compstruc.2014.07.010.

Prager, W. (1959), *An Introduction to Plasticity*, Addison-Wesley Publishing Company. URL: https://books.google.ch/books?id=YAGrAAAAIAAJ

Praticò, Y., Ochsendorf, J., Holzer, S. and Flatt, R. J. (2020), "Post-fire restoration of historic buildings and implications for Notre-Dame de Paris", *Nat. Mater.* **19**(8), 817–820. doi:10.1038/s41563-020-0748-y.

Ramage, M. H., Gatóo, A. and Al Asali, M. W. (2022), Complex Simplicity—Design of Innovative Sustainable Thin-Shell Masonry Structures, *in* G. Milani and V. Sarhosis, eds, "From Corbel Arches to Double Curvature Vaults: Analysis, Conservation and Restoration of Architectural Heritage

Masonry Structures", Research for Development, Springer International Publishing, Cham, pp. 257–281. doi:10.1007/978-3-031-12873-8_10.

Ramage, M. H., Ochsendorf, J., Rich, P., Bellamy, J. K. and Block, P. (2010), "Design and Construction of the Mapungubwe National Park Interpretive Centre, South Africa", *ATDF Journal: Architecture* **7**(1-2), 14–23. URL: https://www.research-collection.ethz.ch/handle/20.500.11850/30041

Ranaudo, F., Van Mele, T. and Block, P. (2021), A low-carbon, funicular concrete floor system: Design and engineering of the HiLo floors, *in* "IABSE Congress Ghent 2021", pp. 2016–2024. doi:10.2749/ghent.2021.2016.

Reccia, E., Milani, G., Cecchi, A. and Tralli, A. (2014), "Full 3D homogenization approach to investigate the behavior of masonry arch bridges: The Venice trans-lagoon railway bridge", *Construction and Building Materials* **66**, 567–586. doi:10.1016/j.conbuildmat.2014.05.096.

Rippmann, M. (2016), Funicular Shell Design: Geometric Approaches to Form Finding and Fabrication of Discrete Funicular Structures, PhD thesis, ETH Zurich, Zurich. doi:10.3929/ethz-a-010656780.

Rippmann, M., Lachauer, L. and Block, P. (2012), "Interactive Vault Design", *International Journal of Space Structures* **27**(4), 219–230. doi:10.1260/0266-3511.27.4.219.

Rippmann, M., Liew, A., Van Mele, T. and Block, P. (2018), "Design, fabrication and testing of discrete 3D sand-printed floor prototypes", *Materials Today Communications* **15**, 254–259. doi:10.1016/j.mtcomm.2018.03.005.

Riveiro, B., DeJong, M. and Conde, B. (2016), "Automated processing of large point clouds for structural health monitoring of masonry arch bridges", *Automation in Construction* **72**, 258–268. doi:10.1016/j.autcon.2016.02.009.

Roca, P., Cervera, M., Gariup, G. and Pelà, L. (2010), "Structural analysis of masonry historical constructions. Classical and advanced approaches", *Archives of Computational Methods in Engineering* **17**(3), 299–325. doi:10.1007/s11831-010-9046-1.

Roca, P., Cervera, M., Pelà, L., Clemente, R. and Chiumenti, M. (2013), "Continuum FE models for the analysis of Mallorca Cathedral", *Engineering Structures* **46**, 653–670. doi:10.1016/j.engstruct.2012.08.005.

Roca, P., Molins, C. and Marí, A. R. (2005), "Strength Capacity of Masonry Wall Structures by the Equivalent Frame Method", *Journal of Structural Engineering* **131**(10), 1601–1610. doi:10.1061/(ASCE)0733-9445(2005)131:10(1601).

Romano, A. and Ochsendorf, J. A. (2010), "The mechanics of Gothic masonry arches", *International Journal of Architectural Heritage* **4**(1), 59–82. doi:10.1080/15583050902914660.

Saldana Ochoa, K., Ohlbrock, P. O., D'Acunto, P. and Moosavi, V. (2021), "Beyond typologies, beyond optimization: Exploring novel structural forms at the interface of human and machine intelligence", *International Journal of Architectural Computing* **19**(3), 466–490. doi:10.1177/1478077120943062.

Sarhosis, V., Lemos, J. and Bagi, K. (2019), Discrete element modeling, *in* B. Ghiassi and G. Milani, eds, "Numerical Modeling of Masonry and Historical Structures", Elsevier, pp. 469–501. doi:10.1016/B978-0-08-102439-3.00013-0.

Scacco, J., Milani, G. and Lourenço, P. B. (2020), "Automatic mesh generator for the non-linear homogenized analysis of double curvature masonry structures", *Advances in Engineering Software* **150**, 102919. doi:10.1016/j.advengsoft.2020.102919.

Schek, H. J. (1974), "The force density method for form finding and computation of general networks", *Computer Methods in Applied Mechanics and Engineering* **3**(1), 115–134. doi:10.1016/0045-7825(74)90045-0.

Shin, H. V., Porst, C. F., Vouga, E., Ochsendorf, J. and Durand, F. (2016), "Reconciling Elastic and Equilibrium Methods for Static Analysis", *ACM Trans. Graph.* **35**(2), 1–16. doi:10.1145/2835173.

Snell, G. (1846), "On the stability of arches", *Minutes of the Proceedings of the Institution of Civil Engineers* **5**(1846), 439–464. doi:10.1680/imotp.1846.24330.

Stevin, S. (1586), *De Beghinselen Des Waterwichts*, Franciscus Raphelengius, Leiden. URL: https://books.google.ch/books?id=UwxjAAAAcAAJ

Symonds, P. S. and Neal, B. G. (1951), "Recent progress in the plastic methods of structural analysis", *Journal of the Franklin Institute* **252**(6), 469–492. doi:10.1016/0016-0032(51)90049-X.

Tam, K.-M. M., Kudenko, D., Khosla, M., Van Mele, T. and Block, P. (2022), Performance-informed pattern modification of reticulated equilibrium shell structures using rules-based Graphic Statics, CW Networks and Reinforcement Learning, *in* "International Association for Shell and Spatial Structures Annual Symposium 2022", Beijing, China, p. 12. URL: https://www.researchgate.net/publication/362704131

Toh, K. C., Todd, M. J. and Tütüncü, R. H. (1999), "SDPT3 — A Matlab software package for semidefinite programming, Version 1.3", *Optimization Methods and Software* **11**(1-4), 545–581. doi:10.1080/10556789908805762.

Tralli, A., Alessandri, C. and Milani, G. (2014), "Computational Methods for Masonry Vaults: A Review of Recent Results", *The Open Civil Engineering Journal* **8**(1), 272–287. doi:10.2174/1874149501408010272.

Ungewitter, G. (1890), *Lehrbuch Der Gotischen Konstruktionen*, T.O. Weigel Nachfolger, Leipzig. URL: https://swisscovery.slsp.ch/permalink/41SLSP_NETWORK/1ufb5t2/alma991138890119705501

Van Mele, T. (2017), "COMPAS: A framework for computational research in architecture and structures". doi:10.5281/zenodo.2594510.

Van Mele, T. and Block, P. (2014), "Algebraic graph statics", *Computer-Aided Design* **53**, 104–116. doi:10.1016/j.cad.2014.04.004.

Van Mele, T., Chen, L., Yang, W., Pastrana, R. and Lee, J. (2021), "Compas TNA: COMPAS package for Thrust Network Analysis". doi:10.5281/zenodo.4737184.

Van Mele, T., Lachauer, L., Rippmann, M. and Block, P. (2012), "Geometry-based understanding of structures", *Journal of the International Association for Shell and Spatial Structures* **53**(174), 285–295.

Van Mele, T., Panozzo, D., Sorkine-Hornung, O. and Block, P. (2014), Best–fit thrust network analysis: Rationalization of freeform meshes, *in* S. Adriaenssens, P. Block, D. Veenendaal and C. Williams, eds, "Shell Structures for Architecture: Form Finding and Optimization", Vol. 9781315849, Taylor & Francis - Routledge, London, pp. 157–169.

Varignon, P. (1725), *Nouvelle mécanique ou Statique, dont le projet fut donné en 1687: ouvrage posthume*, Claude Jombert, Paris. URL: https://catalogue.bnf.fr/ark:/12148/cb31544115g

Virtanen, P., Gommers, R., Oliphant, T. E., Haberland, M., Reddy, T., Cournapeau, D., Burovski, E., Peterson, P., Weckesser, W., Bright, J., van der Walt, S. J., Brett, M., Wilson, J., Millman, K. J., Mayorov, N., Nelson, A. R. J., Jones, E., Kern, R., Larson, E., Carey, C. J., Polat, İ., Feng, Y., Moore, E. W., VanderPlas, J., Laxalde, D., Perktold, J., Cimrman, R., Henriksen, I., Quintero, E. A., Harris, C. R., Archibald, A. M., Ribeiro, A. H., Pedregosa, F., van Mulbregt, P. and SciPy 1.0 Contributors (2020), "SciPy 1.0: Fundamental Algorithms for Scientific Computing in Python", *Nature Methods* **17**, 261–272. doi:10.1038/s41592-019-0686-2.

Wächter, A. and Biegler, L. T. (2006), "On the implementation of an interior-point filter line-search algorithm for large-scale nonlinear programming", *Mathematical Programming* **106**(1), 25–57. doi:10.1007/s10107-004-0559-y.

Wang, Z., Song, P., Isvoranu, F. and Pauly, M. (2019), "Design and structural optimization of topological interlocking assemblies", *ACM Trans. Graph.* **38**(6), 193:1–193:13. doi:10.1145/3355089.3356489.

Whiteley, W., Ash, P. F., Bolker, E. and Crapo, H. (2013), Convex Polyhedra, Dirichlet Tessellations, and Spider Webs, *in* M. Senechal, ed., "Shaping Space: Exploring Polyhedra in Nature, Art, and the Geometrical Imagination", Springer, New York, NY, pp. 231–251. doi:10.1007/978-0-387-92714-5_18.

Whiting, E., Ochsendorf, J. and Durand, F. (2009), "Procedural modeling of structurally-sound masonry buildings", *ACM Trans. Graph.* **28**(5), 1. doi:10.1145/1618452.1618458.

Whiting, E., Shin, H., Wang, R., Ochsendorf, J. and Durand, F. (2012), "Structural optimization of 3D masonry buildings", *ACM Trans. Graph.* **31**(6), 1. doi:10.1145/2366145.2366178.

Wilding, B. V., Dolatshahi, K. M. and Beyer, K. (2017), "Influence of load history on the force-displacement response of in-plane loaded unreinforced masonry walls", *Engineering Structures* **152**, 671–682. doi:10.1016/j.engstruct.2017.09.038.

Williams, C. J. K. (1990), "Generation of a class of structural forms for vaults and sails", *The Structural Engineer* **68**(12), 231–235. URL: https://www.istructe.org/journal/volumes/volume-68-(published-in-1990)/issue-12/the-generation-of-a-class-of-structural-forms-for/

Ye, C., Acikgoz, S., Pendrigh, S., Riley, E. and DeJong, M. J. (2018), "Mapping deformations and inferring movements of masonry arch bridges using point cloud data", *Engineering Structures* **173**, 530–545. doi:10.1016/j.engstruct.2018.06.094.

Zampieri, P., Faleschini, F., Zanini, M. A. and Simoncello, N. (2018), "Collapse mechanisms of masonry arches with settled springing", *Engineering Structures* **156**, 363–374. doi:10.1016/j.engstruct.2017.11.048.

Zampieri, P., Zanini, M. A., Faleschini, F., Hofer, L. and Pellegrino, C. (2017), "Failure analysis of masonry arch bridges subject to local pier scour", *Engineering Failure Analysis* **79**, 371–384. doi:10.1016/j.engfailanal.2017.05.028.

Zessin, J. F. (2012), Collapse Analysis of Unreinforced Masonry Domes and Curving Walls, PhD thesis, MIT, Cambridge. URL: http://dspace.mit.edu/handle/1721.1/70879

Zessin, J., Lau, W. and Ochsendorf, J. (2010), "Equilibrium of cracked masonry domes", *Proceedings of the Institution of Civil Engineers: Engineering and Computational Mechanics* **163**(3), 135–145. doi:10.1680/eacm.2010.163.3.135.

Zucchini, A. and Lourenço, P. B. (2009), "A micro-mechanical homogenisation model for masonry: Application to shear walls", *International Journal of Solids and Structures* **46**(3), 871–886. doi:10.1016/j.ijsolstr.2008.09.034.

Relevant publications by the author

Journal publications

Maia Avelino, R., Iannuzzo, A., Van Mele, T. and Block, P. (2022), "An energy-based strategy to find admissible thrust networks compatible with foundation settlements in masonry structures", *Mechanics Research Communications* **125**, 103978. doi:10.1016/j.mechrescom.2022.103978.

Maia Avelino, R., Iannuzzo, A., Van Mele, T. and Block, P. (2021), "Assessing the safety of vaulted masonry structures using thrust network analysis", *Computers & Structures* **257**, 106647. doi:10.1016/j.compstruc.2021.106647.

Maia Avelino, R., Iannuzzo, A., Van Mele, T. and Block, P. (2021), "Parametric Stability Analysis of Groin Vaults", *Applied Sciences* **11**(8), 3560. doi:10.3390/app11083560.

Liew, A., Maia Avelino, R., Moosavi, V., Van Mele, T. and Block, P. (2019), "Optimising the load path of compression-only thrust networks through independent sets", *Structural and Multidisciplinary Optimization* **60**(1), 231–244. doi:10.1007/s00158-019-02214-w.

Conference Proceedings

Fugger, R., Maia Avelino, R., Iannuzzo, A., Block, P. and de Felice, G. (2022), A new numerical limit analysis-based strategy to retrofit masonry curved structures with FRCM systems, *in* "8th European Congress on Computational Methods in Applied Sciences and Engineering", CIMNE, Oslo, Norway. doi:10.23967/eccomas.2022.020.

Maia Avelino, R., Iannuzzo, A., Van Mele, T. and Block, P. (2021), New Strategies to Assess the Safety of Unreinforced Masonry Structures Using Thrust Network Analysis, *in* "12th International Conference on Structural Analysis of Historical Constructions", CIMNE, Barcelona, Spain, pp. 2124–2135. doi:10.23967/sahc.2021.162.

Iannuzzo, A., Dell'Endice, A., Maia Avelino, R., Kao, G., Van Mele, T. and Block, P. (2021), COMPAS Masonry: A Computational Framework for Practical Assessment of Unreinforced Masonry Structures, *in* "12th International Conference on Structural Analysis of Historical Constructions", CIMNE, Barcelona, Spain, pp 1882–1892. doi:10.23967/sahc.2021.054.

Maia Avelino, R., Lee, J., Van Mele, T. and Block, P. (2021), An interactive implementation of algebraic graphic statics for geometry-based teaching and design of structures, *in* "International Fib Symposium - Conceptual Design of Structures 2021", Attisholz-Areal, Switzerland, pp. 447–454. doi:10.35789/fib.PROC.0055.2021.CDSymp.P054.

Book chapters and magazines

Maia Avelino, R., Van Mele, T. and Block, P. (2023). Advances in Thrust Network Analysis: Constrained equilibrium assessment of vaulted masonry structures, *in* C. Paolocci, D. Aita, G. Benvenuto, M. Corradi and O. Pedemonte, eds, "Edoardo Benvenuto Prize. Collection of papers", Fondazione Franzoni ETS *(to appear)*.

Maia Avelino, R., Van Mele, T. and Block, P. (2023). Thrust Network Analysis for Masonry Assessment, *in* K. Bagi, D. Aita, M. Angelillo, and A. Lemos, eds, "Discrete Computational Mechanics of Masonry Structures", Springer *(to appear)*.

Maia Avelino, R., Olivieri, C., Donval, E., Fugger, R., Lai, M., Saretta, Y., Weichbrodt, A., et al. (2022), "An Integrated Approach To The Structural Assessment Of Historic Buildings: The Case Of St. Angelo Church In Anagni", *Structural* **241**, 1–23. doi:10.12917/STRU241.13.

Monographs

Maia Avelino, R. (2018), Optimisation of Funicular Structures, Master's Thesis, École Nationale des Ponts et Chaussées, France.

Software

Maia Avelino, R. (2023), "Compas TNO: Finding admissible thrust networks in vaulted masonry structures". doi:10.5281/zenodo.7895617.